Measurement of Neutrino and Antineutrino Charged-Current Inclusive Cross Sections with the MINERνA Detector

Joshua D. Devan

Virginia Beach, Virginia

Master of Science, College of William and Mary, 2009
Master of Engineering, Old Dominion University, 2008
Bachelor of Science, North Carolina State University, 2004

A Dissertation presented to the Graduate Faculty
of the College of William and Mary in Candidacy for the Degree of
Doctor of Philosophy

Department of Physics

The College of William and Mary
January, 2016

APPROVAL PAGE

This Dissertation is submitted in partial fulfillment of
the requirements for the degree of

Doctor of Philosophy

Joshua D. Devan

Approved by the Committee, November, 2015

Committee Chair
Professor Jeffrey Nelson, Physics
The College of William and Mary

Professor Carl Carlson, Physics
The College of William and Mary

Associate Professor Michael Kordosky, Physics
The College of William and Mary

Professor Keith Griffioen, Physics
The College of William and Mary

Associate Professor M. Eric Christy, Physics
Hampton University

ABSTRACT

Neutrinos are a nearly massless, neutral particle in the Standard Model that only interact via the weak interaction. Experimental confirmation of neutrino oscillations, in which a neutrino created as a particular type (electron, muon or tau) can be observed as a different type after propagating some distance, earned the 2015 Nobel Prize in Physics. Neutrino oscillation experiments rely on accurate measurements of neutrino interactions with matter, such as that presented here. Neutrinos also provide a unique probe of the nucleus, complementary to electron scattering experiments.

This thesis presents a measurement of the charged-current inclusive cross section for muon neutrinos and antineutrinos in the energy range 2 to 50 GeV with the MINERνA detector. MINERνA is a neutrino scattering experiment in the NuMI neutrino beam at Fermilab, near Chicago. A cross section measures the probability of an interaction occurring, measured here as a function of neutrino energy. To extract a cross section from data, the observed rate of interactions is corrected for detector efficiency and divided by the number of scattering nucleons in the target and the flux of neutrinos in the beam. The neutrino flux is determined with the low-ν method, which relies on the principle that the cross section for interactions with very low recoil energy is nearly constant as a function of neutrino energy. The measured cross section is compared with world data.

TABLE OF CONTENTS

ACKNOWLEDGMENTS

[redacted].

I thank my advisor, Jeff, for his guidance and the independence he has consistently granted me over my graduate career. I thank Rik Gran for the test beam experience and his numerous contributions to my work and growth as a scientific thinker. Experiments like MINERνA are built on the work of innumerable people. I thank all of the graduate students that have come before me for developing the foundations upon which my analysis sits. I thank all of the professors and postdocs for the comments and questions that straddle the line between helpful and frustrating.

Our graduate class consists of some of the best people in the world, which exactly explains why we all intermarried and started procreating. You guys rock and Travis Horrom plays the drums.

[redacted].

LIST OF TABLES

LIST OF FIGURES

MEASUREMENT OF NEUTRINO AND ANTINEUTRINO CHARGED-CURRENT INCLUSIVE CROSS SECTIONS WITH THE MINERνA DETECTOR

CHAPTER 1

Introduction

1.1 Neutrinos and the Standard Model

The Standard Model of Particle Physics describes our best understanding of the fundamental constituents and interactions of matter. The Standard Model includes six quarks denoted by the letters u, d, s, c, b and t. The model additionally includes three charged leptons: the electron (e), muon (μ) and tau (τ). Each of these three charged leptons has a neutral partner lepton, the neutrinos, ν_μ, ν_e and ν_τ. The six quarks and six leptons each have an equivalent antiparticle. For the quarks and neutrinos, the antiparticle is denoted by a bar ($\bar{x}$). For the charged leptons, particle or antiparticle is denoted by a superscript indicating the charge ($x^{\pm}$), with positive charge being the antiparticle.

Quarks are never observed free in nature, they bind into two-quark (mesons) and three-quark (baryons) systems called hadrons. The lightest quarks, u and d, comprise protons (uud) and neutrons (udd), collectively called "nucleons". Together with the lightest lepton, the electron, this forms the familiar matter of our universe. The heavier quarks, comprising more exotic hadrons, and the heavier leptons will decay to the lightest particles (u, d, e).

The Standard Model includes three interactions: electromagnetic, strong and weak. Each of these interactions is mediated by the exchange of a gauge boson. Electromagnetic interactions, the attraction or repulsion of a charged particle in an electric field or deviation of a charged particle in a magnetic field, are mediated by the exchange of a photon (γ). The strong interaction, responsible for the formation of nucleons and the nucleus, is mediated by the exchange of a gluon (g). The weak interaction, responsible for beta decay in heavy elements, is mediated by the exchange of a charged W boson. An additional form of the weak interaction is mediated by the exchange of a neutral Z boson.

Quarks participate in all three interactions. The charged leptons participate in electromagnetic and weak interactions. Neutrinos, the focus of this dissertation, participate only in weak interactions as they possess no electric charge.

The weak interaction can proceed in two channels through the exchange of either a W or Z boson. If a W boson is exchanged, the channel is termed "charged-current" because the W carries a unit of charge. FIG. 1.1 shows the typical charged-current Feynman diagram for a neutrino scattering experiment in which a beam of ν_μ's impacts a fixed target. The ν_μ is converted to its charged lepton partner, a μ^-, by converting a d quark (charge $-\frac{1}{3}$) to a u quark (charge $\frac{2}{3}$). If a Z boson is exchanged, the channel is termed "neutral-current" because the Z carries no charge. FIG. 1.2 shows a typical diagram for a ν_μ scattering off of a target. In a neutral-current interaction, the same particles exist in the initial and final states. The probability of a neutral-current interaction is approximately one third of the equivalent charged-current interaction.

As stated before, quarks are not observed free in nature, only confined to hadrons. This complicates the simple diagrams of weak interactions presented in FIG. 1.1 and FIG. 1.2. The target quark (d for ν_μ or u for $\bar{\nu}_\mu$) is confined to a proton or neutron. The final state quark will either remain in the initial nucleon, converting between proton and neutron, or exit and hadronize, forming new final-state hadrons. Section 1.5 covers

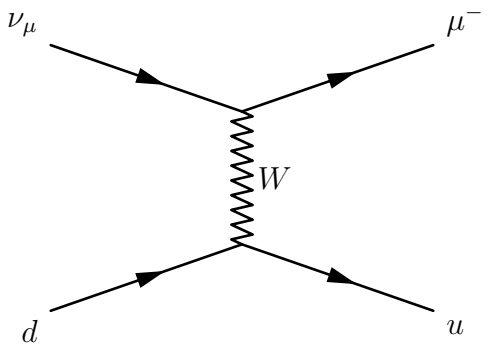

FIG. 1.1: Feynman diagram for a charged-current interaction. A ν_μ is converted to a μ^- by exchange of a W boson with a d quark (charge $-\frac{1}{3}$), which converts to a u quark (charge $\frac{2}{3}$). The W boson carries a unit of charge.

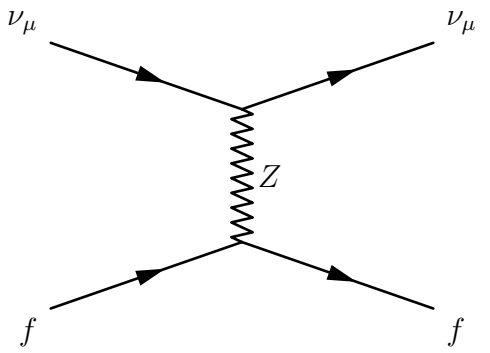

FIG. 1.2: Feynman diagram for a neutral-current interaction. A ν_μ exchanges a Z boson with either a quark or lepton, f. The same particles exist in the initial and final state. The Z boson carries no charge.

the different types of neutrino interactions and the energy scales at which they occur. Additionally, the products of the interaction must exit the nucleus and may interact while doing so. These final-state interactions mean that the particles observed in the detector may not be the same particles created by the initial neutrino interaction. The effect can be alleviated by using very light target nuclei (H or He) at the expense of reducing the interaction rate and statistical significance of the measurement.

1.2 Neutrino oscillations

Neutrinos are created abundantly in nature through fusion in stars, supernovae and the interactions of cosmic rays in the atmosphere. Fusion in the Sun creates a flux of ν_e at MeV energy scales. The impact of cosmic ray protons in the atmosphere creates pions ($u\bar{d}$ or $\bar{u}d$) that decay to ν_μ's at the GeV energy scale through the interactions $\pi^+ \rightarrow \mu^+ + \nu_\mu$ and $\pi^- \rightarrow \mu^- + \bar{\nu}_\mu$. The muons subsequently decay to electrons via the interaction $\mu^- \rightarrow e^- + \nu_\mu + \bar{\nu}_e$. Thus, for atmospheric neutrinos, the ratio of muon type to electron type, ν_μ:ν_e, is 2:1. The interaction of cosmic ray protons in the atmosphere and resulting ν_μ flux is identical to the method utilized to produce neutrino beams at accelerator facilities (Section 2.4).

Neutrinos were initially assumed massless, however experimental observation of neutrino oscillations has confirmed they possess a small, non-zero mass. Neutrino oscillations refer to a property in which a neutrino of a particular type (ν_e, ν_μ or ν_τ) can be observed as a different type after propagating some distance. The first hints of neutrino oscillations came from an observed deficit in the flux of ν_e's from solar fusion, approximately 1/3 of the predicated rate (the "solar neutrino problem"). Later, a deficit of atmospheric ν_μ's relative to ν_e's was observed (the deficit is a function of zenith angle).

Neutrino oscillations occur as a function of L/E, where L is the distance propagated

and E is the neutrino energy[1]. Oscillation experiments are only sensitive to the mass difference between two neutrino states. The absolute mass of $\bar{\nu}_e$'s is constrained by measurements of the electron spectrum in beta decay, which places the limit at $m_{\bar{\nu}_e} < 2.05\,\text{eV}$[2].

Because neutrino oscillations occur as a function of L/E, neutrino oscillation experiments must accurately reconstruct the neutrino energy, E. Doing so requires accurate models of neutrino interactions, in particular, the created final state particles and the interactions that these particles participate in while exiting the nucleus. Experiments rely heavily on neutrino interaction simulations, such as GENIE (Section 7.3), which tune their models based on inclusive cross section data.

1.3 Cross sections

Given a beam of particles impacting a target, a cross section gives the probability for an interaction between an incident particle and a target nucleon. The cross section, σ, is measured in units of $(\textit{length})^2$. For this thesis, the cross section is measured as a function of incident neutrino energy, E.

The interaction rate in the target per unit time, $N(E)$, is given by

$$N(E) = \Phi(E) \times \sigma(E) \times T, \tag{1.1}$$

where $\Phi(E)$ is the incident flux, the number of particles crossing a unit area per unit time, and T is the number of nucleons in the target. $\Phi(E)$ is measured in units of $1/[(\textit{length})^2 \times \textit{time}]$. In order to experimentally measure a cross section, the observed interaction rate is corrected for detector inefficiency to derive $N(E)$, which is then divided

by the flux, $\Phi(E)$, and number of target nucleons, T,

$$\sigma(E) = \frac{N(E)}{\Phi(E) \times T}. \tag{1.2}$$

FIG. 1.3 shows world experimental measurements of the cross section for charged-current inclusive scattering of a ν_μ and $\bar{\nu}_\mu$ on a nucleon. "Inclusive" means that all types of interactions and final state kinematics are included. The cross section on protons and neutrons is different, owing to the differing quark content. Here "nucleon" means the average of the cross section on a proton and a neutron. This would be measured explicitly on an isoscalar target which has an equal number of protons and neutrons (Section 6.4.6).

The charged-current cross section for neutrinos and antineutrinos is linear with neutrino energy at high neutrino energy (equivalently, $\sigma(E)/E$ is constant). As the name implies, the weak interaction is very weak. The mean free path, λ, is given by $\lambda = 1/(\sigma n)$, where n is the number of nucleons per unit volume. At 1 GeV, the mean free path for a neutrino is nearly 2×10^{10} miles of lead. Neutrino experiments only succeed with very massive detectors and intense neutrino sources in order to achieve statistically-significant interaction rates.

1.4 Kinematics

FIG. 1.4 shows the kinematic variables for neutrino-nucleon scattering. A ν_μ or $\bar{\nu}_\mu$ of momentum k_1 scatters off a nucleon of momentum P and mass M, resulting in a $\mu^\pm$ of momentum k_2 and some recoil final state. The recoil final state could be a nucleon in a ground or excited state or any spectrum of hadrons (Section 1.5).

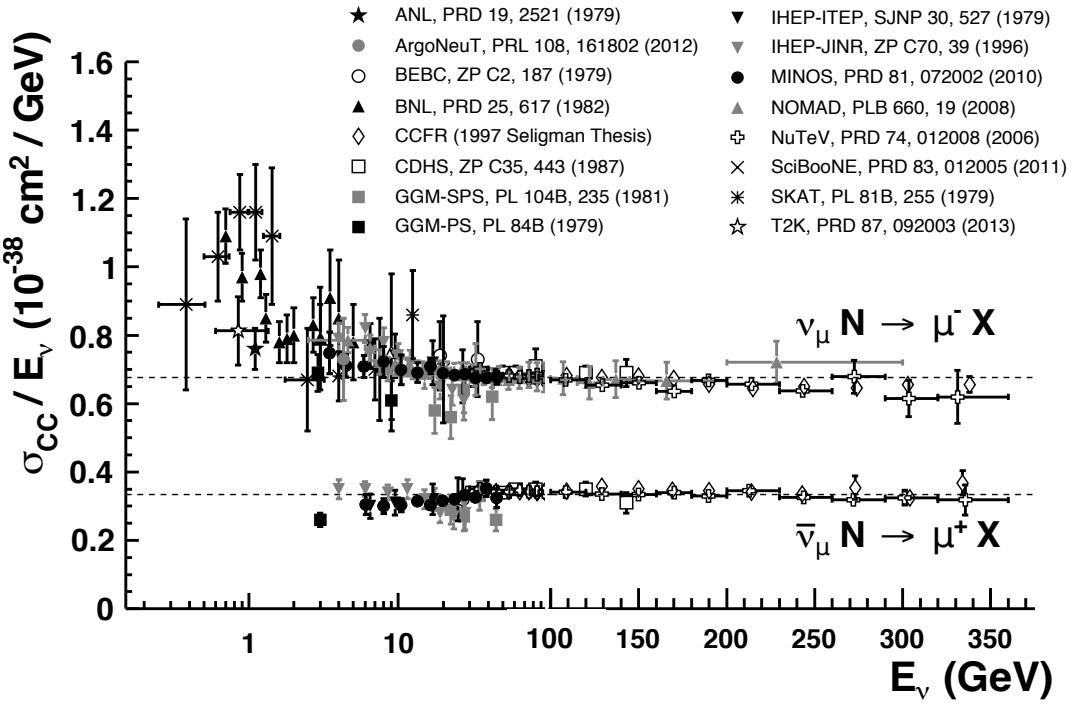

FIG. 1.3: Experimental measurements of the ν_μ and $\bar{\nu}_\mu$ charged-current inclusive cross sections divided by neutrino energy as a function of neutrino energy[1]. At high neutrino energy, $\sigma(E)/E$ is approximately constant. The results of this thesis are not yet included.

The momentum transfer to the nucleon, Q^2, is defined as

$$Q^2 \equiv -q^2 = -(k_1 - k_2)^2. \tag{1.3}$$

The energy transfer to the recoil system, ν, is defined as

$$\nu \equiv \frac{P \cdot q}{M}. \tag{1.4}$$

The Bjorken scaling variable, x, is defined as

$$x \equiv \frac{Q^2}{2P \cdot q}. \tag{1.5}$$

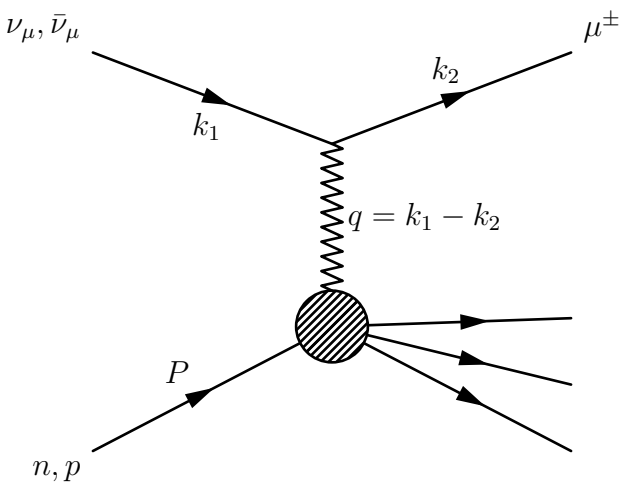

FIG. 1.4: Kinematic variables for neutrino-nucleon scattering. A ν_μ or $\bar{\nu}_\mu$ of momentum k_1 scatters off a nucleon of momentum P and mass M, resulting in a $\mu^\pm$ of momentum k_2 and some recoil final state.

The inelasticity, y, is defined as

$$y \equiv \frac{P \cdot q}{P \cdot k_1}. \tag{1.6}$$

The invariant mass of the recoil system, W, is defined as

$$W^2 \equiv (P + q)^2. \tag{1.7}$$

In a fixed target experiment, the nucleon is at rest, $P = (M, 0, 0, 0)$, and the kinematic variables simplify to

$$\nu = E - E_\mu \tag{1.8}$$

$$x = \frac{Q^2}{2M\nu} \tag{1.9}$$

$$y = \frac{\nu}{E} \tag{1.10}$$

$$W^2 = M^2 + 2M\nu - Q^2, \tag{1.11}$$

where E is the energy of the incoming neutrino and E_μ is the energy of the outgoing muon.

1.5 Neutrino interactions

Analogous to a microscope, the momentum transfer to the nucleon, Q^2, sets the resolving power of the neutrino scattering on a nucleon. At low Q^2, the neutrino "sees" the nucleon as whole rather than comprised of individual quarks. The nucleon will remain intact (quasi-elastic scattering) or be raised to an excited state (resonance production). As Q^2 increases, the individual quarks within the nucleon are visible, but they are still bound within the nuclear medium. At high Q^2, the neutrino sees individual, free quarks (deep inelastic scattering).

1.5.1 Quasi-elastic scattering (QE)

Quasi-elastic scattering occurs when the struck nucleon remains intact, but is ejected from the nucleus. The signature of the event is a muon plus a single proton or neutron in the detector (neglecting final-state interactions). In the case of a neutrino, the interaction is $\nu_\mu + n \to \mu^- + p$; the neutron is converted to a proton by the conversion of a d quark (charge $-\frac{1}{3}$) to a u quark (charge $\frac{2}{3}$). In the case of an antineutrino, the interaction is $\bar{\nu}_\mu + p \to \mu^+ + n$.

1.5.2 Resonance production

Resonance production occurs when the struck nucleon raised to an excited state that promptly decays to a nucleon and a pion. The lightest and most prominent resonance is

the Delta, with a mass of 1.232 GeV. Delta production occurs via these interactions:

$$\nu_\mu + p \to \mu^- + \Delta^{++} \to \mu^- + p + \pi^+ \tag{1.12}$$

$$\nu_\mu + n \to \mu^- + \Delta^{+} \to \mu^- + n + \pi^+ \quad \text{or} \quad \mu^- + p + \pi^0 \tag{1.13}$$

$$\bar{\nu}_\mu + p \to \mu^+ + \Delta^{0} \to \mu^+ + n + \pi^0 \quad \text{or} \quad \mu^+ + p + \pi^- \tag{1.14}$$

$$\bar{\nu}_\mu + n \to \mu^+ + \Delta^{-} \to \mu^+ + n + \pi^- \tag{1.15}$$

The lifetime of the Delta resonances is on the order of 10^{-24} s, so the particle is not observed in the detector, only the nucleon and pion resulting from the decay.

1.5.3 Deep inelastic scattering (DIS)

Deep inelastic scattering occurs when the momentum transfer is sufficient enough that the neutrino interacts with a quasi-free quark within the nucleon. The quark is ejected and hadronizes, forming a spectrum of final state hadrons. The theory of DIS is simplest because the neutrino interacts with a point particle, but the final states can be very complex with many particles. Recoil energy will be carried by charged pions, neutral pions which decay electromagnetically, neutral particles that are invisible in the detector and strange (containing an s quark) mesons and hadrons. FIG. 5.13 – 5.20 show the spectrum of final-state particles generated in the simulation; DIS events are at higher ν.

1.5.4 Summary

FIG. 1.5 shows experimental measurements of the ν_μ quasi-elastic, resonance production and inclusive cross sections versus the prediction from NEUGEN[3]. The inclusive cross section is the sum of quasi-elastic scattering, resonance production and deep inelastic scattering. At low neutrino energy, the interactions are exclusively quasi-elastic,

peaking at 400 MeV. As the neutrino energy rises to the Delta resonance (1.232 GeV), the resonance production cross section peaks. At very high neutrino energy, the interactions become almost exclusively deep inelastic scattering.

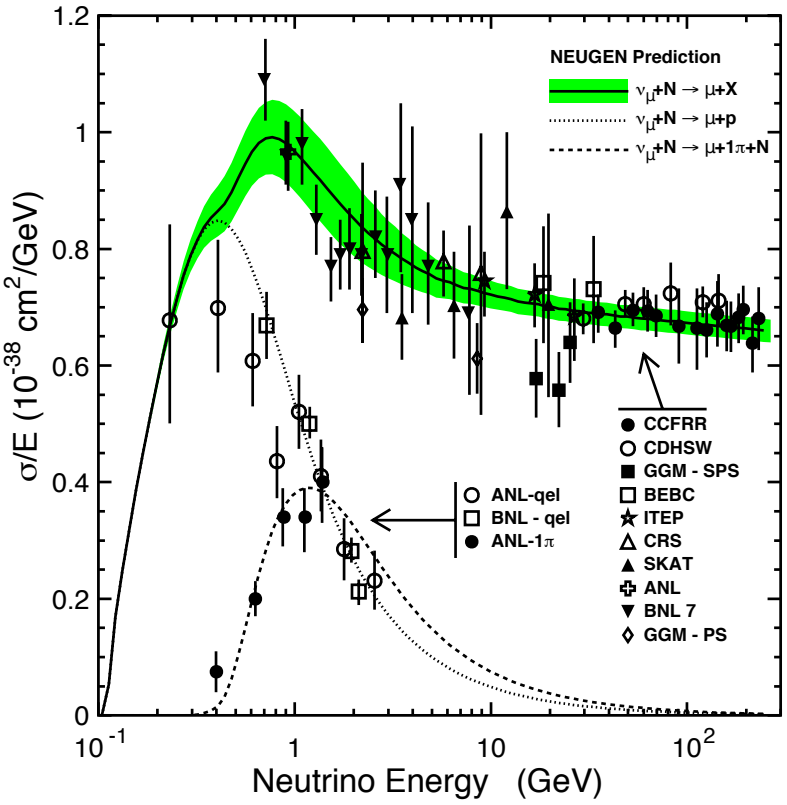

FIG. 1.5: Experimental measurements of the ν_μ quasi-elastic, resonance production and inclusive cross sections divided by neutrino energy versus NEUGEN prediction. The dotted line is quasi-elastic scattering. The dashed line is resonance production. The solid line is inclusive (quasi-elastic, resonance production and deep inelastic scattering).[3]

CHAPTER 2

The MINERνA Experiment

2.1 Overview

MINERνA is a neutrino-scattering experiment in the NuMI beamline at the Fermi National Accelerator Laboratory, near Chicago. MINERνA is designed to measure:

1. **Cross sections** – Neutrino and antineutrino cross sections for inclusive scattering on various nuclei and specific processes (quasi-elastic scattering, charged and neutral pion production, electron neutrino quasi-elastic, etc.).

2. **Final states** – The products of a neutrino interaction and how they are affected by final-state interactions exiting the nucleus.

3. **Nuclear effects** – The effects of the atomic number (Z) and mass (A) of the target nucleus on neutrino interactions. This is achieved by placing multiple heavy targets in the upstream portion of the detector (carbon, lead, iron and water).

The MINERνA detector is a finely-segmented solid-scintillator tracking calorimeter consisting of a fully-active tracking region surrounded by electromagnetic and hadronic

FIG. 2.1: Photograph of an individual scintillator strip (left) and a cross section of the 17 mm thick scintillator plane (right.)

calorimeters (Section 2.2). The detector is capable of tracking final-state particles for moderate multiplicity events, identifying electromagnetic showers from π^0 decays or ν_e scattering, and calorimetrically reconstructing large recoil showers. The MINERνA detector is located immediately upstream of the MINOS detector, which serves as a muon spectrometer (Section 2.3). The two detectors are located in the NuMI neutrino beamline, which delivers an intense, broad spectrum (1 GeV to tens of GeV) neutrino beam (Section 2.4). The beamline can be set to produce either ν_μ's or $\bar{\nu}_\mu$'s.

The detector design and calibration and reconstruction performance are extensively documented in a Nuclear Instruments and Methods article[4].

2.2 MINERνA detector

The MINERνA detector is constructed of a stack of hexagonal modules, supported on a frame along the axis of the neutrino beam. The core of the modules is a 17 mm thick, 2.5 m point-to-point hexagonal plane constructed of 127 triangular scintillator strips arranged in an alternating orientation. FIG. 2.1 shows a photograph of an individual scintillator strip and a cross section of a scintillator plane. The triangular profile allows for precise tracking by considering the charge-sharing between adjacent strips. The orientation of the strips between adjacent planes is rotated by 60° to facilitate three-dimensional reconstruction of multiple particle trajectories.

The detector is divided into five regions:

1. **Tracker** – The tracker is comprised of 62 modules, each constructed of two scintillator planes. The six outer edges of the planes are covered by a 15 mm wide, 2 mm thick lead collar which is utilized for electromagnetic calorimetry of particles exiting the side of the detector. The fully-active tracker region is additionally utilized as the target for studies of neutrino interactions on scintillator. The scintillator planes are comprised of 87.6% carbon, 7.4% hydrogen, 3.2% oxygen and 1.8% miscellaneous by mass[4].

2. **Electromagnetic calorimeter (ECAL)** – The ECAL is comprised of 10 modules, each constructed of two scintillator planes with a 2 mm thick lead sheet covering the entire surface of each plane. The ECAL is located immediately downstream of the tracker.

3. **Hadronic calorimeter (HCAL)** – The HCAL is comprised of 20 modules, each constructed of a single scintillator plane preceded by a 1 in. thick steel absorber sheet covering the entire surface of the plane. The HCAL is located immediately downstream of the ECAL.

4. **Nuclear targets** – The nuclear target region is located immediately upstream of the tracker and contains targets of carbon, lead, iron, water and liquid helium. The carbon, lead and iron targets are implemented as specialized modules constructed of a single target plane the full size of a scintillator panel. The hexagonal shape is divided among the three materials[4]. The water target is also a specialized module with two round kevlar skins forming a bladder for containing water. The carbon, lead, iron and water targets are each separated by four tracker modules (8 planes) for accurately reconstructing vertices into the targets. A cryostat upstream of the module stack contains 0.25 tons of liquid helium. A veto wall is utilized to remove contamination from muons originating from neutrino interactions in the rock upstream of the detector (rock muons) which are incorrectly reconstructed as neutrino interactions in the upstream targets.

5. **Outer detector (OD)** – The OD is a 56 cm wide (orthogonal to the beam) hexagonal steel frame that surrounds the inner detector. The OD provides both support to the inner module structure and is utilized for hadronic calorimetry of particles exiting the side of the detector. Four rectangular scintillator bars are embedded in each of the six sides of the OD steel frame.

FIG. 2.2 shows a drawing of one tracker module of the MINERνA detector. FIG. 2.3 shows a side view of the entire MINERνA detector, showing the nuclear target region, tracker, ECAL, HCAL and OD. The MINOS detector is immediately downstream of the detector.

Scintillation light caused by ionization by charged particles is captured by a wavelength-shifting (WLS) fiber inserted into a hole in the center of each strip (visible in FIG. 2.1). The WLS fiber extends the full length of the strip. Any empty space in the hole is filled with a transparent, injected epoxy. The WLS fibers connect to clear fibers which are connected to a unique channel on a 64 channel photomultiplier tube (PMT). The signal on each channel of the PMT is read by a front end board (FEB) which connects to the data acquisition system (DAQ)[5]. The readout system records the photoelectrons at each channel of the PMT as a function of time over the gate. The amplitude of the signal indicates the scale of the deposited energy. The timing of the signal is used to separate multiple neutrino interactions over the duration of the gate. Chapter 5 covers the reconstruction of neutrino interactions and the energy scale calibration of the detector.

FIG. 2.4 shows a neutrino interaction in the detector in one view of the detector (one of the three orientations of the strips in the planes). The color of each triangle indicates the magnitude of the energy deposition in each strip.

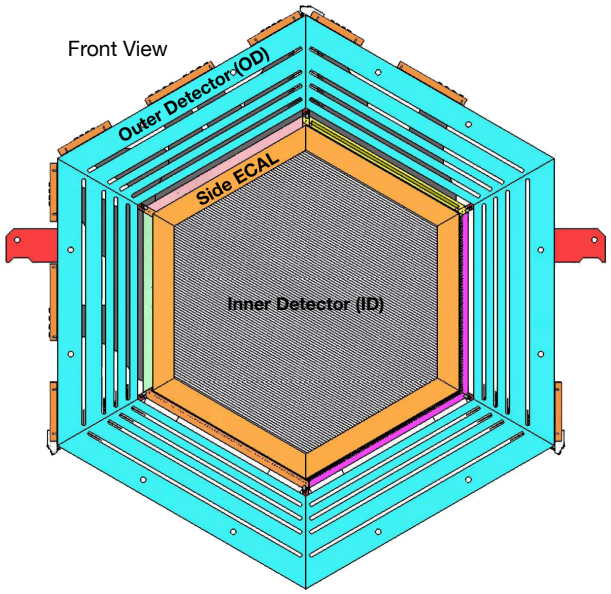

FIG. 2.2: Drawing of one tracker module in the MINERνA detector. The inner detector consists of a scintillator plane (gray) surrounded by a lead collar (orange) for electromagnetic calorimetry. The outer detector (teal) surrounds the inner detector providing support and hadronic calorimetry.

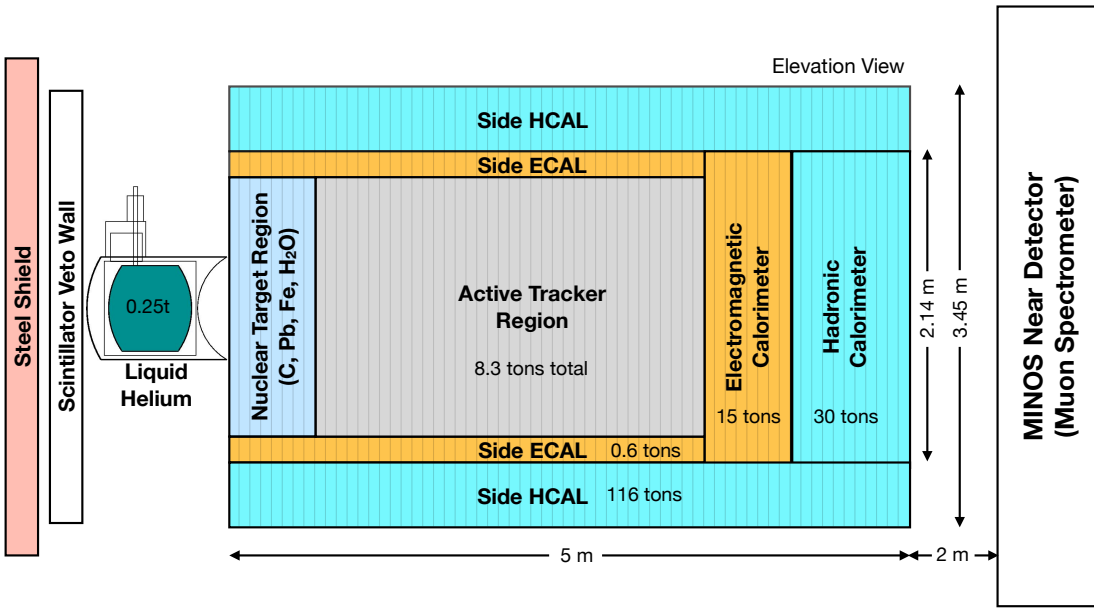

FIG. 2.3: Side view of the MINERνA detector; beam enters from the left. From left to right, the detector is divided into a nuclear targets region (veto wall, cryostat and module targets), tracker, electromagnetic calorimeter and hadronic calorimeters. The MINOS near detector is located immediately downstream.

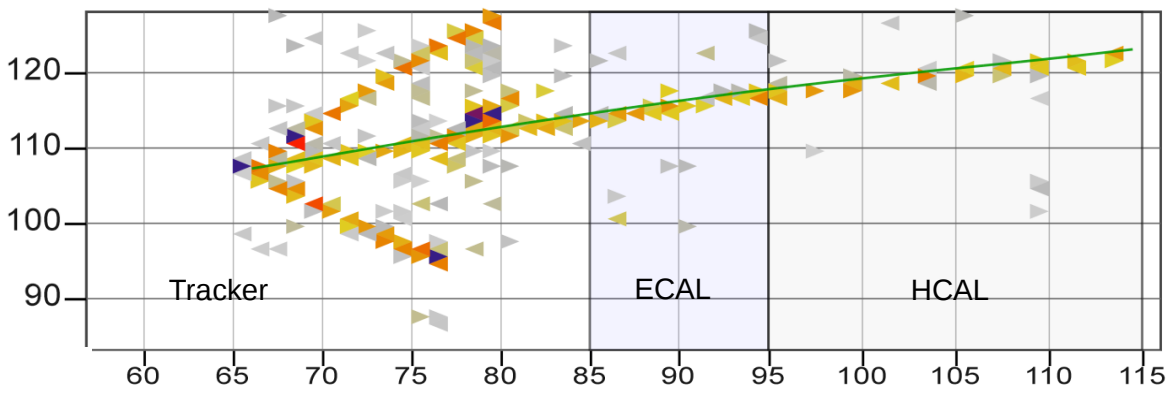

FIG. 2.4: Event display of a neutrino interaction in the MINERνA detector. The color of each triangle indicates the magnitude of the energy deposition in each scintillator strip. A green line indicates the reconstructed muon trajectory.

2.3 MINOS detector

The MINOS experiment[6] is designed to measure neutrino oscillations via ν_μ or $\bar{\nu}_\mu$ disappearance. The experiment consists of two detectors, a near detector located at Fermilab and a far detector located 735 km away at the Soudan Underground Laboratory in northern Minnesota.

The MINERνA detector is placed 2.1 m upstream of the MINOS near detector. The MINOS near detector serves as a muon spectrometer for rear-exiting muons from neutrino interactions in MINERνA. Section 5.4 describes the muon reconstruction algorithm, which finds tracks in MINERνA and matches them to tracks in MINOS.

The MINOS near detector is constructed of a stack of 282 steel plates of 1 in thickness. The steel plates are magnetized by a coil embedded in the entire length of the detector creating a toroidal magnetic field of 1.3 T. The field polarity is set to focus μ^- when the beam is set to produce ν_μ and μ^+ when the beam is set to produce $\bar{\nu}_\mu$. Particles in the detector are tracked by 1 cm thick, 4.1 cm wide scintillator strips alternating by 90° between adjacent planes. An upstream calorimeter region, which serves as the target for neutrino interactions, is fully instrumented with scintillator. A downstream muon spectrometer

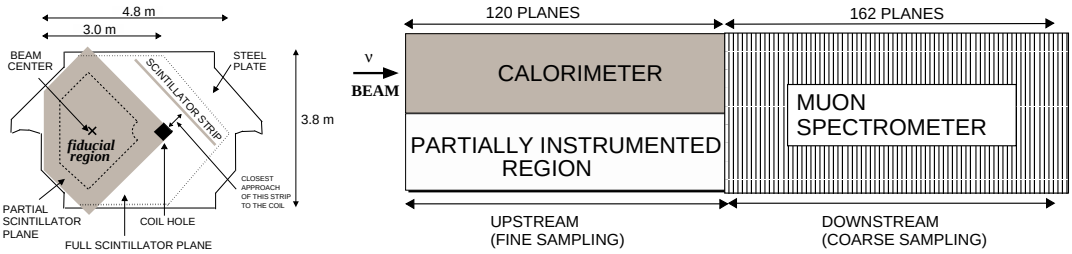

FIG. 2.5: Drawing of one plane of the MINOS near detector (left) and a top view of the detector (right). Beam enters from the left.

region is more sparsely instrumented. FIG. 2.5 shows a drawing of one plane and a top view of the detector.

MINOS determines muon energy by either the range that the muon penetrates in the detector or the curvature of the track in the magnetic field. A range-based measurement is more accurate; the systematic uncertainty is dominated by the uncertainty on the mass of the detector. For muons that exit the detector, the curvature of the track is used to measure momentum. The curvature is inversely proportional to the momentum of the muon. In either case, the curvature of the track, whether it is focused or defocused by the magnetic field, determines the reconstructed charge of the muon.

2.4 NuMI beamline

The NuMI beamline at Fermilab produces an intense, broad spectrum beam of ν_μ's or $\bar{\nu}_\mu$'s. The beam is produced by colliding 120 GeV protons from the Main Injector accelerator on a thick, complex graphite target (FIG. 2.6). The resulting pions and kaons are focused by a pair of magnetic focusing horns. Protons are collided in a 10 μs window every 2.2 s. The horn current is pulsed during this window and the polarity is used to select a primarily ν_μ or $\bar{\nu}_\mu$ beam. The pions and kaons decay in a 675 m, helium filled decay pipe, producing neutrinos. The muons resulting from the decays are stopped by 240 m of rock before the detector hall. FIG. 2.7 shows a diagram of the NuMI beamline.

FIG. 2.8 shows a site plan of the NuMI facility. The MINERνA and MINOS detectors are stationed in the detector hall located 105 m underground in the axis of the beam.

An important feature of the NuMI beamline is that the horn and target positions can be varied to change the energy spectrum of the resulting neutrino beam. FIG. 2.9 shows the neutrino flux for different horn and target positions. LE-10, in which the target is 10 cm from full insertion into the horn, is the nominal configuration for low energy analyses, such as this dissertation. NuMI has recently moved to a higher energy tune for the NOνA experiment.

2.5 MINERνA test beam

In order to validate the simulation of low energy (less than a few GeV) hadrons and electrons in the MINERνA detector, the collaboration developed a test beam experiment. The MINERνA test beam placed a small version of the MINERνA detector in a tertiary beamline at the Fermilab Test Beam Facility. The experiment measured the single particle response of hadrons and electrons in the detector. The project required the development of a new tertiary beamline to produce, identify and momentum-analyze incident particles. The beam is primarily protons and pions, with a small electron and even smaller kaon content. The beamline is documented in Chapter 3. The detector and analysis is documented in Chapter 4.

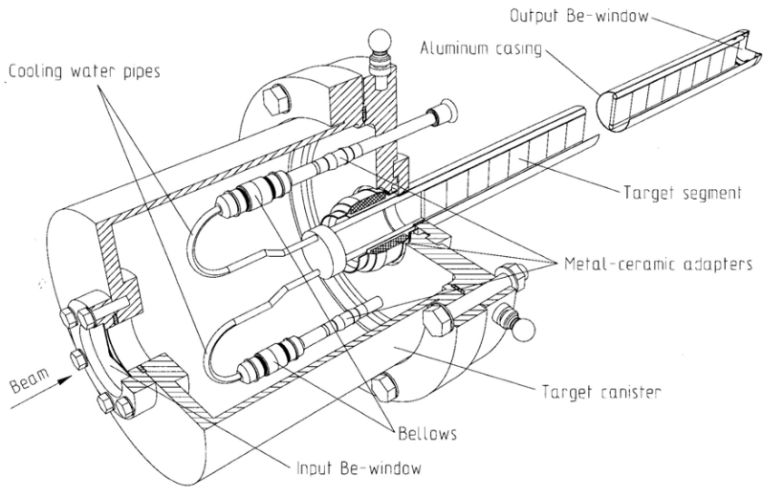

FIG. 2.6: Drawing of the NuMI target. The target is comprised of 47 segments, each 20.0 mm long, 6.4 mm wide and spaced at 0.3 mm. The segments are mounted to a stainless steel cooling pipe. The entire target is contained in a canister with beryllium beam windows and filled with helium.[7]

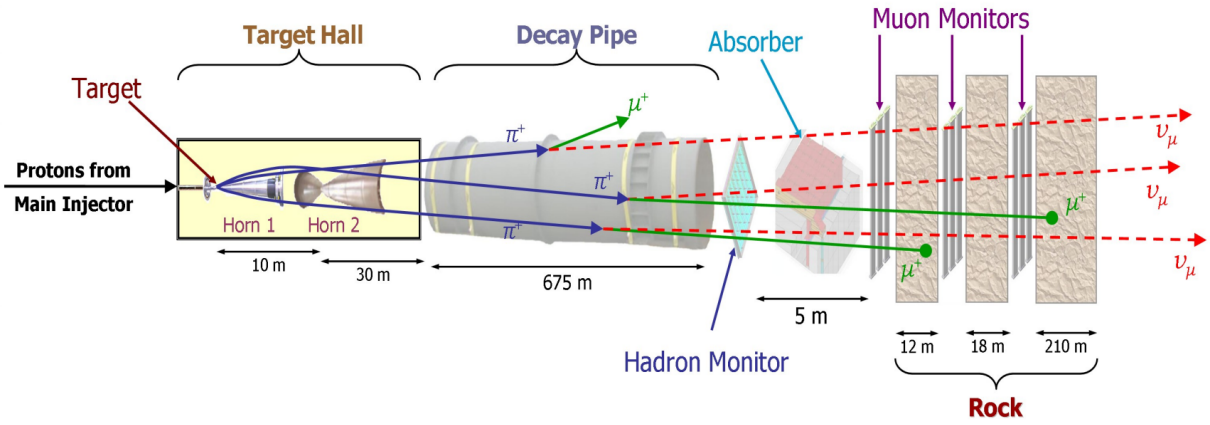

FIG. 2.7: Diagram of the NuMI beamline.[8]

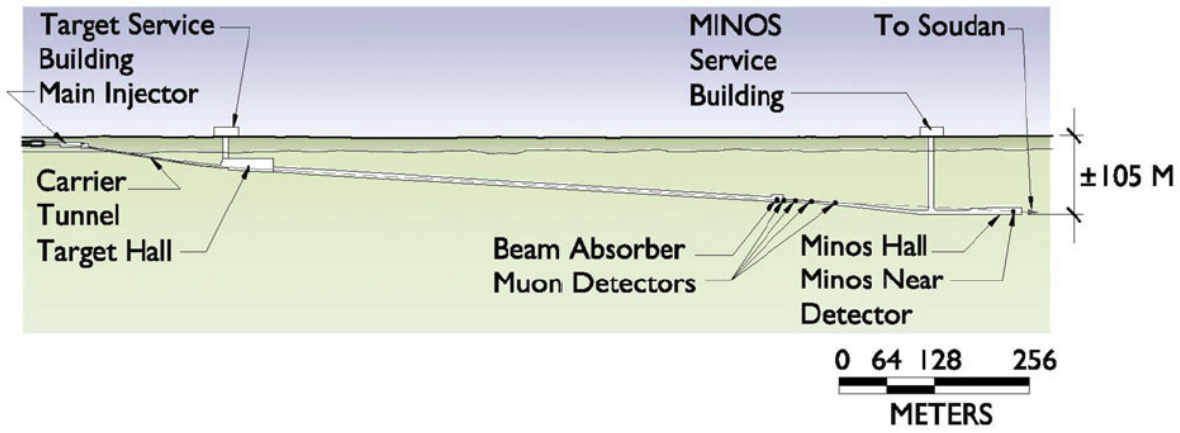

FIG. 2.8: Site plan of the NuMI facility. The MINERνA and MINOS detectors are located in the detector hall on the right, 105 m underground.[7]

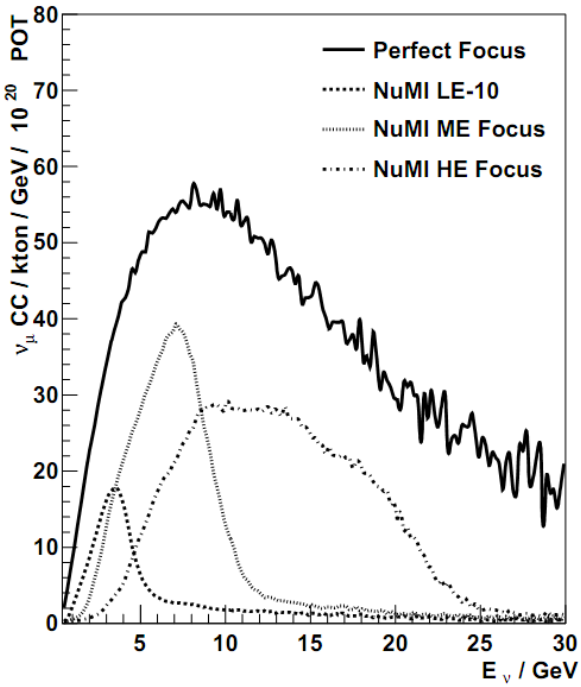

FIG. 2.9: NuMI neutrino flux for different horn and target positions. The solid line (Perfect Focus) is a hypothetical configuration in which every pion is focused onto the beam axis. NuMI LE-10 is the nominal configuration for low energy analyses, such as this dissertation.[8]

CHAPTER 3

Test Beam Beamline

3.1 Physical description

The test beam beamline consists of a target and collimator and two pairs of wire chambers upstream and downstream of a pair of dipole magnets (see photograph in FIG. 3.1 and diagram in FIG. 3.2). Particle momentum is reconstructed by fitting a trajectory through the four chambers and a calculated field map for the dipole magnets. A time-of-flight (TOF) system, consisting of an upstream scintillator paddle on the rear of the collimator and a downstream scintillator wall on the rear of wire chamber 4 (WC4), allows for particle identification. The beamline is approximately 6 m in length from upstream to downstream TOF with a 115 MeV/c transverse momentum kick delivered by the magnetic field.

The Fermilab Test Beam Facility provides a beam of secondary pions at a selected energy and intensity to impact the target. Secondary pions are created by colliding 120 GeV protons from the Main Injector upstream of the facility. For the Summer 2010 run, the secondary beam was tuned to 16 GeV pions at an intensity of 300 k per spill, delivered

once per minute in a 4 s window.

The four wire chambers were initially constructed for the HyperCP experiment[9]. The upstream pair are identical with an aperture of 457 mm × 254 mm and a wire pitch of 1.016 mm. The downstream pair are identical with an aperture of 559 mm × 305 mm and a wire pitch of 1.270 mm. The chambers are constructed of four wire planes, X, U, V and X'. The X and X' planes are aligned vertically with a half wire pitch offset between the two. The U and V planes are aligned at $\pm 26.6^\circ = \pm \arctan(1/2)$ from vertical. The wire pitch, measured orthogonal to the wire direction, is uniform between all planes in a chamber. The readout system for the chambers identifies only whether each wire was hit or not hit in each gate, but provides no additional timing or pulse amplitude information. The material in each wire chamber is 0.2% of a radiation length; the air in the beamline is approximately 2% of a radiation length.

3.2 Reconstruction

The beamline reconstruction begins by searching each plane of each chamber for single wire hits, or two adjacent wire hits, with at least 10 unhit wires to either side. Two adjacent wire hits are merged into a single virtual wire located between the two.

Local, two-dimensional hit positions are reconstructed by identifying wire hits in all four planes consistent with a particle crossing the chamber. The algorithm tests all combinations of wire hits, one hit for each of the four planes, for a common intersection. The intersection is marked as the hit position. The procedure is then repeated for all combinations of three planes. Multiple hits in a chamber occur often, particularly in the upstream chambers, from pile-up in the beamline. FIG. 3.3 shows two events in the beamline. Wire hits are drawn in color; reconstructed hit positions are marked with a circle.

FIG. 3.1: Photograph of the test beam beamline. Secondary pions enter from the left.

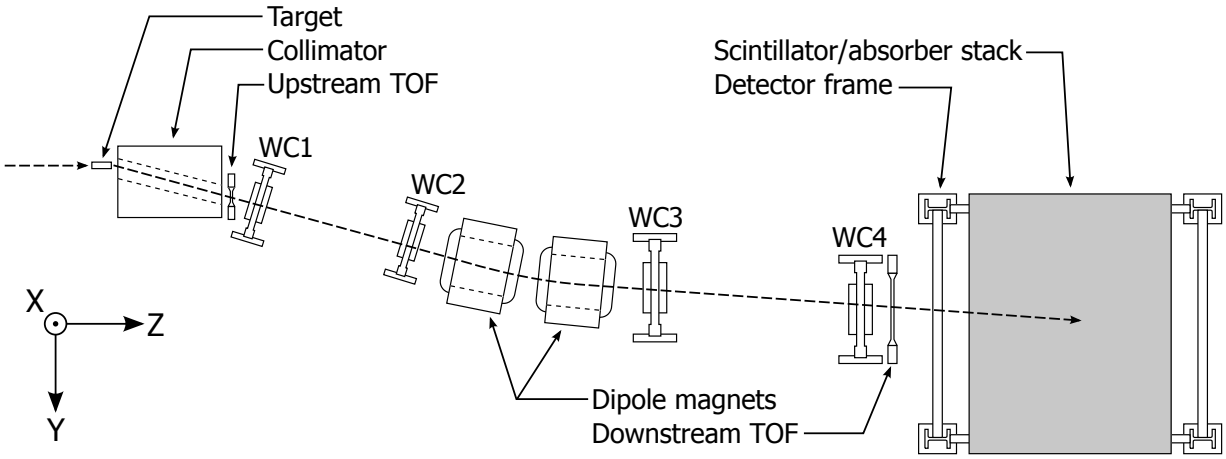

FIG. 3.2: Diagram of the test beam beamline viewed from above. Secondary pions enter from the left.

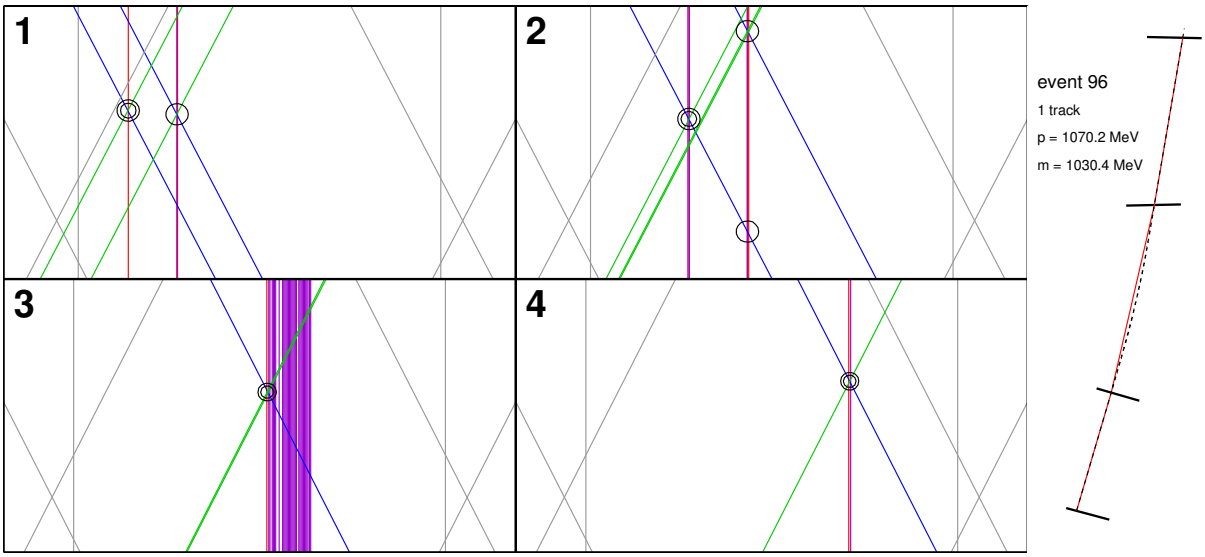

(a) Proton event, $p = 1.1\,\mathrm{GeV/c}$

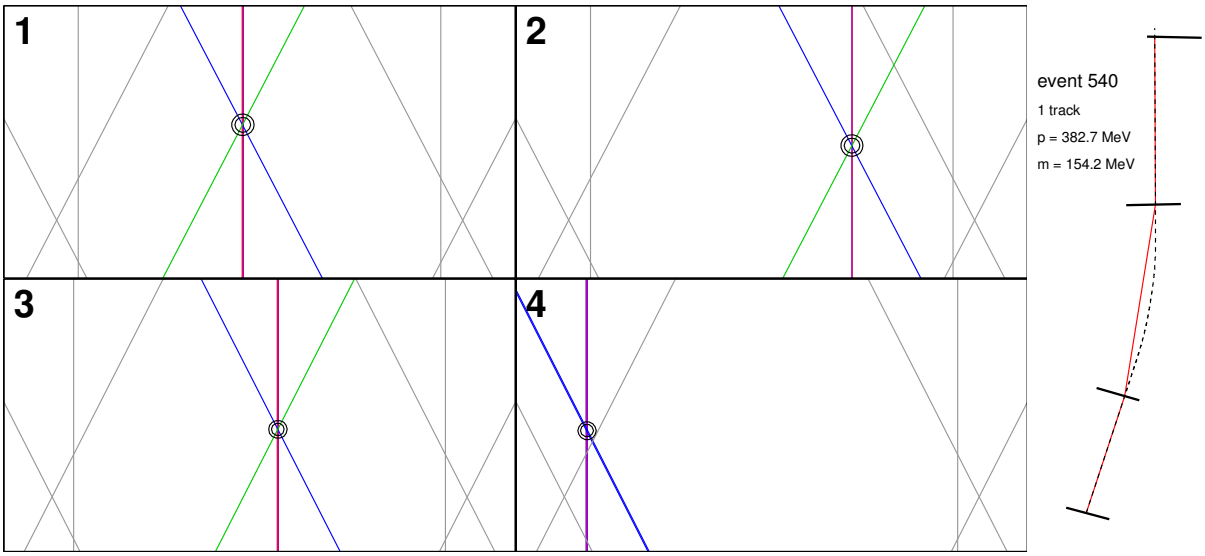

(b) Pion event, $p = 383\,\mathrm{MeV/c}$

FIG. 3.3: Beamline event displays. Wire hits are drawn in color within the four chambers; the limits of the wire planes are drawn in gray. Reconstructed hit positions are marked with a circle; the hit position incorporated in the track is marked with a double circle. On the right, a red line connects the hit position in each chamber; the fit path through the field is marked with a dashed line. In chamber 3 of the upper display, a δ-ray results in a string of adjacent wire hits, which the beamline ignores and proceeds with the remaining three planes of the chamber.

Upstream tracks are formed from all combinations of reconstructed hit positions in the first two chambers, one hit per chamber. The tracks are projected to the collimator and magnet apertures and those falling outside are discarded. The procedure is repeated to form downstream tracks without the collimator projection.

Upstream and downstream tracks are merged by projecting to a plane in the center of the two magnets and verifying a common intersection.

Events with a single merged track are passed to the momentum fitter. The momentum fitter takes a fixed initial trajectory marked by the two upstream chambers (WC1 and WC2) and varies only the momentum as it propagates the particle through the magnetic field to minimize the residual (the distance between the point at which the fit path intersects a chamber and the observed hit position) at WC3. The propagation is performed with a Runge-Kutta stepper at 1 mm increments through a field map created with ANSYS finite-element analysis software. The decision to fit only the residual at WC3 and not at WC4 is explained in Section 3.3.

A particle mass is calculated with the fit momentum and observed time of flight from the TOF system. Offsets in the time of flight from cable length and electronic delays are calibrated per run by aligning the pion and proton mass peaks to accepted values. A particle identification is performed using a combination of mass and TOF cuts to identify pions, kaons, protons, deuterons and electrons.

Events are flagged that pass a set of "loose" and "strict" quality cuts. The loose cuts require a single track passing all four chambers, a valid momentum fit (the fit converges), a maximum magnetic field error integral (the error is set non-zero in the more questionable regions of the field map) and a valid TOF reading. The strict cuts further impose a tighter magnetic field error integral, a cut on the minimum and maximum magnetic field integral, and a maximum fit χ^2. In the Summer 2010 run, 43% of events passed the loose quality cuts; 30% passed the strict cuts. The loose quality events are used for analyses by default,

with the strict events used to evaluate systematic uncertainties. 108,879 events pass the loose cuts; 75,366 events pass the strict cuts.

The reconstructed momentum spectrum is plotted in Figure 3.4, reconstructed momentum versus time of flight in Figure 3.5 and reconstructed mass spectrum in Figure 3.6.

3.3 Momentum resolution

The momentum resolution of the beamline is limited by multiple scattering in the air and chamber material and by non-uniformities in the magnetic field. The deviations from the ideal path at WC4 are the quadrature sum of those at WC3 plus the multiple scattering from WC3 and the air between WC3 and WC4. For this reason, the reconstructed momentum resolution is improved by fitting only the residual at WC3. The residual at WC4 is utilized to validate the multiple scattering model and to evaluate alignment systematics (Section 3.4).

The deviations from multiple scattering and field non-uniformities are modeled event by event with a Kalman filter[10]. The Kalman filter does not model the curvature of the path through the magnetic field; it assumes a straight path with the path lengths and field integral calculated by the momentum fitter. The deviations are taken as perturbations to the ideal fit path. The straight path assumption relies on the magnetic field integral being nearly constant for the small deviations resulting from multiple scattering and field non-uniformities. The Kalman filter calculation is performed separately for the horizontal and vertical coordinates.

The calculation relies on a particle species hypothesis and therefore must be performed after a mass is calculated. The results of the Kalman filter do not influence the momentum fit. The algorithm is run afterwards to compute the momentum resolution per event.

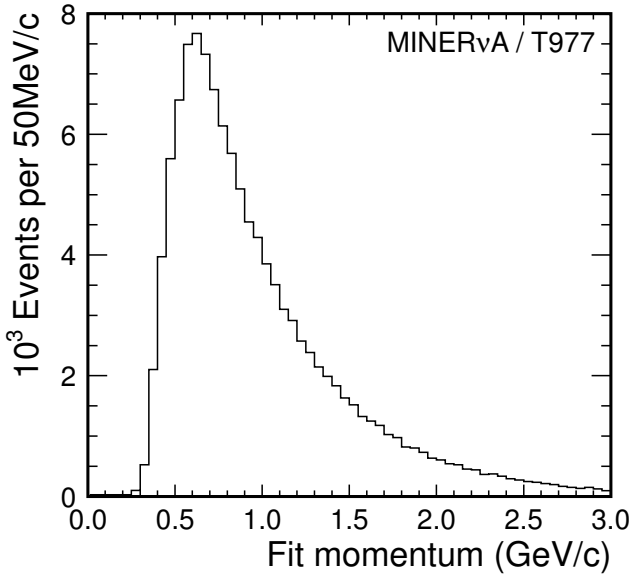

FIG. 3.4: Reconstructed momentum spectrum of all particle species for the Summer 2010 run.

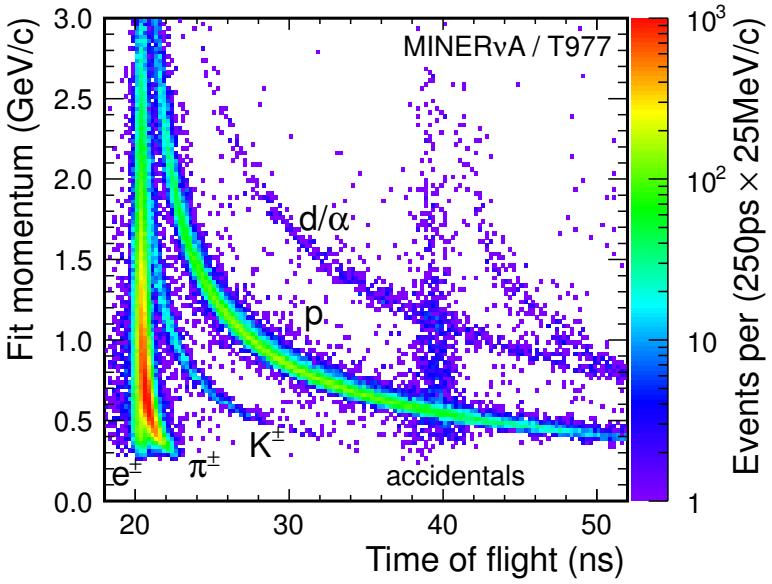

FIG. 3.5: Reconstructed momentum versus time of flight for the Summer 2010 run. The particle species is indicated. The shadow at +19 ns is an artifact of the accelerator beam structure, in which one particle triggers the upstream TOF, but another in a later accelerator bucket triggers the downstream TOF.

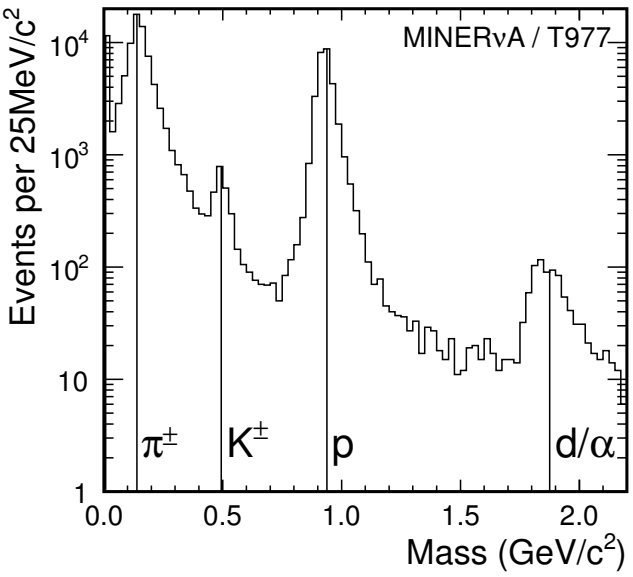

FIG. 3.6: Reconstructed mass spectrum for the Summer 2010 run. The width of the peaks is driven by the ∼250 ps resolution of the TOF system. Vertical lines are drawn at the accepted mass.

The Kalman filter state vector, $\mathbf{x}$, is defined as:

$$\mathbf{x} = \begin{bmatrix} x \\ \theta \end{bmatrix} \tag{3.1}$$

where x is the transverse position deviation from the ideal path and θ is the angle of the particle momentum vector relative to ideal. x and θ are defined to be in either the horizontal or vertical plane.

The initial covariance, $\mathbf{P}_0$, is defined as:

$$\mathbf{P}_0 = \begin{bmatrix} L & 0 \\ 0 & L \end{bmatrix} \tag{3.2}$$

where L is a large number (10^6), reflecting that no information is known about the initial

position or angle. The initial covariance is defined at the collimator. The Kalman filter then performs four steps to the four chambers, updating the covariance matrix with each step.

The state transition model, $\mathbf{F}$, is defined as:

$$\mathbf{F} = \begin{bmatrix} 1 & h \\ 0 & 1 \end{bmatrix} \tag{3.3}$$

where h is the step length from collimator to chamber, or chamber to chamber, as computed by the momentum fitter along the curved path. The state transition model corresponds to a simple linear projection.

The process noise covariance, $\mathbf{Q}$, is defined as:

$$\mathbf{Q} = \mathbf{Q}_1 + \mathbf{Q}_2 \tag{3.4}$$

$$\mathbf{Q}_1 = \begin{bmatrix} h^2\theta_{\text{Al}}^2 & h\theta_{\text{Al}}^2 \\ h\theta_{\text{Al}}^2 & \theta_{\text{Al}}^2 \end{bmatrix} \tag{3.5}$$

$$\mathbf{Q}_2 = \begin{bmatrix} h^2\theta_{\text{air}}^2/3 & h\theta_{\text{air}}^2/2 \\ h\theta_{\text{air}}^2/2 & \theta_{\text{air}}^2 \end{bmatrix} \tag{3.6}$$

$\mathbf{Q}_1$ describes the multiple scattering from a chamber; $\mathbf{Q}_2$ describes the scattering from air. The chambers function as point scatterers, hence the position and angular deviation at the next chamber are absolutely correlated. For scattering in air, position and angle are only partially correlated because the scattering can occur at any point along the track. θ_{Al} and θ_{air} are the one sigma width of the angular deviation from multiple scattering by

aluminum and air, respectively, given by[1]:

$$\theta_0 = \frac{13.6\,\mathrm{MeV}}{\beta cp} z\sqrt{x/X_0}\Big[1 + 0.038\ln\left(x/X_0\right)\Big] \tag{3.7}$$

where $v = \beta c$ is the particle velocity, p is the momentum, z is the charge of the particle and x/X_0 is the thickness of the scatterer in radiation lengths.

The observation model, $\mathbf{H}$, is defined as:

$$\mathbf{H} = \begin{bmatrix} 1 & 0 \\ 0 & 0 \end{bmatrix} \tag{3.8}$$

reflecting that only the position, not the angle, can be measured by a chamber.

The observation noise covariance, $\mathbf{R}$, is defined as:

$$\mathbf{R} = \begin{bmatrix} \mathrm{WP}^2/N & 0 \\ 0 & 1 \end{bmatrix} \tag{3.9}$$

where WP is the wire pitch scaled by a factor, N. For a uniform distribution of width w, the variance is given by $w^2/12$. For a single X plane in the chambers, we expect $N = 12$ for the uncertainty on the horizontal position (orthogonal to the wire direction). Including a single U or V plane, $N = 12/5 = 2.4$ for the vertical uncertainty (from the vertical distance between two adjacent U or V wires). The chambers, however, are constructed of multiple wire planes, so we expect better than this. In practice, N dominates the expected deviations at large momentum, when multiple scattering is small, so N is adjusted to match the data.

In the predict phase of the Kalman filter, the predicted covariance, $\mathbf{P}'$, is given by:

$$\mathbf{P}' = \mathbf{F}\mathbf{P}\mathbf{F}^{\mathrm{T}} + \mathbf{Q} \tag{3.10}$$

In the update phase, the updated covariance, $\mathbf{P}$, is given by:

$$\mathbf{S} = \mathbf{H}\mathbf{P}'\mathbf{H}^{\mathrm{T}} + \mathbf{R} \tag{3.11}$$

$$\mathbf{K} = \mathbf{P}'\mathbf{H}^{\mathrm{T}}\mathbf{S}^{-1} \tag{3.12}$$

$$\mathbf{P} = (\mathbf{I} - \mathbf{K}\mathbf{H})\mathbf{P}' \tag{3.13}$$

where $\mathbf{S}$ is the measurement covariance, $\mathbf{K}$ is the optimal Kalman gain and $\mathbf{I}$ is the identity matrix. The measurement covariance, $\mathbf{S}$, is the uncertainty between the projected and measured (fit and observed) state. $\sqrt{\mathbf{S}(0,0)}$ is the one sigma width of the residual from multiple scattering and field non-uniformities. The updated covariance, $\mathbf{P}$, is the uncertainty after including the measured hit at a chamber, but before considering scattering by that chamber.

To a good approximation, the fit momentum, p, is given by:

$$p = \frac{p_t}{\theta} \tag{3.14}$$

where p_t is the transverse momentum kick from the magnetic field, equal to the field integral times the charge of the particle and θ is the bend angle between the upstream and downstream tracks. p_t is typically $\sim$115 MeV/c for unit charge particles in the beamline.

The reconstruction takes the initial particle trajectory at WC1 and WC2 as fixed and varies the momentum to minimize the residual at WC3. The fixed initial trajectory and small non-primary components (primary is global X) of the magnetic field force the vertical

residuals at WC3 and WC4 effectively at a linear projection from upstream. By varying the momentum, the horizontal residual at WC3 will approach zero (within the permitted range of the momentum and without negating the charge of the particle). This leaves three residuals with which to evaluate the multiple scattering and field non-uniformity model: the vertical residual at WC3 and both the horizontal and vertical residuals at WC4.

FIG. 3.7 – 3.9 show the normalized residuals (residual over one sigma uncertainty) for the three samples on the left. On the right, the one sigma width of a Gaussian fit to the residual as a function of momentum times velocity, $p \times v$, is plotted for pions (blue), protons (red) and combined (black). Multiple scattering, as calculated in Eq. 3.7, is a function of $p \times v$, so pions and protons overlap on this plot (though protons populate the lower values as the two particles have roughly the same momentum spectrum, but the velocity term is lower for protons). The Kalman filter prediction for the one sigma width of the residual ($\sqrt{\mathbf{S}(0,0)}$ from above) is plotted in purple.

In order to achieve agreement with the data, two parameters of the Kalman filter were tuned. The first is the scale on the wire pitch term, N in Eq. 3.9, which sets the uncertainty in the high momentum limit. For the horizontal residual, N was left at the predicted value of 12. For the vertical residuals, N was raised to 3, slightly better than the predicted value of 2.4. The second parameter accounts for the non-uniformities of the magnetic field, which is only present in the horizontal residual from the primary component of the field.

One can imagine that the calculated magnetic field map is too ideal; that the true field has non-uniformities from the composition or geometry of the steel, such as the upper or lower surface of the magnet aperture deviating from flat. These inconsistencies produce regions of high or low field. A particle traversing the field would experience more or less transverse force, causing the particle to effectively scatter. The deviations can occur anywhere along the track so we expect the correlations between position and angle to be

similar to those from multiple scattering. To include field non-uniformities in the Kalman filter, the multiple scattering from air between WC2 and WC3, θ_{air} in Eq. 3.6, was scaled for the horizontal residual. It was found that raising θ_{air} by 30% fit the residuals at WC4 observed in the beamline data.

However, when the momentum resolution implied by this was utilized to smear events in our simulation, it was observed that the smearing in simulation was greater than in data. The observation was made with the range of the stropping proton sample used for the Birks' parameter analysis (Section 4.11). Tuning to the stopping proton sample found that θ_{air} was best left at the nominal value, with no scaling. It thus under-predicts the width of the residual at WC4.

FIG. 3.10 shows the fit χ^2, defined as the quadrature sum of the three normalized residuals. A fit to the data finds the number of degrees of freedom to be nearly 3, as expected from the sum of three Gaussians of unity width.

An uncertainty on the fit momentum is calculated for each event by taking the derivative of Eq. 3.14 with respect to θ,

$$\mathrm{d}p = -\frac{p_t}{\theta^2}\mathrm{d}\theta = -\frac{p^2}{p_t}\mathrm{d}\theta, \tag{3.15}$$

where p_t is computed by the field integral from the momentum fitter. $\mathrm{d}\theta$ is taken to be the one sigma width of the horizontal residual at WC3 ($\sqrt{\mathbf{S}(0,0)}$) divided by half the path length from WC2 to WC3. If you imagine the downstream track rotating as a result of the uncertainty at WC3, this places the pivot point at roughly the center of the two magnets. The half path length assumption was confirmed with a sample in which the hit position at WC3 was explicitly shifted in the reconstruction by the uncertainty and a new momentum was fit.

FIG. 3.11 shows the fractional momentum resolution as a function of momentum.

Multiple scattering and field non-uniformities limit the momentum resolution to a few percent, but contribute no systematic bias.

3.4 Alignment uncertainties

The analysis of the alignment of the wire chambers in the test beam beamline is a twofold problem. The first is the internal alignment; the relative positions of the four planes within a chamber and the position of those planes within the frame of the chamber. The second is the external alignment; the positions of the chambers within the hall, in particular, relative to the detector.

The relative alignment of the four planes within a chamber can be validated for the horizontal axis (the more important axis in calculating particle momentum) by comparing the local X coordinate computed only from the X plane, the X' plane, or a combination of the U and V planes. The difference in local X for each combination of planes versus the particle's angle of incidence is plotted in FIG. 3.12. This plot contains an angle of incidence correction which accounts for the planes of the wire chamber being separated in Z, along the particle's trajectory. The angle of incidence correction corrects to X at the center of the chamber, between the U and V planes (the planes are stacked X, U, V, X', upstream to downstream). The deviations plane to plane are $\sim$0.2 mm at worst.

The uncertainty on the relative positions of the wire chambers within the hall can be constrained with three data samples:

1. **Magnet off, beam muons** – With the beam dump in place, the detector is sprayed with muons resulting from pion decays in the secondary beam. This sample was primarily used in the energy scale calibration of the detector, but we also triggered events in the beamline. The muons travel along the global Z axis, intersecting chambers 2, 3,

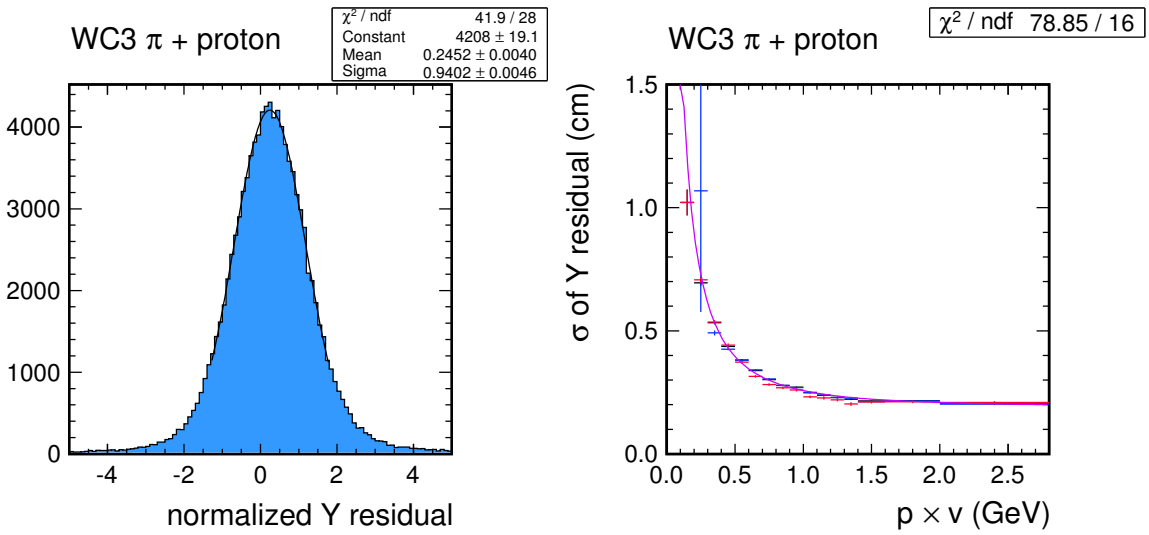

FIG. 3.7: **Left:** WC3 normalized Y (vertical) residual, equivalent to the difference between the fit trajectory and the observed hit location on the wire chamber, normalized by the uncertainty from multiple scattering per event. Pions and protons combined. All momenta. $\sigma \approx 1$ indicates that scattering is well modeled. **Right:** One σ width of a Gaussian fit to the residual for pions (blue), protons (red) and both (black) versus $p \times v$. Kalman filter prediction in purple.

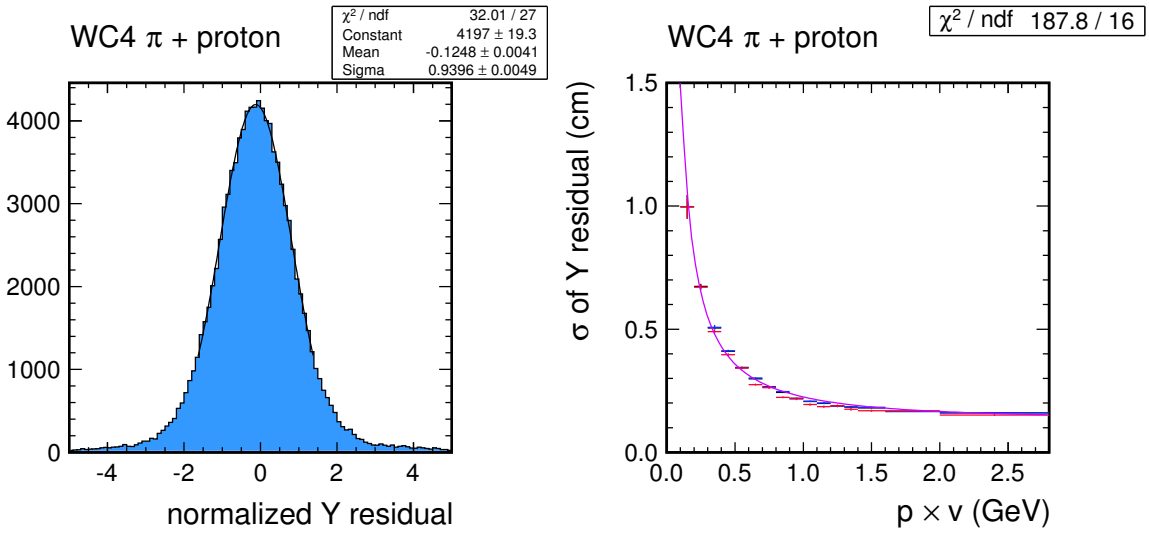

FIG. 3.8: **Left:** WC4 normalized Y (vertical) residual, equivalent to the difference between the fit trajectory and the observed hit location on the wire chamber, normalized by the uncertainty from multiple scattering per event. Pions and protons combined. All momenta. $\sigma \approx 1$ indicates that scattering is well modeled. **Right:** One σ width of a Gaussian fit to the residual for pions (blue), protons (red) and both (black) versus $p \times v$. Kalman filter prediction in purple.

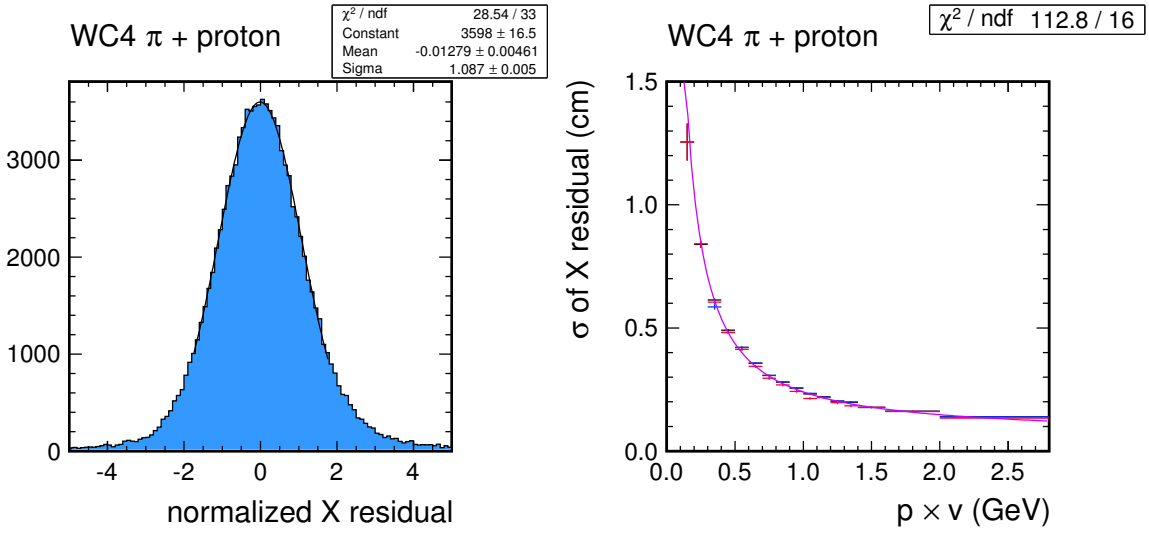

FIG. 3.9: **Left:** WC4 normalized X (horizontal) residual, equivalent to the difference between the fit trajectory and the observed hit location on the wire chamber, normalized by the uncertainty from multiple scattering per event. Pions and protons combined. All momenta. $\sigma \approx 1$ indicates that scattering is well modeled. **Right:** One σ width of a Gaussian fit to the residual for pions (blue), protons (red) and both (black) versus $p \times v$. Kalman filter prediction in purple.

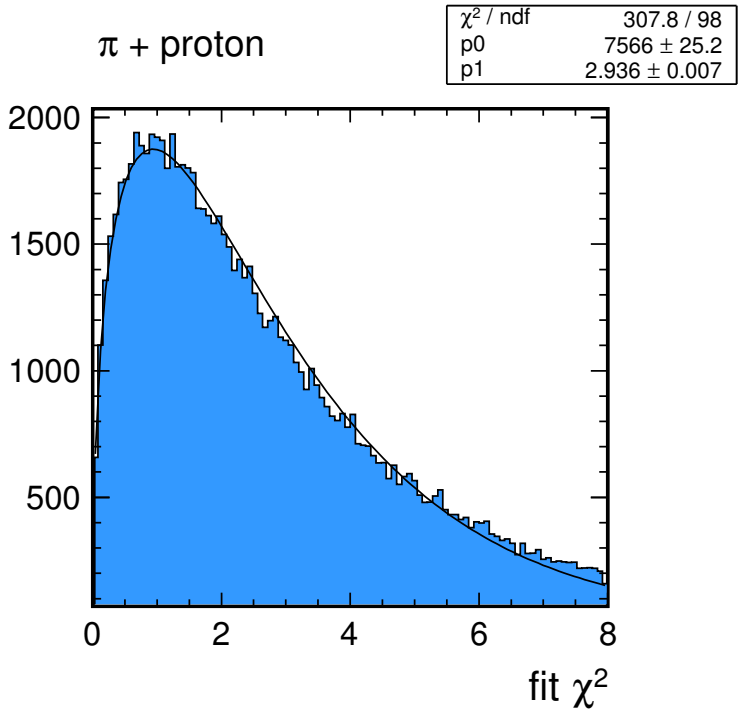

FIG. 3.10: Momentum fit χ^2, defined as the quadrature sum of the three normalized residuals (FIG. 3.7 – 3.9). The data is fit to a χ^2 distribution; $p0$ is a scale, $p1$ is the number of degrees of freedom. $p1 \approx 3$ indicates that scattering is well modeled.

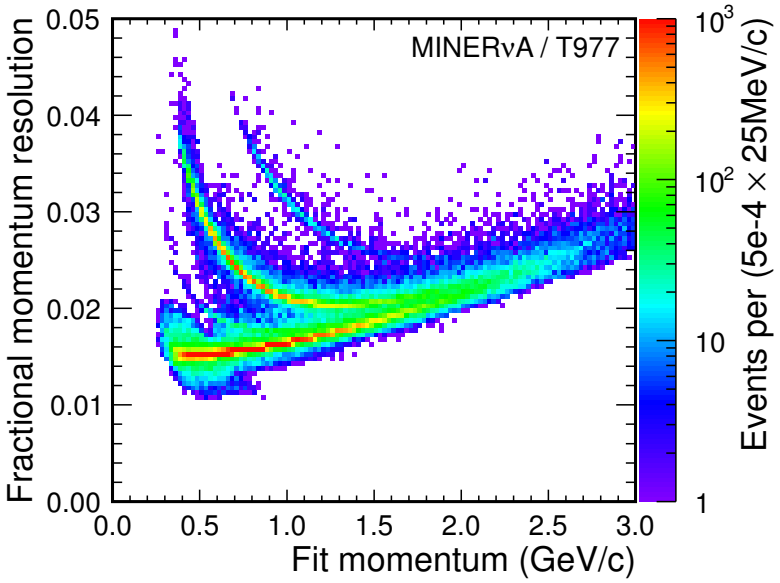

FIG. 3.11: Fractional momentum resolution versus reconstructed momentum from the scattering model of the beamline. The bands correspond to particle species, with the lowest uncertainty on pions, then kaons, protons, and deuterons.

and 4. FIG. 3.13 plots the residual observed at WC2 from the projection of WC3 and WC4. The statistics are very low in this sample.

2. **Magnet off, tertiary beam particles** – We recorded a small set of tertiary beam particles with the magnets disabled. These emerge from the collimator and pass through chambers 1, 2 and 3. FIG. 3.14 shows the residual observed at WC3 from the projection of WC1 and WC2.

3. **Magnet on, tertiary beam particles** – This sample has, obviously, the highest statistics, but is complicated by the curvature of the particle trajectory through the magnetic field. FIG. 3.15 plots the residual observed at WC4, defined as the intersection of the path from the momentum fitter minus the observed hit.

One cannot determine a unique set of alignment corrections from this data. A shift of any one chamber is degenerate with shifting the other three in the opposite direction. Translations and rotations of the entire beamline will not affect the observed residuals

or calculated momentum. Vertical translations have a negligible affect on momentum, so alignment is restricted to the horizontal direction. The chambers were surveyed at three points on the frame, separated by $\sim$0.5 m, so uncertainties on the angles of the chambers are negligible.

The alignment of the beamline is restricted to only shifting two chambers. A third could be effectively shifted by fixing the position of the fourth and rotating the entire beamline, which has no affect on momentum. In practice, it is chosen to align the two upstream chambers so that the projections of tracks onto the detector, set by the two downstream chambers, is not affected. The projected tracks have previously been aligned by observing the trajectories of particles in the detector relative to the projection from the beamline.

The final alignment correction for WC2 is set by the beam muon data, 1.3 mm along the local X (horizontal) axis. The position for WC1 was then shifted to align the tertiary beam data, both magnet on and off. The final alignment correction of WC1 is identical to WC2, 1.3 mm. This might allude to the relative alignment of the planes within the chamber frame; the two upstream chambers are identical, but different than the two identical downstream chambers.

The change in reconstructed momentum after performing the alignment is momentum-dependent, 1% per GeV/c, which is taken as the systematic uncertainty.

The final uncertainty of the beamline alignment is the position of the dipole magnets relative to the chambers. This was estimated by shifting the magnets 5 mm along the beam axis resulting in a momentum shift of 0.5%, taken as the uncertainty. The 5 mm shift arises from the uncertainty of the survey measurement of the magnet positions.

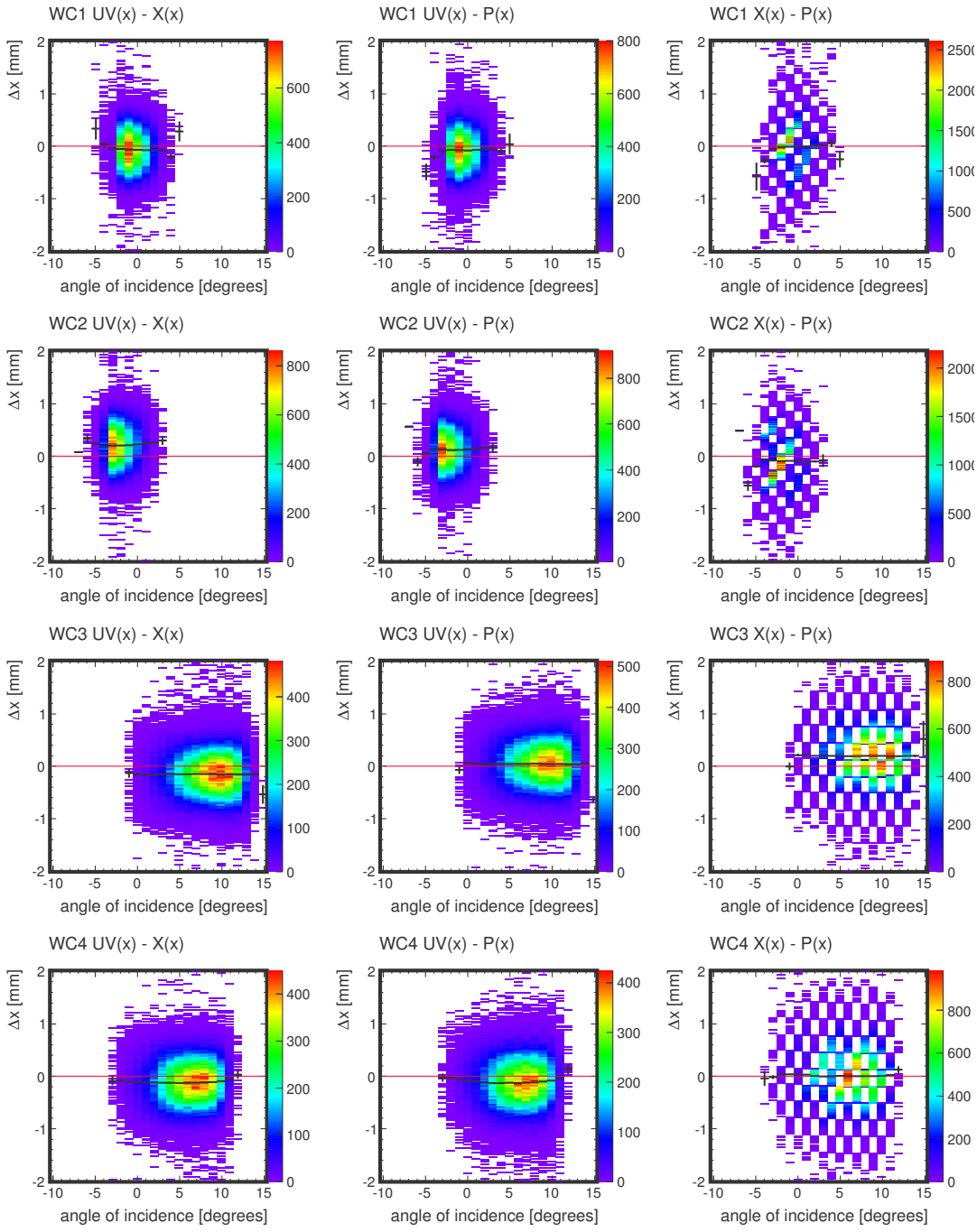

FIG. 3.12: Relative alignment of the four planes within the four wire chambers, plotted as the difference in local X (horizontal) calculated from the X plane, U & V planes and X' plane (labeled "P" in the titles) versus angle of incidence after the angle of incidence correction. The profile of the distribution is shown in black. The checkered pattern on the right occurs because the difference in X and X' is limited to discrete multiples of the wire pitch, but is shifted and smeared by the angle of incidence, binned on the horizontal axis of the plot.

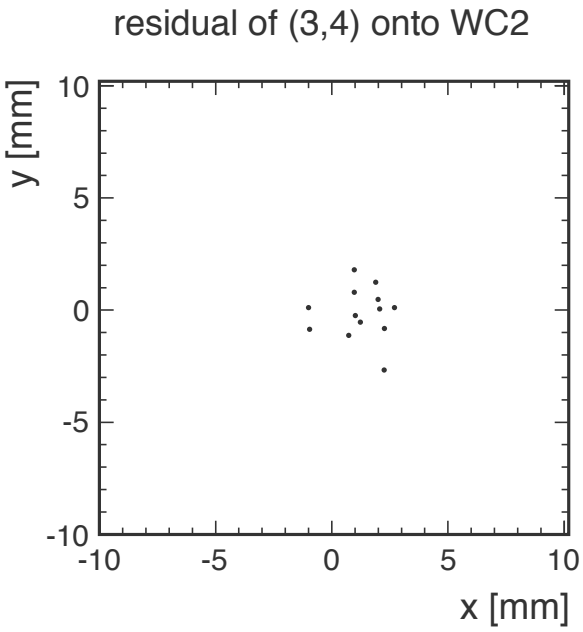

FIG. 3.13: WC2 residual for beam muon, magnet off data. The vector from WC3 and WC4 is projected onto WC2 and the difference to the observed hit plotted (before alignment corrections). Mean X (horizontal) is 1.3 mm; mean Y (vertical) is -0.2 mm.

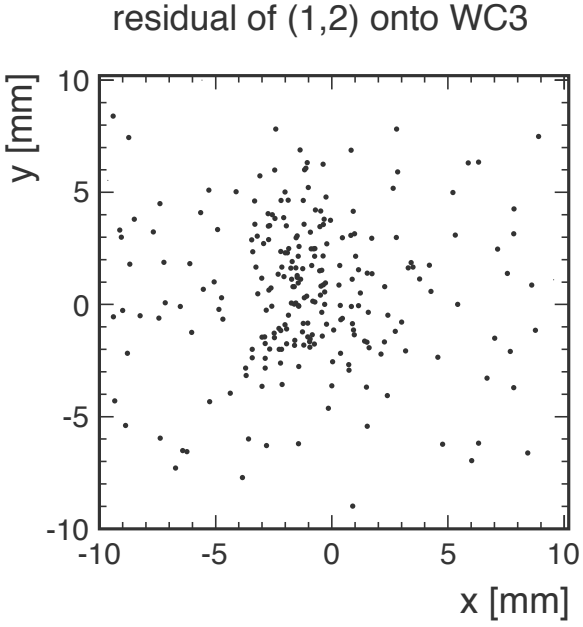

FIG. 3.14: WC3 residual for tertiary beam, magnet off data. The vector from WC1 and WC2 is projected onto WC3 and the difference to the observed hit plotted (before alignment corrections). Mean X (horizontal) is -1.0 mm; mean Y (vertical) is 0.7 mm.

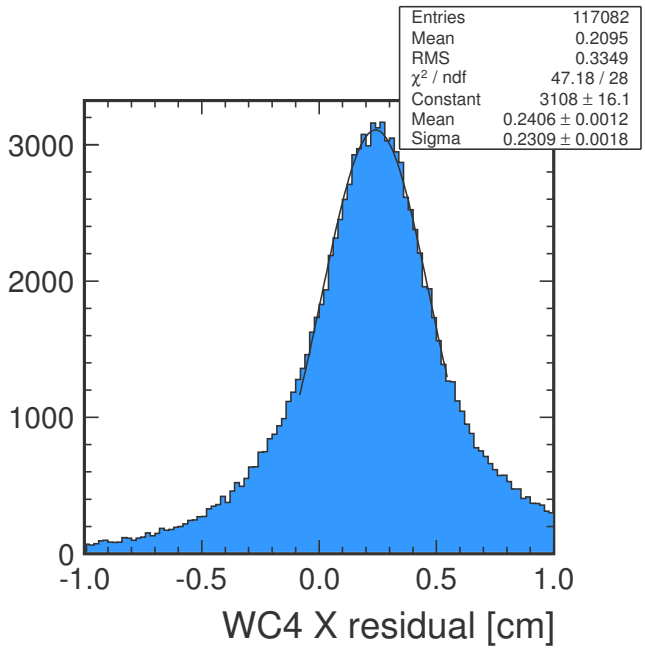

FIG. 3.15: WC4 horizontal residual for tertiary beam, magnet on data. The residual is the intersection from the momentum fit minus the observed hit (before alignment corrections). Mean X (horizontal) is 2.1 mm.

3.5 Magnetic field uncertainties

The magnetic field map utilized for momentum reconstruction is produced by ANSYS finite-element analysis software which calculates the magnetic field vector in a three dimensional space at discrete points spaced 5 mm apart. The calculated field map is validated with measurements performed with a three axis Hall probe at 1 in spacing on a peg board placed in the magnet aperture. The calculated field is scaled down by 0.9942 to equal the measured field in the magnet aperture, then scaled up by 1.003 to account for the slightly higher current employed during data collection.

The calculated and measured magnetic field profile show tension in the longitudinal extent of the magnetic field[11]. This could arise simply from the simulated dimensions of the magnets. The extent of the field directly affects the field integral along a particle's trajectory and thus the reconstructed momentum. The observed discrepancy is consistent

with a 0.5% uncertainty on reconstructed momentum.

Various other magnetic field uncertainties were evaluated (dimensions, relative placement of the two magnets, B/H curves)[11] and found to contribute an additional 0.5% uncertainty.

3.6 Systematic uncertainty summary

The systematic uncertainties on reconstructed momentum in the test beam beamline are summarized in Table 3.1.

Wire chamber alignment	1.0% per GeV/c
Magnet alignment	0.5%
Magnetic field longitudinal extent	0.5%
Other magnetic field errors	0.5%
Quadrature sum	1.0% at 500 MeV/c, 1.3% at 1 GeV/c

TABLE 3.1: Summary of systematic uncertainties on reconstructed momentum in the test beam beamline.

CHAPTER 4

Test Beam Proton Calorimetry

4.1 Overview

The MINERνA test beam experiment is designed to calibrate and validate the simulation of low energy (less than a few GeV) hadrons and electrons in the MINERνA detector. Properly simulating these particles is essential to developing algorithms to reconstruct neutrino interaction kinematics, particularly setting the energy scale for calorimetry (Section 5.6).

The test beam detector is a small version of the larger MINERνA detector, which was exposed to a wide band beam of protons and pions with a small electron content. The species, momentum and trajectory of each particle impacting the detector is measured by the upstream beamline (Chapter 3). The goal of the test beam experiment is to measure single particle response, thus the intensity of the beam is set to deliver approximately one particle per 16 μs readout window.

The final states of few-GeV neutrino interactions are dominated by protons, neutrons, charged pions ($\pi^{\pm}$) and neutral pions (π^0). In many analyses, the energy of these particles

is reconstructed calorimetrically (Section 5.6). The analysis of calorimetry of protons and pions in the test beam detector sets the systematic uncertainty on calorimetric reconstruction of the recoil energy in MINERνA analyses (Section 7.8). External measurements are utilized to constraint the uncertainty of neutron response[12]. The response of neutral pions, which rapidly decay to a pair of photons creating electromagnetic showers, is constrained by reconstructing the π^0 invariant mass[13], the spectrum of Michel electrons from muon decays[14], and electron response in the test beam detector.

A measurement of Birks' parameter, controlling the saturation of scintillation light during heavy ionization, was utilized to tune the simulation resulting in significantly better agreement with the data for proton calorimetry.

The test beam beamline, detector and results from the Summer 2010 run are published in a Nuclear Instruments and Methods article[15].

4.2 Test beam detector

The test beam detector consists of 40 scintillator planes of approximately one square meter of active area. The planes are constructed of 63 triangular scintillator strips of length 107 cm. The orientation of the strips is rotated by 60° between adjacent planes allowing for three-dimensional track reconstruction. Scintillation light is captured by a wavelength-shifting (WLS) fiber in the center of the strip that is connected directly to a 64 channel photomultiplier tube (PMT). The scintillator strips, 60° rotation between planes and readout system are identical to the larger MINERνA detector with the one exception that the MINERνA detector includes a clear fiber run between the WLS fiber and PMT. The reduced attenuation from the shorter scintillator strips and fiber runs results in a 50% higher light yield in the test beam detector compared to main MINERνA detector.

FIG. 4.1: Photograph of the test beam detector in the EH (ECAL/HCAL) configuration. Beam enters from the right.

The test beam detector is reconfigurable; the planes can be interleaved with 2 mm lead or 1 in steel absorber to emulate the downstream calorimeters of the MINERνA detector. In the Summer 2010 run, data was recorded in two configurations. The first consists of 20 scintillator planes without absorber followed by 20 planes interleaved with lead, emulating the tracker and ECAL regions of the MINERνA detector. The second configuration included lead absorber in the first 20 planes and iron absorber in the last 20 planes, emulating the ECAL and HCAL regions of the MINERνA detector. In this chapter, "TE" refers to the tracker/ECAL detector; "EH" refers to the ECAL/HCAL detector. A photograph of the EH configuration is shown in FIG. 4.1.

4.3 Monte-Carlo simulation

The Monte-Carlo (MC) simulation of the test beam detector is based on GEANT4[16], and is identical to the larger MINERνA detector. The readout simulation utilizes the same software, modified to account for the differing dimensions and lack of clear fiber in the

test beam detector. The test beam simulation is seeded by particle species, momenta and trajectories from events selected in beamline data. The momentum and trajectory of each particle is randomly smeared by a momentum-dependent model of the beamline resolution (Section 3.3). The MC sample is generated at 20 times statistics; each data particle is simulated twenty times with a different smearing.

In the data, it is possible that the species of a particle is misidentified; that a proton is actually a pion, for example. In the simulation, this is never the case. The simulation also does not include pile-up, which is overlayed activity from other particles adjacent in time. In the data this occurs from multiple particle production in the tertiary beamline target or from muons created by pion decays in the secondary beamline. There is also some flux of neutrons from interactions in the target, detector, and experiment hall.

4.4 Event selection

For the proton calorimetry analysis, the event sample must pass the following cuts:

1. **Loose beamline quality** – The beamline reconstruction software (Section 3.2) identifies events passing a set of "loose" and/or "strict" quality cuts. These cuts require a particle track through all four wire chambers, a valid momentum fit with a trajectory that doesn't stray too much into the poorly-simulated regions of the magnetic field, a valid time-of-flight (TOF) measurement and for the strict cuts, a maximum fit χ^2. The loose cuts are implemented by default. As a systematic study, the strict cuts are also included.

2. **Beamline identified proton** – The beamline reconstruction software sets a particle identification code based on a combination of mass and TOF cuts. Protons are identified by a calculated mass within $\pm 20\%$ of 938.3 MeV. The width of the reconstructed mass

peak is driven by the TOF resolution.

3. **Beamline to detector match** – The reconstruction software performs a beamline to detector matching algorithm by projecting from the beamline measured particle trajectory to the face of the detector. The algorithm verifies the presence of scintillator activity within 6 cm of this point and the absence of activity away from this point which indicates a stray particle entered the detector.

4. **No adjacent time slice within 250 ns before and 500 ns after the primary proton** – During reconstruction, hits in the detector are grouped by time into "time slices." Particle showers from upstream interactions can cause a number of time slices to be generated adjacent to each other. This can produce a number of technical problems, such as dead readout electronics time, the wrong slice identified as the proton or even tracks separated into separate time slices. It is also observed that when time slices are spaced closely together, the primary slice is more likely to have pile-up background.

5. **TOF outside 19 ns shadow region** – As an artifact of the 19 ns separation of adjacent accelerator buckets, the TOF spectrum is shadowed at +19 ns (FIG. 3.5). Events between 38.0 and 41.0 ns, which are potentially misidentified pions, are rejected.

6. **Background vetoes** – In the lower energy bins, where the proton is expected to be well contained in the upstream portion of the detector, downstream modules are utilized as background vetoes. Events are rejected with significant visible energy in these modules which is likely the result of beam backgrounds, such as muons. This cut is detailed in the following section.

7. **Absurd calorimetric reconstruction** – Events are rejected for which the ratio of the calorimetric response to proton kinetic energy is greater than 2.0. In the simulation,

such events are nearly non-existent. In the data, it is evidence of a background particle interaction in the detector.

The energy spectrum of protons passing these cuts is displayed in FIG. 4.2 for the TE detector and FIG. 4.3 for the EH detector.

4.5 Calorimetry

The calorimetric response of the test beam detector is computed as a sum of the visible energy depositions in the detector weighted by calorimetric constants to account for the active fraction of the scintillator and the energy loss from the passive absorbers (lead and steel). The calorimetric response, E_{cal}, is defined as

$$E_{cal} \equiv \sum_i c_i E_i \tag{4.1}$$

$$c_{TRAK} = 1.26 \tag{4.2}$$

$$c_{ECAL} = 2.08 \tag{4.3}$$

$$c_{HCAL} = 10.73, \tag{4.4}$$

where the summation is over hits in the detector and the calorimetric constant, c_i, is set to the appropriate region in the detector (tracker, ECAL or HCAL). The calorimetric constants are calculated from the energy loss per unit length, $\mathrm{d}E/\mathrm{d}x$, of a minimum ionizing particle at normal incidence and include the active fraction of the scintillator plane (Section 5.6).

The data has backgrounds from three sources: muons from pion decays in the secondary pion beam, pions from interactions in the target of our tertiary beamline and a persistent flux of low energy neutrons from interactions in the target, detector and hall.

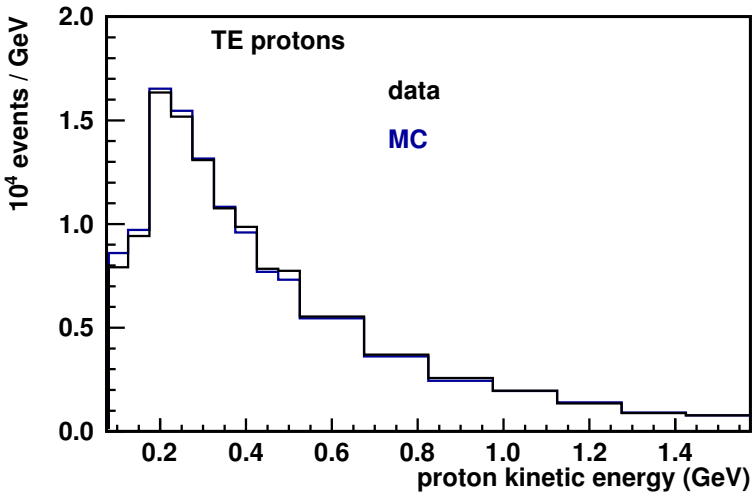

FIG. 4.2: Proton kinetic energy spectrum in the TE (tracker/ECAL) detector. The Monte-Carlo (MC) simulation is area normalized to the data.

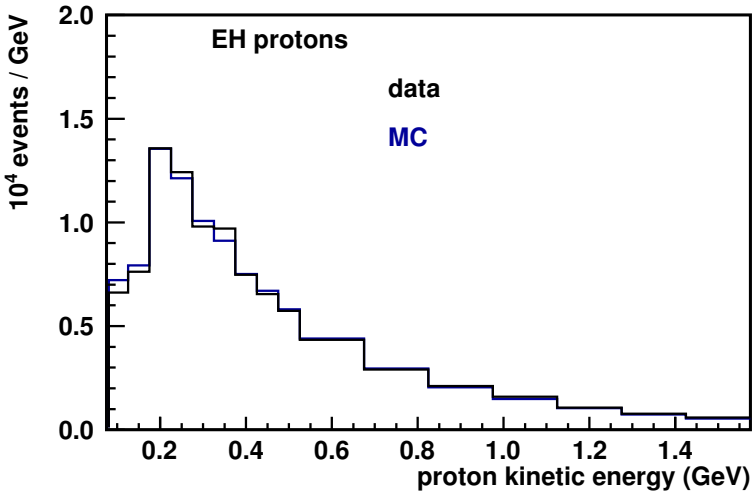

FIG. 4.3: Proton kinetic energy spectrum in the EH (ECAL/HCAL) detector. The Monte-Carlo (MC) simulation is area normalized to the data.

The muon and pion background can be rejected by identifying a secondary particle entering the front of the detector (as performed in the third cut of the event selection) and identifying a highly penetrating particle, uncharacteristic of a proton.

The neutron flux is more difficult to reject. An observation of energy in the detector earlier in time than the proton interaction sets the magnitude of the neutron flux as a few MeV per event, calorimetrically weighted. In the lowest kinetic energy bin of 100 MeV, this amounts to a few percent correction, which is severe on what is to be a few percent measurement. To mitigate the effects, the following scheme is implemented:

1. In the lowest kinetic energy bins, $\leq$ 150 MeV (TE) 200 MeV (EH), only the upstream half of the detector is integrated calorimetrically because the proton is well contained upstream at those energies. The downstream half is utilized as a muon/pion veto, rejecting events with greater than 10.0 MeV summed, unweighted visible energy.

2. For higher energy, $\leq$ 300 MeV (TE) 750 MeV (EH), the entire detector is integrated. The last four planes are utilized as a muon/pion veto, rejecting events with greater than 2.0 MeV summed, unweighted visible energy.

3. For the highest energy bins, the entire detector is integrated and no veto is incorporated.

The magnitude of the effect of including this scheme is shown in FIG. 4.33.

The analysis is performed by histogramming the calorimetric response divided by proton kinetic energy in bins of proton kinetic energy. FIG. 4.4 – 4.6 show this quantity for data and simulation for the TE detector. FIG. 4.7 – 4.9 show the equivalent for the EH detector. FIG. 4.10 – 4.11 show the average energy per event deposited in each module in bins of proton kinetic energy for the TE detector. FIG. 4.13 – 4.15 show the equivalent for the EH detector. In the TE detector above 450 MeV, it is clear from the energy deposition

profiles that many protons exit the back of the detector. For the TE detector, the analysis is limited to $\leq 450\,\mathrm{MeV}$, though the bins above are plotted for reference.

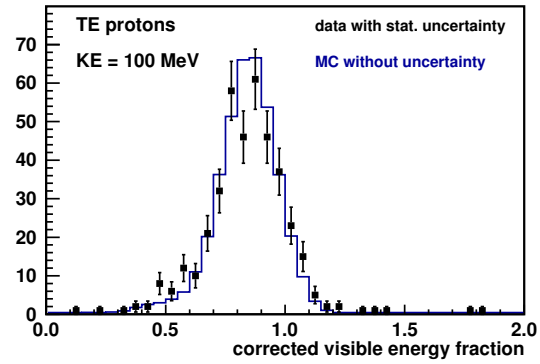

(a) KE = 100 MeV

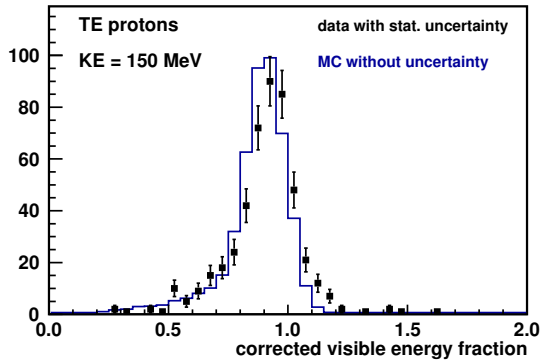

(b) KE = 150 MeV

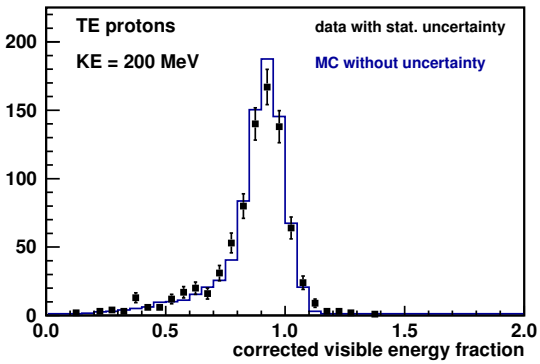

(c) KE = 200 MeV

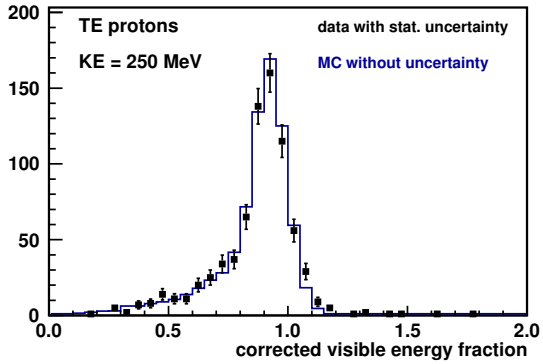

(d) KE = 250 MeV

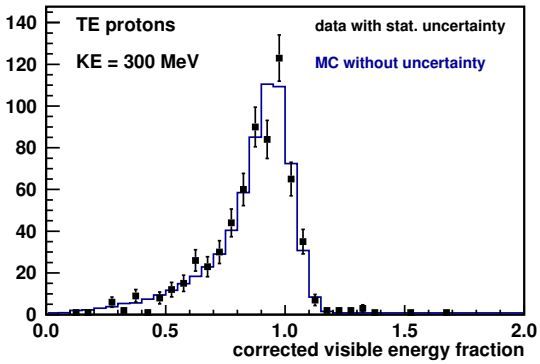

(e) KE = 300 MeV

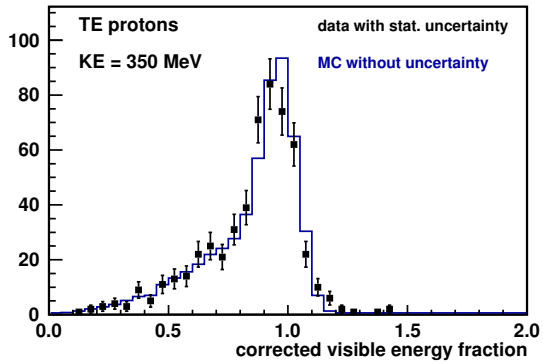

(f) KE = 350 MeV

FIG. 4.4: Calorimetric response divided by proton kinetic energy (KE) for KE = $[100, 350]$ MeV in the TE (tracker/ECAL) detector. The Monte-Carlo (MC) simulation is area normalized to the data.

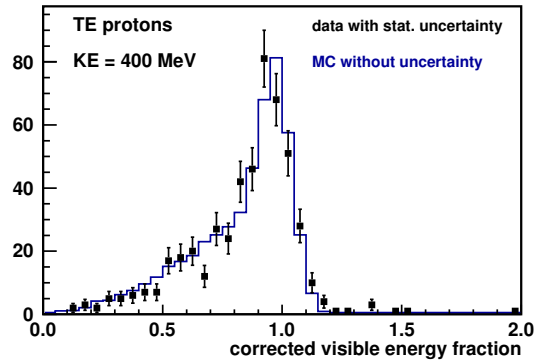

(a) KE = 400 MeV

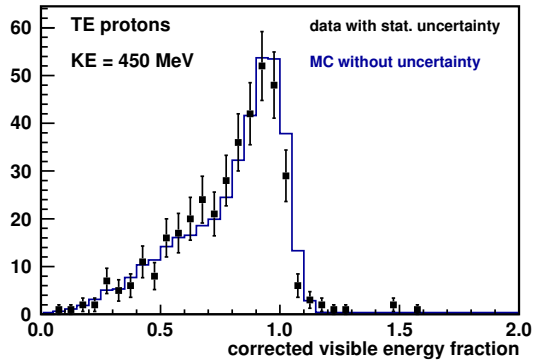

(b) KE = 450 MeV

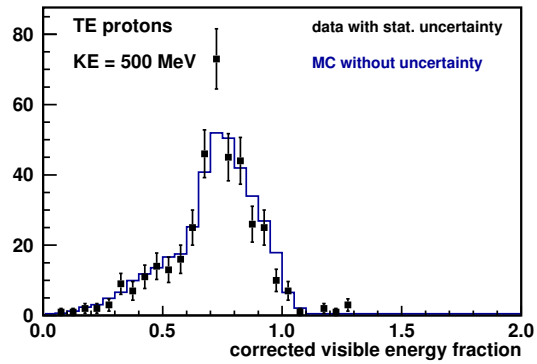

(c) KE = 500 MeV

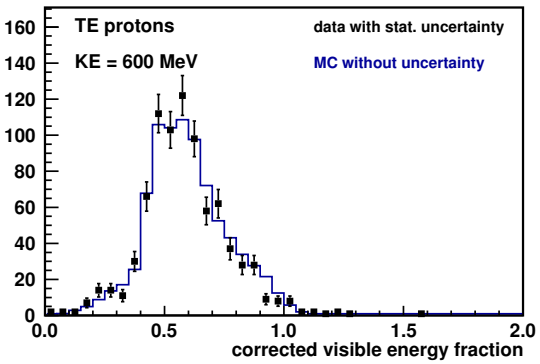

(d) KE = 600 MeV

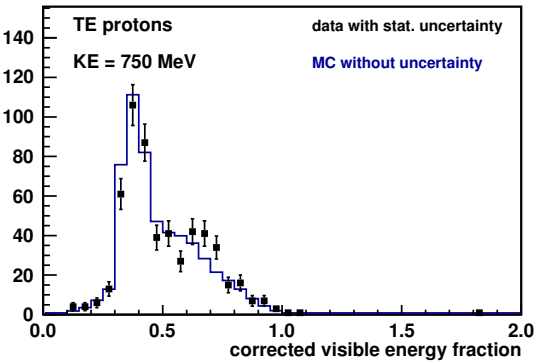

(e) KE = 750 MeV

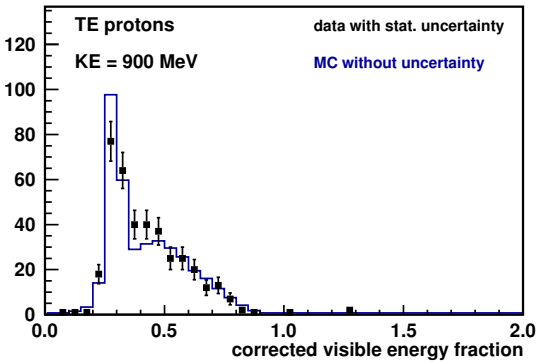

(f) KE = 900 MeV

FIG. 4.5: Calorimetric response divided by proton kinetic energy (KE) for KE = [400, 900] MeV in the TE (tracker/ECAL) detector. The Monte-Carlo (MC) simulation is area normalized to the data.

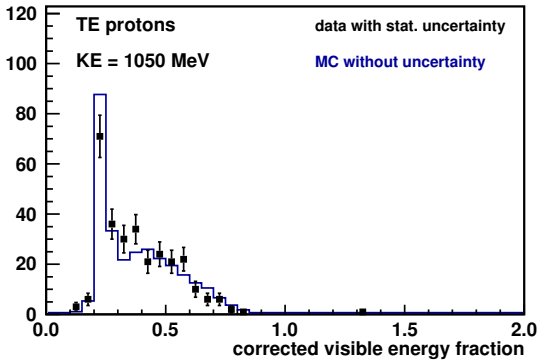

(a) KE = 1050 MeV

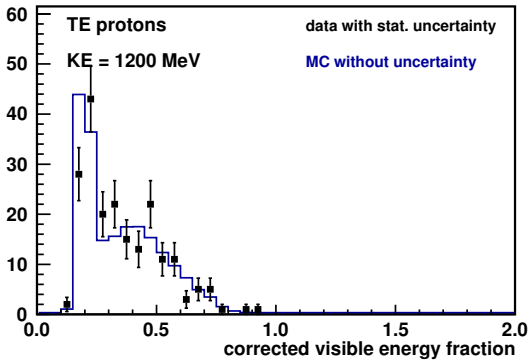

(b) KE = 1200 MeV

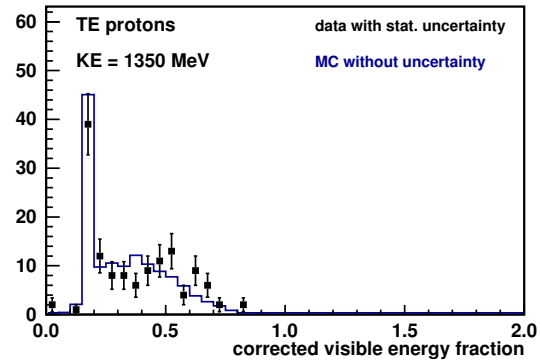

(c) KE = 1350 MeV

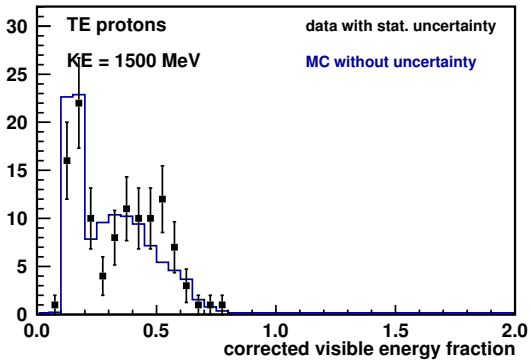

(d) KE = 1500 MeV

FIG. 4.6: Calorimetric response divided by proton kinetic energy (KE) for KE = $[1.05, 1.5]$ GeV in the TE (tracker/ECAL) detector. The Monte-Carlo (MC) simulation is area normalized to the data.

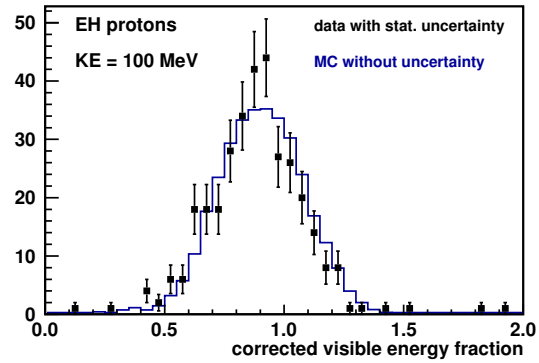

(a) KE = 100 MeV

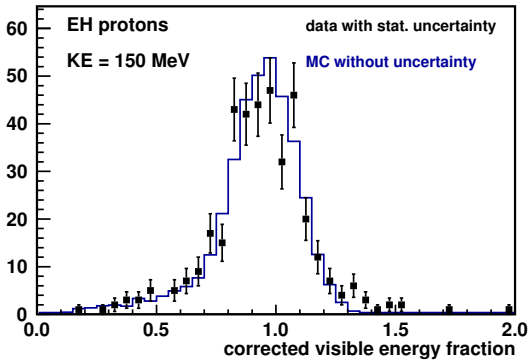

(b) KE = 150 MeV

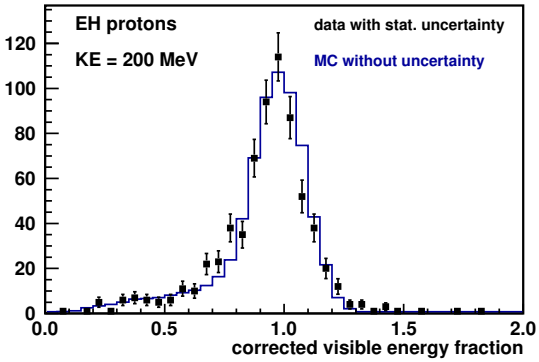

(c) KE = 200 MeV

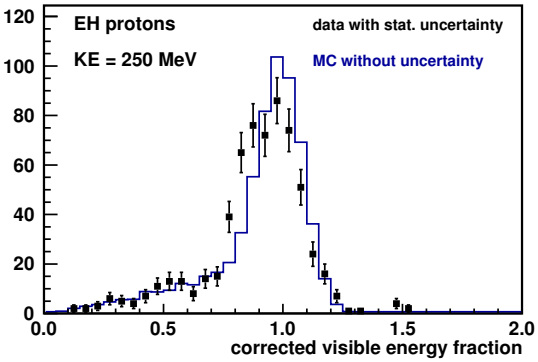

(d) KE = 250 MeV

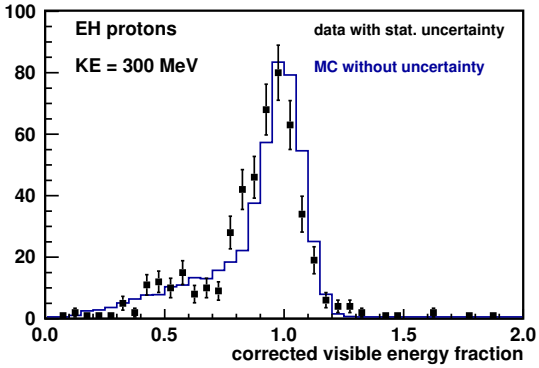

(e) KE = 300 MeV

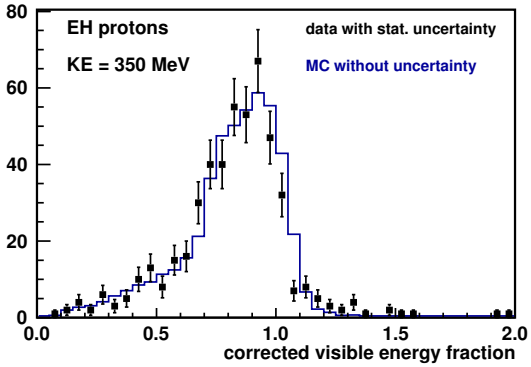

(f) KE = 350 MeV

FIG. 4.7: Calorimetric response divided by proton kinetic energy (KE) for KE = $[100, 350]$ MeV in the EH (ECAL/HCAL) detector. The Monte-Carlo (MC) simulation is area normalized to the data.

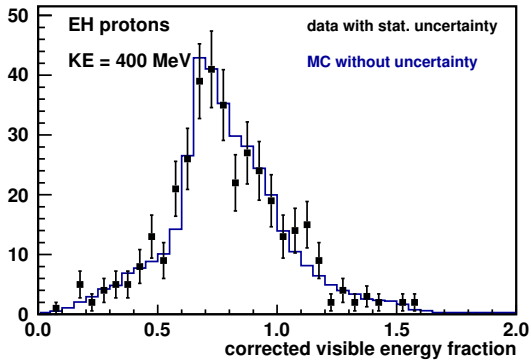

(a) KE = 400 MeV

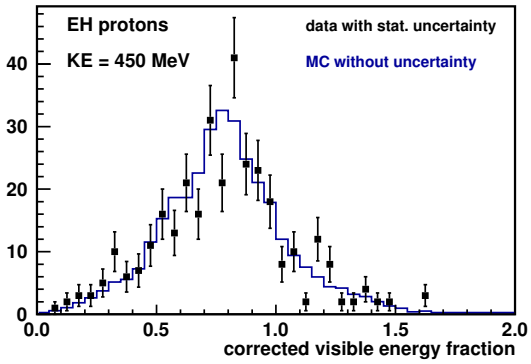

(b) KE = 450 MeV

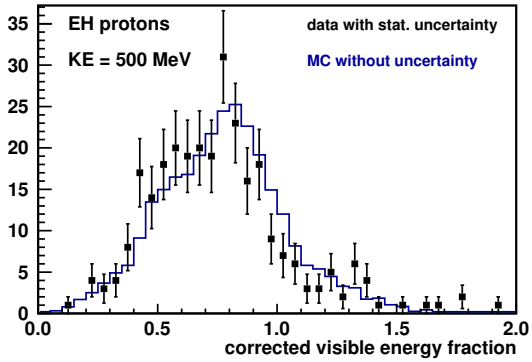

(c) KE = 500 MeV

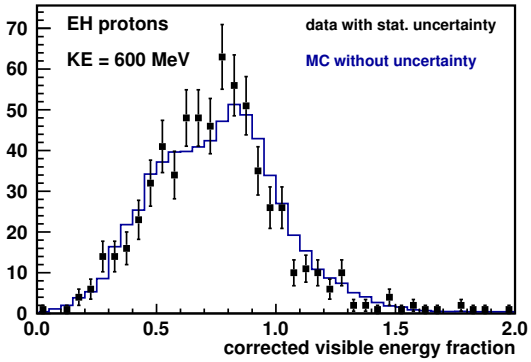

(d) KE = 600 MeV

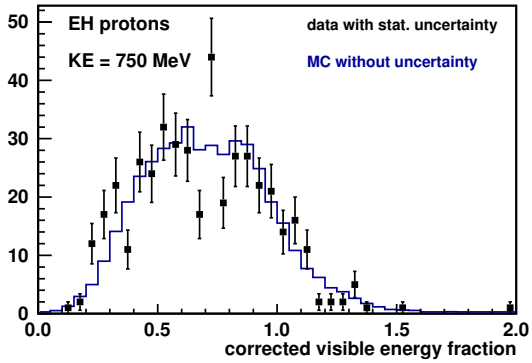

(e) KE = 750 MeV

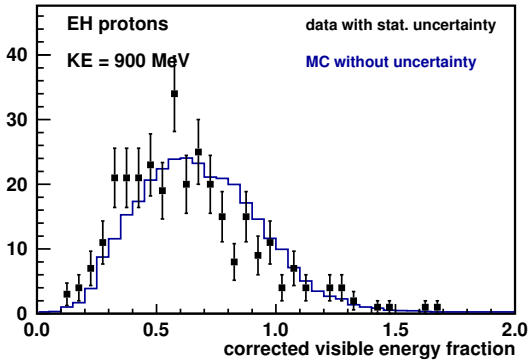

(f) KE = 900 MeV

FIG. 4.8: Calorimetric response divided by proton kinetic energy (KE) for KE = [400, 900] MeV in the EH (ECAL/HCAL) detector. The Monte-Carlo (MC) simulation is area normalized to the data.

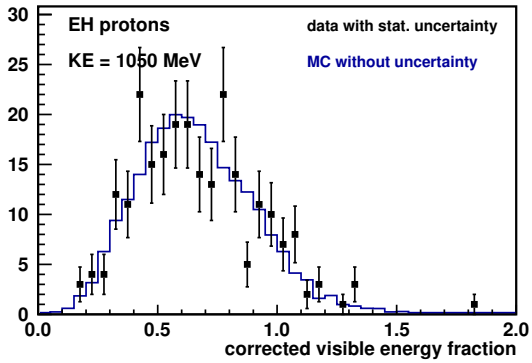

(a) KE = 1050 MeV

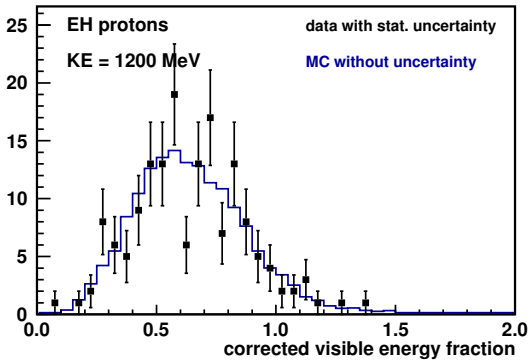

(b) KE = 1200 MeV

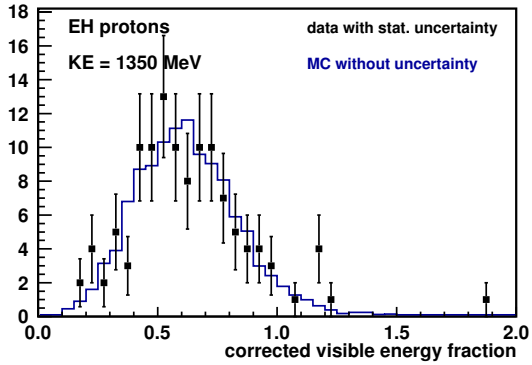

(c) KE = 1350 MeV

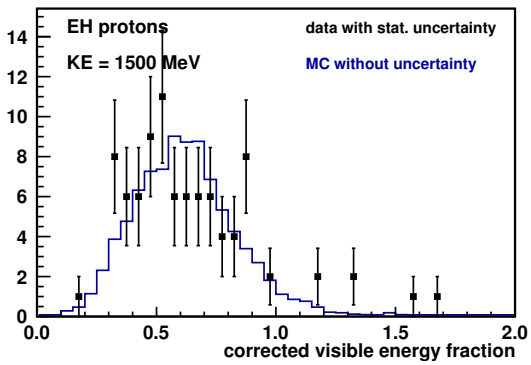

(d) KE = 1500 MeV

FIG. 4.9: Calorimetric response divided by proton kinetic energy (KE) for KE = $[1.05, 1.5]$ GeV in the EH (ECAL/HCAL) detector. The Monte-Carlo (MC) simulation is area normalized to the data.

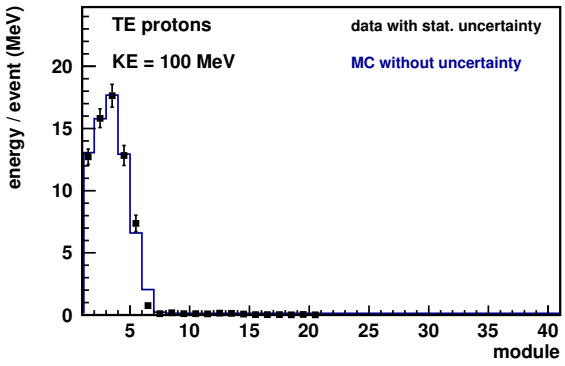

(a) KE = 100 MeV

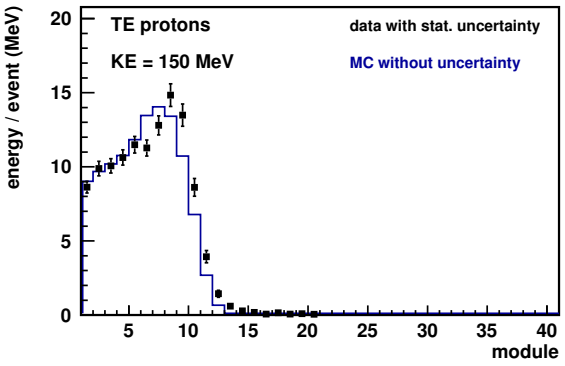

(b) KE = 150 MeV

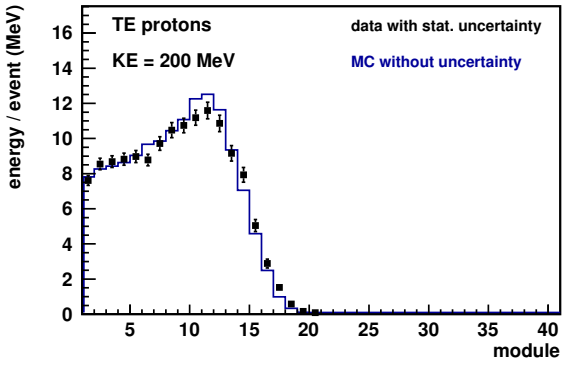

(c) KE = 200 MeV

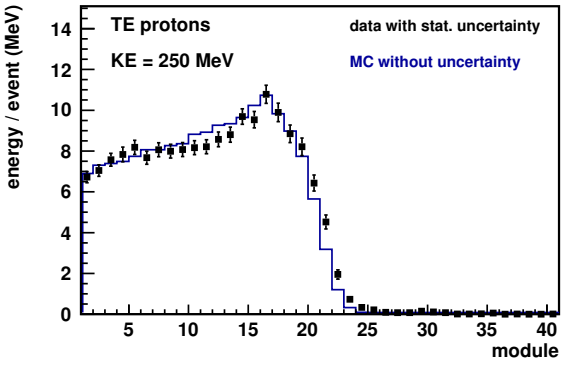

(d) KE = 250 MeV

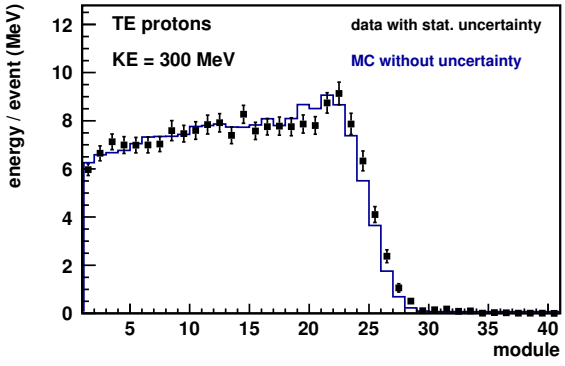

(e) KE = 300 MeV

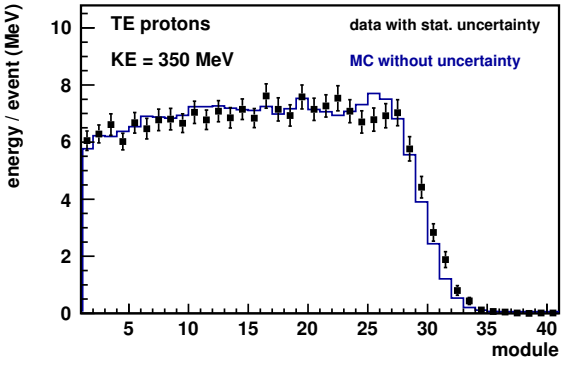

(f) KE = 350 MeV

FIG. 4.10: Average energy per event deposited in each module for proton kinetic energy, KE = [100, 350] MeV in the TE (tracker/ECAL) detector. The Monte-Carlo (MC) simulation is area normalized to the data. Beam enters from the left at module 1.

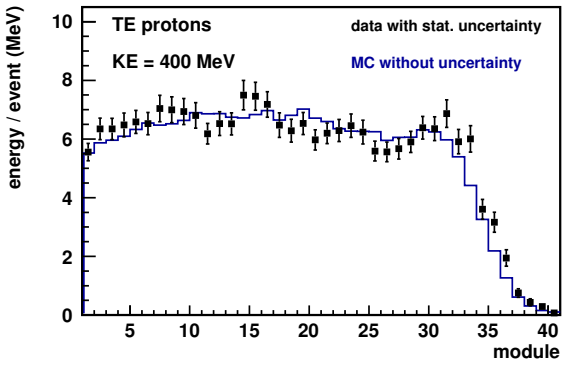

(a) KE = 400 MeV

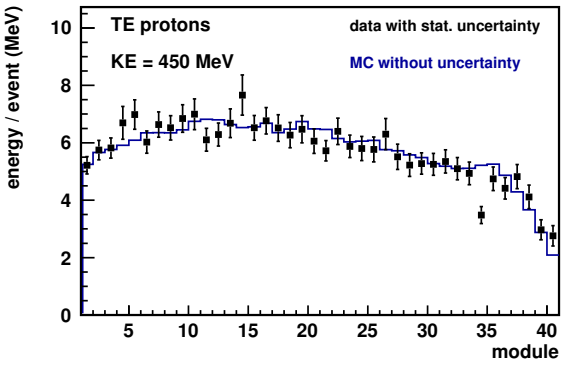

(b) KE = 450 MeV

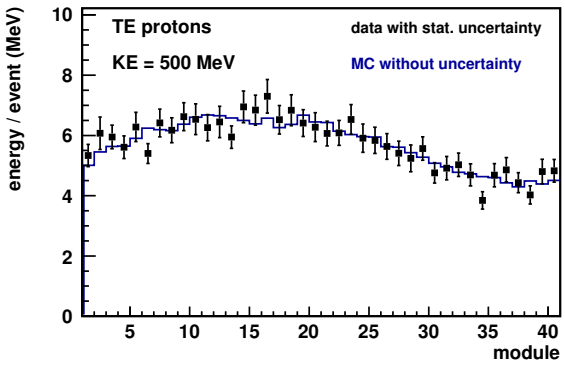

(c) KE = 500 MeV

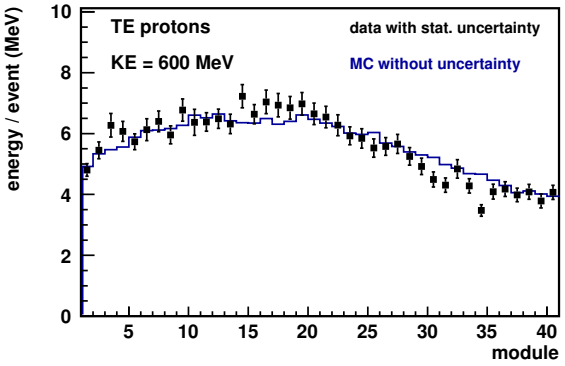

(d) KE = 600 MeV

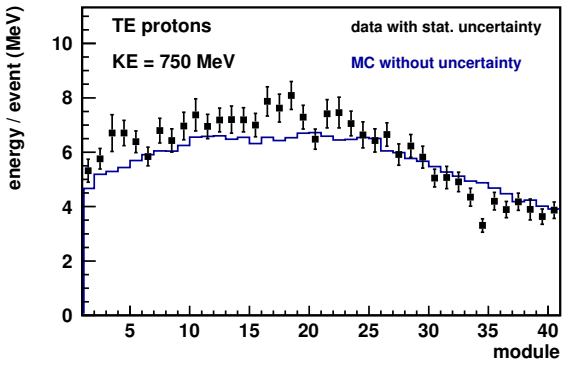

(e) KE = 750 MeV

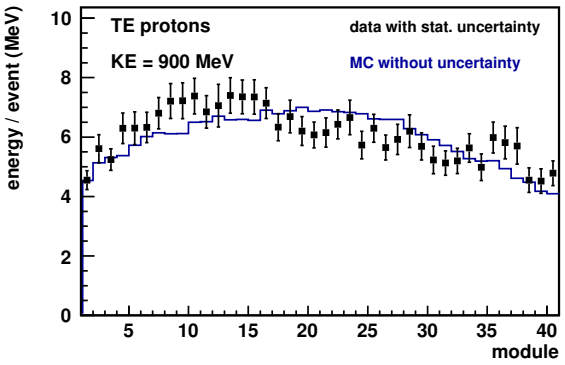

(f) KE = 900 MeV

FIG. 4.11: Average energy per event deposited in each module for proton kinetic energy, KE = [400, 900] MeV in the TE (tracker/ECAL) detector. The Monte-Carlo (MC) simulation is area normalized to the data. Beam enters from the left at module 1.

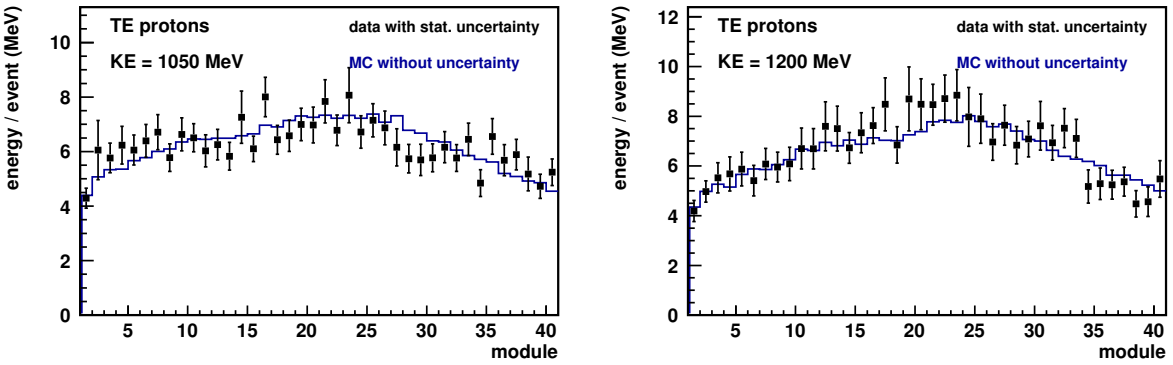

(a) KE = 1050 MeV

(b) KE = 1200 MeV

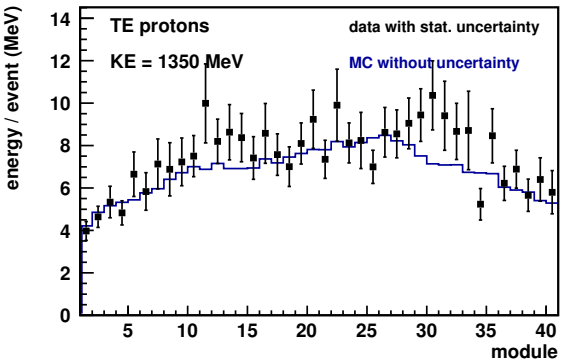

(c) KE = 1350 MeV

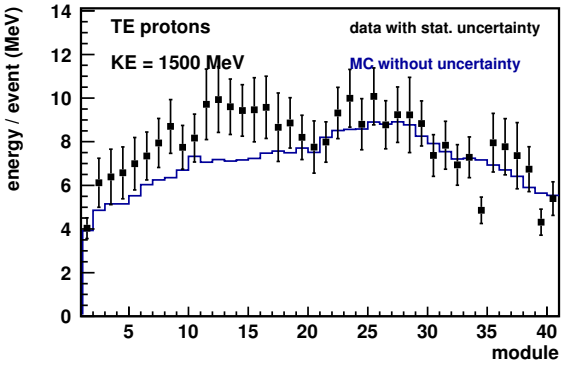

(d) KE = 1500 MeV

FIG. 4.12: Average energy per event deposited in each module for proton kinetic energy, KE = $[1.05, 1.5]$ GeV in the TE (tracker/ECAL) detector. The Monte-Carlo (MC) simulation is area normalized to the data. Beam enters from the left at module 1.

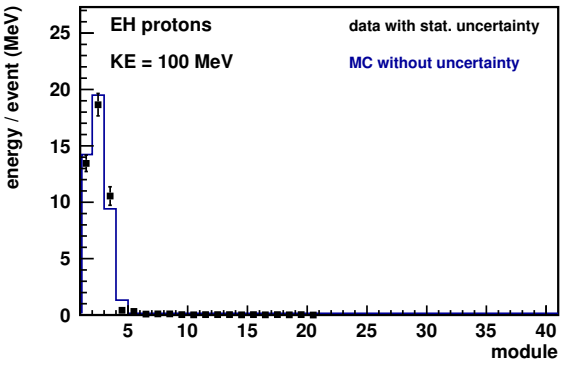

(a) KE = 100 MeV

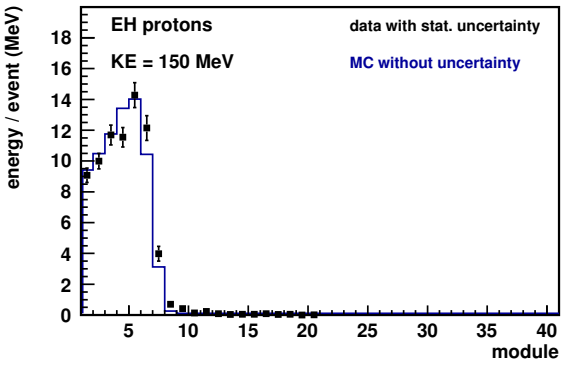

(b) KE = 150 MeV

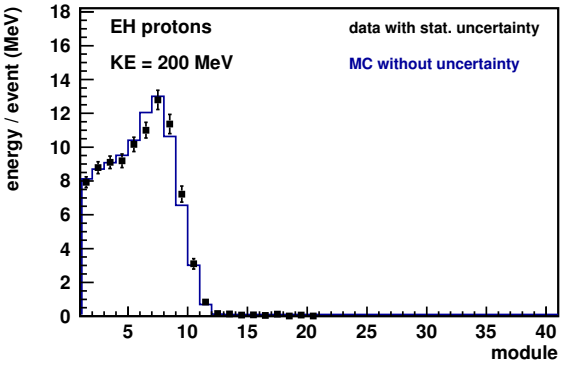

(c) KE = 200 MeV

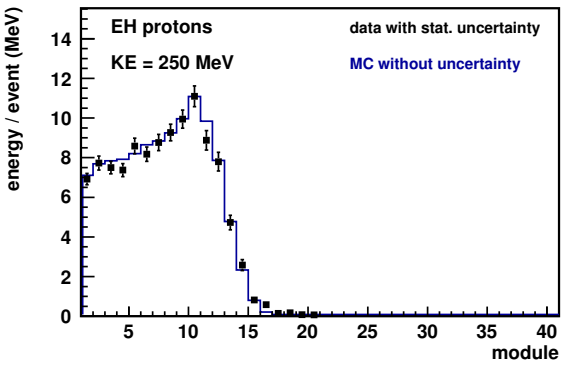

(d) KE = 250 MeV

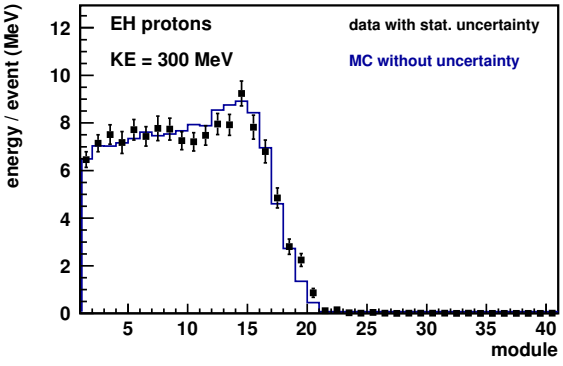

(e) KE = 300 MeV

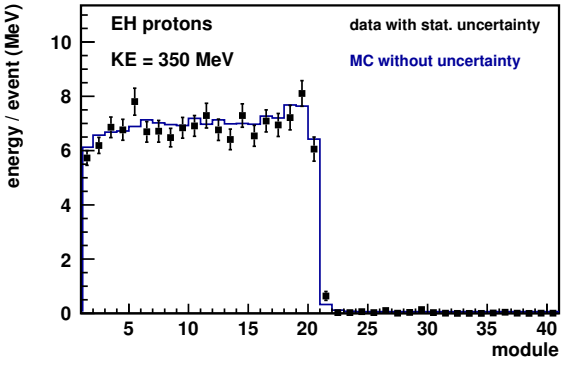

(f) KE = 350 MeV

FIG. 4.13: Average energy per event deposited in each module for proton kinetic energy, KE = [100, 350] MeV in the EH (ECAL/HCAL) detector. The Monte-Carlo (MC) simulation is area normalized to the data. Beam enters from the left at module 1.

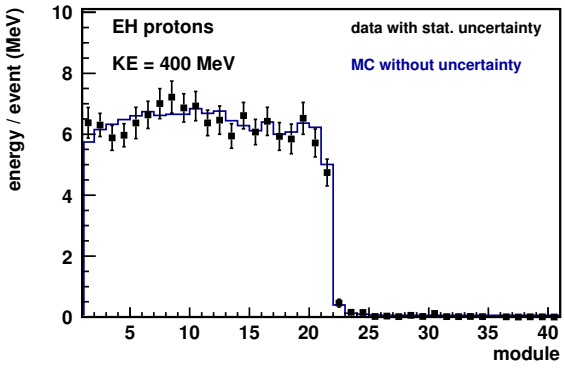

(a) KE = 400 MeV

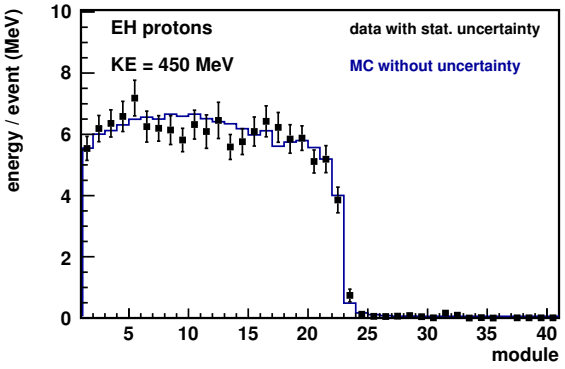

(b) KE = 450 MeV

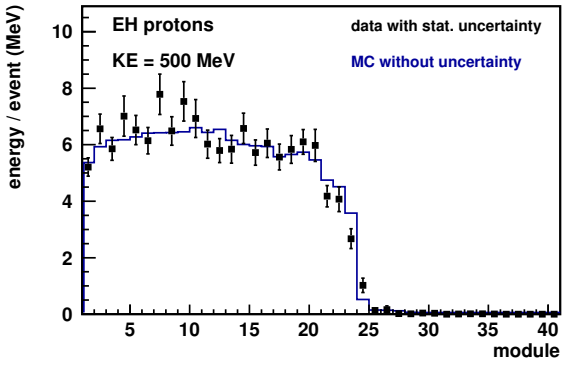

(c) KE = 500 MeV

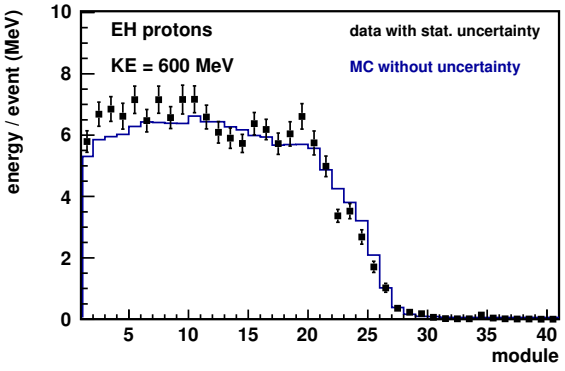

(d) KE = 600 MeV

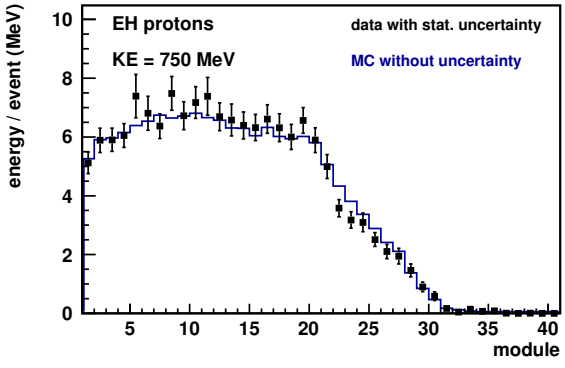

(e) KE = 750 MeV

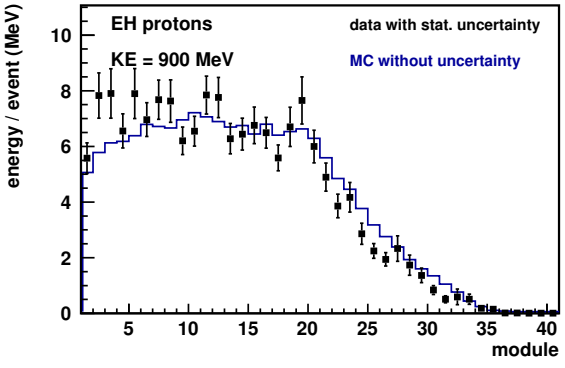

(f) KE = 900 MeV

FIG. 4.14: Average energy per event deposited in each module for proton kinetic energy, KE = [400, 900] MeV in the EH (ECAL/HCAL) detector. The Monte-Carlo (MC) simulation is area normalized to the data. Beam enters from the left at module 1.

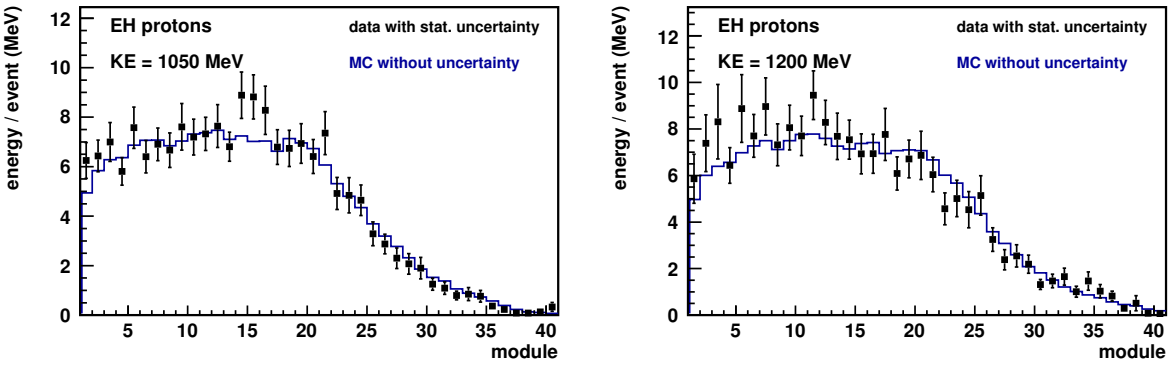

(a) KE = 1050 MeV

(b) KE = 1200 MeV

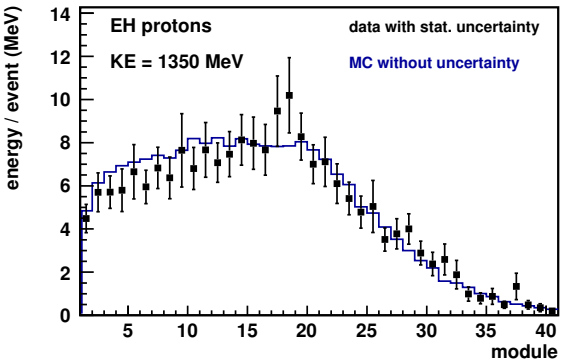

(c) KE = 1350 MeV

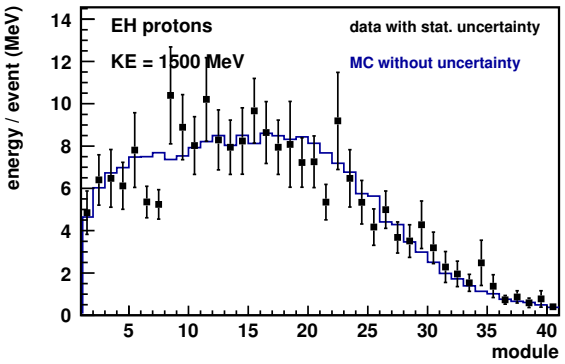

(d) KE = 1500 MeV

FIG. 4.15: Average energy per event deposited in each module for proton kinetic energy, KE = $[1.05, 1.5]$ GeV in the EH (ECAL/HCAL) detector. The Monte-Carlo (MC) simulation is area normalized to the data. Beam enters from the left at module 1.

4.6 Results

FIG. 4.16 shows the mean calorimetric response of protons in the TE (tracker/ECAL) detector versus proton kinetic energy. FIG. 4.17 shows the same for the EH (ECAL/HCAL) detector. The calorimetric response rises nearly linearly with proton kinetic energy. It is not important that the slope is not identically one, as in the larger MINERνA detector, the calorimetric constants are fit to return the desired response (Section 5.6). In the TE detector, protons above 450 MeV penetrate out of the back of the detector, so the analysis is truncated at that energy. The points in the hatched region show values above this, where the calorimetric response is nearly flat with energy.

FIG. 4.18 shows the mean calorimetric response divided by proton kinetic energy for the TE detector. FIG. 4.19 shows the same for the EH detector. The points in the plot are the mean of the distributions in FIG. 4.4 – 4.9. FIG. 4.20 shows the data/MC ratio of the mean calorimetric response divided by proton kinetic energy for the TE detector (FIG. 4.18). FIG. 4.21 shows the same for the EH detector (FIG. 4.19). FIG. 4.22 shows the RMS of the mean calorimetric response divided by proton kinetic energy for the TE detector. FIG. 4.23 shows the same for the EH detector.

The data and Monte-Carlo (MC) simulation show excellent agreement for both the mean and RMS of the calorimetric response of protons over the measured range of proton kinetic energy within systematic uncertainties (detailed in the following section).

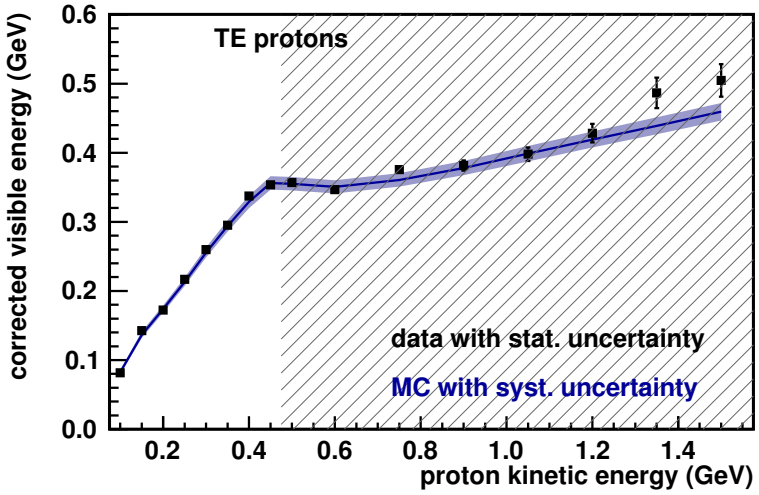

FIG. 4.16: Mean calorimetric response of protons in the TE (tracker/ECAL) detector versus proton kinetic energy. Data are plotted with statistical uncertainties. Monte-Carlo (MC) simulation is plotted with systematic uncertainties. The hatched region indicates energies at which protons penetrate out of the back of the detector.

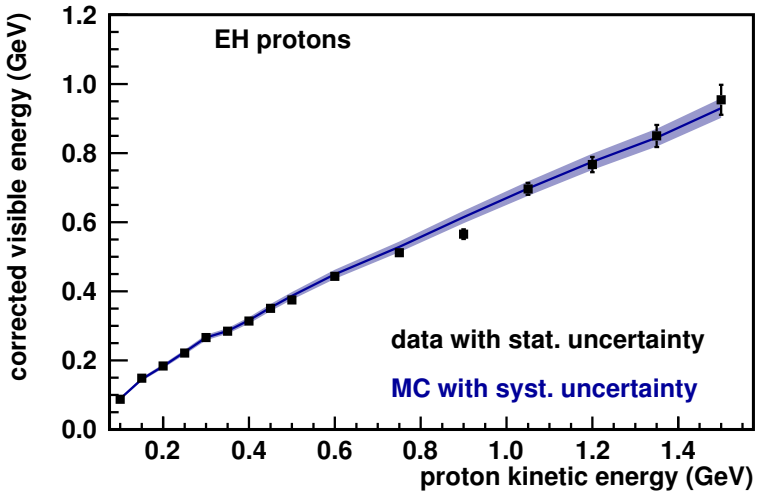

FIG. 4.17: Mean calorimetric response of protons in the EH (ECAL/HCAL) detector versus proton kinetic energy. Data are plotted with statistical uncertainties. Monte-Carlo (MC) simulation is plotted with systematic uncertainties.

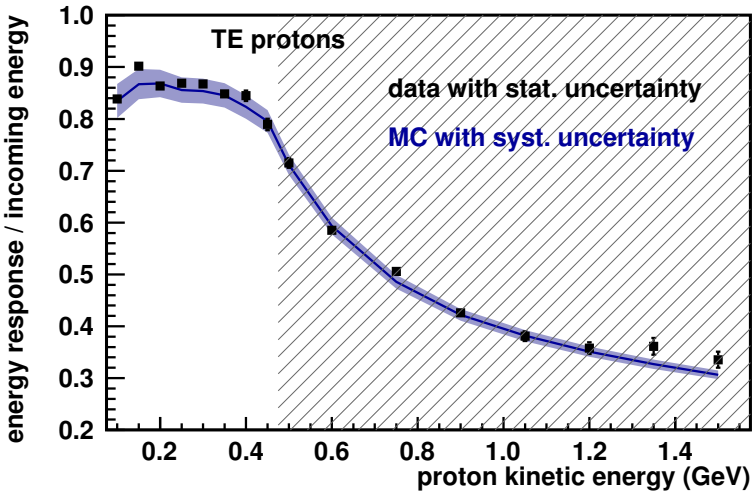

FIG. 4.18: Mean calorimetric response divided by proton kinetic energy in the TE (tracker/ECAL) detector. Data are plotted with statistical uncertainties. Monte-Carlo (MC) simulation is plotted with systematic uncertainties. The hatched region indicates energies at which protons penetrate out of the back of the detector.

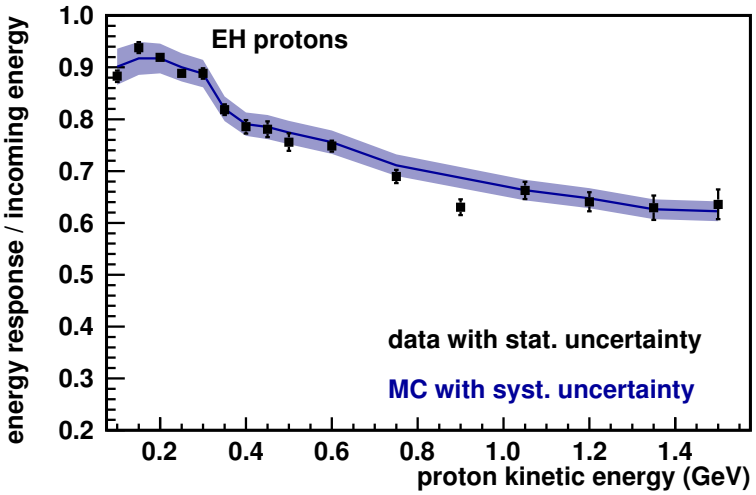

FIG. 4.19: Mean calorimetric response divided by proton kinetic energy in the EH (ECAL/HCAL) detector. Data are plotted with statistical uncertainties. Monte-Carlo (MC) simulation is plotted with systematic uncertainties.

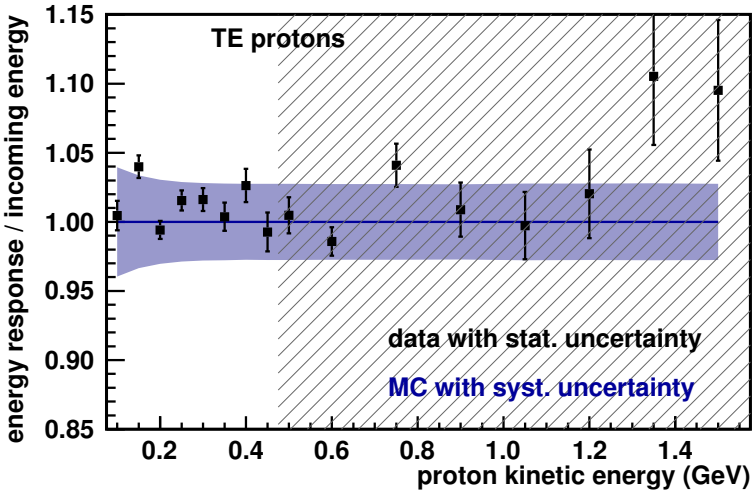

FIG. 4.20: Data/MC ratio of the mean calorimetric response divided by proton kinetic energy in the TE (tracker/ECAL) detector (FIG. 4.18). Data/MC ratio is plotted with statistical uncertainties. The error band at 1.0 shows the MC systematic uncertainties. The hatched region indicates energies at which protons penetrate out of the back of the detector.

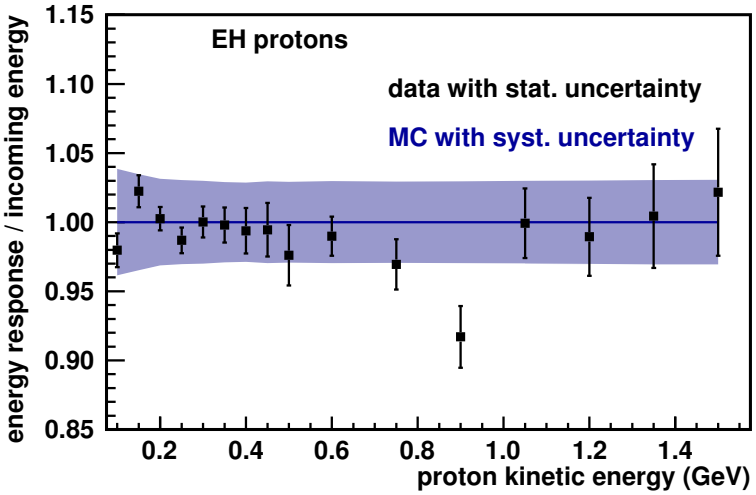

FIG. 4.21: Data/MC ratio of the mean calorimetric response divided by proton kinetic energy in the EH (ECAL/HCAL) detector (FIG. 4.19). Data/MC ratio is plotted with statistical uncertainties. The error band at 1.0 shows the MC systematic uncertainties.

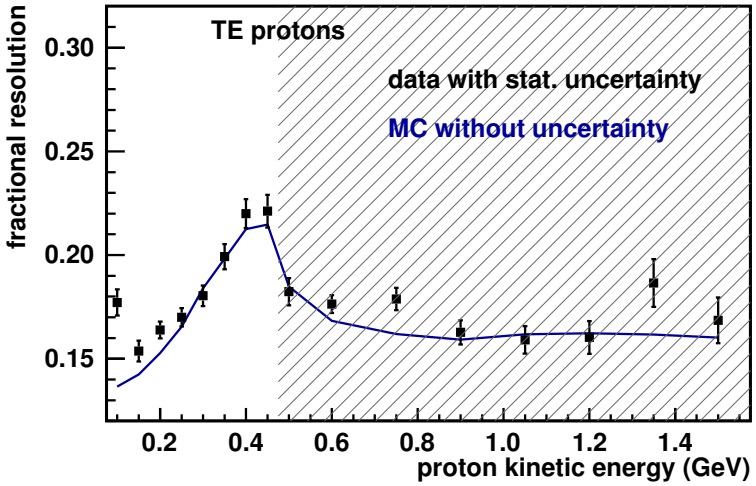

FIG. 4.22: RMS of the calorimetric response divided by proton kinetic energy in the TE (tracker/ECAL) detector. Data are plotted with statistical uncertainties. Monte-Carlo (MC) simulation is plotted without uncertainties. The hatched region indicates energies at which protons penetrate out of the back of the detector.

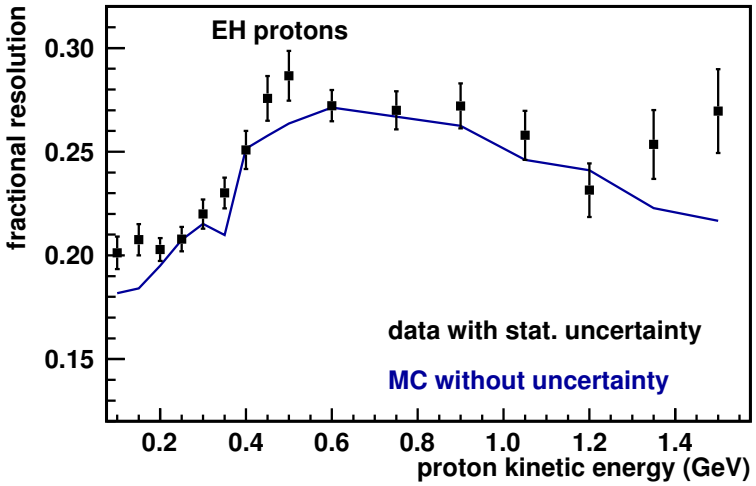

FIG. 4.23: RMS of the calorimetric response divided by proton kinetic energy in the EH (ECAL/HCAL) detector. Data are plotted with statistical uncertainties. Monte-Carlo (MC) simulation is plotted without uncertainties.

4.7 Systematic uncertainties

4.7.1 Beamline momentum and mass model

The systematic uncertainties on the reconstructed momentum in the beamline are described in Chapter 3. The uncertainty includes a momentum-dependent 1.0% per GeV/c term plus three constant 0.5% terms, summed in quadrature. FIG. 4.24 shows the effect of shifting the beamline momentum in the simulation by -1σ; FIG. 4.25 shows the $+1\sigma$ shift. The uncertainty is taken as 1.9% constant. The one odd point on the EH plots occurs because the proton is ranging out at the ECAL/HCAL boundary.

An additional uncertainty arises from the mass of the material in the beamline, primarily the thickness of the aluminum foils in the wire chambers. FIG. 4.26 shows the effect of a 2σ (400%) variation in the aluminum foil thickness. The 1σ uncertainty applied to the analysis is half the 2σ effect, taken as 0.7% at 100 MeV, linearly falling to zero at 300 MeV.

4.7.2 Energy scale calibration

The energy scale of the test beam detector is calibrated identically to the larger MINERνA detector, by first calculating a light yield (LY) factor which is used in the simulation to convert from photons in the scintillator/fibers to photoelectrons at the photomultiplier tube (PMT). The LY factor is determined such that the photoelectron spectrum in the simulation matches that in the data for through-going muon events. In the MINERνA detector, the muon sample is produced by neutrino interactions in the rock upstream of the detector ("rock muons"); in the test beam detector, cosmic muons are utilized. The second calibration step is to determine a muon-equivalent unit (MEU) factor, which is used to convert from photoelectrons at the PMT to deposited energy in the

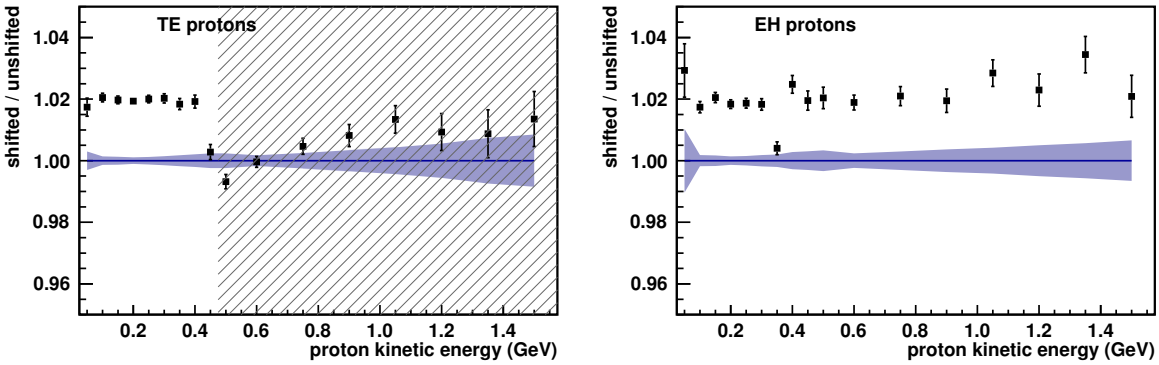

FIG. 4.24: Shifted over unshifted ratio of the mean calorimetric response divided by proton kinetic energy for a -1σ shift of the beamline momentum in the simulation. Plotted with statistical uncertainties only.

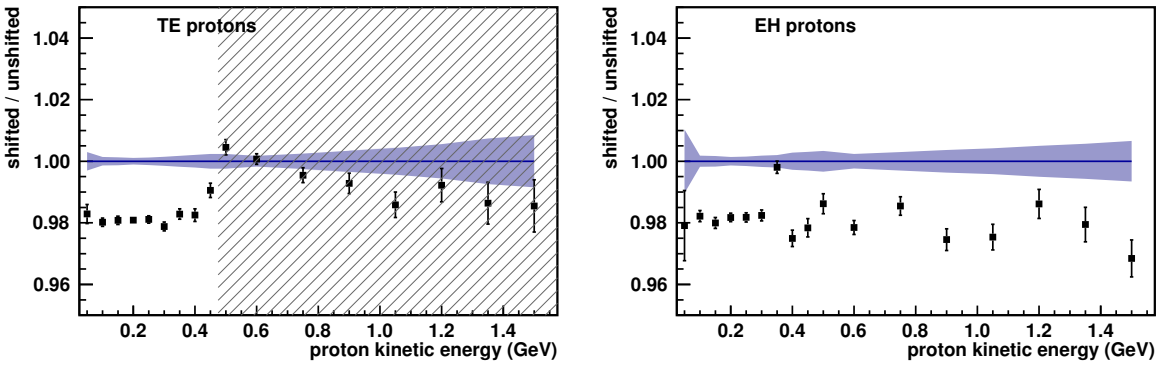

FIG. 4.25: Shifted over unshifted ratio of the mean calorimetric response divided by proton kinetic energy for a $+1\sigma$ shift of the beamline momentum in the simulation. Plotted with statistical uncertainties only.

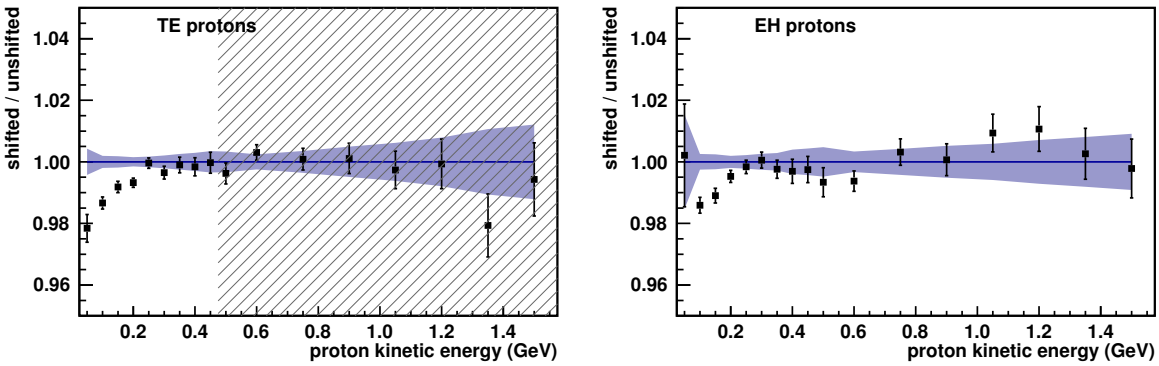

FIG. 4.26: Shifted over unshifted ratio of the mean calorimetric response divided by proton kinetic energy for a $+2\sigma$ (400%) shift of the thickness of the aluminum foils in the beamline wire chambers in the simulation. Plotted with statistical uncertainties only.

scintillator. The MEU factor is calculated such that the reconstructed energy matches the true deposited energy in the active scintillator of the planes, where true deposited energy is defined by the simulation.

This procedure inherently produces excellent data-simulation agreement in the relative energy scale. The uncertainty on the absolute energy scale is driven by the uncertainty on the mass of the scintillator planes and lead and iron absorbers. The absolute uncertainty on the energy scale is 2.0%[15]. An observed discrepancy in the calibrations of the TE and EH detectors, which is not completely understood, leads to a 0.6% uncertainty on the relative energy scale between data and simulation[15].

4.7.3 Birks' law parameter

The value of Birks' law parameter in the simulation is set to the measured parameter in data (Section 4.11). The uncertainty on the measurement is 15%. FIG. 4.27 shows the effect of shifting the parameter -15% in the simulation; FIG. 4.28 shows the +15% shift. The effect is 2.3% at 100 MeV and 1.2% (TE) 1.5% (EH) at higher kinetic energy. A change to Birks' parameter affects the energy scale calibration of the detector. A 15% shift in Birks' parameter causes a 0.3% shift in the MEU factor. This component of the uncertainty is already included in the relative energy scale uncertainty and is subtracted from the energy-dependent Birks' uncertainty, yielding a final uncertainty of 2.0% at 100 MeV and 0.9% (TE) 1.2% (EH) at higher kinetic energy.

4.7.4 PMT non-linearity

Photomultipler tube (PMT) non-linearity is not enabled by default in the simulation. The magnitude of the non-linearity is derived from bench measurements and specifications for the devices[17]. The effect of a 2σ addition of non-linearity is shown in FIG. 4.29. The

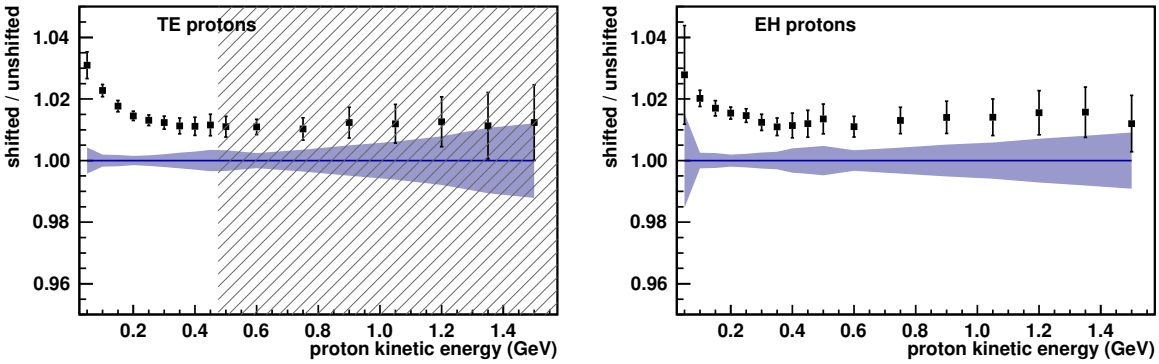

FIG. 4.27: Shifted over unshifted ratio of the mean calorimetric response divided by proton kinetic energy for a -1σ (-15%) shift of Birks' parameter in the simulation. Plotted with statistical uncertainties only.

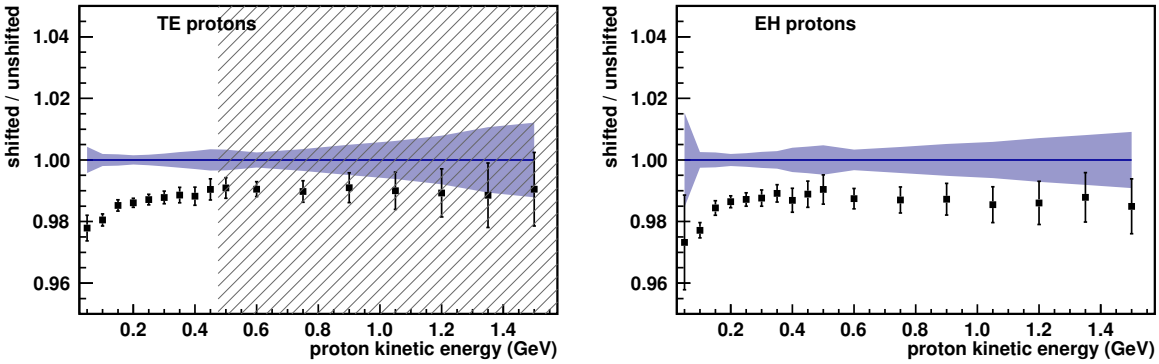

FIG. 4.28: Shifted over unshifted ratio of the mean calorimetric response divided by proton kinetic energy for a $+1\sigma$ (+15%) shift of Birks' parameter in the simulation. Plotted with statistical uncertainties only.

1σ effect is 0.7% constant across kinetic energy. While this is a one-sided uncertainty (non-linearity can only decrease the response), it is incorporated as a symmetric uncertainty.

4.7.5 Cross-talk

A measurement of the cross-talk in data finds an average of $4.2 \pm 0.5\%$ over the first 25 planes. The cross-talk in the simulation is scaled to this value. The MEU calibration, however, only considers energy deposited on the muon track and thus is tuning $100\% - 4.2\% = 95.8\%$ of the photoelectrons to 100% of the true deposited energy. This results in the absolute energy scale being high by 4.2%. For this and other calorimetry analyses, the absolute response in data and simulation is scaled down by this value.

The systematic effect of cross-talk is evaluated by excluding hits less than 0.5 MeV in the calorimetric sum. Hits with energies this low are predominantly cross-talk. FIG. 4.30 shows the effect as a double ratio of mean calorimetric response. The systematic uncertainty is taken as 0.7% for the TE detector and 0.9% for the EH detector.

4.7.6 Adjacent time slices

During reconstruction, hits in the detector are grouped by time into "time slices." The default cut requires no adjacent slices within 250 ns before and 500 ns after the slice. As a systematic study, the window was doubled to 500 ns before and 1000 ns after the slice. FIG. 4.31 shows the effect as a double ratio of mean calorimetric response. The systematic uncertainty is taken as 0.3% in the TE detector and 0.6% in the EH detector.

The origin of this systematic is not immediately clear; adjacent time slices can be caused by beam backgrounds (only in data), PMT after-pulsing (only in data), late neutron hits, Michel electrons, and other decay products.

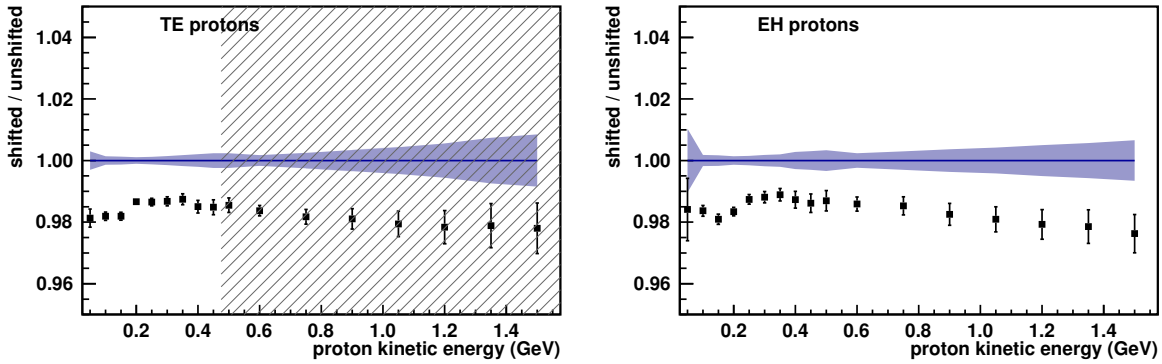

FIG. 4.29: Shifted over unshifted ratio of the mean calorimetric response divided by proton kinetic energy for a $+2\sigma$ addition of PMT non-linearity in the simulation. Plotted with statistical uncertainties only.

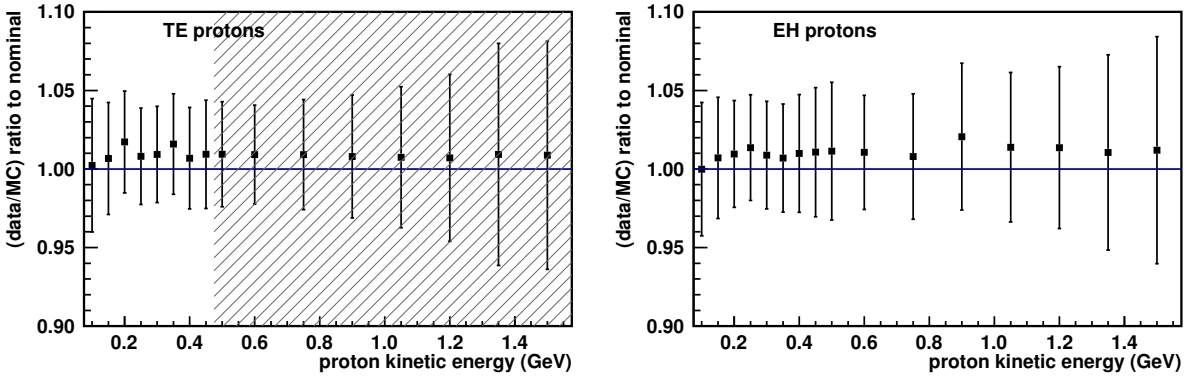

FIG. 4.30: Double ratio of data over simulation mean calorimetric response for cutting hits less than 0.5 MeV in the calorimetric sum over nominal. Plotted with statistical uncertainties only.

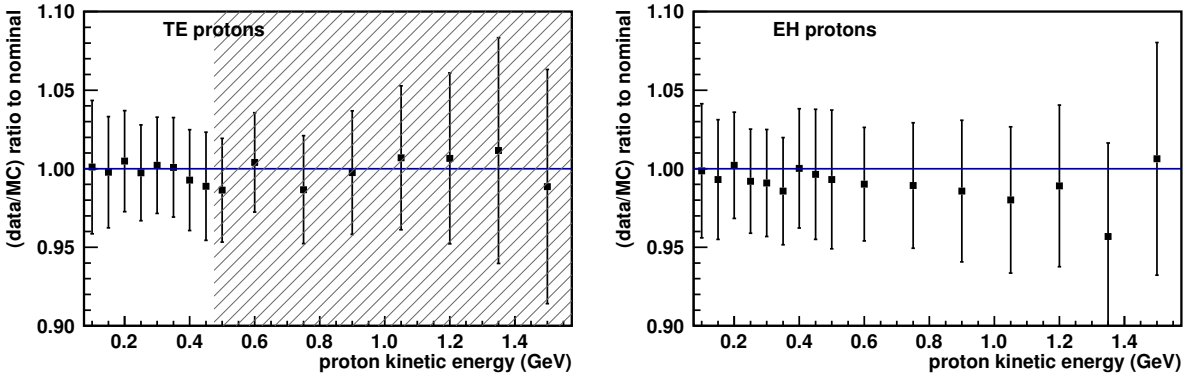

FIG. 4.31: Double ratio of data over simulation mean calorimetric response for doubling the adjacent time slices cut window over nominal. Plotted with statistical uncertainties only.

4.7.7 Temperature stability

The temperature in the experiment hall varied wildly during the Summer 2010 run due to a failed air conditioning unit. The temperature was lowest at 4 AM for the start of data taking each day and highest at 6 PM when the beam was disabled each evening. The average hall temperature rose as the run proceeded late into Summer. The approximately 0.4% per degree Celsius degradation in light output was corrected during calibration[18]. A remaining systematic uncertainty of 1% was evaluated by separating the data sample into a high and low temperature subset and comparing the mean calorimetric response.

4.7.8 Event selection

The default beamline selection is the "loose" quality cuts; as a systematic study, the "strict" quality cuts are implemented, which includes additional limits on the magnetic field integral, magnetic error integral and fit χ^2. FIG. 4.32 shows the effect as a double ratio of mean calorimetric response. The strict cuts are not expected to affect the simulation in any way other than varying the momentum distribution of protons. As evidenced in the plot, the data are not affected either. No additional systematic uncertainty is included for this effect.

4.7.9 Pile-up

The default analysis ignores the downstream half of the detector for very low energy events to avoid integrating the background of neutrons drifting through the hall from upstream interactions. The downstream planes are also used as a veto to remove muon and pion contamination. FIG. 4.33 shows the effect of removing this veto and always calorimetrically summing the entire detector. This is not taken as a systematic uncertainty, only an illustration of the magnitude of the effect.

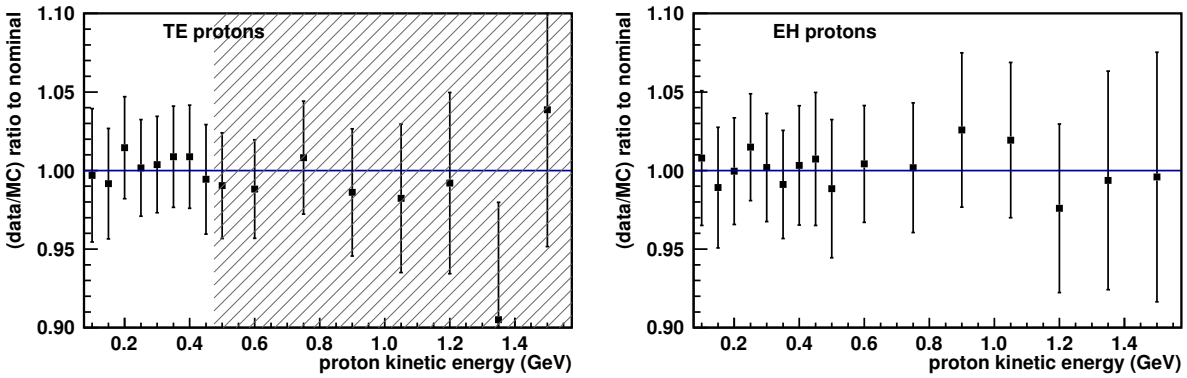

FIG. 4.32: Double ratio of data over simulation mean calorimetric response for including the strict beamline quality cuts over nominal. Plotted with statistical uncertainties only.

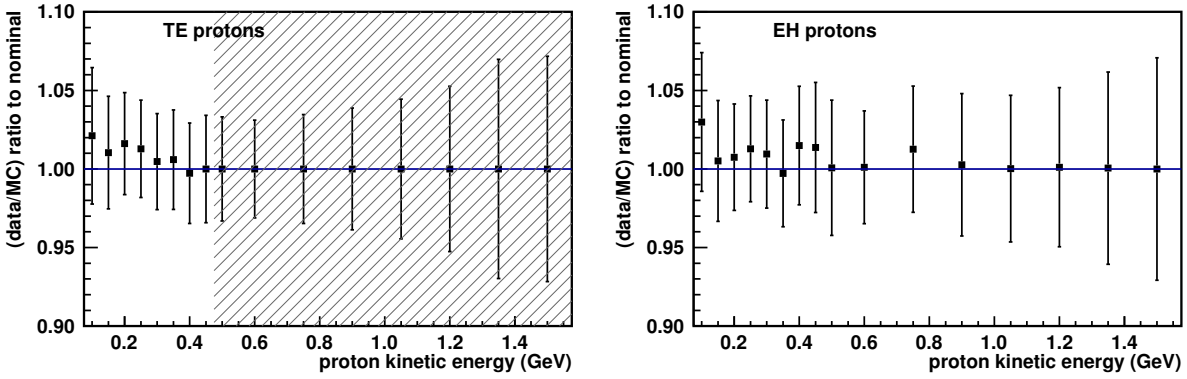

FIG. 4.33: Double ratio of data over simulation mean calorimetric response for removing the muon/pion veto and calorimetrically summing the full detector over nominal. Plotted with statistical uncertainties only.

4.8 Proton calorimetry conclusions

The results of the test beam proton calorimetry analysis set the systematic uncertainty on calorimetric reconstruction of protons in the recoil system for MINERνA analyses. The agreement between data and the Monte-Carlo simulation is shown by the ratio in FIG. 4.20 for the TE detector and FIG. 4.21 for the EH detector. The vast majority of the data points lie within the systematic uncertainty band of the simulation. Thus, the proton calorimetry systematic uncertainty in MINERνA analyses is not driven by a data-simulation discrepancy, but rather by the systematic uncertainties of the test beam analysis. Table 4.1 summarizes the systematic uncertainties on the calorimetric response of protons in the test beam detector for the two configurations (TE and EH). A proton calorimetry uncertainty of 3% covers the systematics of the test beam analysis at all but the lowest proton energies and is applied to MINERνA analyses.

Systematic uncertainty	TE (tracker/ECAL)	EH (ECAL/HCAL)
Beamline momentum	1.9%	1.9%
Beamline mass model	0.7% (100 MeV)	0.7% (100 MeV)
Relative energy scale	0.6%	0.6%
Birks' parameter	2.0% (100 MeV) 0.9% (400 MeV)	2.0% (100 MeV) 1.2% (1 GeV)
PMT non-linearity	0.7%	0.7%
Cross-talk	0.7%	0.9%
Adjacent time slices	0.3%	0.6%
Temperature stability	1.0%	1.0%
Quadrature sum	3.2% (100 MeV) 2.6% (400 MeV)	3.3% (100 MeV) 2.8% (1 GeV)

TABLE 4.1: Summary of systematic uncertainties on the calorimetric response of protons in the test beam detector for data-simulation comparisons. The absolute energy scale contributes an additional 2.0% uncertainty equally affecting data and simulation.

4.9 Pion calorimetry

The pion calorimetry analysis is performed identically to the proton calorimetry analysis described earlier. The analysis is performed for both positive pions (π^+), measured concurrently with the protons, and negative pions (π^-), obtained by reversing the magnet polarity in the beamline. Pions at comparable momentum to protons penetrate deeper into the detector, thus the analysis is restricted to the EH (ECAL/HCAL) detector due to the poor containment of the TE (tracker/ECAL) detector.

FIG. 4.34 shows the mean calorimetric response divided by pion total energy for the π^+ sample. FIG. 4.35 shows the same for the π^- sample. These plots are constructed identically to the proton calorimetry plots in FIG. 4.18 and FIG. 4.19. Systematic uncertainties are 2.6% (π^+) 2.9% (π^-) at low energy and 3.4% (π^+) 3.6% (π^-) at high energy, comparable in magnitude to the proton analysis[15]. The discrepancy between data and simulation leads to a 5% uncertainty on the calorimetric reconstruction of recoil pions in MINERνA analyses.

4.10 Electron calorimetry

A sample of low-energy electrons exists in the primarily proton and pion beam, though the time-of-flight resolution is insufficient to cleanly separate electrons from the much greater flux of pions. The electrons are barely visible at low momentum at the speed of light boundary in FIG. 3.5. A sample of electrons was selected for a calorimetry analysis between 400 MeV and 500 MeV energy using a set of topological cuts on the detector response. An example of a topological cut is the variations of the shower plane to plane; electromagnetic showers have far less fluctuations than inelastic pion interactions.

The analysis shows a 3% higher calorimetric response in data than simulation in both

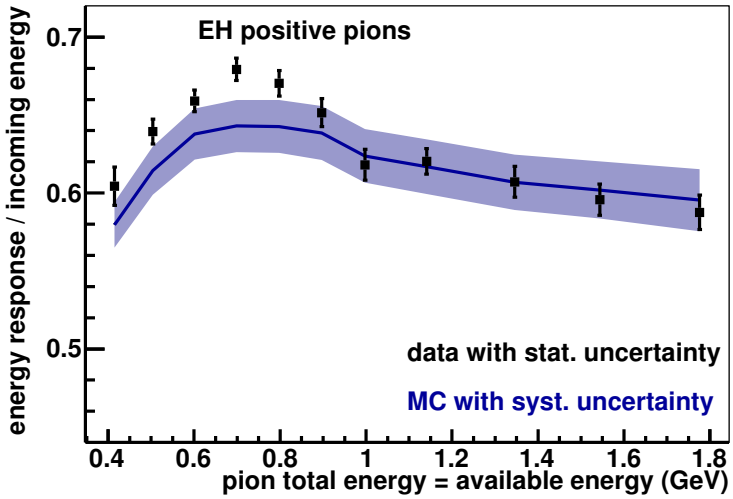

FIG. 4.34: Mean calorimetric response divided by pion total energy for π^+ in the EH (ECAL/HCAL) detector. Data are plotted with statistical uncertainties. Monte-Carlo (MC) simulation is plotted with systematic uncertainties.[15]

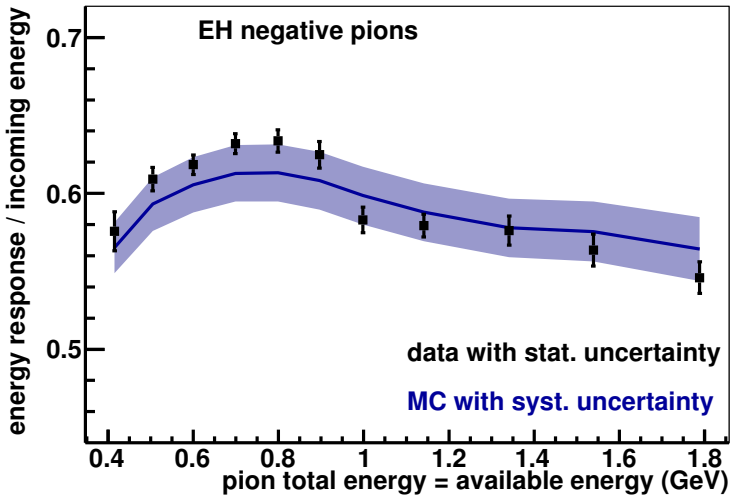

FIG. 4.35: Mean calorimetric response divided by pion total energy for π^- in the EH (ECAL/HCAL) detector. Data are plotted with statistical uncertainties. Monte-Carlo (MC) simulation is plotted with systematic uncertainties.[15]

the TE and EH detector configurations. This discrepancy is consistent with a result from Michel electrons[4] and neutral pions[13] in the MINERνA detector. FIG. 4.36 shows the calorimetric response divided by electron energy for the two detector configurations.

4.11 Birks' law parameter

Birks' law describes the saturation of scintillation light caused by heavy ionization[19]. This results in a non-linear, reduced response of the detector. Birks' parameter, k_B, contributes to a suppression factor defined by

$$\text{suppression factor} \equiv \frac{1.0}{1.0 + k_B \times \mathrm{d}E/\mathrm{d}x}, \tag{4.5}$$

where $\mathrm{d}E/\mathrm{d}x$ is the energy deposition per unit length. Stopping protons exhibit a sharp rise in $\mathrm{d}E/\mathrm{d}x$ at the end of the trajectory as the proton energy falls below minimum ionization in the Bethe equation. In this sharp rise, the effects of Birks' suppression can be observed.

Birks' parameter is measured in the data by isolating a clean sample of non-interacting protons which stop in planes 9–19 of the TE (tracker/ECAL) detector. For the plane in which the proton stops, the energy deposition in that plane is histogrammed. This histogram contains a range of incident proton energies, stopping at different planes in the detector, but the energy of the proton is comparable at the end of the track. The procedure is repeated for the planes upstream of the stopping plane. FIG. 4.37 shows the mean of this energy deposition, plotted as a function of the number of planes from the end of the track, zero indicating the stopping plane. An effective Birks' parameter is derived by varying the parameter in the simulation until it matches the data.

The data is best described by a Birks' parameter, $k_B = 0.0905 \pm 0.015\,\mathrm{mm/MeV}$,

which is just outside the 30% uncertainty on the pre-fit value of 0.133 mm/MeV. The tuned Birks' parameter is incorporated into the simulation utilized in the proton and pion calorimetry analyses presented in this chapter, partially explaining the excellent agreement in the proton case.

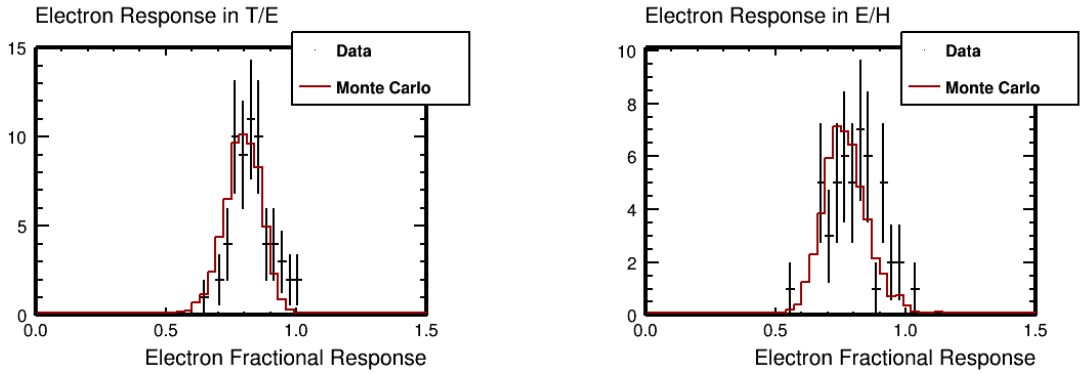

FIG. 4.36: Calorimetric response divided by electron energy for 400 MeV to 500 MeV electrons in the TE detector (left) and EH detector (right). Data are plotted with statistical uncertainties. Monte-Carlo (MC) simulation is plotted without uncertainties.

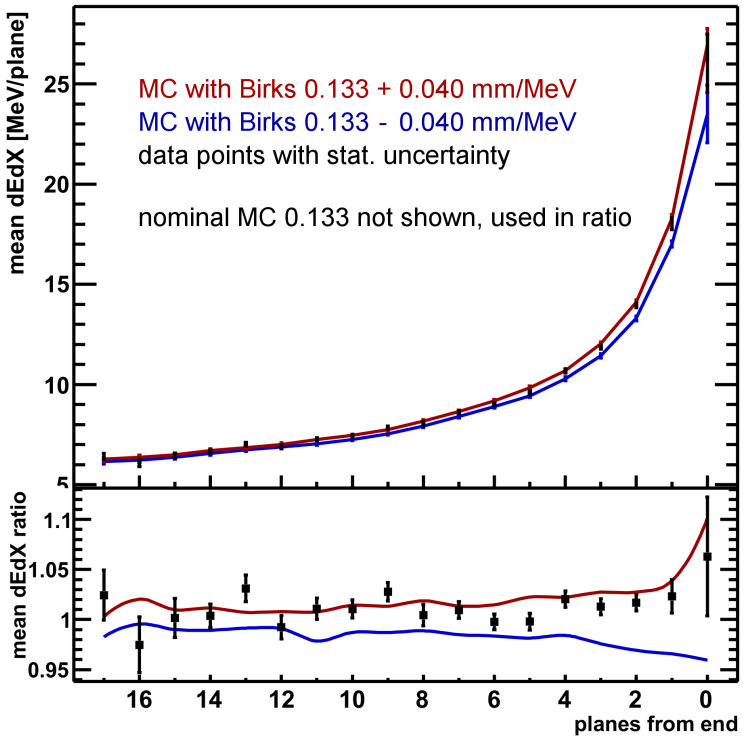

FIG. 4.37: Mean $\mathrm{d}E/\mathrm{d}x$ at the end of a clean, stopping proton track. Data are plotted with statistical uncertainties. The red and blue curves show a +30% (bottom) and -30% (top) variation in Birks' parameter. The bottom plot shows a data ratio to the before-fit Birks' parameter value of 0.133 mm/MeV.[15]

CHAPTER 5

Reconstruction and Calorimetry

5.1 Overview

The MINERνA detector records data in 16 μs gates triggered by a spill from the NuMI beamline (Section 2.4). NuMI generates a 10 μs neutrino beam spill every 2.2 s. The additional 6 μs of the MINERνA gate catches Michel electrons and other decay products. Though the readout system has some nuances, effectively each channel (corresponding to one scintillator strip) of the detector records the number of photoelectrons generated by scintillation light as a function of time over the gate[5].

The intensity of the NuMI beam results in multiple neutrino interactions in the MINERνA detector for each gate. There also exists a large flux of muons generated by neutrino interactions in the rock upstream of the detector. These "rock muons" provide a valuable sample for calibrating and aligning the components of the detector. The first step in reconstructing neutrino interactions is to group hits in time (Section 5.2). Hits are then grouped in space (Section 5.3). Long tracks (strings of hits tracing a particle's trajectory) in the detector are identified and if one should match to a track in MINOS,

it is designated as a muon, indicating a ν_μ or $\bar{\nu}_\mu$ interaction in MINERνA (Section 5.4). The existing, off-track energy resulting from the recoil system of the neutrino interaction is reconstructed calorimetrically (Section 5.6). The energy of the incoming neutrino is calculated as the sum of the muon and recoil energy.

The detector, calibration and reconstruction are extensively documented in a Nuclear Instruments and Methods article[4].

5.2 Event formation

Hits in the detector are grouped by time into "time slices" using a peak-finding algorithm. The algorithm scans a 80 ns window across the gate searching for greater than 10 photoelectrons within the window, corresponding to 2/3 of the deposition of a minimum ionizing particle across a plane. The window is then expanded to capture additional activity at earlier and later times. Typically, a time slice will capture all of the activity from a neutrino interaction other than Michel electrons and thermalized neutrons. FIG. 5.1 shows the distribution of the number of slices per gate in the neutrino- and antineutrino-focusing beam configurations.

5.3 Cluster formation

A particle traversing a plane in the detector will typically illuminate two or more adjacent scintillator strips as a result of the overlapping triangular profile of the strips. To associate this activity together, immediately adjacent hits within a single plane and within a single time slice are grouped into "clusters." Clusters may be identified as "trackable" if they appear to result from a single particle crossing the plane. Trackable clusters must have total energy between 1 and 12 MeV and a width of 4 or less adjacent strips. Large showers

can result in very wide clusters which are not deemed trackable. An algorithm identifies cross-talk clusters, which occur when light from one channel leaks to another, typically caused by misalignment of the fibers in connecting to the 64 channel photomultiplier tubes[20].

5.4 Muon reconstruction

Particle tracks within the detector are initially constructed independently in each of the three views (X, U and V) by stringing together trackable clusters that appear colinear. The algorithm then merges these two-dimensional tracks into three-dimensional tracks. This is performed first for trajectories in which the track is clearly visible in all three views and second for trajectories in which one view is obscured by the recoil shower. The tracking algorithm also allows for kinks in the track resulting from hard elastic scatters. The final track is fit by walking a Kalman filter[10] model with multiple scattering down the clusters that comprise the track.

Tracks that exit the back of MINERνA are matched to tracks in MINOS by projecting between the two detectors and searching for compatibility. The algorithm additionally allows for a hard scatter in the support structure between the two detectors. MINOS returns a momentum measurement by either the range that the particle penetrates into the detector or by the curvature of the track in the magnetic field[6]. The curvature of the track is used to determine the charge of the particle.

A track that begins in the fiducial volume of MINERνA and penetrates deeply enough into MINOS to be tracked has passed several interaction lengths of material and is assumed to be a muon, indicating a ν_μ or $\bar{\nu}_\mu$ interaction in MINERνA. The energy of the muon is calculated from the MINOS measurement plus the amount of energy lost in the material traversed within MINERνA.

Clusters that are incorporated into the muon track are flagged so as not to be used in calorimetric reconstruction of the recoil system (Section 5.6). In the case that the muon passes through a large, non-trackable cluster, the expected energy from a minimum ionizing particle is removed from that cluster with the remainder assigned to the recoil system.

5.5 Energy scale calibration

The energy scale of the MINERνA detector is calibrated via a number of *ex situ* and *in situ* means. Before installation in the MINERνA detector, the response of each channel of each plane is mapped by placing a radioactive source along a fine grid of points and measuring the resulting signal. These data are used to determine the attenuation curve of the wavelength-shifting fiber in each strip. The process also allows for determining any dead channels in the detector. When the three-dimensional position of a hit in the detector can be determined (typically when it is incorporated into a track), an attenuation correction is applied to the measured signal. Additionally the front end board readout electronics have a non-linear response which is corrected based on bench measurements.

Between neutrino beam spills, the detector records pedestal data to determine the photomultiplier tube (PMT) dark current (the signal when no external photons are present). The pedestal value is subtracted from the observed signal at the PMT. A light injection (LI) system utilizes light emitting diodes (LEDs) coupled to fibers to illuminate all of the pixels within each PMT. The LI system monitors drifts in the gains of the PMTs, which are used to set the high voltage supply to the PMT. The pedestal values are measured approximately twice per day. The LI system measures PMT gains approximately once per day.

Variations in the response between strips are corrected using rock muon data. These

corrections scale the observed photoelectron distributions to correct non-uniformities in the detector. Rock muon data are also utilized to measure the magnitude of cross-talk for each PMT, which is used to set the level in the simulation.

The final energy calibrations are based on data-simulation comparisons of rock muons. The selected sample of muons is required to be momentum-analyzed by MINOS. The energy spectrum and trajectories of muons observed in data are used to seed the simulation. A light yield (LY) factor is calculated such that simulated spectrum of photoelectrons in clusters along the muon track matches that observed in data. The absolute energy scale of the detector is determined with a muon-equivalent unit (MEU) factor, which scales from photoelectrons to deposited energy. The MEU factor is calculated such that the reconstructed deposited energy in clusters along the muon track matches the true deposited energy in the active scintillator in the simulation. The procedure assumes that the simulation models the energy loss of muons well and the dominant uncertainty comes from the mass model of the detector and active scintillator fraction (Section 7.5). FIG. 5.2 shows the corrected energy distribution of clusters along a rock muon track in data and simulation. The distribution exhibits the characteristic Landau shape, with a peak at around 3 MeV and a long tail from δ-rays and bremsstrahlung radiation.

In order to correct for the degradation in the response of the scintillator over time, the data stream is divided into short (approximately two day) periods and MEU calibration is performed independently for each period. This normalizes the energy scale of the detector over the experimental run.

Small corrections to the alignment of the detector geometry are derived from rock muon data-simulation comparisons. The large rock muon statistics and precise tracking of MINERνA allow for the observation of the triangular profile of the scintillator strips. Small translations and rotations of the detector modules are fit to match the simulation to the data.

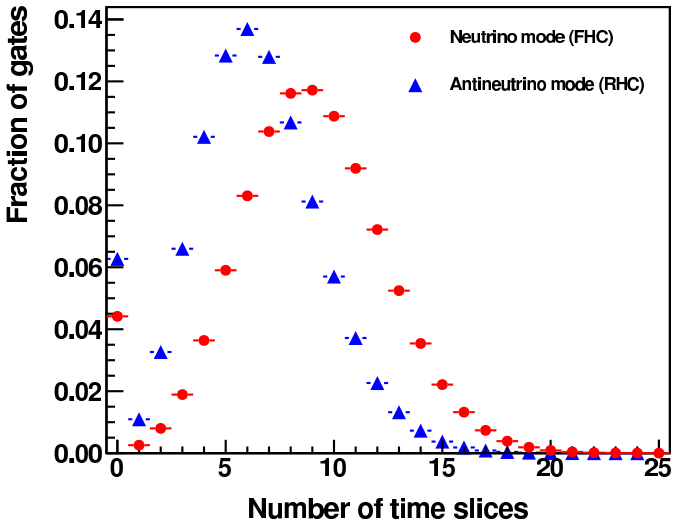

FIG. 5.1: Number of slices per gate at typical beam intensity for the forward horn current (FHC), neutrino-focusing beam and reverse horn current (RHC), antineutrino-focusing beam.[4]

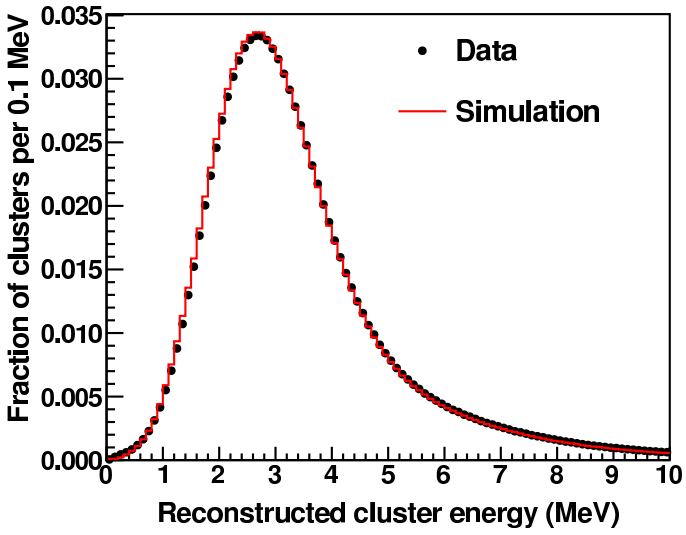

FIG. 5.2: Energy distribution of clusters along a rock muon track.[4]

.

5.6 Calorimetry

The energy of the recoil system (everything other than the muon) is reconstructed calorimetrically, by summing energy depositions in the detector weighted by a calorimetric constant. The calorimetric constant corrects for the energy loss in passive absorbers and the inactive fraction of the scintillator planes. For the low-ν analysis (Chapter 6), the energy of the recoil system is denoted by ν, defined as

$$\nu \equiv E - E_{\mu}, \tag{5.1}$$

where E is the energy of the incoming neutrino and E_{μ} is the energy of the outgoing muon. The actual energy deposition in the detector will be lower than ν because of final state interactions, neutrons that fail to promptly interact, and the possible lack of containment of the recoil system within the detector.

The reconstructed recoil energy, ν_{reco}, is defined as

$$\nu_{\text{reco}} \equiv \alpha \times \sum_{i} C_i E_i, \tag{5.2}$$

where the summation is over clusters in the detector, E_i is the energy of the cluster, C_i is the appropriate calorimetric constant and the overall scale is set by α. The clusters selected for calorimetry are all clusters not associated with the muon track in a $[-20, 35]$ ns window around the interaction time and not identified as cross-talk. The low-ν analysis (Chapter 6) additionally enforces a minimum cluster energy of 1.5 MeV and ignores the outer detector (OD). The default calorimetry for MINERνA analyses includes the OD and enforces a 1.0 MeV minimum cluster energy. The additional constraints for the low-ν analysis are designed to remove biases from pile-up in the OD and poorly simulated very low energy hits (electronic cross-talk). The results presented in this section are for the

low-ν definition of calorimetry; the default calorimetry is presented in [4].

The calorimetric constants, C, are calculated by the energy loss per unit length, $\mathrm{d}E/\mathrm{d}x$, of a minimum ionizing particle at normal incidence as

$$C = \frac{E_{\mathrm{abs}} + E_{\mathrm{sc}}}{f \times E_{\mathrm{sc}}}, \tag{5.3}$$

where E_{abs} is the energy loss in one absorber plane, E_{sc} is the energy loss in one scintillator plane and f is the active fraction of the scintillator plane. For the tracking region, with no absorber, $E_{\mathrm{abs}} = 0$ and the active fraction, $f = 0.8185$, yields $C_{\mathrm{tracker}} = 1/f = 1.222$. For the ECAL region, $C_{\mathrm{ECAL}} = 2.013$; for the HCAL region, $C_{\mathrm{HCAL}} = 10.314$.

The overall scale, α, is set such that the reconstructed recoil energy, ν_{reco}, matches the true recoil energy, ν_{true}, in the simulation. The scale is set to minimize the quality factor,

$$Q = \frac{1}{N} \sum_i \left(\arctan\left(\frac{\nu_{\mathrm{reco},i}}{\nu_{\mathrm{true},i}} \right) - \frac{\pi}{4} \right)^2 \tag{5.4}$$

where the summation is over events with true recoil energy between 1.0 and 10.0 GeV and N is the total number of such events. Because the distribution of ν_{reco} is bounded on the left at zero (one cannot reconstruct negative energies), but trails off to the right from very high energy hits in the calorimeters, a more standard "χ^2" style quality factor of $(\nu_{\mathrm{reco}} - \nu_{\mathrm{true}})^2$ will inevitably set the peak of the ν_{reco} distribution below the peak of the ν_{true} distribution. The quality factor in Eq. 5.4 is less susceptible to the asymmetric tails of the ν_{reco} distribution.

After fitting α, any non-linearities in the calorimetric response are corrected with a "polyline", which maps uncorrected recoil energy, $\bar{\nu}_{\mathrm{reco}}$, to corrected recoil energy, ν_{reco}. The polyline is constructed by histogramming the quantity $\Delta\nu/\nu_{\mathrm{true}} = (\nu_{\mathrm{reco}} - \nu_{\mathrm{true}})/\nu_{\mathrm{true}}$

in bins of ν_{true}. Each histogram contributes one node to the polyline with

$$x = \bar{\nu}_{\text{reco}} = \langle \nu_{\text{true}} \rangle \times (1 + \eta) \tag{5.5}$$

$$y = \nu_{\text{reco}} = \langle \nu_{\text{true}} \rangle, \tag{5.6}$$

where $\langle \nu_{\text{reco}} \rangle$ is the average true recoil energy in the bin and η is the mean of a Gaussian fit to the distribution. For example, if a bin with $\langle \nu_{\text{reco}} \rangle = 1.0\,\text{GeV}$ is 5% low ($\eta = -0.05$), the polyline maps 0.95 GeV to 1.0 GeV. The lowest point of the polyline is fixed at (0.0,0.0) GeV, the highest point is fixed at (50.0,50.0) GeV.

The calorimetric tuning process is performed independently for neutrino and antineutrino events. For neutrinos, the fit finds $\alpha = 1.87$ with the polyline shown in FIG. 5.3. For antineutrinos, the fit finds $\alpha = 1.92$ with the polyline shown in FIG. 5.4. FIG. 5.5 – 5.6 show the $\Delta\nu/\nu_{\text{true}}$ distributions for neutrinos after applying the polyline correction; the higher energy bins are presented in Appendix A. FIG. 5.7 – 5.8 show the same for antineutrinos; the higher energy bins are presented in Appendix B. The mean of a Gaussian fit to these distributions is shown in FIG. 5.9 for neutrinos and in FIG. 5.10 for antineutrinos. The width of the distributions characterizes the calorimetric energy resolution, shown in FIG. 5.11 for neutrinos and FIG. 5.12 for antineutrinos. For neutrinos, the calorimetric energy resolution is $\sigma/\nu = 0.132 \oplus 0.329/\sqrt{\nu}$. For antineutrinos, the calorimetric energy resolution is $\sigma/\nu = 0.163 \oplus 0.283/\sqrt{\nu}$, where ν is in units of GeV.

The calorimetric energy resolution is a convolution of several effects: final state interactions, deposition in the passive absorber, attenuation along the strip, containment in the detector, and the response of the scintillator, PMTs and electronics. An additional important component is recoil shower fluctuations to electromagnetic, hadronic and neutral components. The energy of a recoil π^0, which rapidly decays to two photons creating electromagnetic showers, is very well reconstructed because electromagnetic activity is the

result of a many-particle cascade with very small statistical fluctuations in the fraction of energy deposited by charged particles (electrons and positrons). A recoil $\pi^{\pm}$, however, may occasionally inelastically scatter transferring much energy to neutrons. Because neutral particles do not ionize the scintillator, they are invisible and the energy in a neutron is often lost unless it promptly interacts in the detector. Thus, how well an interaction is reconstructed is a function of the composition of the recoil system. FIG. 5.13 – 5.16 show the composition of the recoil system as simulated for neutrinos. FIG. 5.17 – 5.20 show the same for antineutrinos as simulated.

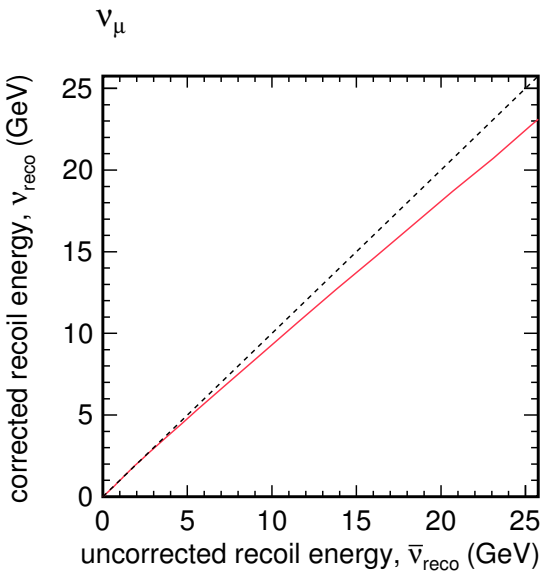

FIG. 5.3: Polyline correction (red) to calorimetric recoil energy for charged-current neutrino interactions.

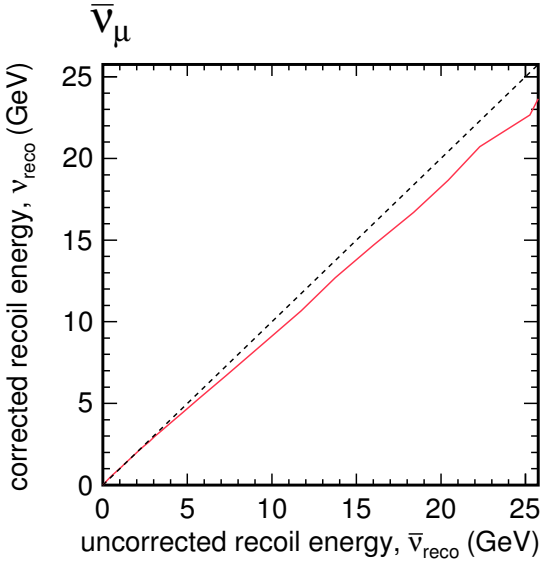

FIG. 5.4: Polyline correction (red) to calorimetric recoil energy for charged-current antineutrino interactions.

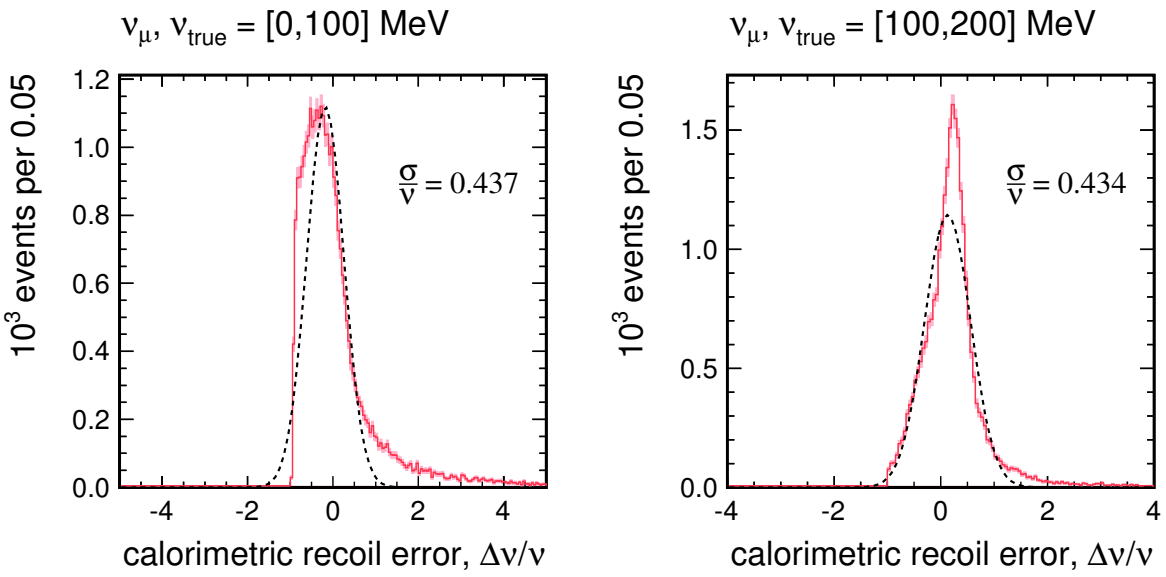

(a) $\nu_{true} = [0, 100]$ MeV

(b) $\nu_{true} = [100, 200]$ MeV

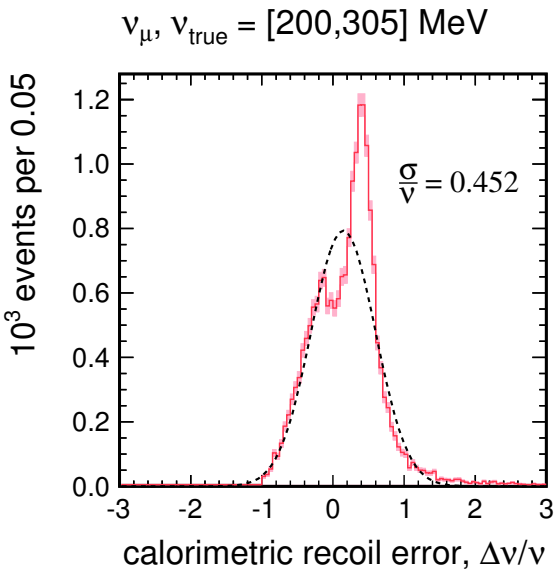

(c) $\nu_{true} = [200, 305]$ MeV

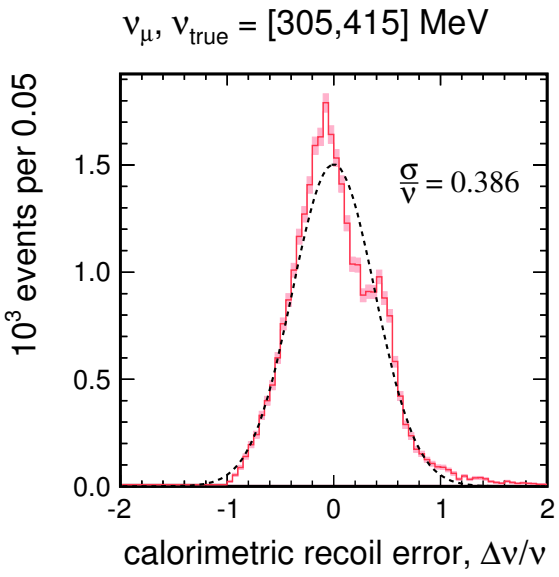

(d) $\nu_{true} = [305, 415]$ MeV

FIG. 5.5: Calorimetric recoil error, $\Delta\nu/\nu = (\nu_{reco} - \nu_{true})/\nu_{true}$ for charged-current neutrino interactions; $\nu_{true} = [0, 415]$ MeV. The two-peak structure arises from a single proton final state (the peak to the right) or a more complicated final state (the peak to the left).

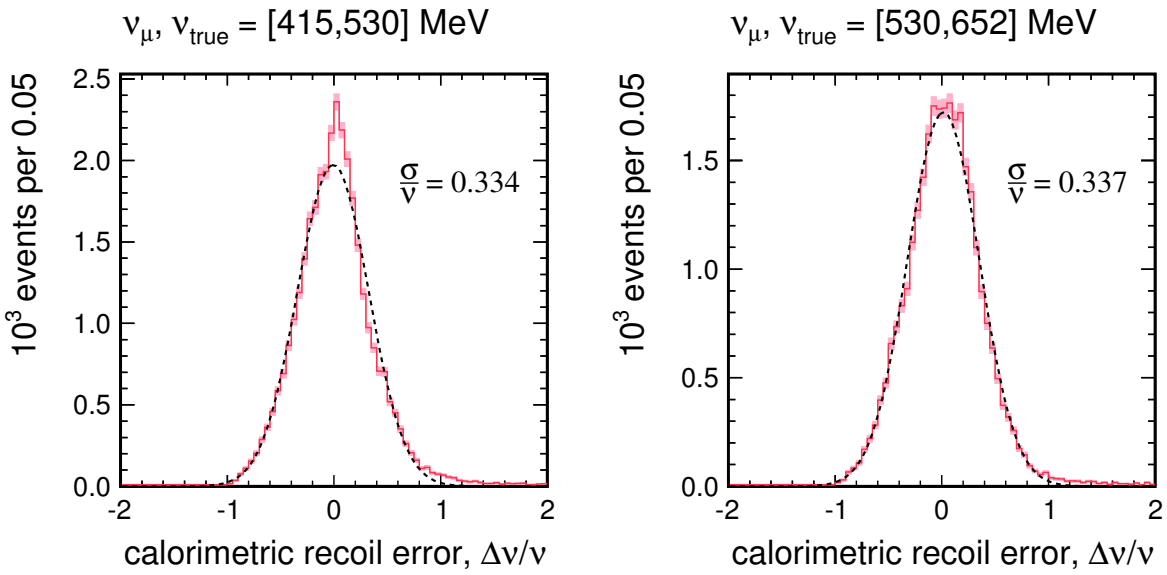

(a) $\nu_{true} = [415, 530]$ MeV

(b) $\nu_{true} = [530, 652]$ MeV

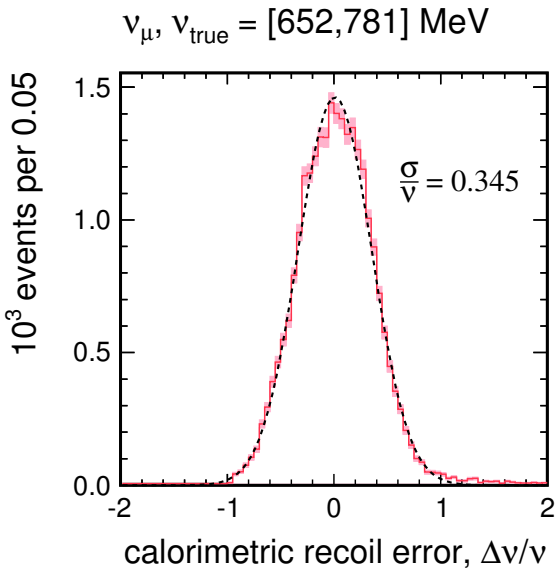

(c) $\nu_{true} = [652, 781]$ MeV

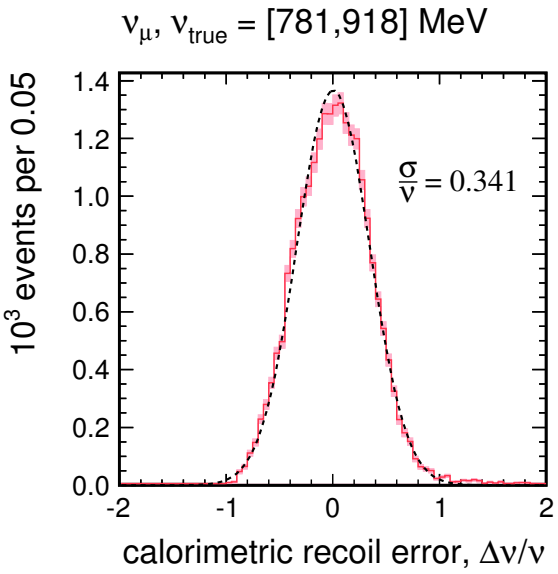

(d) $\nu_{true} = [781, 918]$ MeV

FIG. 5.6: Calorimetric recoil error, $\Delta\nu/\nu = (\nu_{reco} - \nu_{true})/\nu_{true}$ for charged-current neutrino interactions; $\nu_{true} = [415, 918]$ MeV.

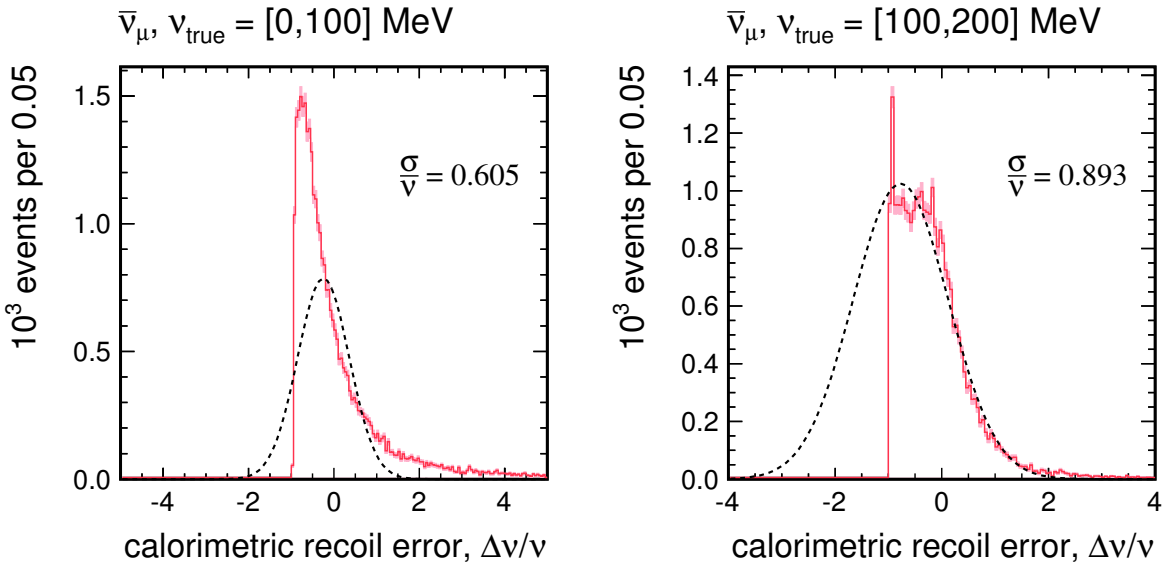

(a) $\nu_{true} = [0, 100]$ MeV

(b) $\nu_{true} = [100, 200]$ MeV

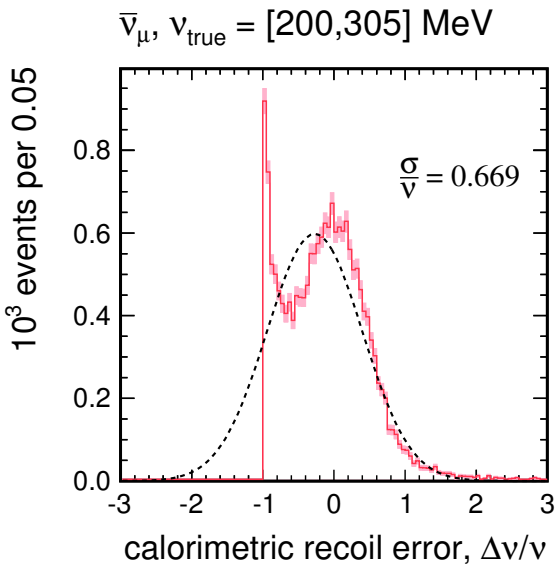

(c) $\nu_{true} = [200, 305]$ MeV

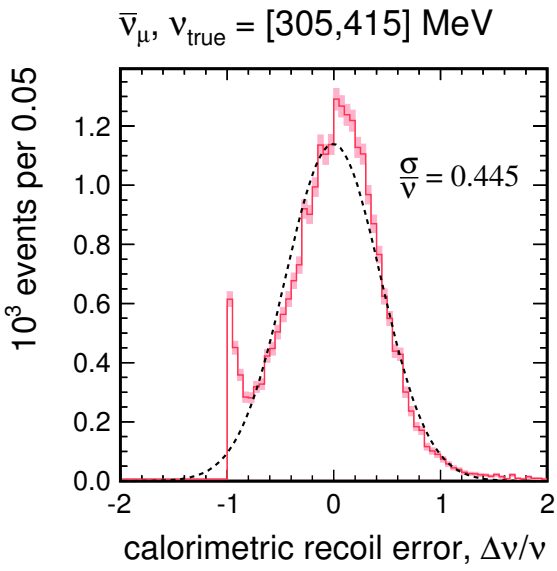

(d) $\nu_{true} = [305, 415]$ MeV

FIG. 5.7: Calorimetric recoil error, $\Delta\nu/\nu = (\nu_{reco} - \nu_{true})/\nu_{true}$ for charged-current antineutrino interactions; $\nu_{true} = [0, 415]$ MeV. The peak at $\Delta\nu/\nu = -1$ ($\nu_{reco} = 0$) arises from a single neutron final state which fails to promptly interact in the detector.

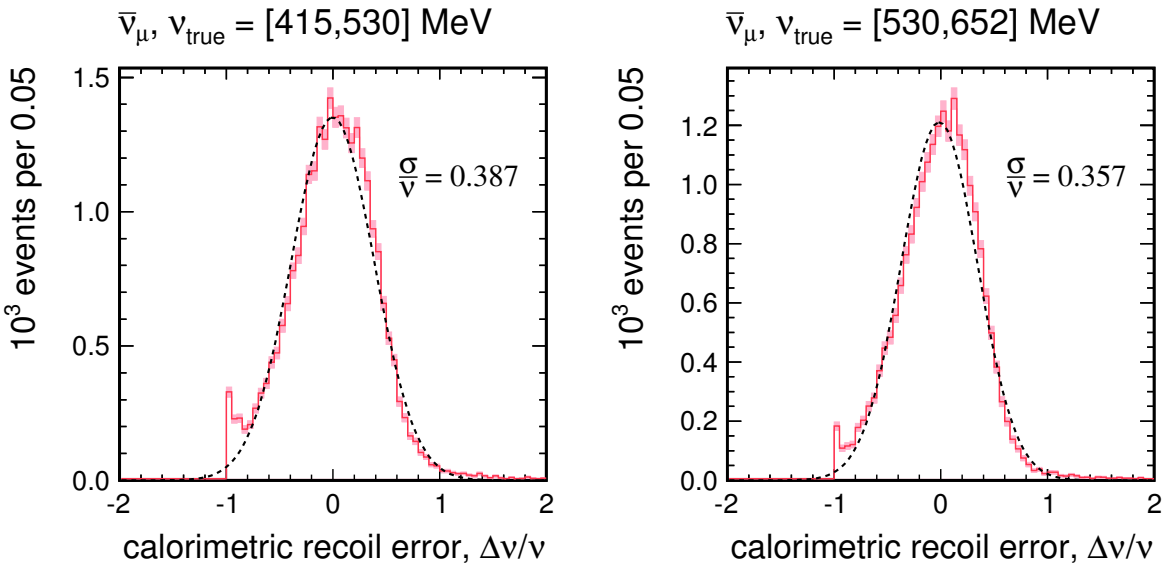

(a) $\nu_{true} = [415, 530]$ MeV

(b) $\nu_{true} = [530, 652]$ MeV

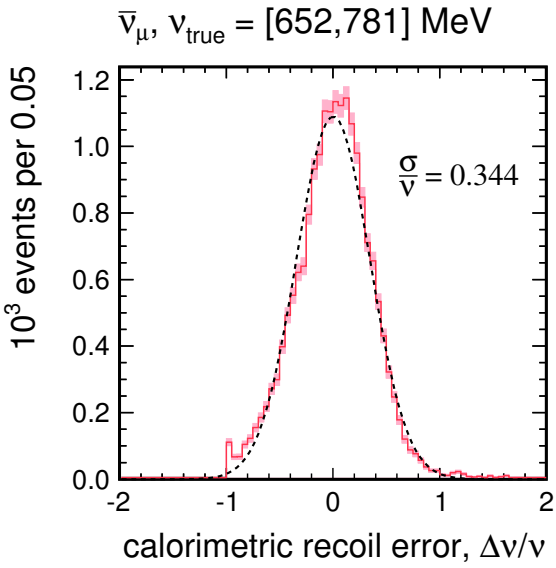

(c) $\nu_{true} = [652, 781]$ MeV

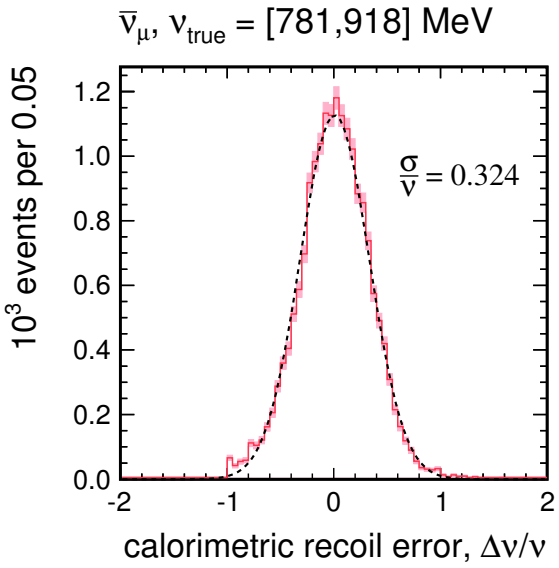

(d) $\nu_{true} = [781, 918]$ MeV

FIG. 5.8: Calorimetric recoil error, $\Delta\nu/\nu = (\nu_{reco} - \nu_{true})/\nu_{true}$ for charged-current antineutrino interactions; $\nu_{true} = [415, 918]$ MeV.

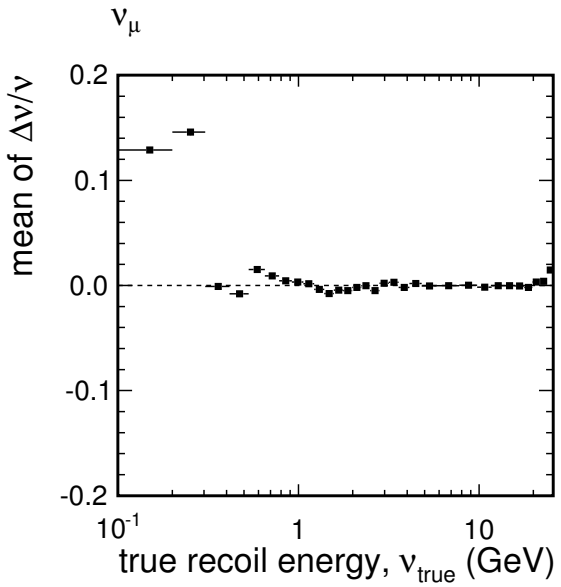

FIG. 5.9: Mean of calorimetric recoil error, $\Delta\nu/\nu = (\nu_{reco} - \nu_{true})/\nu_{true}$ for charged-current neutrino interactions from a Gaussian fit to the distributions in FIG. 5.5 – 5.6 and FIG. A.1 – A.6.

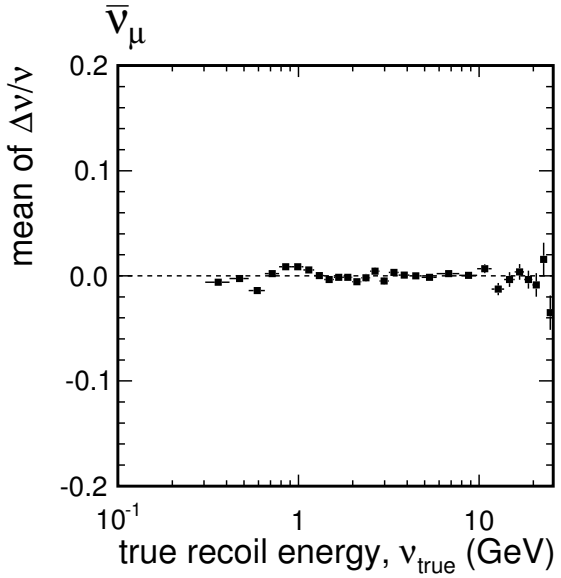

FIG. 5.10: Mean of calorimetric recoil error, $\Delta\nu/\nu = (\nu_{reco} - \nu_{true})/\nu_{true}$ for charged-current antineutrino interactions from a Gaussian fit to the distributions in FIG. 5.7 – 5.8 and FIG. B.1 – B.6.

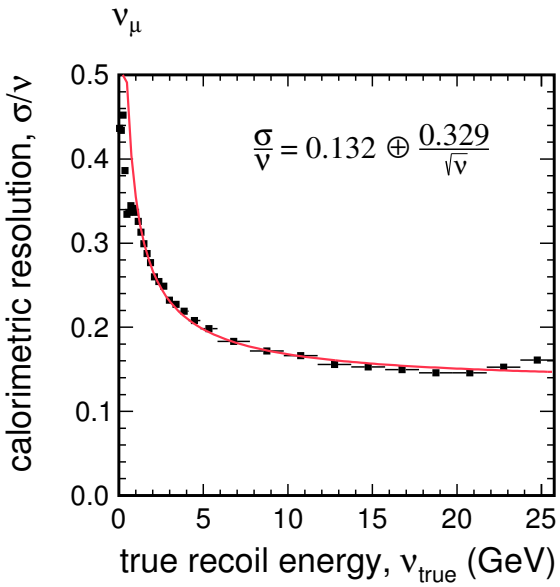

FIG. 5.11: Calorimetric energy resolution, σ/ν, for charged-current neutrino interactions. The points are the standard deviation of a Gaussian fit to the distributions in FIG. 5.5 – 5.6 and FIG. A.1 – A.6. The red line is a functional fit to the points, $a \oplus b/\sqrt{\nu}$, yielding a 13.2% constant term and $32.9\%/\sqrt{\nu}$ energy-dependent term.

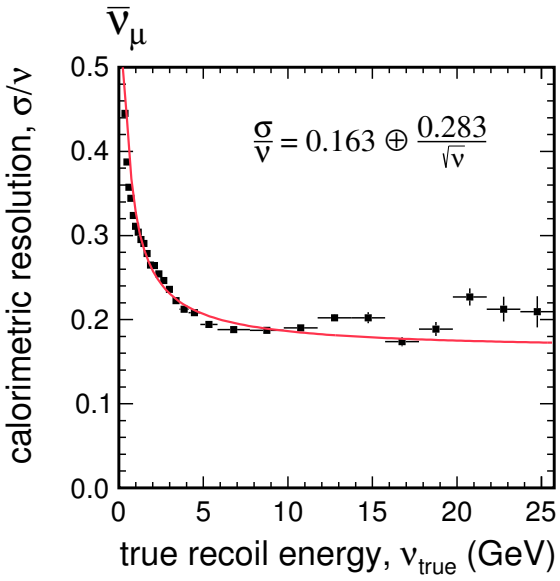

FIG. 5.12: Calorimetric energy resolution, σ/ν, for charged-current antineutrino interactions. The points are the standard deviation of a Gaussian fit to the distributions in FIG. 5.7 – 5.8 and FIG. B.1 – B.6. The red line is a functional fit to the points, $a \oplus b/\sqrt{\nu}$, yielding a 16.3% constant term and $28.3\%/\sqrt{\nu}$ energy-dependent term.

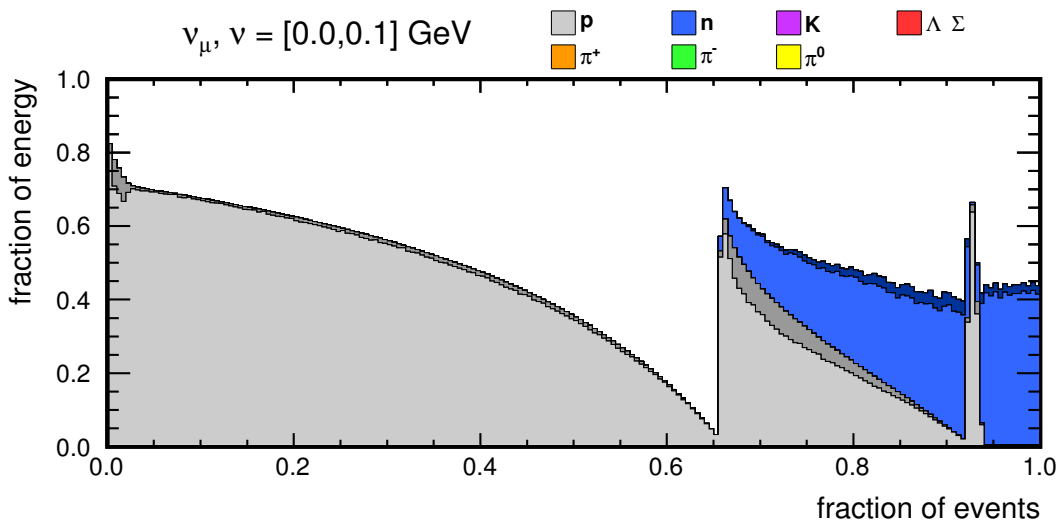

(a) $\nu_{true} = [0.0, 0.1]$ GeV

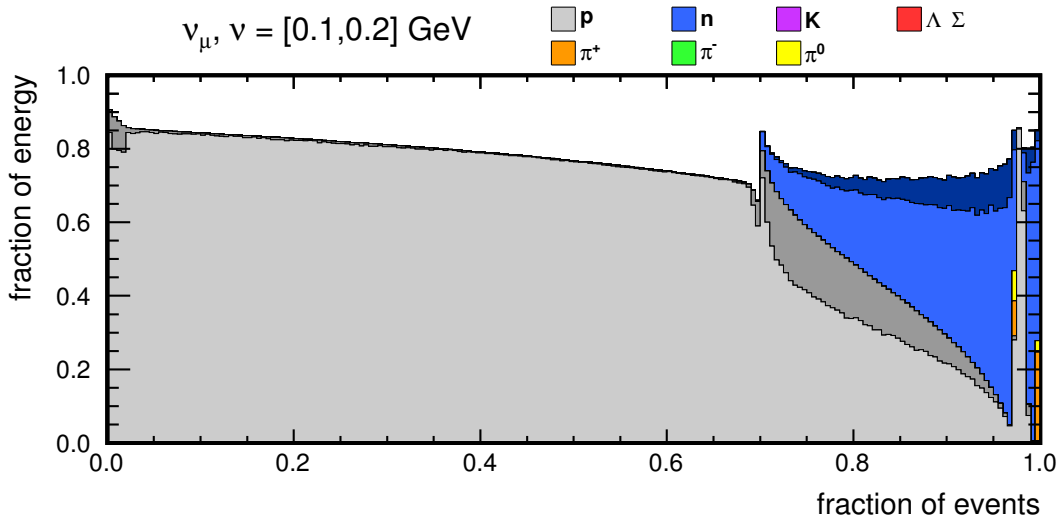

(b) $\nu_{true} = [0.1, 0.2]$ GeV

FIG. 5.13: Simulated recoil system composition for charged-current neutrino interactions; $\nu_{true} = [0.0, 0.2]$ GeV. The plot is constructed as follows: for each simulated event, the fraction of energy carried by each species of recoil particle is computed. This fraction of energy is the kinetic energy (rest mass subtracted) of protons and neutrons or the total energy of pions and kaons, divided by ν_{true}. For strange baryons (Λ, Σ), the rest mass of a proton is subtracted from the total energy. The fractions of energy will not sum to 1.0 because of final state interactions and binding energy. The events are arranged along the X–axis by class (all proton, proton + neutron, proton + π^+, etc.) and sorted within this class by energy. Each bin on the plot represents the average of several similar events. The X–axis is arbitrarily ranged from 0.0 to 1.0, but can be interpreted as 0 to n_{events}. Within a given species of particle, the two color shades show the lead (most energetic) particle in lighter shade and the sum of all other particles in darker shade.

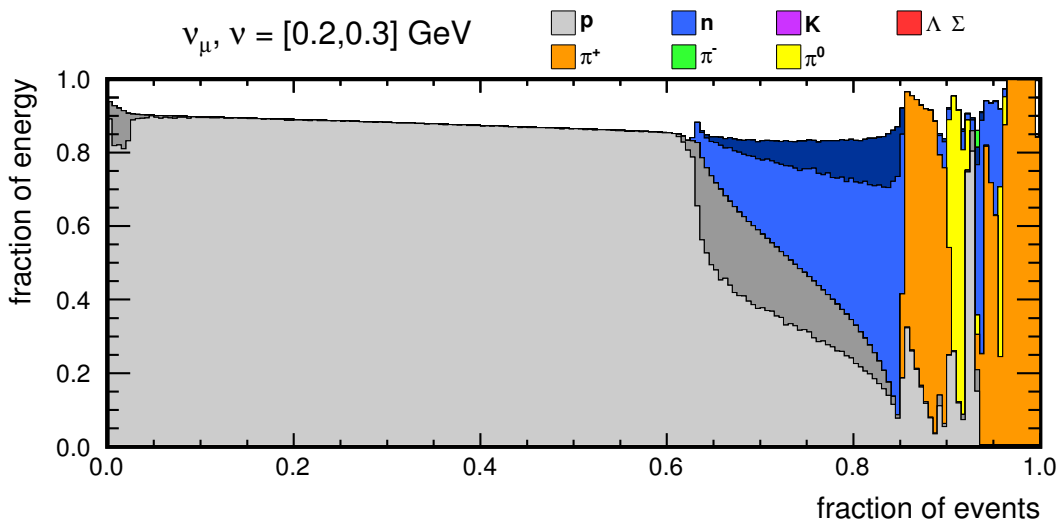

(a) $\nu_{true} = [0.2, 0.3]$ GeV

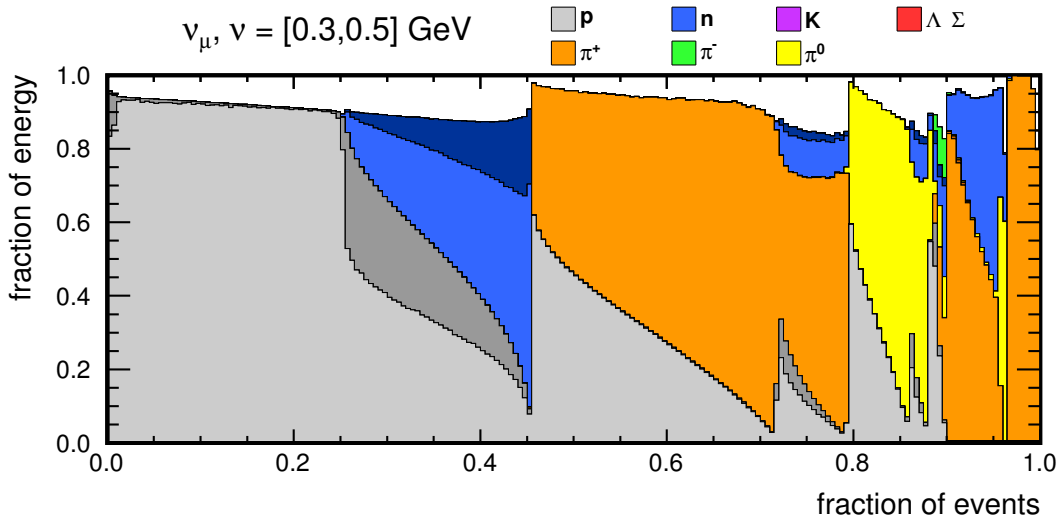

(b) $\nu_{true} = [0.3, 0.5]$ GeV

FIG. 5.14: Simulated recoil system composition for charged-current neutrino interactions; $\nu_{true} = [0.2, 0.5]$ GeV. The plot is constructed as follows: for each simulated event, the fraction of energy carried by each species of recoil particle is computed. This fraction of energy is the kinetic energy (rest mass subtracted) of protons and neutrons or the total energy of pions and kaons, divided by ν_{true}. For strange baryons (Λ, Σ), the rest mass of a proton is subtracted from the total energy. The fractions of energy will not sum to 1.0 because of final state interactions and binding energy. The events are arranged along the X–axis by class (all proton, proton + neutron, proton + π^+, etc.) and sorted within this class by energy. Each bin on the plot represents the average of several similar events. The X–axis is arbitrarily ranged from 0.0 to 1.0, but can be interpreted as 0 to n_{events}. Within a given species of particle, the two color shades show the lead (most energetic) particle in lighter shade and the sum of all other particles in darker shade.

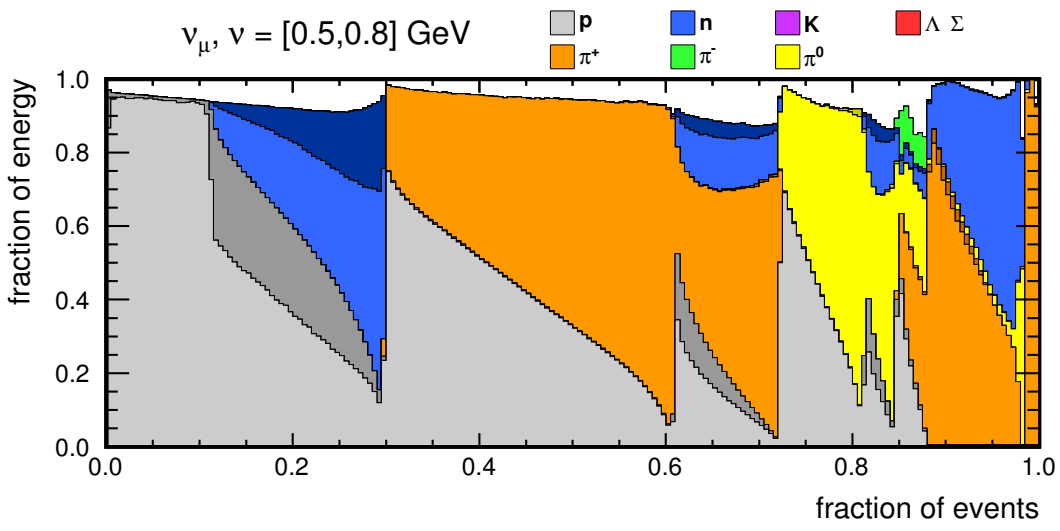

(a) $\nu_{true} = [0.5, 0.8]$ GeV

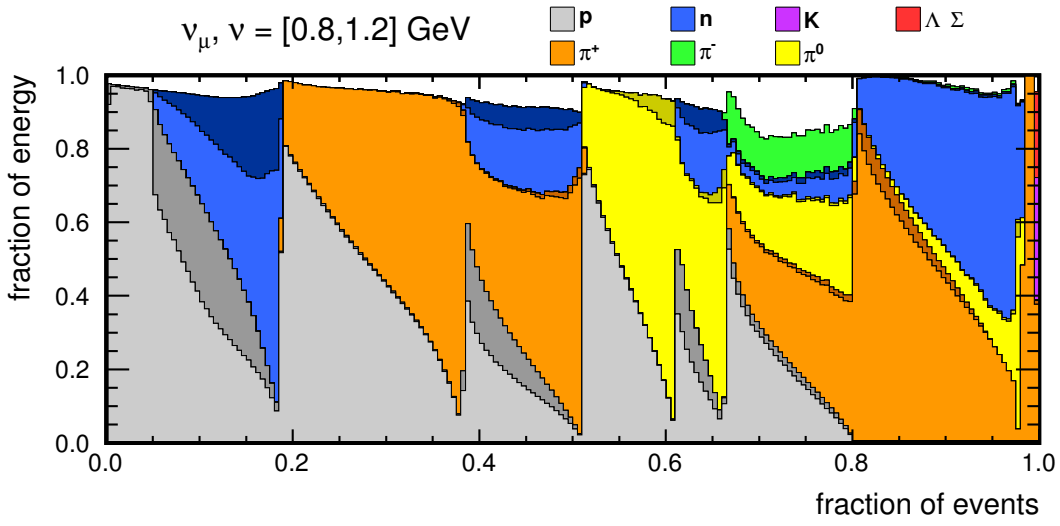

(b) $\nu_{true} = [0.8, 1.2]$ GeV

FIG. 5.15: Simulated recoil system composition for charged-current neutrino interactions; $\nu_{true} = [0.5, 1.2]$ GeV. The plot is constructed as follows: for each simulated event, the fraction of energy carried by each species of recoil particle is computed. This fraction of energy is the kinetic energy (rest mass subtracted) of protons and neutrons or the total energy of pions and kaons, divided by ν_{true}. For strange baryons (Λ, Σ), the rest mass of a proton is subtracted from the total energy. The fractions of energy will not sum to 1.0 because of final state interactions and binding energy. The events are arranged along the X–axis by class (all proton, proton + neutron, proton + π^+, etc.) and sorted within this class by energy. Each bin on the plot represents the average of several similar events. The X–axis is arbitrarily ranged from 0.0 to 1.0, but can be interpreted as 0 to n_{events}. Within a given species of particle, the two color shades show the lead (most energetic) particle in lighter shade and the sum of all other particles in darker shade.

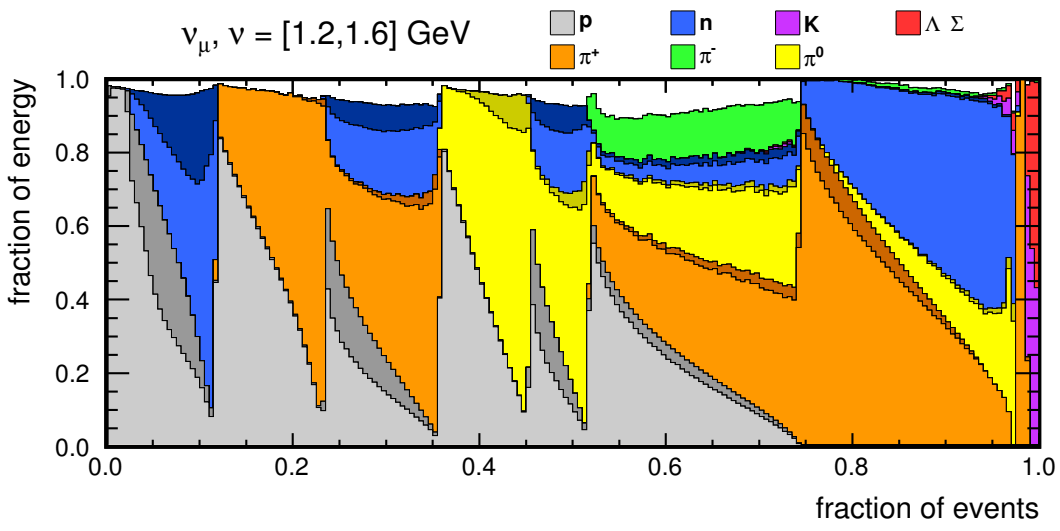

(a) $\nu_{true} = [1.2, 1.6]$ GeV

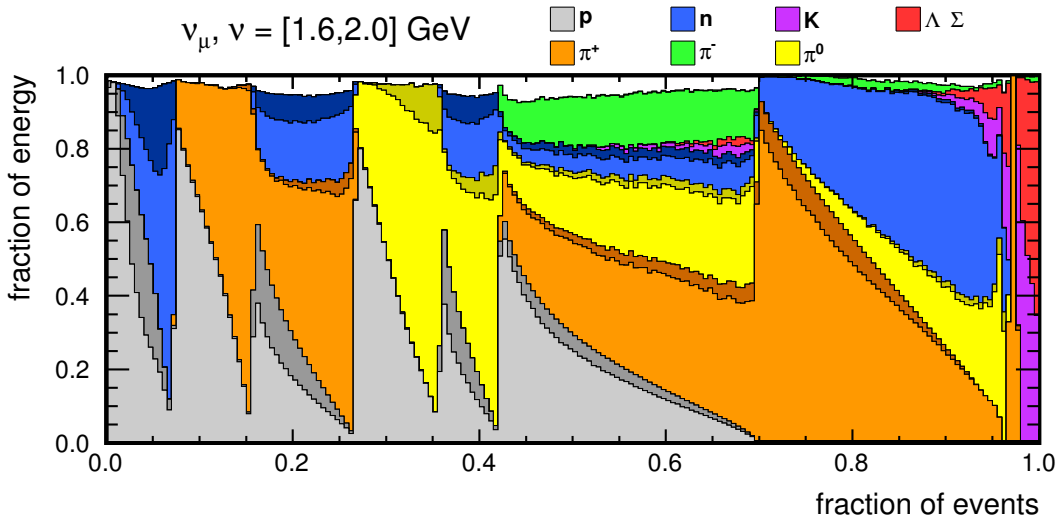

(b) $\nu_{true} = [1.6, 2.0]$ GeV

FIG. 5.16: Simulated recoil system composition for charged-current neutrino interactions; $\nu_{true} = [1.2, 2.0]$ GeV. The plot is constructed as follows: for each simulated event, the fraction of energy carried by each species of recoil particle is computed. This fraction of energy is the kinetic energy (rest mass subtracted) of protons and neutrons or the total energy of pions and kaons, divided by ν_{true}. For strange baryons (Λ, Σ), the rest mass of a proton is subtracted from the total energy. The fractions of energy will not sum to 1.0 because of final state interactions and binding energy. The events are arranged along the X–axis by class (all proton, proton + neutron, proton + π^+, etc.) and sorted within this class by energy. Each bin on the plot represents the average of several similar events. The X–axis is arbitrarily ranged from 0.0 to 1.0, but can be interpreted as 0 to n_{events}. Within a given species of particle, the two color shades show the lead (most energetic) particle in lighter shade and the sum of all other particles in darker shade.

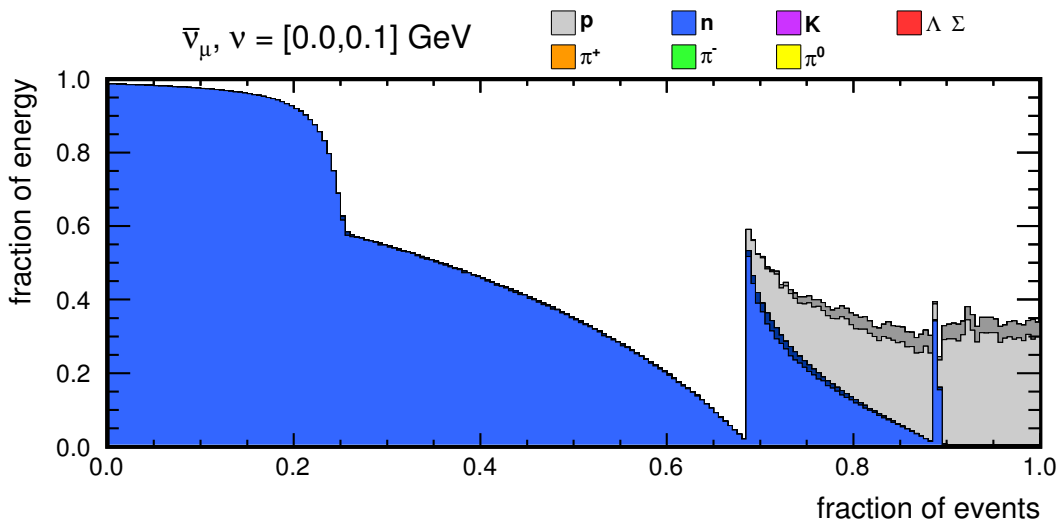

(a) $\nu_{true} = [0.0, 0.1]$ GeV

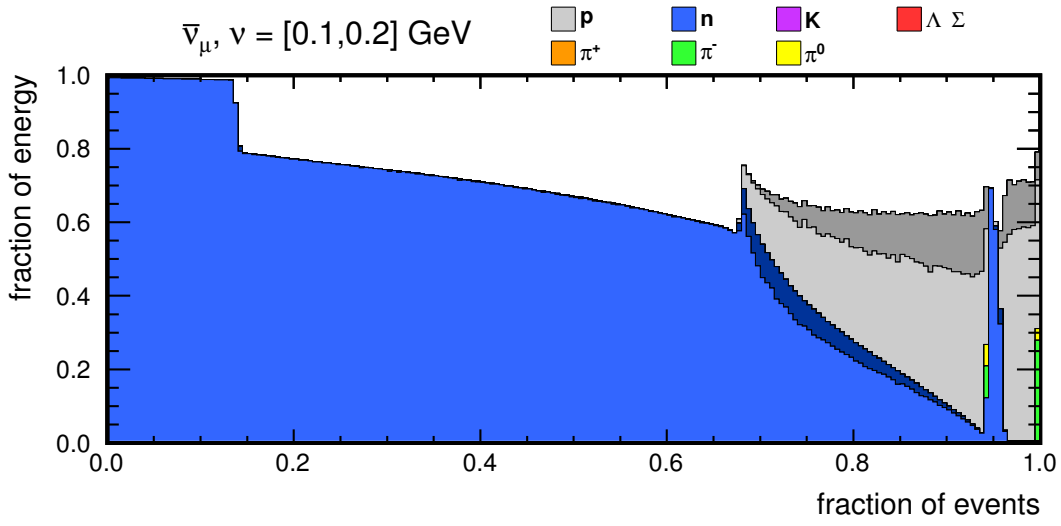

(b) $\nu_{true} = [0.1, 0.2]$ GeV

FIG. 5.17: Simulated recoil system composition for charged-current antineutrino interactions; $\nu_{true} = [0.0, 0.2]$ GeV. The plot is constructed as follows: for each simulated event, the fraction of energy carried by each species of recoil particle is computed. This fraction of energy is the kinetic energy (rest mass subtracted) of protons and neutrons or the total energy of pions and kaons, divided by ν_{true}. For strange baryons (Λ, Σ), the rest mass of a proton is subtracted from the total energy. The fractions of energy will not sum to 1.0 because of final state interactions and binding energy. The events are arranged along the X–axis by class (all neutron, neutron + proton, neutron + π^-, etc.) and sorted within this class by energy. Each bin on the plot represents the average of several similar events. The X–axis is arbitrarily ranged from 0.0 to 1.0, but can be interpreted as 0 to n_{events}. Within a given species of particle, the two color shades show the lead (most energetic) particle in lighter shade and the sum of all other particles in darker shade.

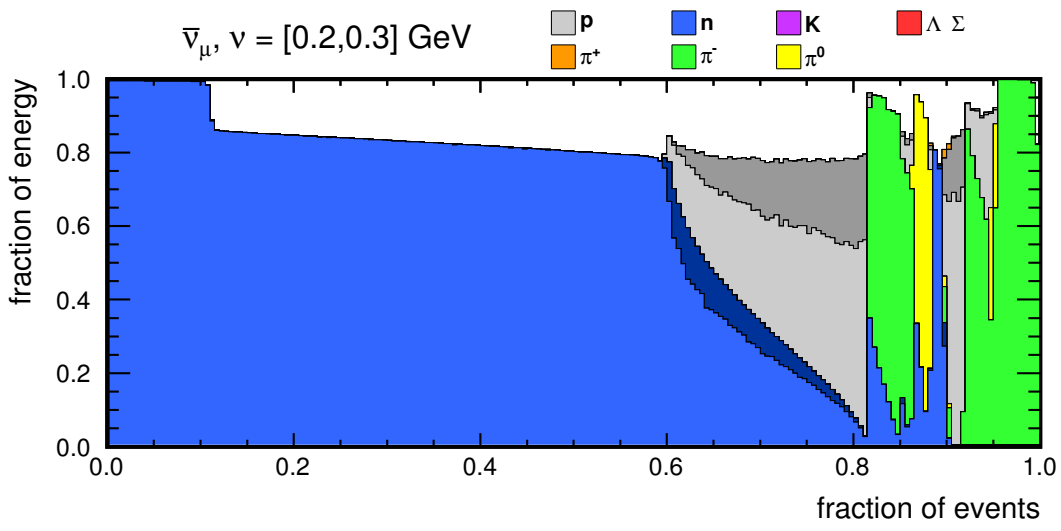

(a) $\nu_{true} = [0.2, 0.3]$ GeV

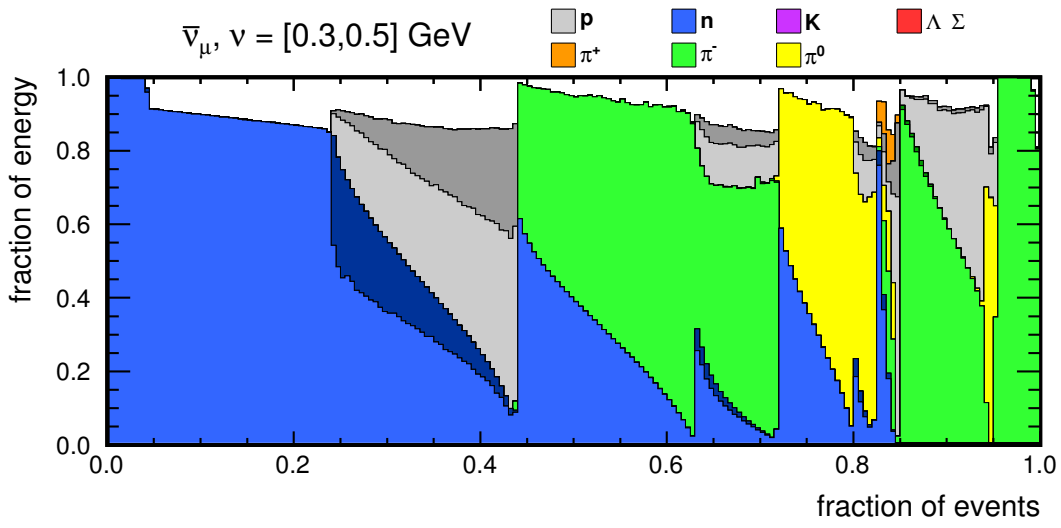

(b) $\nu_{true} = [0.3, 0.5]$ GeV

FIG. 5.18: Simulated recoil system composition for charged-current antineutrino interactions; $\nu_{true} = [0.2, 0.5]$ GeV. The plot is constructed as follows: for each simulated event, the fraction of energy carried by each species of recoil particle is computed. This fraction of energy is the kinetic energy (rest mass subtracted) of protons and neutrons or the total energy of pions and kaons, divided by ν_{true}. For strange baryons (Λ, Σ), the rest mass of a proton is subtracted from the total energy. The fractions of energy will not sum to 1.0 because of final state interactions and binding energy. The events are arranged along the X–axis by class (all neutron, neutron + proton, neutron + π^-, etc.) and sorted within this class by energy. Each bin on the plot represents the average of several similar events. The X–axis is arbitrarily ranged from 0.0 to 1.0, but can be interpreted as 0 to n_{events}. Within a given species of particle, the two color shades show the lead (most energetic) particle in lighter shade and the sum of all other particles in darker shade.

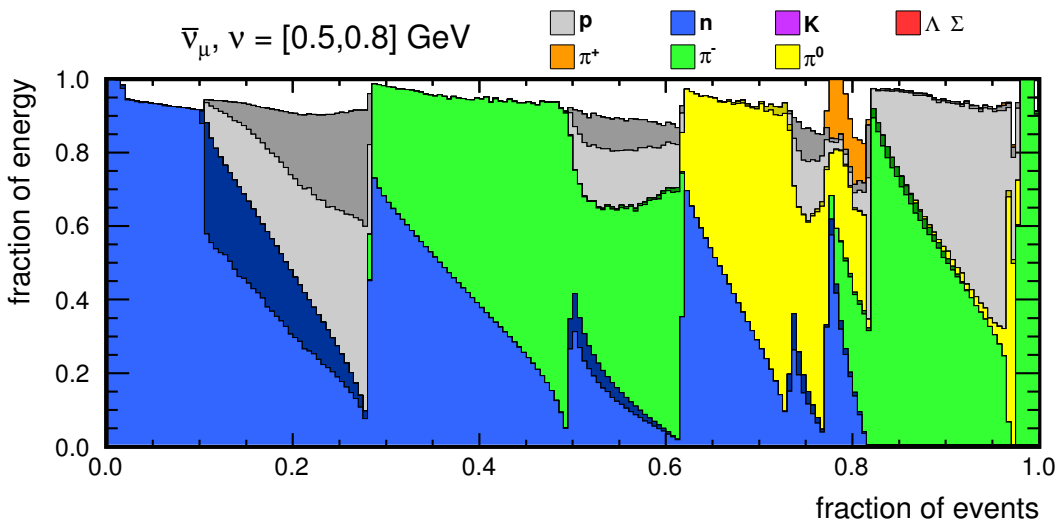

(a) $\nu_{true} = [0.5, 0.8]$ GeV

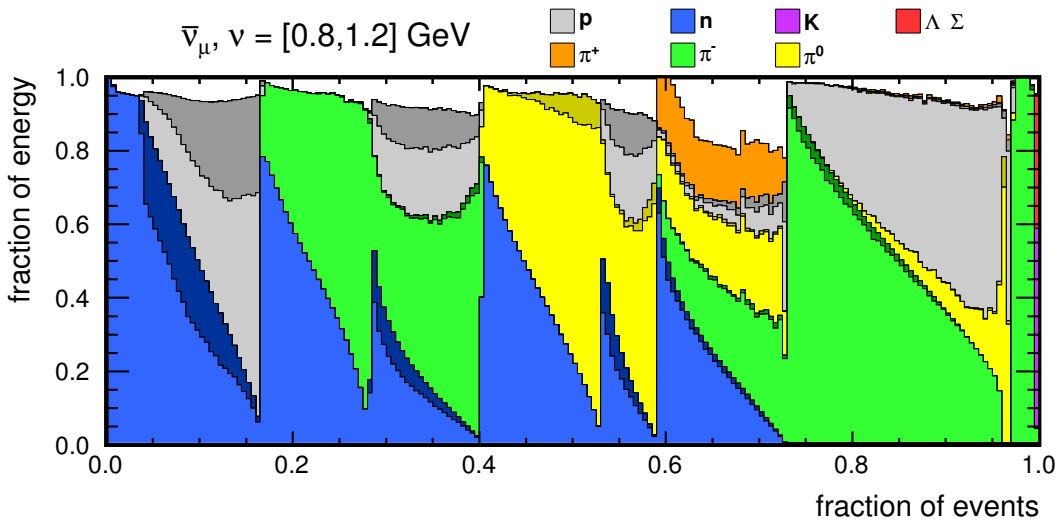

(b) $\nu_{true} = [0.8, 1.2]$ GeV

FIG. 5.19: Simulated recoil system composition for charged-current antineutrino interactions; $\nu_{true} = [0.5, 1.2]$ GeV. The plot is constructed as follows: for each simulated event, the fraction of energy carried by each species of recoil particle is computed. This fraction of energy is the kinetic energy (rest mass subtracted) of protons and neutrons or the total energy of pions and kaons, divided by ν_{true}. For strange baryons (Λ, Σ), the rest mass of a proton is subtracted from the total energy. The fractions of energy will not sum to 1.0 because of final state interactions and binding energy. The events are arranged along the X–axis by class (all neutron, neutron + proton, neutron + π^-, etc.) and sorted within this class by energy. Each bin on the plot represents the average of several similar events. The X–axis is arbitrarily ranged from 0.0 to 1.0, but can be interpreted as 0 to n_{events}. Within a given species of particle, the two color shades show the lead (most energetic) particle in lighter shade and the sum of all other particles in darker shade.

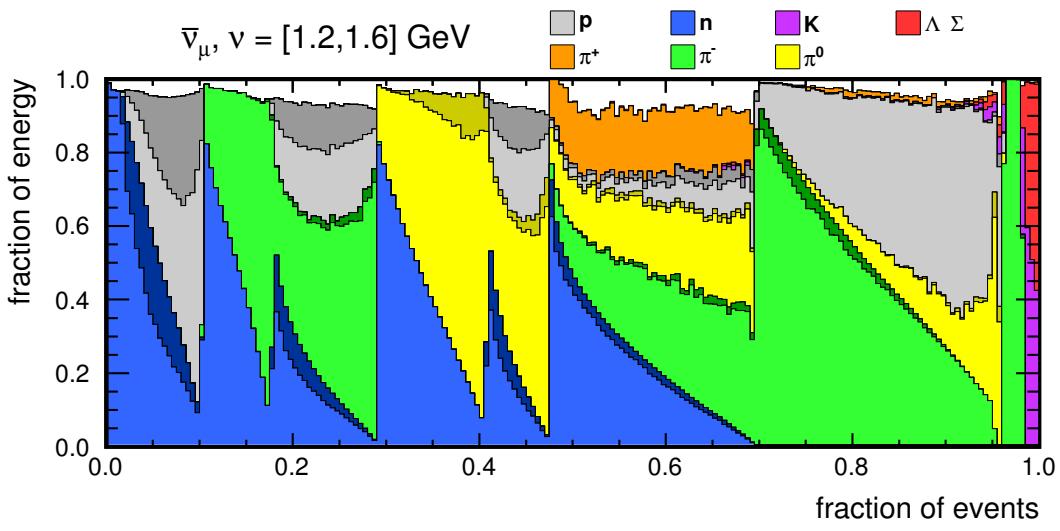

(a) $\nu_{true} = [1.2, 1.6]$ GeV

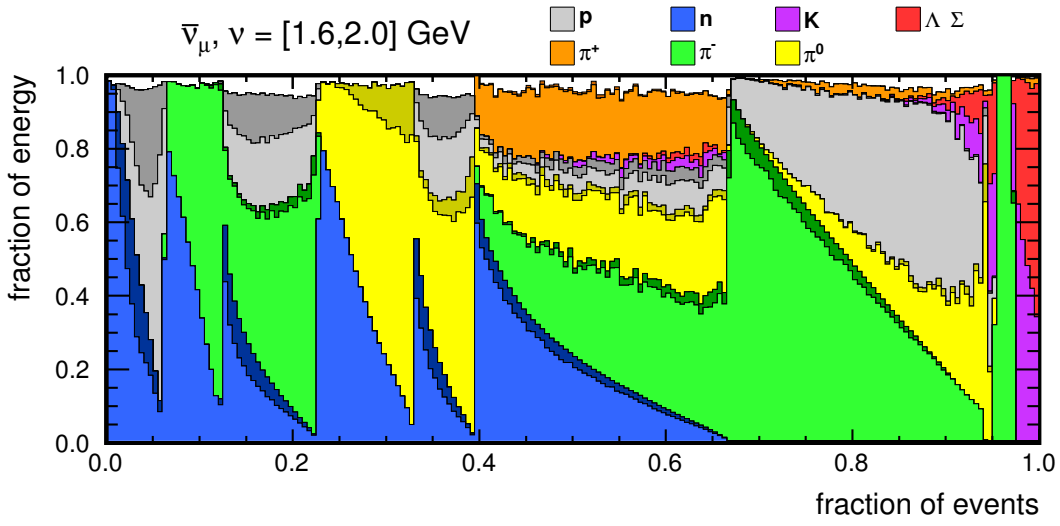

(b) $\nu_{true} = [1.6, 2.0]$ GeV

FIG. 5.20: Simulated recoil system composition for charged-current antineutrino interactions; $\nu_{true} = [1.2, 2.0]$ GeV. The plot is constructed as follows: for each simulated event, the fraction of energy carried by each species of recoil particle is computed. This fraction of energy is the kinetic energy (rest mass subtracted) of protons and neutrons or the total energy of pions and kaons, divided by ν_{true}. For strange baryons (Λ, Σ), the rest mass of a proton is subtracted from the total energy. The fractions of energy will not sum to 1.0 because of final state interactions and binding energy. The events are arranged along the X–axis by class (all neutron, neutron + proton, neutron + π^-, etc.) and sorted within this class by energy. Each bin on the plot represents the average of several similar events. The X–axis is arbitrarily ranged from 0.0 to 1.0, but can be interpreted as 0 to n_{events}. Within a given species of particle, the two color shades show the lead (most energetic) particle in lighter shade and the sum of all other particles in darker shade.

5.7 Vertex correction

For events in which only a single track (the muon) is reconstructed, the interaction vertex is determined as the most upstream node on the track. If multiple tracks are reconstructed, a more complex scheme is utilized which finds the point of closest approach of tracks that appear to originate from a common vertex. This algorithm works well for quasi-elastic and other low multiplicity interactions. However, in the event that the muon track is obscured near the vertex by a large recoil shower, the muon will not be tracked into the shower and the vertex will be assigned far downstream of its true location.

In order to correct for this, the low-ν analysis includes an additional correction which searches for visible activity in a cone upstream of the muon track and continues to move the vertex location upstream along the muon trajectory as long as energy is detected. This propagates the muon track into the shower. The cone is one scintillator strip wide at the module immediately upstream of the nominal reconstructed vertex and expands by one strip for every additional upstream module. Any clusters above a 1.5 MeV threshold cause the algorithm to shift the vertex, and gaps of one module are permitted. The approximate energy deposition of a muon traversing a plane (3.0 MeV times the calorimetric constants) is removed from the recoil system for every plane the vertex is shifted.

FIG. 5.21 shows the default and corrected vertex Z residual for low and high energy recoil systems for neutrinos. FIG. 5.22 shows the equivalent for antineutrinos. Though the correction is not perfect, the RMS of the distributions is improved. The bias is shifted to tending to reconstruct the vertex upstream of true rather than downstream. This is preferable, as the issue was initially encountered by observing interactions in the upstream nuclear targets reconstructed into the fiducial volume. The downstream extent of the fiducial volume is chose to be sufficiently upstream of the ECAL such that interactions in the lead are not included in the sample.

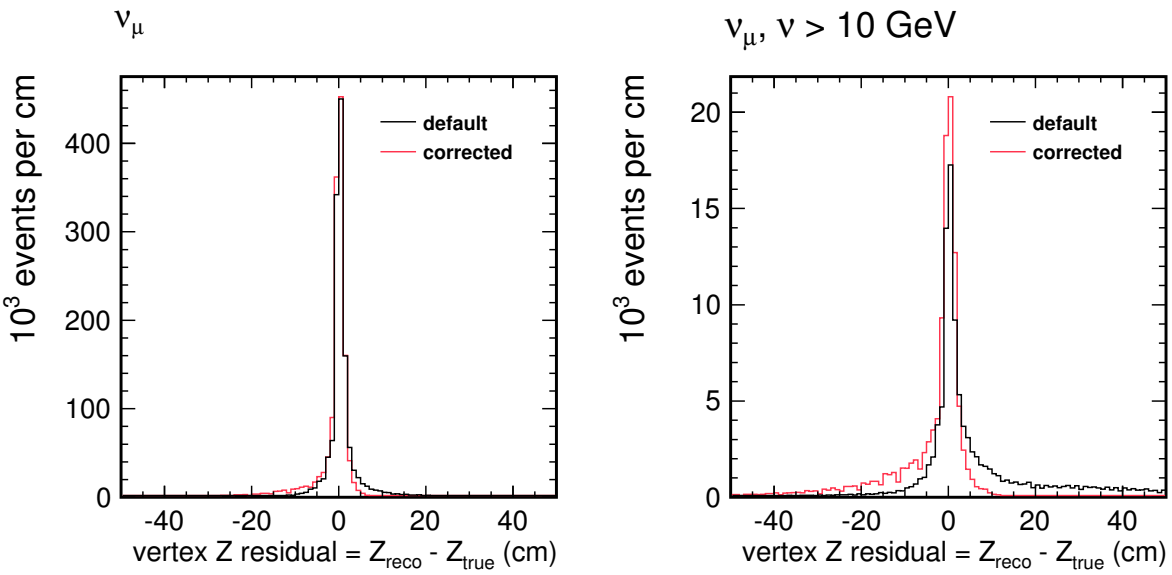

FIG. 5.21: Vertex Z residual $= Z_{reco} - Z_{true}$ for ν_μ interactions, for all ν (left) and $\nu > 10\,\text{GeV}$ (right). RMS is 8.8 cm corrected (10.3 cm default) for all ν; 15.2 cm corrected (22.7 cm default) for $\nu > 10\,\text{GeV}$.

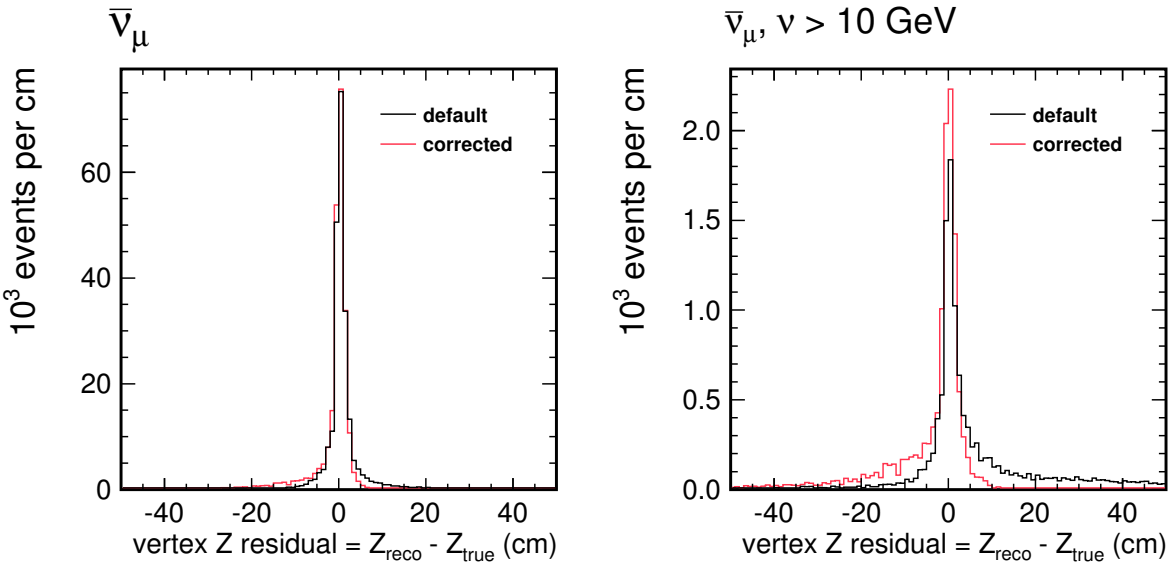

FIG. 5.22: Vertex Z residual $= Z_{reco} - Z_{true}$ for $\bar{\nu}_\mu$ interactions, for all ν (left) and $\nu > 10\,\text{GeV}$ (right). RMS is 8.8 cm corrected (9.5 cm default) for all ν; 15.1 cm corrected (22.1 cm default) for $\nu > 10\,\text{GeV}$.

CHAPTER 6

Low-ν Analysis

6.1 Overview

For a charged-current neutrino interaction, the quantity ν is the energy transfer to the recoil system (synonymous with "recoil energy"), defined as the difference between incoming neutrino energy, E, and outgoing lepton (typically muon) energy, E_μ:

$$\nu \equiv E - E_\mu. \tag{6.1}$$

The low-ν method, proposed by Mishra[21], pioneered by the CCFR[22] and NuTeV[23] collaborations, and utilized by the NOMAD[24] and MINOS[25] collaborations, relies on the principle that in the limit of ν being small, the charged-current cross section for neutrinos and antineutrinos is approximately constant as a function of neutrino energy. Thus, a measurement of the low-ν interaction rate as a function of neutrino energy is equivalent to a measurement of the shape of the neutrino flux (scaled by the value of the low-ν cross section). It is not necessary to know the value of the low-ν cross section *a priori*; it is constrained by the analysis. An inclusive cross section calculated with this flux is, likewise,

a shape measurement (scaled by an arbitrary value which is later constrained).

At high neutrino energy, the charged-current inclusive cross section for both neutrinos and antineutrinos divided by neutrino energy, $\sigma(E)/E$, approaches a constant. Exploiting this fact, the absolute normalization of the extracted cross section and flux is determined by scaling the extracted flux such that the extracted cross section matches a target value at high neutrino energy.

For this analysis, the primary results are normalized to the charged-current inclusive cross section implemented in the event generator GENIE (Chapter 8). As an alternative result, the neutrino cross section is normalized to the results of the NOMAD experiment (Chapter 9).

For this experiment, ν is reconstructed calorimetrically from visible energy depositions in the detector (Section 5.6). Low-ν events are selected by requiring this calorimetric recoil energy to be less than a cut value.

6.2 Low-ν method

In the limit of the momentum transfer to the nucleon, Q^2, being much less than the mass of the W boson ($Q^2 \ll M_{\mathrm{W}}$), the cross section for charged-current inclusive scattering of a neutrino on a nucleon is given by

$$\frac{\mathrm{d}^2\sigma}{\mathrm{d}x\mathrm{d}y} = \frac{G_F^2 ME}{\pi}\left(\left[1 - y\left(1 + \frac{Mx}{2E}\right) + \frac{y^2}{2}\left(\frac{1 + (2Mx/Q)^2}{1 + R_L}\right)\right]F_2 \pm \left[y - \frac{y^2}{2}\right]xF_3\right), \tag{6.2}$$

where $x = \frac{Q^2}{2M\nu}$ is the Bjorken scaling variable, $y = \nu/E$ is inelasticity, G_F is the Fermi weak coupling constant, M is the mass of the struck nucleon, and E is the incident neutrino energy. The "$\pm$" before the xF_3 term is positive for neutrinos and negative for antineutrinos. The internal structure of the nucleon is contained in the structure func-

tions, $F_2(x,Q^2)$, $xF_3(x,Q^2)$ and $R_L(x,Q^2)$, where R_L is the ratio of the cross section for scattering from longitudinally polarized W bosons to transversely polarized. R_L is defined from F_1 and F_2 via

$$R_L(x,Q^2) = \frac{F_2(x,Q^2)(1+4M^2x^2/Q^2) - 2xF_1(x,Q^2)}{2xF_1(x,Q^2)}. \tag{6.3}$$

Substituting $y = \nu/E$ and $Q^2 = 2M\nu x$ into Eq. 6.2, grouping by ν/E terms and integrating over x yields

$$\begin{aligned}\frac{\mathrm{d}\sigma}{\mathrm{d}\nu} = \frac{G_F^2 M}{\pi}\Bigg(&\int_0^1 F_2\,\mathrm{d}x - \frac{\nu}{E}\int_0^1 \left[F_2 \mp xF_3\right]\,\mathrm{d}x \\ &+ \frac{\nu}{2E^2}\int_0^1 \left[\frac{Mx(1-R_L)}{1+R_L}F_2\right]\,\mathrm{d}x + \frac{\nu^2}{2E^2}\int_0^1 \left[\frac{F_2}{1+R_L} \mp xF_3\right]\,\mathrm{d}x\Bigg).\end{aligned} \tag{6.4}$$

Integrating Eq. 6.4 to a small value of ν ($\nu_0 \ll E$) causes the terms proportional to ν/E, ν/E^2 and ν^2/E^2 to vanish, yielding a cross section, $\sigma(\nu < \nu_0, E)$, approximately constant in neutrino energy. The cross section deviates from exactly constant because of both the non-zero value of ν and the small Q^2 dependence (Bjorken scaling violation) of the structure functions, $F_2(x,Q^2)$, $xF_3(x,Q^2)$ and $R_L(x,Q^2)$.

The low-ν interaction rate, $N(\nu < \nu_0, E)$, is given by the flux, $\Phi(E)$, times the cross section, $\sigma(\nu < \nu_0, E)$. Due to the independence of the low-ν cross section with respect to neutrino energy, the interaction rate is proportional to the flux:

$$N(\nu < \nu_0, E) = \Phi(E) \times \sigma(\nu < \nu_0, E) \propto \Phi(E). \tag{6.5}$$

The ν/E dependence of the cross section can be corrected with a low-ν correction,

$$S(\nu_0, E) = \frac{\sigma(\nu < \nu_0, E)}{\sigma(\nu < \nu_0, E \to \infty)}. \tag{6.6}$$

For this analysis, the correction is computed by dividing the interaction rate by the low-ν cross section derived from the event generator GENIE, ignoring the (constant) denominator of Eq. 6.6 (Section 6.4.4). The extracted flux is then normalized such that the extracted cross section matches a target value at high neutrino energy (Section 6.4.5). The normalization of the flux is thus approximately one and indicates the deviation of the low-ν cross section model in GENIE relative to the measured.

In the literature, [22][23][25][26], Eq. 6.4 is presented as a polynomial in ν/E, with three coefficients, A, B and C and an additional term, $\tilde{R}$:

$$\frac{\mathrm{d}\sigma}{\mathrm{d}\nu} = A + B\frac{\nu}{E} - C\frac{\nu^2}{2E^2} \tag{6.7}$$

$$A = \frac{G_F^2 M}{\pi}\int_0^1 F_2(x,Q^2)\,\mathrm{d}x \tag{6.8}$$

$$B = -\frac{G_F^2 M}{\pi}\int_0^1 \left(F_2(x,Q^2) \mp xF_3(x,Q^2)\right)\,\mathrm{d}x \tag{6.9}$$

$$C = B - \frac{G_F^2 M}{\pi}\int_0^1 F_2(x,Q^2)\tilde{R}\,\mathrm{d}x \tag{6.10}$$

$$\tilde{R} = \frac{1+2Mx/\nu}{1+R_L} - \frac{Mx}{\nu} - 1. \tag{6.11}$$

This formulation hides a ν dependence into $\tilde{R}$, which blows up as $\nu \to 0$.

6.3 Event selection

Following the event reconstruction described in Chapter 5, charged-current interactions are selected with the following set of cuts:

1. **Fiducial volume** – Events are required to have a reconstructed vertex z (along the beam axis) within $6.02\,\mathrm{m} < z < 8.15\,\mathrm{m}$ and a reconstructed apothem $< 0.75\,\mathrm{m}$. This corresponds to 47 modules (94 planes) in the fully-active tracking region of the detector and a total of 2.232×10^{30} nucleons.

2. **MINOS match** – Events are required to have a reconstructed track in MINERνA that matches to a reconstructed track in MINOS, with MINOS returning a momentum measurement by either range or curvature. Due to the number of interaction lengths of material traversed, this long track is presumed to be a muon, indicating a ν_μ or $\bar{\nu}_\mu$ interaction in MINERνA.

3. **MINOS** q/p – MINOS returns a charge significance, q/p, the ratio of the muon charge, q, to momentum, p. Muons (μ^-) are selected by $q/p < 0$; antimuons (μ^+) are selected by $q/p > 0$. MINOS additionally returns an uncertainty on the significance of the charge-sign determination. A cut enforces $|\sigma^{q/p}| < 0.3$.

4. **Dead electronics** – The readout electronics have a 200 ns dead time after recording visible activity. This can cause reconstruction failures for events later in time, particularly in vertex identification. A cut is enforced that no more than one dead discriminator can exist along the projection of the muon track in the two modules upstream of the reconstructed vertex.

5. **Low-ν** – For the low-ν samples utilized in flux extraction, a cut is placed on the calorimetrically reconstructed recoil energy of $\nu < \nu_0$.

6.4 Cross section and flux extraction

The charged-current inclusive cross section is computed as

$$\sigma(E) = \frac{U(D-B)}{\epsilon \Phi T \times \Delta E}, \tag{6.12}$$

where $D(E)$ is the reconstructed inclusive interaction rate in data binned as a function of neutrino energy, $B(E)$ is the background interaction rate (neutral-current, wrong-sign

ν_μ and ν_e contamination) predicted by the simulation (Section 6.4.1), U is the unfolding procedure (Section 6.4.2), $\epsilon(E)$ is the acceptance correction (Section 6.4.3), $\Phi(E)$ is the neutrino flux determined by the low-ν method, T is the number of target nucleons in the fiducial volume and ΔE is the width of the neutrino energy bin.

The flux, $\Phi(E)$, is determined by the low-ν method:

$$\Phi(E) = \eta \frac{U(D_\nu - B_\nu)}{\epsilon \sigma_\nu T \times \Delta E}, \tag{6.13}$$

where the subscript, ν, indicates that the data, D_ν, and background, B_ν, have been selected with a cut on reconstructed ν. The ν/E dependence of the low-ν cross section is corrected by dividing by the low-ν cross section, $\sigma_\nu \equiv \sigma(\nu < \nu_0, E)$, derived from the event generator GENIE (Section 6.4.4). The normalization factor, η, is set such that the extracted cross section over neutrino energy, $\sigma(E)/E$, matches a target value at high neutrino energy (Section 6.4.5).

The cross section and flux extraction procedure is repeated in parallel for three ν cuts, 300 MeV, 800 MeV and 2 GeV, with the resulting cross sections cross-normalized by independently varying the normalization factors, η, for each extracted flux (Section 6.4.5).

For neutrinos, the distribution of $y = \nu/E$, is approximately flat; any value of ν between zero and the neutrino energy, E, is equally probable. For antineutrinos, the distribution is falling with increasing y. For both neutrinos and antineutrinos, the reconstructed y distribution is sculpted into a falling distribution by the acceptance of muons into MINOS (see plots in Section 7.3.1). This results from both angular acceptance and the approximately 2 GeV muon energy threshold required to punch through the calorimeters of MINERνA and penetrate deeply enough to produce a track in MINOS.

At large neutrino energy, beyond the peak of the NuMI flux, it is desirable to increase the ν cut to accept a larger fraction of the events and reduce the statistical uncertainty on

the extracted flux. However, as the cut is applied to lower neutrino energy, the fraction passing the ν cut increases, eventually becoming the majority of the events. In the limit, $E < \nu_0$, all events pass the ν cut, the events used to determine the flux and cross section are identical and the extracted cross section is the low-ν cross section, σ_ν. By lowering the ν cut, the method can proceed to lower neutrino energy, ultimately limited by the large systematic uncertainties on low energy neutrino interactions.

FIG. 6.1 – 6.2 show the fraction of the inclusive data sample with reconstructed ν less than the given ν cut. For each cut, the fraction passing the cut rises with decreasing neutrino energy. The minimum neutrino energy for each ν cut is set to keep the overlap less than 50%: $E > 2\,\text{GeV}$ for $\nu < 300\,\text{MeV}$, $E > 5\,\text{GeV}$ for $\nu < 800\,\text{MeV}$ and $E > 9\,\text{GeV}$ for $\nu < 2\,\text{GeV}$. In the lowest bin of the $\bar{\nu}_\mu$ in RHC sample, 2–3 GeV, this condition is not met, with the overlap of the 300 MeV cut rising to 67% as a result of the falling y distribution for antineutrinos.

FIG. 6.3 – 6.6 show the reconstructed inclusive and low-ν interaction rates of neutrinos in the forward horn current (FHC), neutrino-focusing beam for data and simulation. A ratio of data to simulation is also provided. FIG. 6.7 – 6.10 show the reconstructed inclusive and low-ν interaction rates of antineutrinos in the reverse horn current (RHC), antineutrino-focusing beam. The equivalent plots for the defocused samples (RHC neutrinos and FHC antineutrinos) are provided in Appendices C and D. Chapter 7 discusses the systematic uncertainty band on the plots.

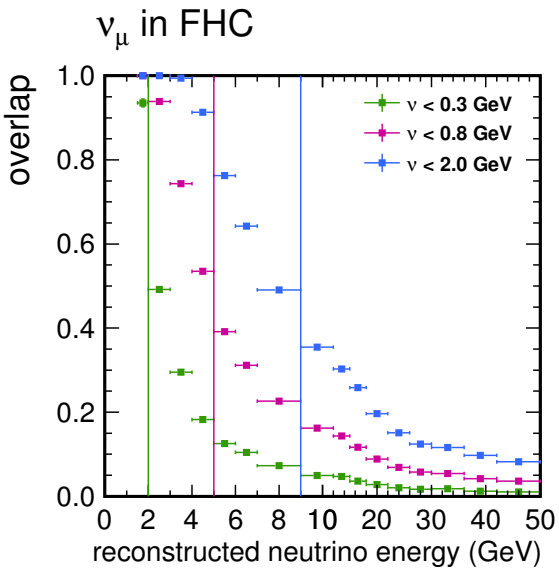

FIG. 6.1: The fraction of the inclusive data sample with reconstructed ν less than the given ν cut for neutrinos in the forward horn current (FHC), neutrino-focusing beam; equivalent to the ratio of the low-ν interaction rates (FIG. 6.4 – 6.6) to the inclusive interaction rate (FIG. 6.3). Error bars show statistical uncertainties only. Vertical lines mark the minimum neutrino energy for each ν cut.

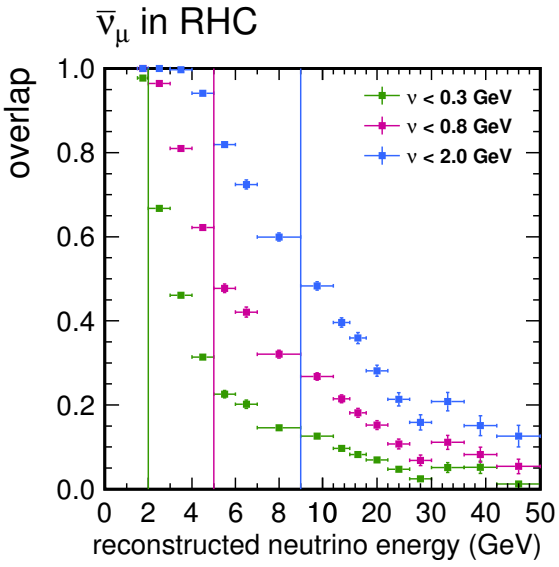

FIG. 6.2: The fraction of the inclusive data sample with reconstructed ν less than the given ν cut for antineutrinos in the reverse horn current (RHC), antineutrino-focusing beam; equivalent to the ratio of the low-ν interaction rates (FIG. 6.8 – 6.10) to the inclusive interaction rate (FIG. 6.7). Error bars show statistical uncertainties only. Vertical lines mark the minimum neutrino energy for each ν cut.

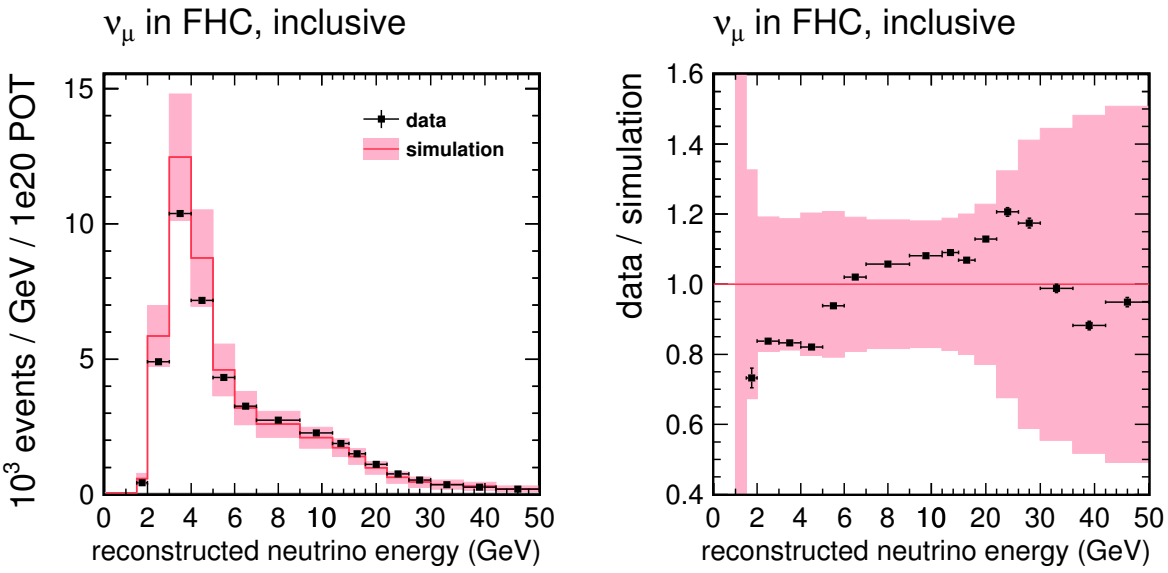

FIG. 6.3: Reconstructed inclusive neutrino interaction rate (left) and ratio of data to simulation (right) in the forward horn current (FHC), neutrino-focusing beam. Data are plotted with statistical uncertainties; simulated data are plotted with statistical and systematic uncertainties.

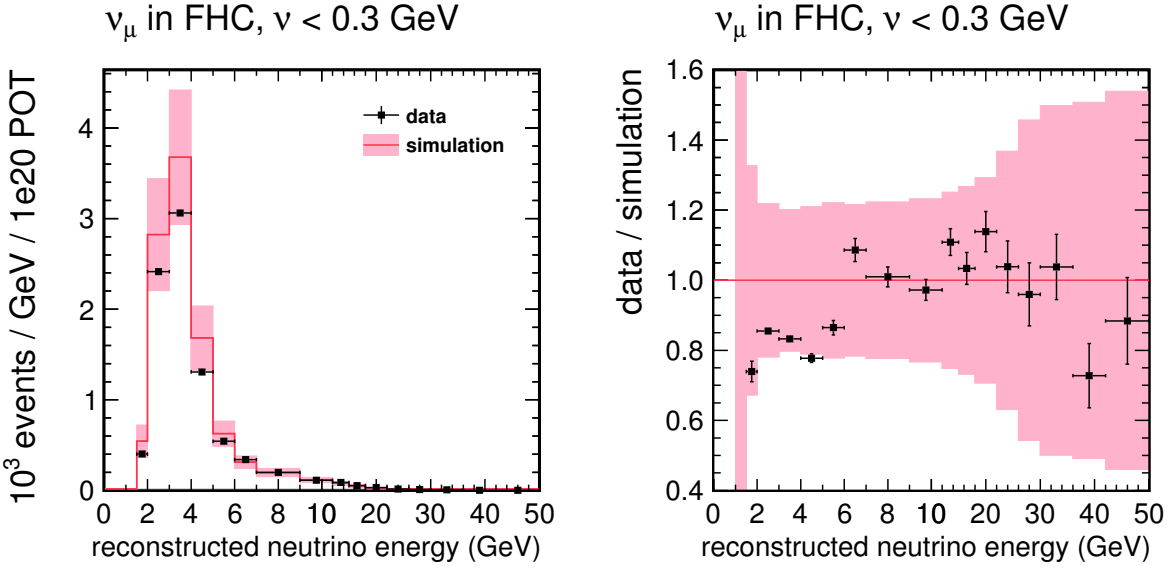

FIG. 6.4: Reconstructed $\nu < 300\,\text{MeV}$ neutrino interaction rate (left) and ratio of data to simulation (right) in the forward horn current (FHC), neutrino-focusing beam. Data are plotted with statistical uncertainties; simulated data are plotted with statistical and systematic uncertainties.

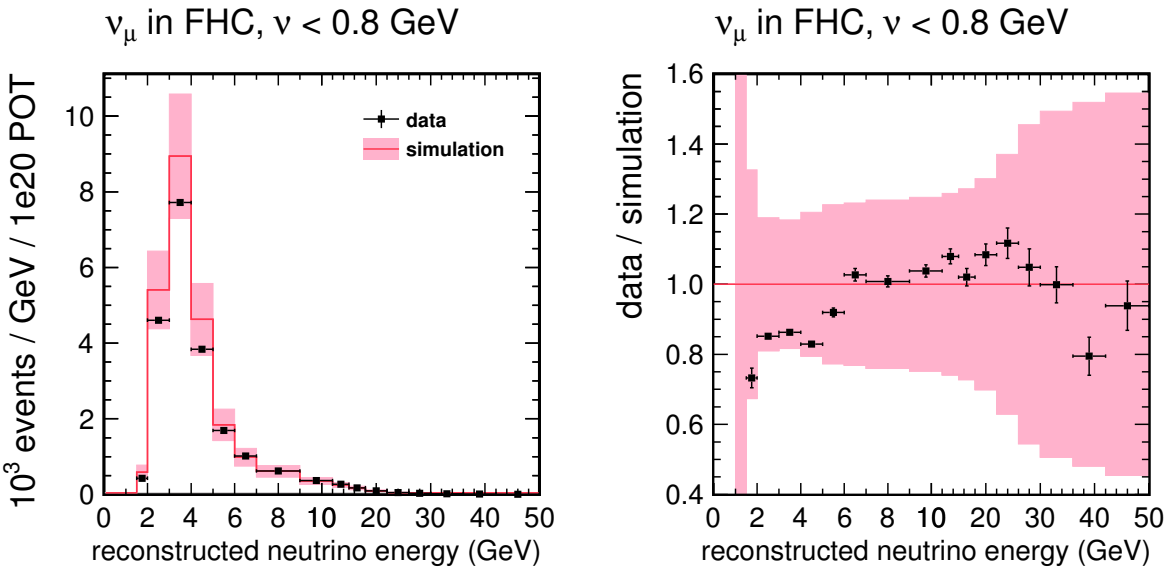

FIG. 6.5: Reconstructed $\nu < 800\,\text{MeV}$ neutrino interaction rate (left) and ratio of data to simulation (right) in the forward horn current (FHC), neutrino-focusing beam. Data are plotted with statistical uncertainties; simulated data are plotted with statistical and systematic uncertainties.

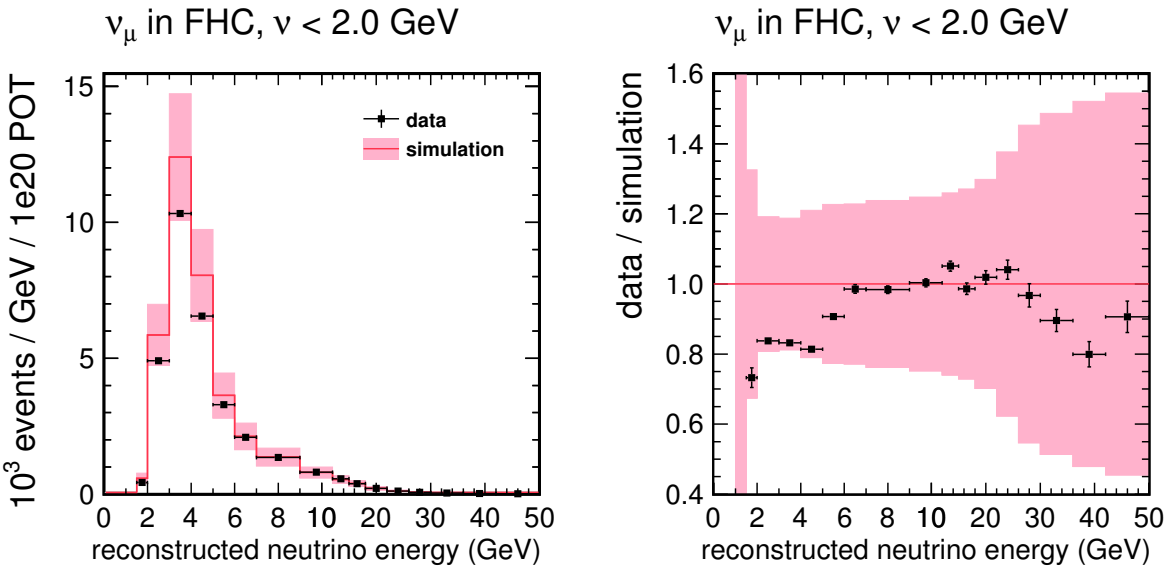

FIG. 6.6: Reconstructed $\nu < 2\,\text{GeV}$ neutrino interaction rate (left) and ratio of data to simulation (right) in the forward horn current (FHC), neutrino-focusing beam. Data are plotted with statistical uncertainties; simulated data are plotted with statistical and systematic uncertainties.

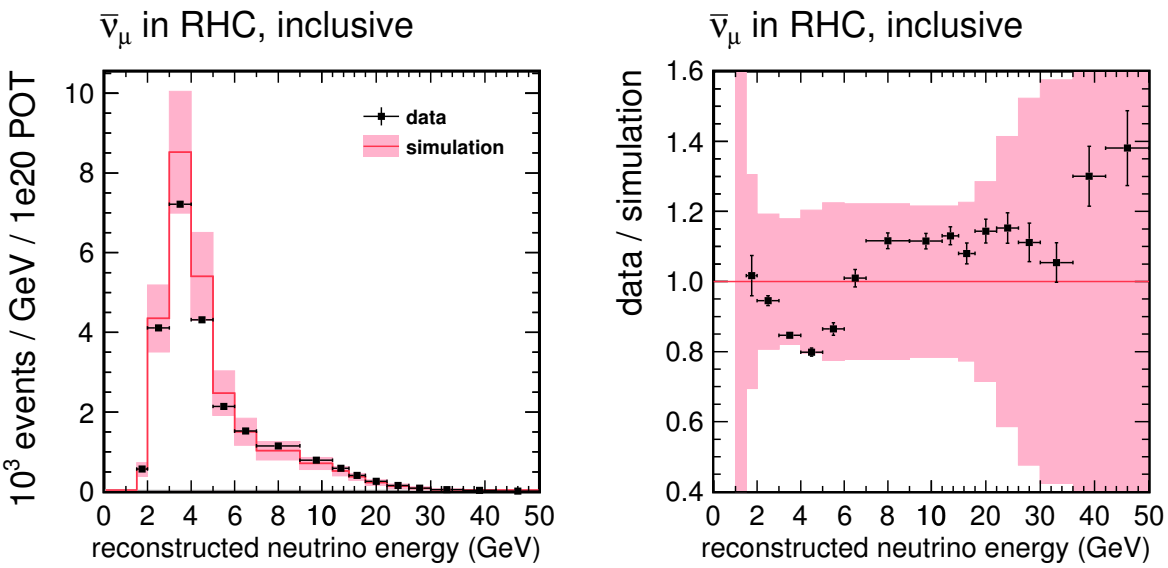

FIG. 6.7: Reconstructed inclusive antineutrino interaction rate (left) and ratio of data to simulation (right) in the reverse horn current (RHC), antineutrino-focusing beam. Data are plotted with statistical uncertainties; simulated data are plotted with statistical and systematic uncertainties.

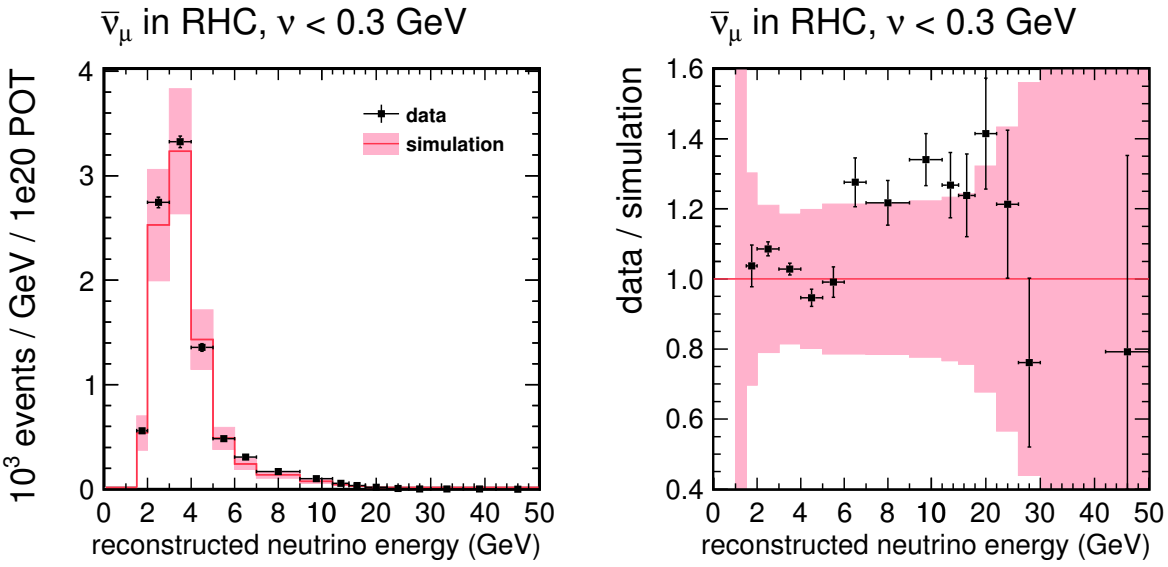

FIG. 6.8: Reconstructed $\nu < 300\,\mathrm{MeV}$ antineutrino interaction rate (left) and ratio of data to simulation (right) in the reverse horn current (RHC), antineutrino-focusing beam. Data are plotted with statistical uncertainties; simulated data are plotted with statistical and systematic uncertainties.

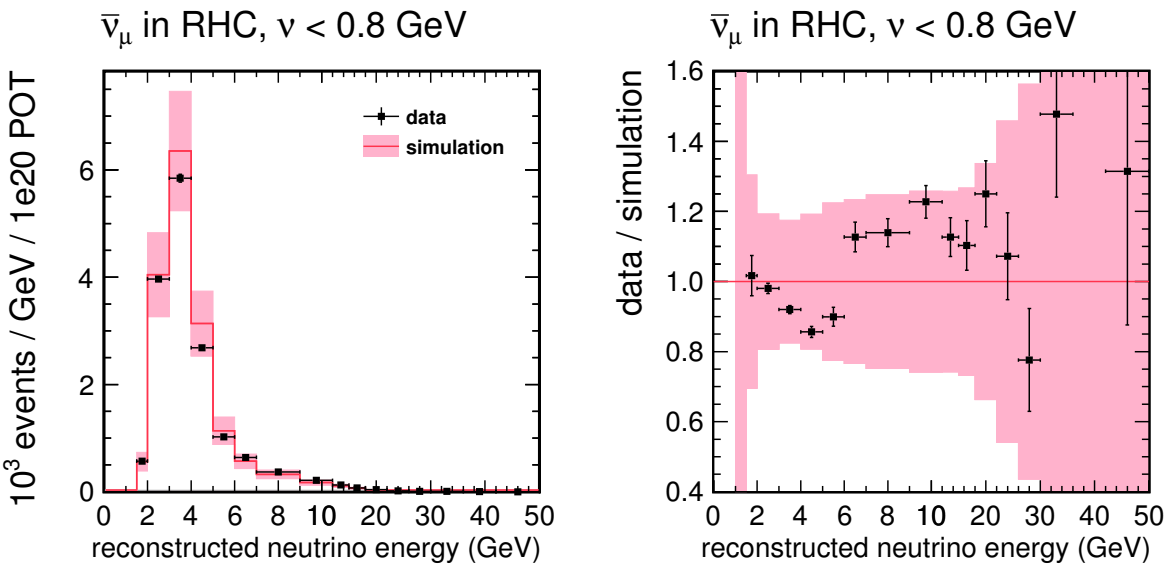

FIG. 6.9: Reconstructed $\nu < 800\,\text{MeV}$ antineutrino interaction rate (left) and ratio of data to simulation (right) in the reverse horn current (RHC), antineutrino-focusing beam. Data are plotted with statistical uncertainties; simulated data are plotted with statistical and systematic uncertainties.

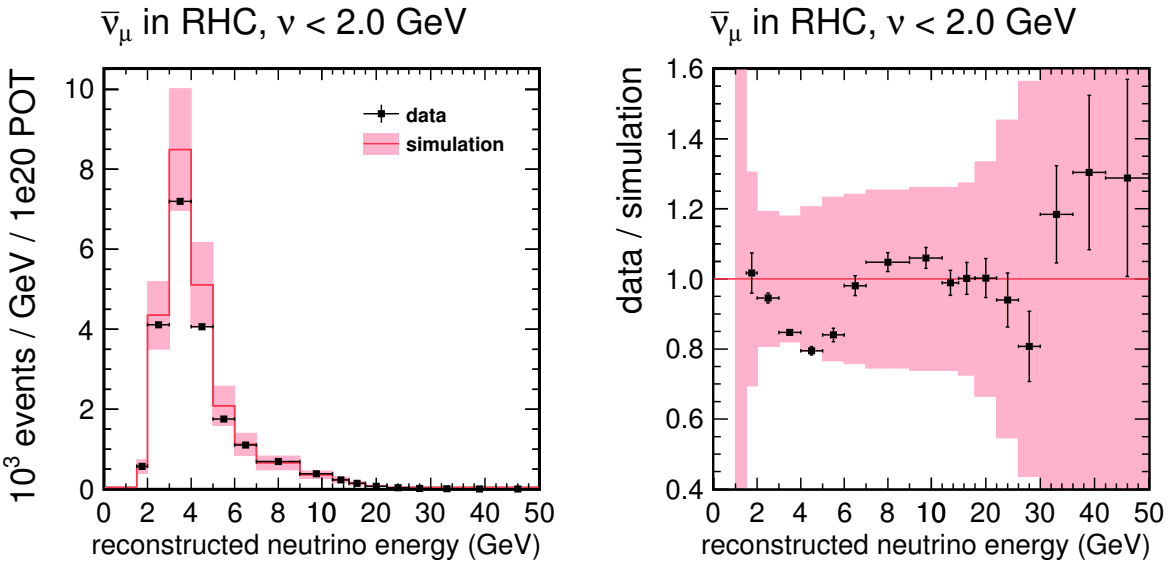

FIG. 6.10: Reconstructed $\nu < 2\,\text{GeV}$ antineutrino interaction rate (left) and ratio of data to simulation (right) in the reverse horn current (RHC), antineutrino-focusing beam. Data are plotted with statistical uncertainties; simulated data are plotted with statistical and systematic uncertainties.

6.4.1 Background subtraction

The simulation is utilized to predict background contamination in the selected set of events. Backgrounds include neutral-current, wrong-sign ν_μ and ν_e interactions. ν_τ interactions are not simulated, but are negligible. Neutral-current and ν_e interactions may reconstruct as charged-current ν_μ if a final state pion penetrates into the MINOS detector before interacting or decays in flight to a muon. Wrong-sign ν_μ contaminate the sample when multiple scattering in the MINOS detector causes the curvature of the track to be reconstructed opposite the muon charge. For the focused samples (FHC ν_μ and RHC $\bar{\nu}_\mu$), backgrounds are negligible. For the defocused samples (FHC $\bar{\nu}_\mu$ and RHC ν_μ), backgrounds are visible in the peak of the flux distribution (see the reconstructed interaction rate plots in Appendix D and Appendix C).

In Eq. 6.12 and Eq. 6.13, the reconstructed data interaction rates, $D(E)$ and $D_\nu(E)$, must pass the full set of reconstruction cuts, including a cut on reconstructed ν for $D_\nu(E)$. The reconstructed background interaction rates, $B(E)$ and $B_\nu(E)$, must also pass the reconstruction cuts, including a cut on reconstructed ν for $B_\nu(E)$, and not be true charged-current and true ν_μ (or $\bar{\nu}_\mu$ for antineutrinos). Defining the reconstructed signal interaction rates, $S(E)$ and $S_\nu(E)$, as events passing the reconstruction cuts, including a cut on reconstructed ν for $S_\nu(E)$, and true charged-current and true ν_μ (or $\bar{\nu}_\mu$), the total simulated reconstructed interaction rate, $S + B$, is scaled to the data so that the background subtraction, $D - B$, is actually performed as

$$D - B \rightarrow D \times \frac{S}{S+B}. \tag{6.14}$$

$D(E)$ and $B(E)$ are filled by reconstructed neutrino energy, E. The distributions are then unfolded (Section 6.4.2) to true neutrino energy using an unfolding matrix populated with the same events as $S(E)$.

6.4.2 Bayesian unfolding

Unfolding refers to a number of procedures to remove the effects of detector resolution and bias from a reconstructed distribution. Detector resolution and bias cause events to migrate between adjacent bins. Unfolding utilizes a simulated model of the detector to determine a best estimate of the true distribution underlying a reconstructed one. For this analysis, a Bayesian unfolding procedure[27] is utilized to unfold neutrino energy distributions to remove detector resolution and bias in muon and recoil energy reconstruction.

The estimated number of true interactions, t_i, in neutrino energy bin i is given by

$$t_i = \sum_{j=1}^{n} r_j P(T_i|R_j), \tag{6.15}$$

where n is the number of neutrino energy bins, r_j is the number of reconstructed events in bin j and $P(T_i|R_j)$ is the probability that a reconstructed event in bin j was caused by a true event in bin i.

The probabilities, $P(T_i|R_j)$, can be determined by Bayes' theorem:

$$P(T_i|R_j) = \frac{P(R_j|T_i)P(T_i)}{\sum_{i=1}^{n} P(R_j|T_i)P(T_i)}, \tag{6.16}$$

where $P(R_j|T_i)$ is the probability that a true event in bin i is reconstructed to bin j, $P(T_i)$ is an *a priori* estimate of the true underlying distribution and the denominator is equivalent to $P(R_j)$, an *a priori* estimate of the reconstructed distribution.

The probabilities $P(R_j|T_i)$ are estimated by a simulated model of detector resolution, expressed as a migration matrix of true versus reconstructed neutrino energy. FIG. 6.11 – 6.12 show the migration matrices for neutrinos in the FHC beam and antineutrinos in the RHC beam for the inclusive and low-ν samples. Note that unfolding is performed independently in each of the inclusive and low-ν samples using a migration matrix derived

from that sample. The equivalent plots for the defocused samples (RHC neutrinos and FHC antineutrinos) are provided in Appendices C and D.

FIG. 6.13 – 6.14 show the energy purity, the diagonal elements of the migration matrices, equivalent to the fraction of events reconstructed to a given neutrino energy bin with true energy also within the bin. The neutrino energy bin widths are chosen to keep the energy purity sufficiently high.

The power of the Bayesian unfolding method lies in performing the procedure iteratively, updating the estimated true distribution with each pass. Starting with an initial true distribution, $P_0(T_i)$, the information from the reconstructed distribution is incorporated to produce an updated true distribution, $P_1(T_i) = t_i / \sum_{i=1}^{n} t_i$. D'Agostini[27] recommends iterating until the updated distributions are within errors of the prior. In practice, this was found to occur at two iterations and the procedure is terminated at that number.

6.4.3 Acceptance correction

The acceptance correction, $\epsilon(E)$, primarily accounts for the loss of reconstruction efficiency resulting from the requirement that a muon track is observed by MINOS. In order to be accepted by MINOS, the muon momentum must be sufficiently forward directed with a magnitude greater than approximately 2 GeV. The acceptance additionally corrects for any net migration in to or out of the fiducial volume, and in the case of the low-ν samples, any net migration across the cut on reconstructed ν.

The acceptance correction, $\epsilon(E)$, is derived from the simulation via

$$\epsilon(E) = \frac{S(E)}{N(E)}, \tag{6.17}$$

where $S(E)$ is the reconstructed signal interaction rate and $N(E)$ is the true signal interaction rate. As the acceptance correction is performed after unfolding, the histograms are

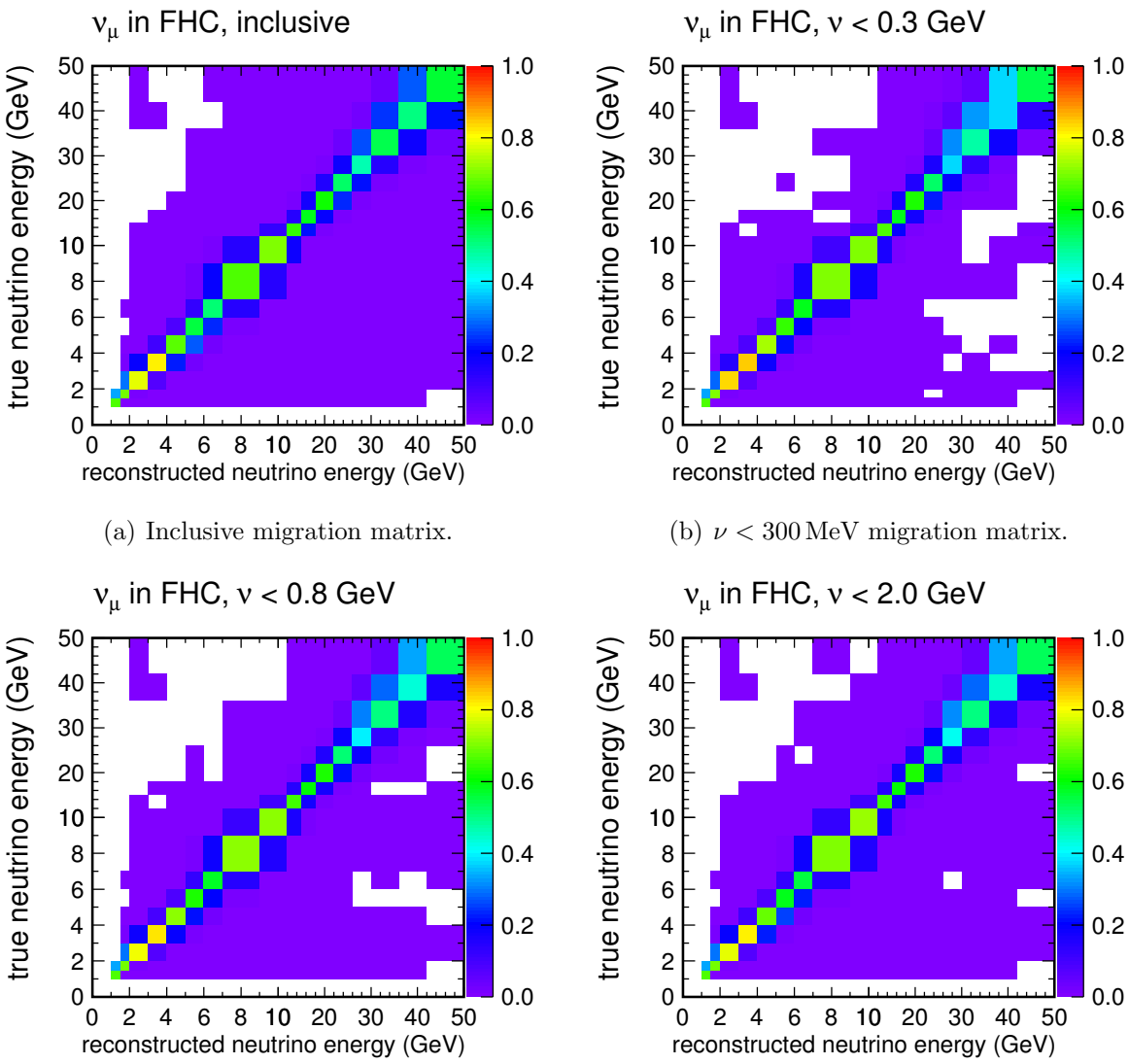

(a) Inclusive migration matrix.

(b) $\nu < 300\,\text{MeV}$ migration matrix.

(c) $\nu < 800\,\text{MeV}$ migration matrix.

(d) $\nu < 2\,\text{GeV}$ migration matrix.

FIG. 6.11: Migration matrices for the inclusive and low-ν samples for neutrinos in the forward horn current (FHC) beam.

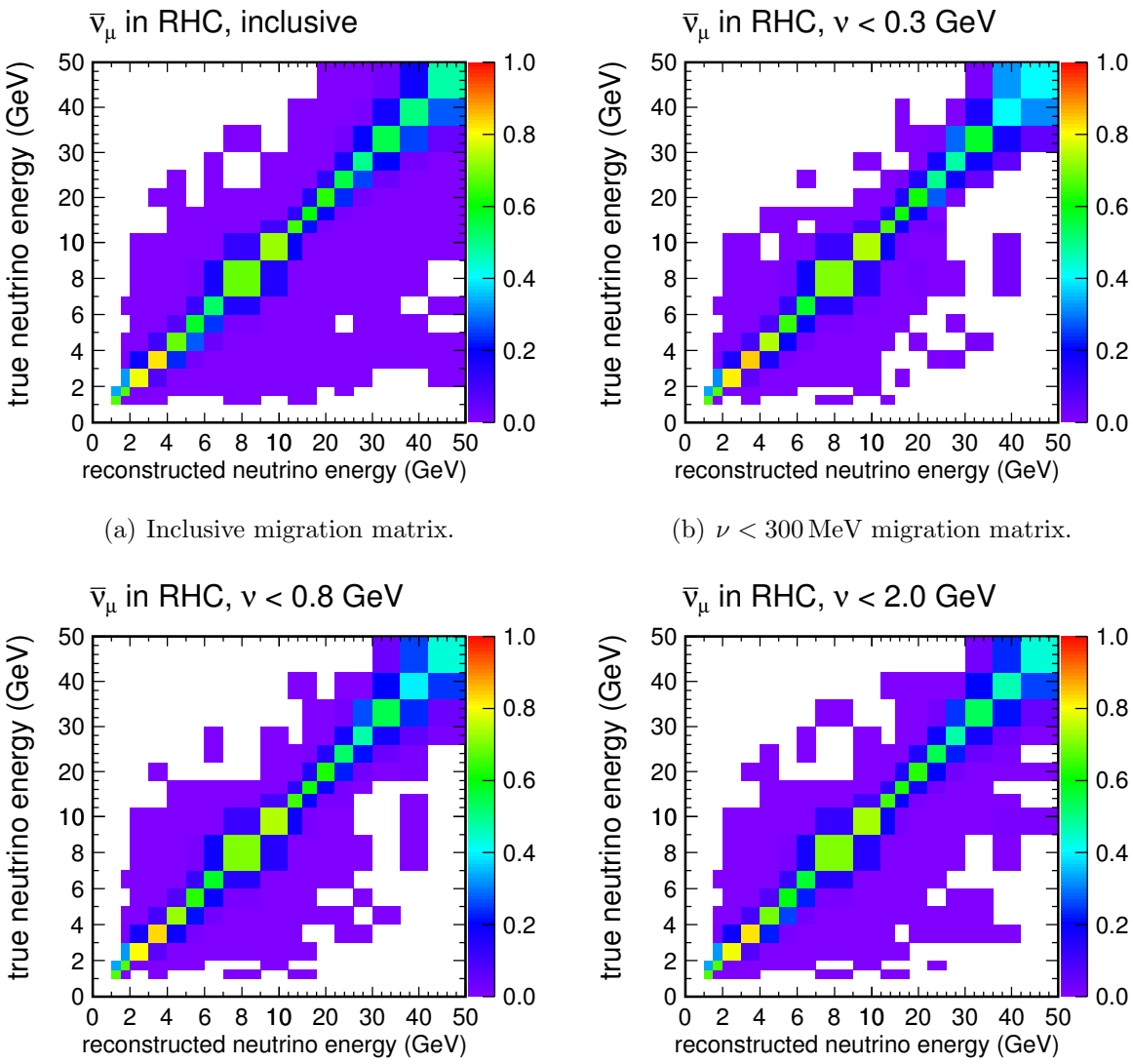

(a) Inclusive migration matrix.

(b) $\nu < 300\,\text{MeV}$ migration matrix.

(c) $\nu < 800\,\text{MeV}$ migration matrix.

(d) $\nu < 2\,\text{GeV}$ migration matrix.

FIG. 6.12: Migration matrices for the inclusive and low-ν samples for antineutrinos in the reverse horn current (RHC) beam.

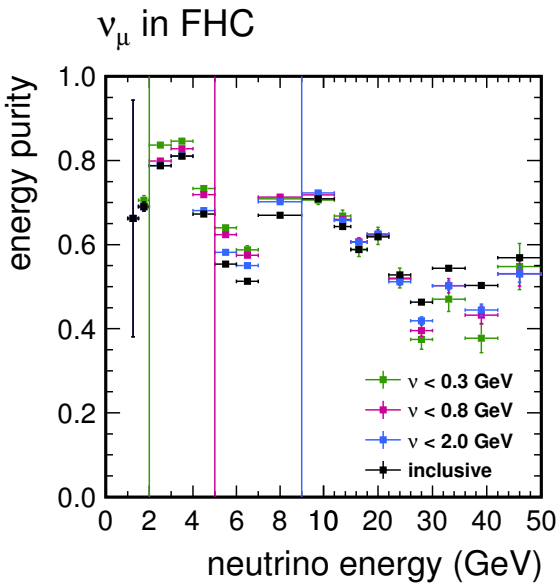

FIG. 6.13: The fraction of events reconstructed to a given neutrino energy bin with true energy also within the bin for neutrinos in the forward horn current (FHC) beam; equivalent to the diagonal elements of the migration matrices in FIG. 6.11. Error bars show statistical uncertainties only. Vertical lines mark the minimum neutrino energy for each ν cut.

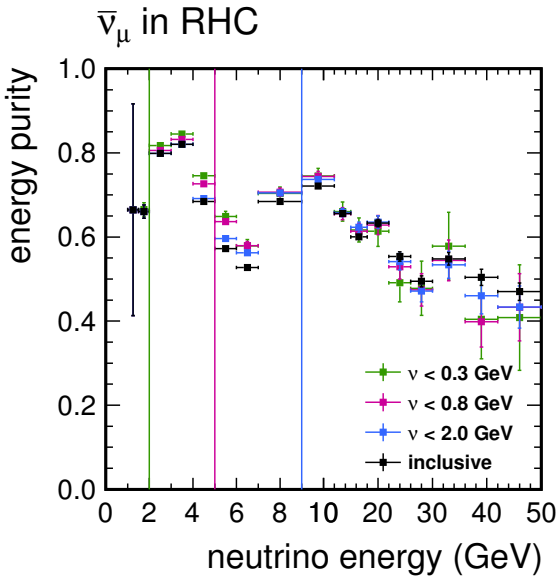

FIG. 6.14: The fraction of events reconstructed to a given neutrino energy bin with true energy also within the bin for antineutrinos in the reverse horn current (RHC) beam; equivalent to the diagonal elements of the migration matrices in FIG. 6.12. Error bars show statistical uncertainties only. Vertical lines mark the minimum neutrino energy for each ν cut.

filled by true neutrino energy, E. The events populating $N(E)$ are all true charged-current and true ν_μ (or $\bar{\nu}_\mu$), with a true vertex in the fiducial volume and for the low-ν samples, a cut on true ν. The events populating $S(E)$ must pass the full set of reconstruction cuts (Section 6.3), including a cut on reconstructed ν for the low-ν samples and be true charged-current and true ν_μ (or $\bar{\nu}_\mu$) (acceptance is corrected after background subtraction).

FIG. 6.15 – 6.16 show the acceptance correction, $\epsilon(E)$, for neutrinos in the FHC beam and antineutrinos in the RHC beam. The equivalent plots for the defocused samples (RHC neutrinos and FHC antineutrinos) are provided in Appendices C and D.

The acceptance increases with neutrino energy due to the increase in the average muon energy and the more forward direction of the muon. For the low-ν samples, the cut on ν enforces that most of the neutrino energy goes to the muon. Thus, the acceptance for the low-ν samples is greater than for the inclusive sample. Particularly for the $\nu < 300\,\text{MeV}$ sample, the muon energy is effectively equivalent the incoming neutrino energy. The dip at around 10 GeV for the low-ν samples results from muons penetrating out of the back of the MINOS detector and the momentum reconstruction transitioning from range-based to curvature-based.

6.4.4 Low-ν correction

The low-ν correction accounts for the ν/E dependence of the low-ν cross section, $\sigma_\nu \equiv \sigma(\nu < \nu_0, E)$, arising from both the non-zero value of ν and the small Q^2 dependence (Bjorken scaling violation) of the structure functions (Section 6.2). For this measurement, the correction is implemented by dividing the extracted flux by the low-ν cross section derived from the event generator GENIE (Eq. 6.13). The normalization factor, η, is thus approximately one and indicates the deviation of the measured low-ν cross section relative to the GENIE model.

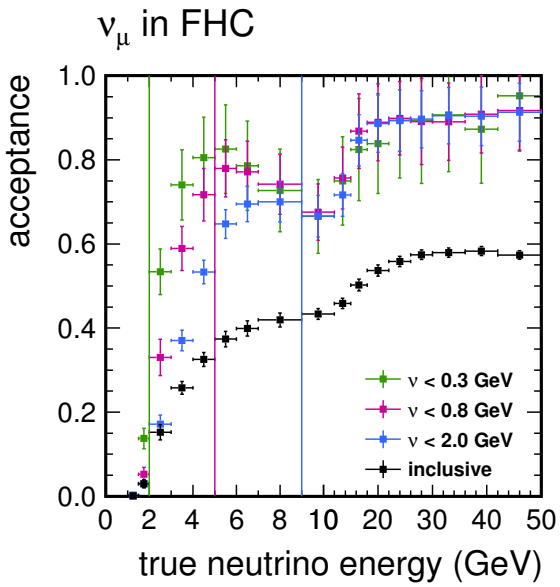

FIG. 6.15: The ratio of reconstructed signal events (reconstructed $\nu < \nu_i$ or inclusive, true CC ν_μ) to all simulated signal events (true $\nu < \nu_i$ or inclusive, true CC ν_μ) for neutrinos in the forward horn current (FHC) beam. See the text for a complete definition (Section 6.4.3). Error bars show statistical and systematic uncertainties (Chapter 7). Vertical lines mark the minimum neutrino energy for each ν cut.

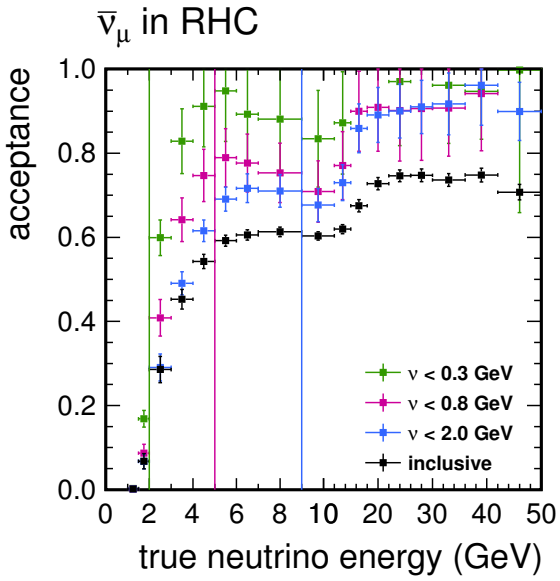

FIG. 6.16: The ratio of reconstructed signal events (reconstructed $\nu < \nu_i$ or inclusive, true CC $\bar{\nu}_\mu$) to all simulated signal events (true $\nu < \nu_i$ or inclusive, true CC $\bar{\nu}_\mu$) for antineutrinos in the reverse horn current (RHC) beam. See the text for a complete definition (Section 6.4.3). Error bars show statistical and systematic uncertainties (Chapter 7). Vertical lines mark the minimum neutrino energy for each ν cut.

FIG. 6.17 shows the low-ν cross sections for neutrinos for the three ν cuts (300 MeV, 800 MeV and 2 GeV) as modeled in GENIE. FIG. 6.18 shows the equivalent for antineutrinos. The cross sections are extracted from the simulation by dividing the true signal interaction rate (with a cut on true ν), $N(\nu < \nu_0, E)$, by the true flux, $\Phi(E)$.

6.4.5 Normalization

The absolute normalization of the extracted cross section divided by neutrino energy, $\sigma(E)/E$, and extracted flux, $\Phi(E)$, is set by the normalization factor, η (Eq. 6.13). This process is performed semi-independently for each ν cut, thus η is a set of three values.

Normalization begins with the highest ν cut, $\nu < 2$ GeV, with η calculated such that the cross section, $\sigma(E)/E$, extracted with the $\nu < 2$ GeV flux matches the charged-current inclusive cross section derived from GENIE in the lowest bin of the $\nu < 2$ GeV result, 9–12 GeV. The choice of target cross section is arbitrary; an alternative result, normalized to the results of the NOMAD experiment, is presented in Chapter 9. The normalization bin is selected to be high enough in neutrino energy such that $\sigma(E)/E$ is approximately constant, but not so far into the tail of the neutrino flux that statistical uncertainties degrade the measurement.

The charged-current inclusive cross section, $\sigma(E)/E$, is extracted from the simulation by dividing the true inclusive signal interaction rate, $N(E)$, by the true flux, $\Phi(E)$, and dividing by the energy at bin center of each neutrino energy bin. This inherently produces a cross section that is the flux weighted average of $\sigma(E)/E$ over the width of the bin. The cross section extracted from data is, likewise, a flux weighted average within each bin and the division $\sigma(E)/E$ is performed using the energy at bin center.

After normalizing the highest ν-cut result to an external constraint, the lower ν-cut results are cross-normalized to this in order of decreasing ν. This is performed by fitting

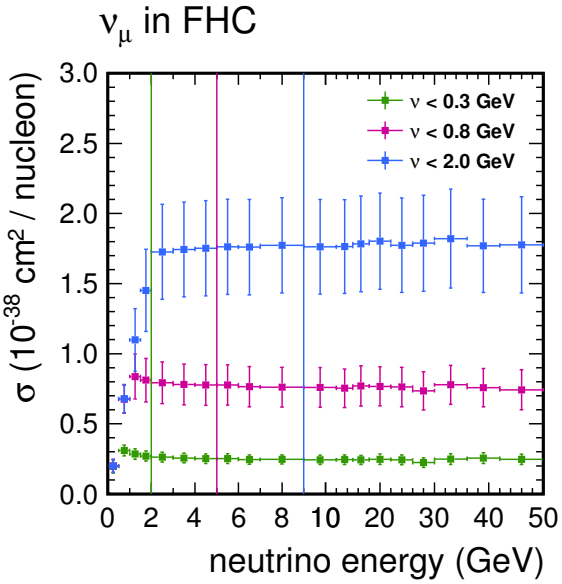

FIG. 6.17: Low-ν cross sections for neutrinos as derived from the GENIE event generator. Error bars show statistical and systematic uncertainties (Chapter 7). Vertical lines mark the minimum neutrino energy for each ν cut.

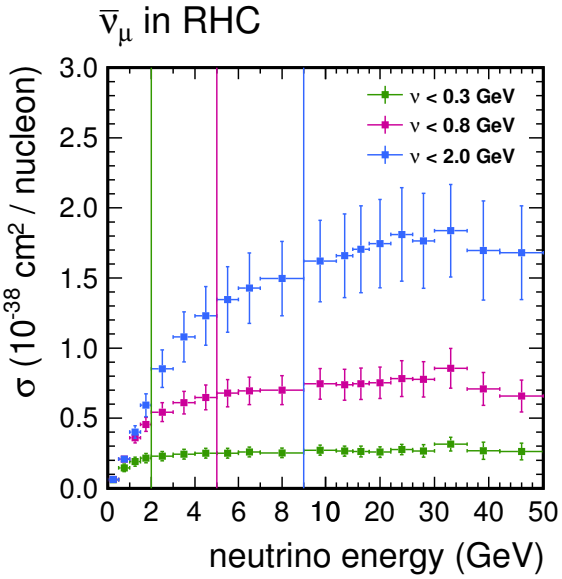

FIG. 6.18: Low-ν cross sections for antineutrinos as derived from the GENIE event generator. Error bars show statistical and systematic uncertainties (Chapter 7). Vertical lines mark the minimum neutrino energy for each ν cut.

the normalization factor of the lower ν cut to minimize a χ^2 comparison between the two extracted cross sections. The χ^2 comparison is performed in the region where the two results overlap (above the minimum neutrino energy of the higher ν cut, but below an imposed limit of 22 GeV, where systematic uncertainties become large [Chapter 7]). Thus, the $\nu < 800$ MeV result is cross-normalized to the $\nu < 2$ GeV result in the region $E = [9, 22]$ GeV and the $\nu < 300$ MeV result is cross-normalized to a combined result in the region $E = [5, 22]$ GeV.

Defining the inverse of the normalization factor, $\eta' \equiv 1/\eta$, the χ^2 comparison is computed as

$$\chi^2 = \sum_{i=1}^{n} \frac{(\eta' \sigma_i^0 - \sigma_i^1)^2}{\eta' e_i^0 e_i^1}, \tag{6.18}$$

where the summation is over n neutrino energy bins of overlap, σ_i^0 and e_i^0 are the unnormalized cross section and statistical uncertainty in bin i of the lower ν cut and σ_i^1 and e_i^1 are the normalized cross section and statistical uncertainty in bin i of the higher ν cut. The systematic uncertainty is handled by the many universes method (Section 7.2).

Cross-normalizing the $\nu < 800$ MeV result to the $\nu < 2$ GeV result, the normalization of the $\nu < 2$ GeV result is set by the external constraint and is applied to the cross section and uncertainty before utilizing Eq. 6.18. The normalization factor of the $\nu < 800$ MeV result, η', is fit by the MINUIT[28] algorithm to minimize the χ^2 comparison. In contrast to cross-normalizing in a single bin of overlap, this method utilizes all of the available information in a manner that respects the relative uncertainties of each bin.

After the normalized $\nu < 800$ MeV results in the 5–9 GeV bins are merged with the $\nu < 2$ GeV results, the process is repeated for the $\nu < 300$ MeV result by fitting the normalization to minimize the χ^2 comparison to the combined result from $\nu < 800$ MeV and $\nu < 2$ GeV. The normalized $\nu < 300$ MeV results are then merged in the 2–5 GeV bins.

The normalization of the cross section to an external constraint adds a systematic uncertainty arising from the uncertainty on the external constraint. This is added as a flat uncertainty to both the cross section and flux, which is the quadrature sum of the external uncertainty and the statistical uncertainty of the bin used for normalization (9–12 GeV). The cross-normalization, additionally, adds an uncertainty arising from the statistical uncertainty in fitting η' for the two lower ν cuts (Section 7.1). The systematic uncertainty is handled by the many universes method (Section 7.2).

The calculated normalization factors, $\eta' \equiv 1/eta$, are listed in Table 8.2 for neutrinos and Table 8.5 for antineutrinos. FIG. 6.19 – 6.20 show the normalized, extracted fluxes for the three ν cuts overlaid for FHC neutrinos and RHC antineutrinos. FIG. 6.21 – 6.22 show the normalized, extracted cross sections for the three ν cuts and two samples. The equivalent plots for the defocused samples (RHC neutrinos and FHC antineutrinos) are provided in Appendices C and D.

6.4.6 Isoscalar correction

An isoscalar target contains an equal number of protons and neutrons and, therefore, an equal number of u and d quarks. Real targets rarely meet this constraint. For the MINERνA detector, the material assessment estimates a 15% excess of protons over neutrons in the fiducial volume.

In order to compare to external measurements, which are typically corrected to an isoscalar target, the extracted cross section is multiplied by the ratio

$$\frac{\sigma_{\mathrm{C12}}(E)}{\sigma_{\mathrm{MINER}\nu\mathrm{A}}(E)}, \tag{6.19}$$

where $\sigma_{\mathrm{C12}}(E)$ is the cross section of C^{12} derived from GENIE and $\sigma_{\mathrm{MINER}\nu\mathrm{A}}(E)$ is the cross section of the mix of materials in the fiducial volume of MINERνA derived from

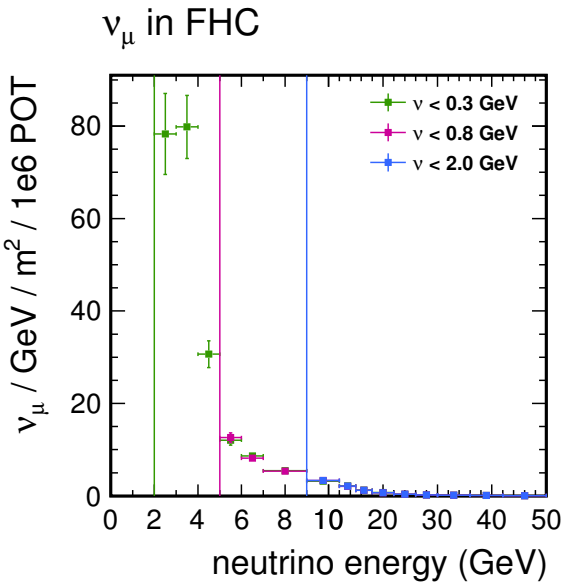

FIG. 6.19: Extracted neutrino flux from the three low-ν samples in the forward horn current (FHC) beam. Error bars show statistical and systematic uncertainties (Chapter 7). Vertical lines mark the minimum neutrino energy for each ν cut.

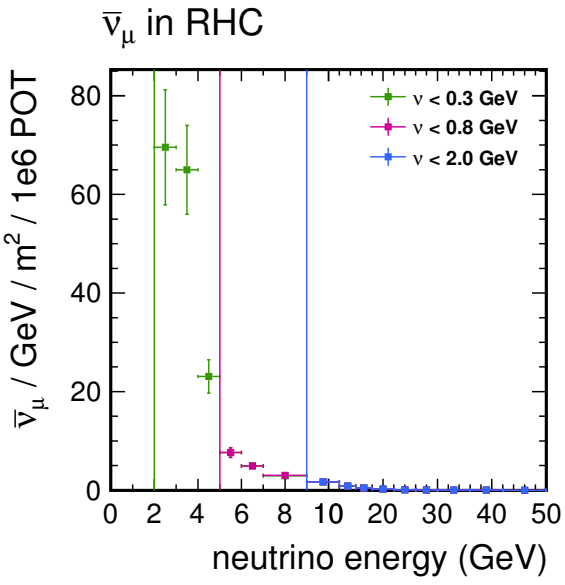

FIG. 6.20: Extracted antineutrino flux from the three low-ν samples in the reverse horn current (RHC) beam. Error bars show statistical and systematic uncertainties (Chapter 7). Vertical lines mark the minimum neutrino energy for each ν cut.

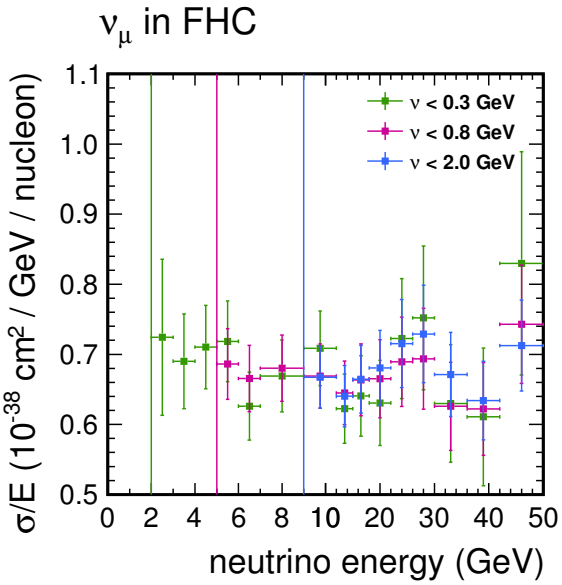

FIG. 6.21: Extracted cross section divided by energy for neutrinos as derived from the three low-ν fluxes (FIG. 6.19) in the forward horn current (FHC) beam. Error bars show statistical and systematic uncertainties (Chapter 7). Vertical lines mark the minimum neutrino energy for each ν cut.

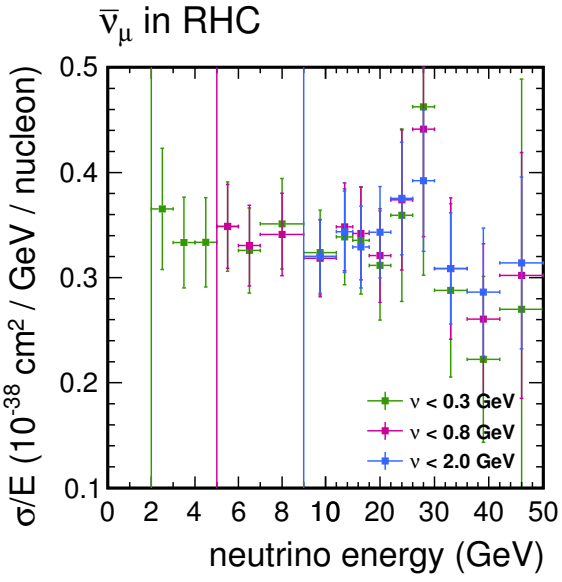

FIG. 6.22: Extracted cross section divided by energy for antineutrinos as derived from the three low-ν fluxes (FIG. 6.20) in the reverse horn current (RHC) beam. Error bars show statistical and systematic uncertainties (Chapter 7). Vertical lines mark the minimum neutrino energy for each ν cut.

GENIE. The C^{12} cross section is derived from the simulation by identifying the target nucleus of the interaction and selecting only events that interact on C^{12}. FIG. 6.23 shows the isoscalar correction for neutrinos, while FIG. 6.24 shows the isoscalar correction for antineutrinos.

Note that the isoscalar correction is applied only when the cross section is compared to external measurements (Chapter 9). For the primary result, the cross section derived from GENIE is inherently for the ensemble of materials comprising the MINERνA fiducial volume (primarily scintillator) as defined in the simulated geometry (Section 7.5).

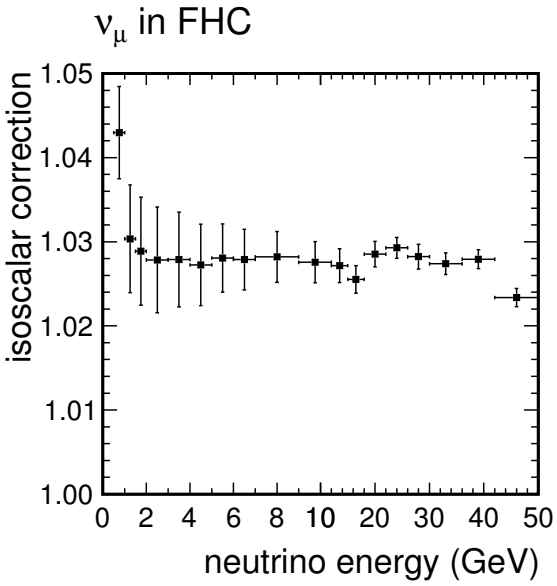

FIG. 6.23: Isoscalar correction for neutrinos as derived from the GENIE event generator. Error bars show statistical and systematic uncertainties (Chapter 7).

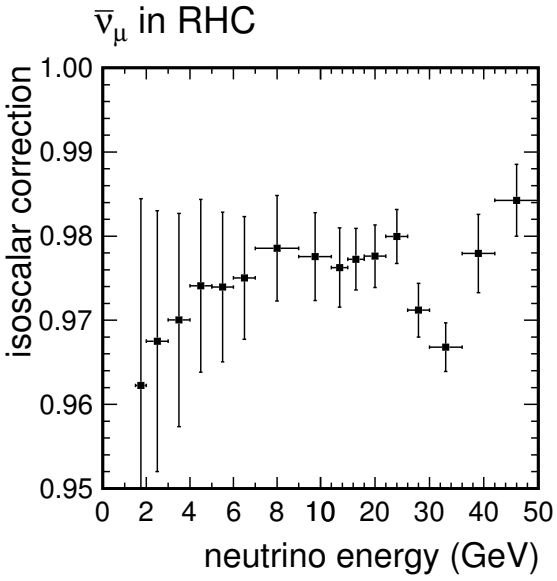

FIG. 6.24: Isoscalar correction for antineutrinos as derived from the GENIE event generator. Error bars show statistical and systematic uncertainties (Chapter 7).

CHAPTER 7

Uncertainties

7.1 Statistical uncertainties

In propagating statistical uncertainties, this function is frequently encountered:

$$f = \frac{A}{A+B}. \tag{7.1}$$

A and B are two random variables, typically event counts in a particular bin. Here, the events comprising the numerator are a subset of the denominator. This occurs, for example, with an acceptance correction (Section 6.4.3), where the numerator is the reconstructed subset of the events in the denominator.

The statistical uncertainty on f, σ_f, is calculated via

$$\sigma_f = \sqrt{\left(\frac{\partial f}{\partial A}\right)^2 \sigma_A^2 + \left(\frac{\partial f}{\partial B}\right)^2 \sigma_B^2}. \tag{7.2}$$

Evaluating the partial derivatives and grouping the σ_X/X terms (the fractional uncertain-

ties) yields

$$\sigma_f = \frac{AB}{(A+B)^2}\sqrt{\left(\frac{\sigma_A}{A}\right)^2 + \left(\frac{\sigma_B}{B}\right)^2}. \tag{7.3}$$

The fractional uncertainty of f, σ_f/f, is then

$$\frac{\sigma_f}{f} = \frac{B}{A+B}\sqrt{\left(\frac{\sigma_A}{A}\right)^2 + \left(\frac{\sigma_B}{B}\right)^2}. \tag{7.4}$$

Conveniently, the inverse function, $g = (A+B)/A$, yields the same fractional uncertainty.

Neglecting unfolding and recalling Eq. 6.14, the low-ν flux (Eq. 6.13) is computed as

$$\Phi(E) = \eta D_\nu \frac{S_\nu}{S_\nu + B_\nu} \underbrace{\frac{N_\nu}{S_\nu}}_{1/\epsilon} \underbrace{\frac{N}{N_\nu}\frac{1}{\sigma_{\text{GENIE}}}}_{1/\sigma_\nu} \frac{1}{T \times \Delta E}, \tag{7.5}$$

where D is the reconstructed interaction rate in data, S is the reconstructed signal (true CC ν_μ or CC $\bar{\nu}_\mu$) rate, B is the reconstructed background (not true CC ν_μ or CC $\bar{\nu}_\mu$) rate and N is the true signal rate. The subscript ν indicates samples selected with a cut on reconstructed ν for D, S and B or a cut on true ν for N. The $1/\sigma_\nu$ term reflects how the true flux is derived from the simulation by dividing the true inclusive rate, N, by the inclusive cross section spline implemented in GENIE, σ_{GENIE}.

The equation simplifies to

$$\Phi(E) = \frac{\eta}{\sigma_{\text{GENIE}}} D_\nu \frac{N}{S_\nu + B_\nu}\frac{1}{T \times \Delta E}, \tag{7.6}$$

indicating that the fractional statistical uncertainty on the flux, $\Phi(E)$, is the quadrature sum of a data component, D_ν, and a simulation component, $N/(S_\nu + B_\nu)$. For the focused samples (FHC ν_μ and RHC $\bar{\nu}_\mu$), backgrounds are negligible, the reconstructed low-ν signal rate, S_ν, is a subset of the true inclusive signal rate, N, and the fractional statistical

uncertainty is given by Eq. 7.4.

Following the same logic, the cross section (Eq. 6.12) is computed as

$$\sigma(E) = D\frac{S}{S+B}\underbrace{\frac{N}{S}}_{1/\epsilon}\frac{1}{\Phi(E)}\frac{1}{T\times\Delta E}. \tag{7.7}$$

Substituting Eq. 7.6 and simplifying yields

$$\sigma(E) = \frac{\sigma_{\text{GENIE}}}{\eta}\frac{D}{D_\nu}\frac{S_\nu+B_\nu}{S+B}, \tag{7.8}$$

where the denominator of the data component, D_ν, is a subset of the numerator, D, and the numerator of the simulation component, $S_\nu+B_\nu$, is a subset of the denominator, $S+B$. The fractional statistical uncertainty is given by Eq. 7.4.

The cross-normalization procedure (Section 6.4.5) adds an uncertainty arising from the statistical uncertainty in fitting the normalization factors, η, for the two lower ν cuts. The normalization factor, η, is effectively the ratio of the two cross sections in the region of overlap and the uncertainty is derived from

$$\frac{\sigma_1}{\sigma_2} = \frac{\eta_2}{\eta_1}\frac{D_{\nu_2}}{D_{\nu_1}}\frac{S_{\nu_1}+B_{\nu_1}}{S_{\nu_2}+B_{\nu_2}}, \tag{7.9}$$

where the ν_1 cut is lower in energy than ν_2, $\nu_1 < \nu_2$, so the events passing the lower $\nu < \nu_1$ cut are a subset of the $\nu < \nu_2$ events. Cross-normalizing the $\nu < 800\,\text{MeV}$ result to the $\nu < 2\,\text{GeV}$ result, the uncertainty is given by the ratio of the cross sections in the neutrino energy range 9 GeV to 22 GeV; for the $\nu < 300\,\text{MeV}$ result, the range is 5 GeV to 22 GeV.

7.2 Many universes method

The many universes method[29] is a means of calculating a systematic uncertainty band on an arbitrary distribution by performing the analysis in parallel for a number of systematic shifts. Each shift constitutes an "universe". The results for each universe are stored as one entry in an array of histograms. The uncertainty in any one bin is defined by the spread of values in that bin across all of the universes. Shifts can be either vertical or lateral.

In a vertical shift, the probability of an event occurring is more or less likely, but the properties of the event are unchanged. Thus, when filling a histogram of kinematic quantities, the event remains in the same bin. The event is weighted by a value other than 1.0, which is added to the histogram bin. A weight less than 1.0 indicates that an event is less likely than the nominal model; a weight greater than 1.0 indicates that an event is more likely than the nominal model. Systematic uncertainties on cross section models are examples of vertical shifts.

In a lateral shift, the properties of the event are changed and the event may populate a different bin in a particular histogram. Systematic uncertainties on reconstructed energy scales are examples; changing the reconstructed kinematics will cause event migration between bins.

A simple systematic uncertainty, representing one parameter of a model, may be evaluated with only two universes corresponding to $+1\sigma$ and -1σ shifts of the systematic. A more complex systematic uncertainty, comprising of many correlated or uncorrelated parameters, may be evaluated with hundreds of universes, with each universe representing an ensemble of underlying parameters. For this analysis, flux uncertainties are evaluated with 100 universes; all others are evaluated by two universes, or in some cases, a single universe. A single universe is used to assess alternative models where the model is either

on (the shift) or off (the central value).

For a given systematic uncertainty, the covariance of bins j and k is defined by

$$\mathrm{cov}(j,k) = \frac{1}{N}\sum_{i=1}^{N}(x_{ij} - \eta_j)(x_{ik} - \eta_k), \tag{7.10}$$

where the summation is over N universes, x_{ij} and x_{ik} are the values of bin j or k in the i'th universe, and η_j and η_k are the mean value across the universes in bin j or k. The uncertainty on bin j is given by the standard deviation, which is the square root of the diagonals of the covariance matrix:

$$\sigma_j = \sqrt{\mathrm{cov}(j,j)} = \sqrt{\frac{1}{N}\sum_{i=1}^{N}(x_{ij} - \eta_j)^2}. \tag{7.11}$$

The total systematic uncertainty is given by the quadrature sum of the uncertainty calculated for each systematic:

$$\sigma_{j,\mathrm{total}} = \sqrt{\sum_{l}\sigma_{j,l}^2}, \tag{7.12}$$

where the summation is over all evaluated systematic uncertainties.

For this analysis, systematic shifts are applied only to simulated events, but affect the data through background subtraction, unfolding, acceptance correction, low-ν correction and isoscalar correction.

7.3 GENIE cross section model

The event generator, GENIE[30], is responsible for simulating neutrino interactions in the MINERνA detector. GENIE begins by being supplied with a description of the flux (Section 7.4), defined by a vector of neutrino species (ν_e, ν_μ, ν_τ), production vertex, energy and momentum vector, and utilizes a number of models to generate the final state

leptons and hadrons of a neutrino interaction. These final state particles are fed into a GEANT4[16] simulation of the detector, modelling secondary interactions and energy depositions. The simulation then models scintillation and the optical collection and electronic readout of the resulting photons. For this analysis, the version of GENIE utilized is v2r6p2 with the GRV98LO parton density functions.

GENIE includes a number of models:

1. **Nuclear physics** – GENIE utilizes a relativistic Fermi gas (RFG) model for the momentum distribution of nucleons (protons and neutrons) within the nucleus. While a true Fermi gas models the particles as non-interacting within a potential well, GENIE includes the Bodek-Ritchie modifications to partially incorporate short-range nucleon-nucleon correlations[31].

2. **Cross section** – GENIE computes the total neutrino interaction rate as the product of the inclusive cross section and flux. An event channel (quasi-elastic, resonance, deep inelastic, etc.) and kinematics are then selected using models of these processes (described later).

3. **Hadronization** – GENIE utilizes the AGKY (Andreopoulos-Gallagher-Kehayias-Yang) model to simulate the production of hadrons in inelastic interactions. AGKY models the hadron multiplicity and kinematics of low energy showers and transitions to PYTHIA/JETSET[32] at high energy.

4. **Intranuclear rescattering (Final state interactions)** – GENIE simulates the scattering of the products of a neutrino interaction within the nuclear environment with the INTRANUKE[33] package. Final state interactions include absorption, charge exchange, and inelastic and elastic scattering.

GENIE simulates three fundamental interaction channels in addition to coherent

neutrino-nucleus scattering, charm production, inverse muon decay and neutrino-electron elastic scattering:

1. **Quasi-elastic scattering (QE)** – Quasi-elastic scattering, $\nu_\mu + n \to \mu^- + p$ or $\bar{\nu}_\mu + p \to \mu^+ + n$, in which the struck nucleon remains intact, is implemented with the Llewellyn-Smith[34] model. Vector form factors are derived from electron scattering experiments. A dipole axial form factor is assumed with $M_A = 0.99\,\mathrm{GeV/c^2}$.

2. **Resonance production** – Baryon resonance production, such as $\nu_\mu + n \to \mu^- + \Delta^+$ with the Δ^+ rapidly decaying to $p + \pi^+$, is simulated with the Rein-Sehgal[35] model.

3. **Deep inelastic scattering (DIS)** – Deep inelastic scattering, in which the neutrino interacts with a single quark within a nucleon, is modeled with an effective leading order model corrected with Bodek-Yang[36] at low momentum transfer, Q^2.

Systematic uncertainties arising from the models implemented in GENIE are evaluated with the many universes method (Section 7.2) by varying parameters of the models at $+1\sigma$ and -1σ uncertainty. Table 7.1 lists the parameters assessed as systematic uncertainties. Parameters listed with a $\pm X\%$ uncertainty are evaluated with two universes; those that involve toggling an alternative model on or off are evaluated with a single universe.

The MaCCQE parameter, the charged-current quasi-elastic axial mass (M_A^{CCQE}) was deemed to be redundant with the random phase approximation and meson exchange currents uncertainty detailed in Section 7.3.1 and was not included in the GENIE systematic uncertainty band. GENIE, by default, includes a large uncertainty on M_A^{CCQE} (-15% and +25% from the nominal $0.99\,\mathrm{GeV/c^2}$) to cover observed discrepancies in experimental data. In 2009, the NOMAD collaboration reported a measurement of $M_A = 1.05 \pm 0.06\,\mathrm{GeV/c^2}$[37]; in 2010, the MiniBooNE collaboration reported $M_A = 1.35 \pm 0.17\,\mathrm{GeV/c^2}$[38]. Such discrepancies in M_A, as well as observations of the Q^2 dependence

of the quasi-elastic cross section, show that the dipole axial form factor may not be the ideal model for QE scattering.

7.3.1 Random phase approximation and meson exchange currents

The random phase approximation (RPA) model is an alternative to the relativistic Fermi gas (RFG) model for determining the excitation levels of the nucleus. RPA includes long-range nucleon-nucleon correlations resulting in a reduced inclusive cross section at low momentum transfers, Q^2. The RPA model is evaluated as a systematic uncertainty by applying a reweight as a function of ν and three momentum transfer, $q^3 = \sqrt{\nu^2 + Q^2}$, as shown in FIG. 7.1. The reweight is the ratio of events in a given $[\nu, q^3]$ bin in a modified GENIE simulation[39] over the default simulation.

Meson exchange currents (MEC) describe a process in which nucleons within a nucleus exchange momentum via a pion, resulting in two nucleon final states and an increased cross section at low energies (in the "dip" region between quasi-elastic scattering and resonance production). GENIE does not directly simulate these two nucleon states (except when they occur through final state interactions). However, making the assumption that two nucleon states behave calorimetrically similar to the final states implemented in GENIE, the effect of the increased cross section can be evaluated by reweighting events as a function of ν as shown in FIG. 7.2. As with the RPA weight, the MEC weight is determined from a modified GENIE simulation[39].

RPA and the combination RPA+MEC are individually evaluated as a component of the GENIE systematic uncertainty band using a single universe in the many universes method. The effect of the models on the ν and $y = \nu/E$ distributions in bins of neutrino energy, E, is shown in FIG. 7.3 – 7.4 for neutrinos and FIG. 7.5 – 7.6 for antineutrinos.

Parameter	Description	$\pm1\sigma$ Uncertainty
MaCCQE	Charged-current quasi-elastic (CCQE) axial mass, M_A^{CCQE}	-15% +25%
VecFFCCQEshape	CCQE electromagnetic form factor	BBBA2005 (default) or dipole
MaRES	Charged-current resonance axial mass, M_A^{CCRES}	$\pm20\%$
MvRES	Charged-current resonance vector mass, M_V^{CCRES}	$\pm10\%$
Rvp1pi	Non-resonance 1π production in νp interactions	$\pm50\%$
Rvn1pi	Non-resonance 1π production in νn interactions	$\pm50\%$
Rvp2pi	Non-resonance 2π production in νp interactions	$\pm50\%$
Rvn2pi	Non-resonance 2π production in νn interactions	$\pm50\%$
FrAbs_N	Intranuclear absorption probability for nucleons	$\pm20\%$
FrAbs_pi	Intranuclear absorption probability for pions	$\pm20\%$
FrCEx_N	Intranuclear charge exchange probability for nucleons	$\pm50\%$
FrCEx_pi	Intranuclear charge exchange probability for pions	$\pm50\%$
FrElas_N	Intranuclear elastic scattering probability for nucleons	$\pm30\%$
FrElas_pi	Intranuclear elastic scattering probability for pions	$\pm10\%$
FrInel_N	Intranuclear inelastic scattering probability for nucleons	$\pm40\%$
FrInel_pi	Intranuclear inelastic scattering probability for pions	$\pm40\%$
FrPiProd_N	Intranuclear π-production probability for nucleons	$\pm20\%$
FrPiProd_pi	Intranuclear π-production probability for pions	$\pm20\%$
MFP_N	Intranuclear mean free path for nucleons	$\pm20\%$
MFP_pi	Intranuclear mean free path for pions	$\pm20\%$
AGKYxF1pi	Feynman x_F distribution in 1π states in AGKY model	$\pm20\%$
ThetaDelta2Npi	π angular distribution in $\Delta \to \pi N$	isotropic (default) or Rein-Sehgal
RDecBR1gamma	Radiative decay branching ratio, $\Delta \to \gamma X$	$\pm50\%$
RPA	Random phase approximation model	off (default) or on
RPA+MEC	Random phase approximation and meson exchange currents model	off (default) or on
EFNUCR	Effective nuclear radius for intranuclear interactions	±0.6 fm
FZONE	Formation zone time (when a quark is free in the nucleus)	$\pm50\%$
Hadronization_Alt	Hadronization model with more isotropic final states	off (default) or on

TABLE 7.1: GENIE model parameters evaluated in the systematic uncertainty band. Parameters listed with a $\pm1\sigma$ uncertainty are evaluated with two universes (Section 7.2); those toggled on or off are evaluated with one universe. The MaCCQE uncertainty was deemed redundant with the random phase approximation and meson exchange currents uncertainty (Section 7.3.1) and was not included in the uncertainty band.

For the antineutrino analysis, the same reweight is naively applied, though it was determined explicitly for neutrinos. Note that these plots are in bins of neutrino energy and area normalized in all universes of the many-universes uncertainty band to remove any dependence on the flux. However, this also hides any change to the normalization of the cross section resulting from an alternative model, leaving only the shape change visible. The distributions at higher neutrino energy are presented in Appendix E for neutrinos and Appendix F for antineutrinos.

The net effect of the RPA and RPA+MEC reweights is to reduce the simulated cross section (and thus simulated interaction rate) at very low $\nu < 200\,\text{MeV}$. While the ν and $y = \nu/E$ distributions still show data points outside of the simulation uncertainty band, the important feature is the shape of the distributions around the ν cuts (300 MeV, 800 MeV and 2 GeV) as the shape is important in predicting migration over the ν cut from biases and resolution in calorimetry. At the $\nu = 300\,\text{MeV}$ cut, the shape agreement between the simulation and data is significantly improved with the RPA+MEC reweight. The RPA+MEC reweights are implemented only as a component of the systematic uncertainty band, not as a change to the nominal cross section in the simulation.

7.4 Flux model

To first order, the low-ν analysis is insensitive to the neutrino flux modeled in the simulation. Any normalization uncertainty in the flux is removed as the extracted cross section is normalized to an external constraint (Section 6.4.5). However, changes in the shape of the simulated flux will subtly affect acceptance corrections (Section 6.4.3).

The flux in the simulation is derived from a Monte-Carlo simulation of the neutrino beamline, which models 120 GeV proton collisions on the thick, complex NuMI target, the focusing of the resulting hadrons by a pair of magnetic horns and the decay of pions and

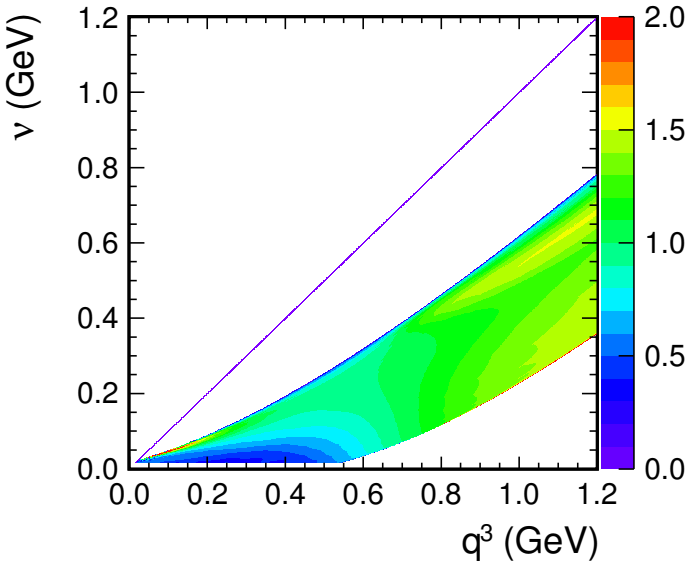

FIG. 7.1: Random phase approximation (RPA) event weight as a function of true ν and three momentum transfer, $q^3 = \sqrt{\nu^2 + Q^2}$[39]. Event weight is the ratio of events in a given bin of ν and q^3 with the RPA model on over off (default GENIE). Event weight is applied to true quasi-elastic events only.

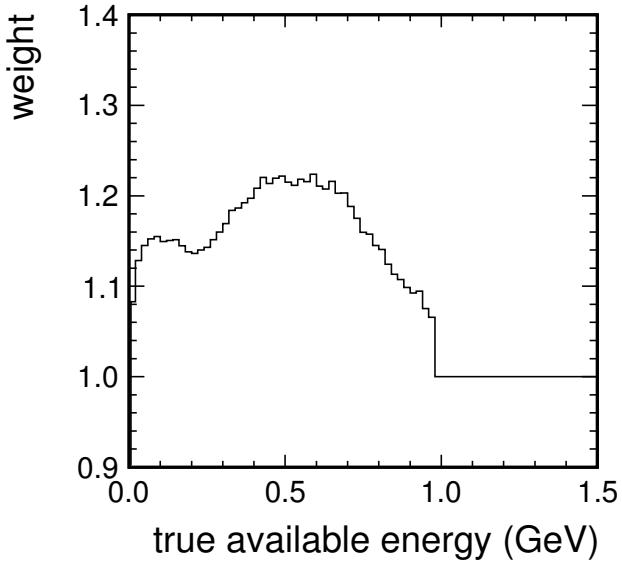

FIG. 7.2: Meson exchange currents (MEC) event weight as a function of "true available energy"[39]. True available energy approximates the visible energy in the detector, defined as the sum of the kinetic energy of all final state protons and charged pions, the full energy of neutral pions, electrons and photons and neglecting neutrons. Event weight is applied to all events after applying the RPA weight (FIG. 7.1)

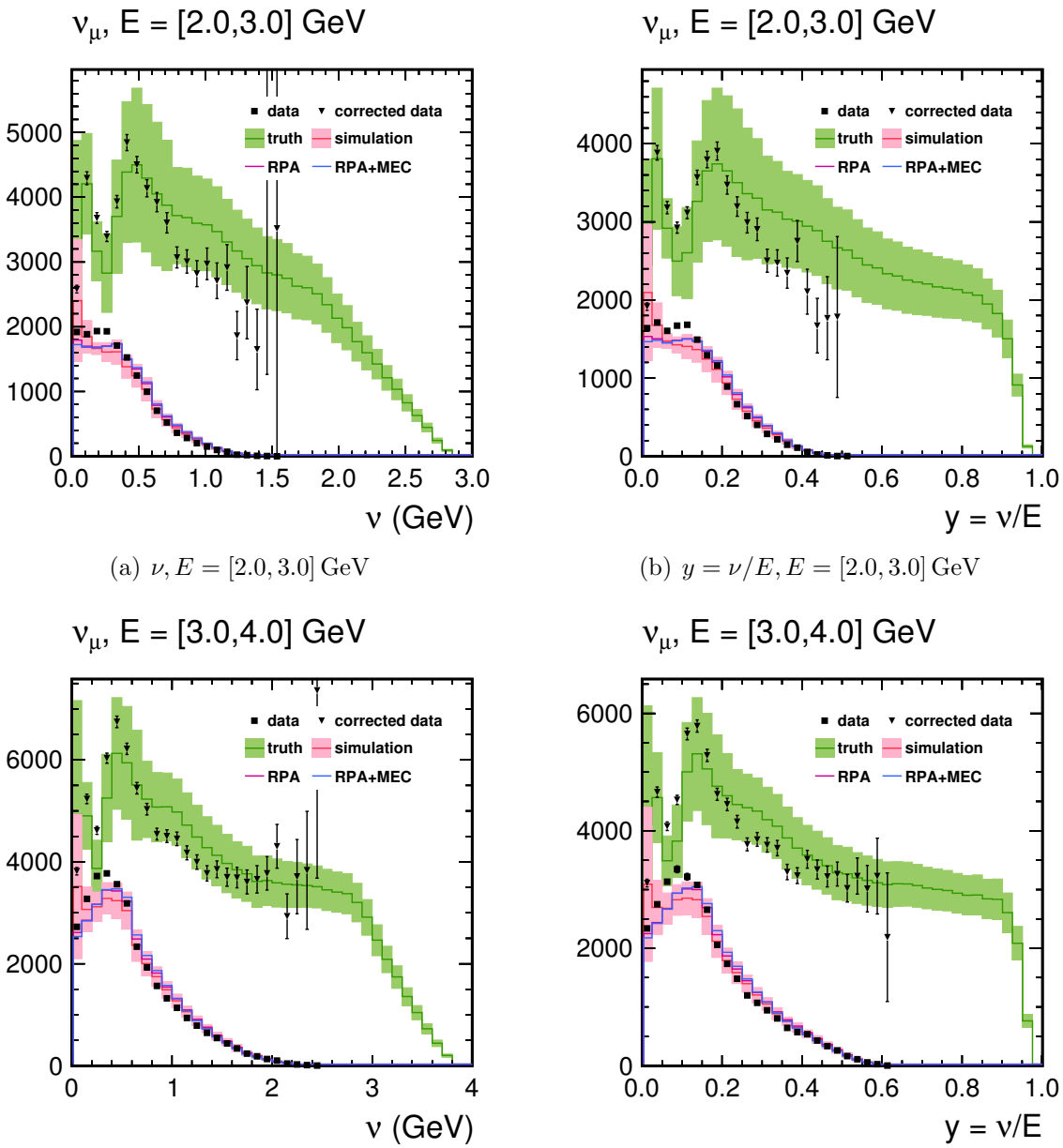

(a) $\nu, E = [2.0, 3.0]$ GeV

(b) $y = \nu/E, E = [2.0, 3.0]$ GeV

(c) $\nu, E = [3.0, 4.0]$ GeV

(d) $y = \nu/E, E = [3.0, 4.0]$ GeV

FIG. 7.3: ν and $y = \nu/E$ for neutrino energy, $E = [2.0, 4.0]$ GeV for neutrinos in the forward horn current (FHC) beam. "Simulation" (red) is reconstructed, simulated events. "Truth" (green) is all simulated events, absent acceptance losses. Simulation is area normalized to data in all universes of the many universe uncertainty band, truth is scaled by the same value. "Corrected data" (black triangles) is acceptance corrected with the ratio of truth to simulation. Data and corrected data are plotted with statistical uncertainties; truth and simulation are plotted with statistical and systematic uncertainties. Two universes of the simulation uncertainty band, RPA and RPA+MEC, are plotted overlaid.

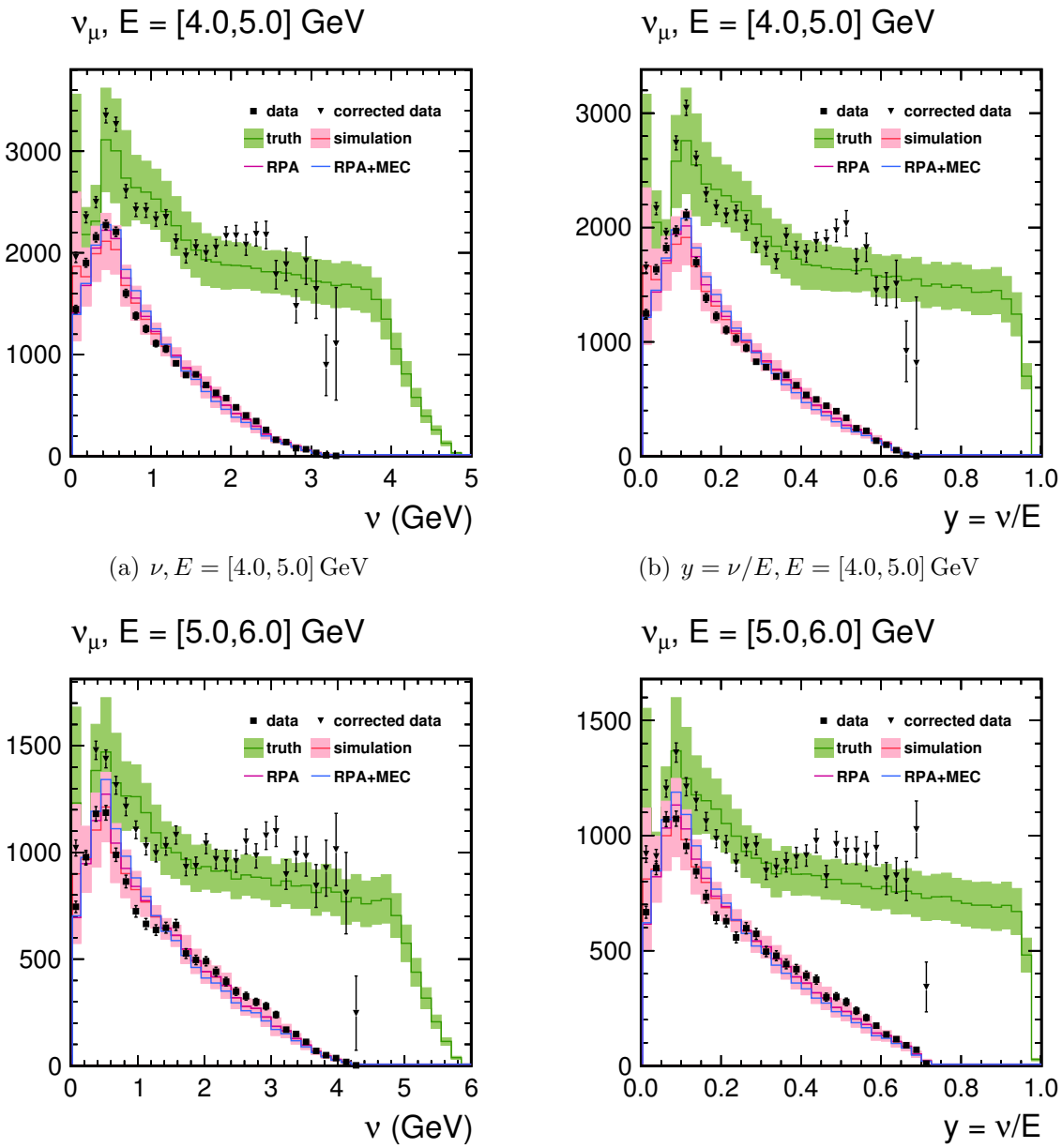

(a) $\nu, E = [4.0, 5.0]$ GeV

(b) $y = \nu/E, E = [4.0, 5.0]$ GeV

(c) $\nu, E = [5.0, 6.0]$ GeV

(d) $y = \nu/E, E = [5.0, 6.0]$ GeV

FIG. 7.4: ν and $y = \nu/E$ for neutrino energy, $E = [4.0, 6.0]$ GeV for neutrinos in the forward horn current (FHC) beam. "Simulation" (red) is reconstructed, simulated events. "Truth" (green) is all simulated events, absent acceptance losses. Simulation is area normalized to data in all universes of the many universe uncertainty band, truth is scaled by the same value. "Corrected data" (black triangles) is acceptance corrected with the ratio of truth to simulation. Data and corrected data are plotted with statistical uncertainties; truth and simulation are plotted with statistical and systematic uncertainties. Two universes of the simulation uncertainty band, RPA and RPA+MEC, are plotted overlaid.

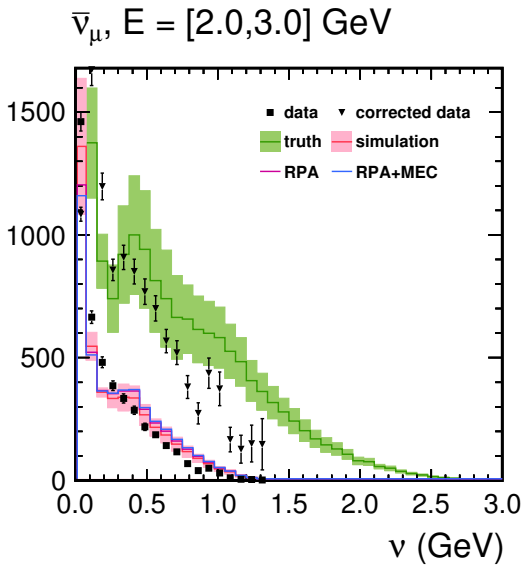

(a) $\nu, E = [2.0, 3.0]$ GeV

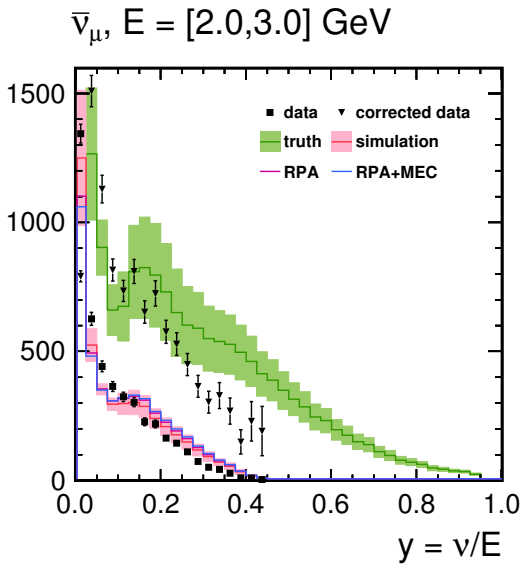

(b) $y = \nu/E, E = [2.0, 3.0]$ GeV

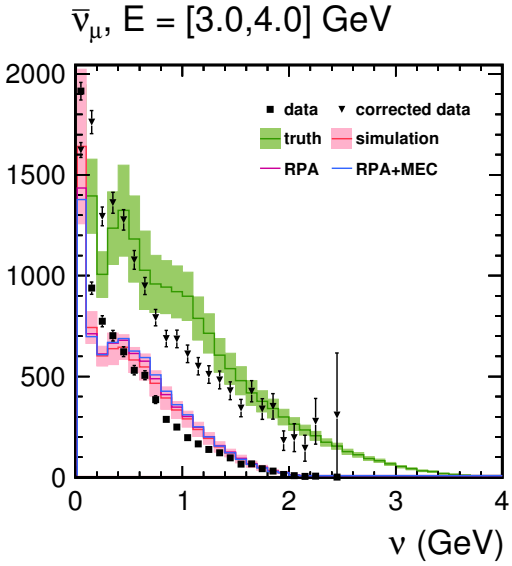

(c) $\nu, E = [3.0, 4.0]$ GeV

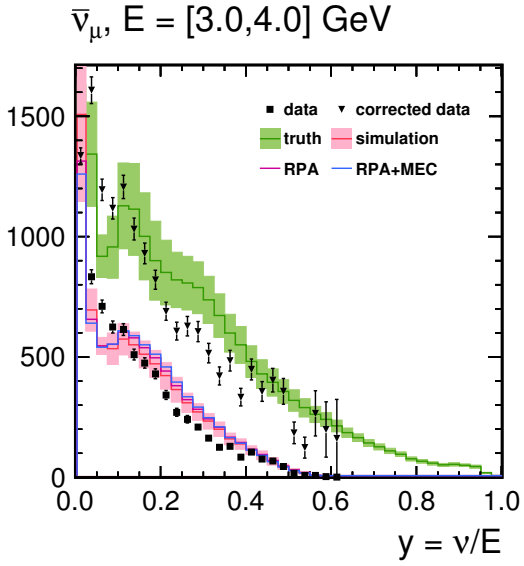

(d) $y = \nu/E, E = [3.0, 4.0]$ GeV

FIG. 7.5: ν and $y = \nu/E$ for neutrino energy, $E = [2.0, 4.0]$ GeV for antineutrinos in the reverse horn current (RHC) beam. "Simulation" (red) is reconstructed, simulated events. "Truth" (green) is all simulated events, absent acceptance losses. Simulation is area normalized to data in all universes of the many universe uncertainty band, truth is scaled by the same value. "Corrected data" (black triangles) is acceptance corrected with the ratio of truth to simulation. Data and corrected data are plotted with statistical uncertainties; truth and simulation are plotted with statistical and systematic uncertainties. Two universes of the simulation uncertainty band, RPA and RPA+MEC, are plotted overlaid.

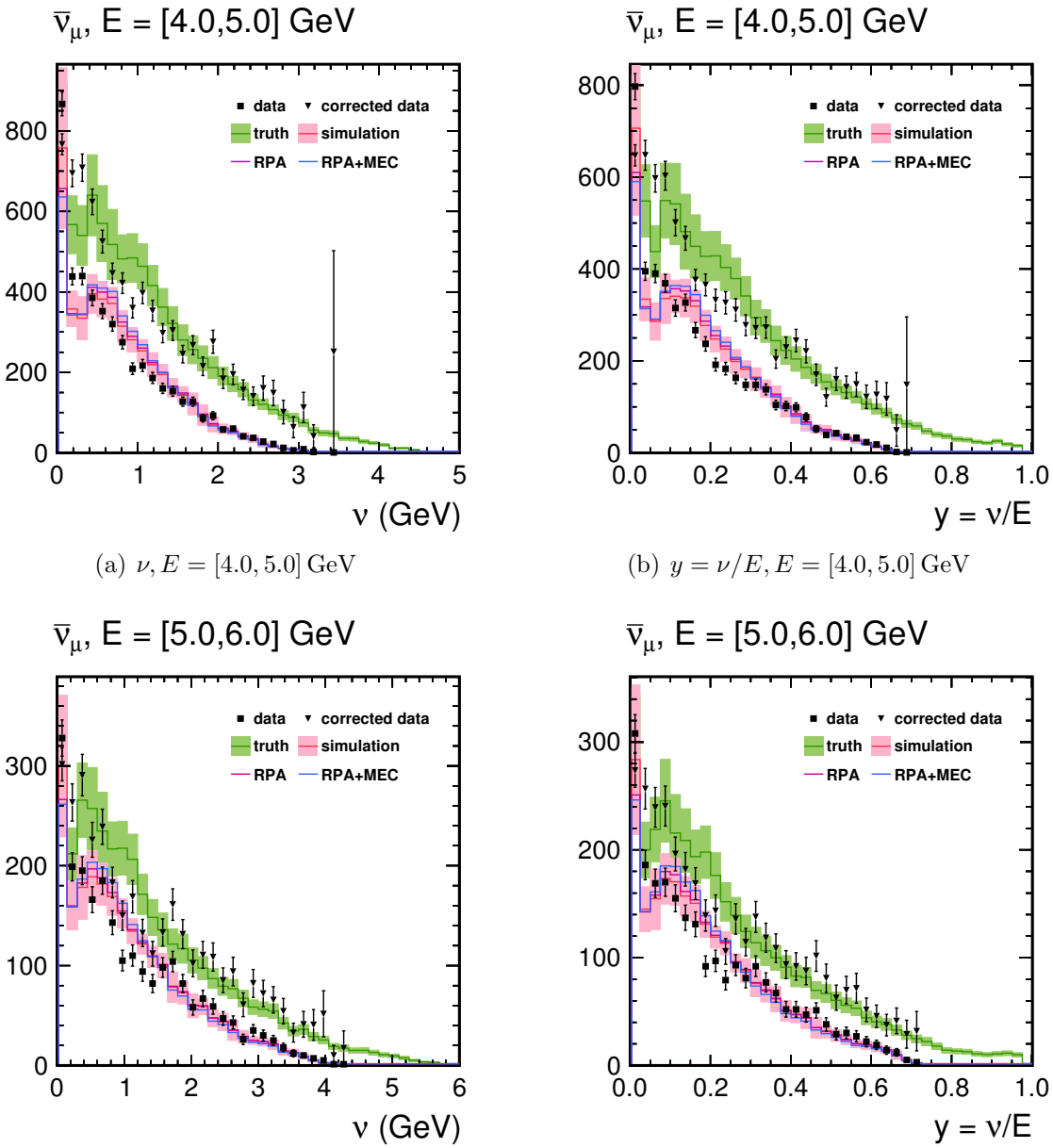

(a) $\nu, E = [4.0, 5.0]$ GeV

(b) $y = \nu/E, E = [4.0, 5.0]$ GeV

(c) $\nu, E = [5.0, 6.0]$ GeV

(d) $y = \nu/E, E = [5.0, 6.0]$ GeV

FIG. 7.6: ν and $y = \nu/E$ for neutrino energy, $E = [4.0, 6.0]$ GeV for antineutrinos in the reverse horn current (RHC) beam. "Simulation" (red) is reconstructed, simulated events. "Truth" (green) is all simulated events, absent acceptance losses. Simulation is area normalized to data in all universes of the many universe uncertainty band, truth is scaled by the same value. "Corrected data" (black triangles) is acceptance corrected with the ratio of truth to simulation. Data and corrected data are plotted with statistical uncertainties; truth and simulation are plotted with statistical and systematic uncertainties. Two universes of the simulation uncertainty band, RPA and RPA+MEC, are plotted overlaid.

kaons in the decay pipe. The proton-carbon cross section in the beamline simulation is corrected using external hadron production datasets which measure the cross section and resulting kinematics of $p + C \to \pi^{\pm} + X$, $p + C \to K^{\pm} + X$ and $p + C \to p^{\pm} + X$[40]. The effect of the correction (implemented as a reweight of simulated events) is shown in FIG. 7.7 – 7.8.

The beamline simulation utilizes GEANT4 version v9r2p03 with the FTFP model. The external hadron production datasets are from the NA49 and Barton experiments, and where taken at proton energies of 158 GeV. The data is corrected to 120 GeV proton energy using the FLUKA Monte-Carlo simulation. Kaon/pion production ratios are constrained with thin target data from the MIPP experiment.

For events reweighted with external datasets, systematic uncertainties are derived from the uncertainty of the external measurement. An additional class of events, primarily tertiary interactions in which a pion re-interacts in the target or horns, is not reweighted. For these events, systematic uncertainties are derived from the spread of different models in the GEANT4 simulation. Systematic uncertainties from beam focusing are derived from the simulation by varying the positions of the magnetic focusing horns and target, and horn current within measurement uncertainties.

The three types of flux uncertainties (thin target reweighted, tertiary model spread and beam focusing) are each evaluated with 100 universes in the many-universes method and the results are added in quadrature.

7.5 Mass model

The systematic uncertainty on the mass of a scintillator plane, which includes the triangular scintillator bars, epoxy, tape and skins, is 1.4%[42]. In normalizing the extracted cross section to an external constraint (Section 6.4.5), any dependence on the mass model

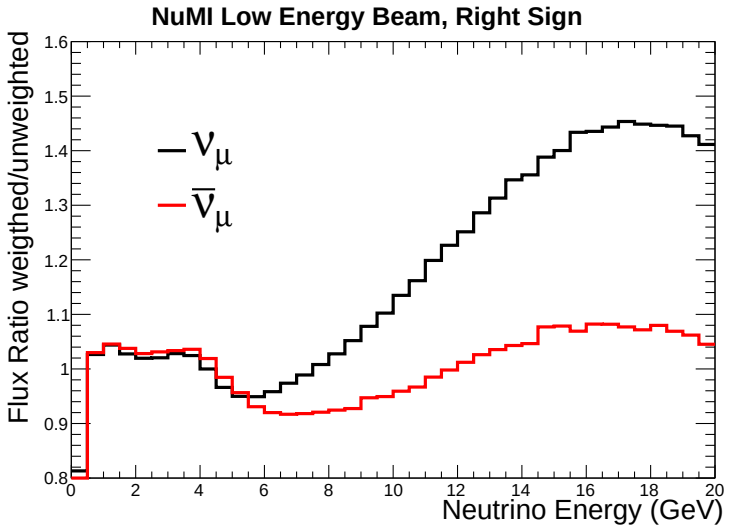

FIG. 7.7: Ratio of thin target reweighted to nominal flux for the focused samples (neutrinos in the forward horn current (FHC) beam and antineutrinos in the reverse horn current (RHC) beam)[41].

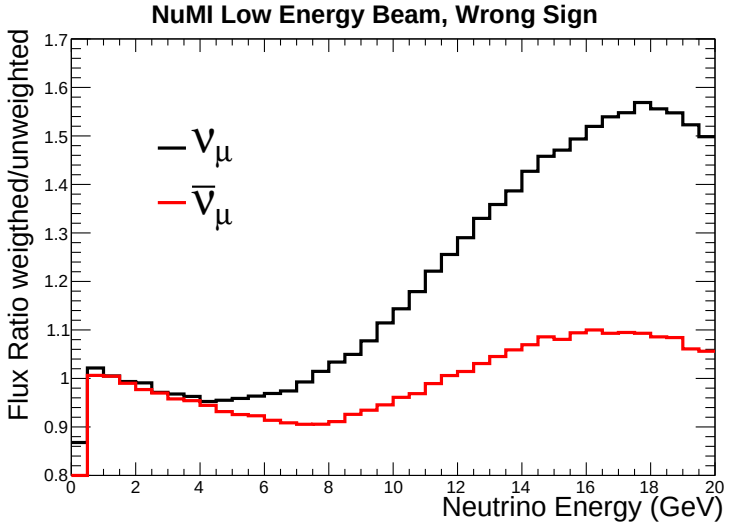

FIG. 7.8: Ratio of thin target reweighted to nominal flux for the defocused samples (neutrinos in the reverse horn current (RHC) beam and antineutrinos in the forward horn current (FHC) beam)[41].

is removed. However, the uncertainty remains in the extracted flux, which is dependent on the number of target nucleons.

7.6 Muon reconstruction efficiency

The muon reconstruction efficiency corrections and uncertainties cover the observed discrepancy in muon reconstruction in data versus simulation. Reconstructing a muon requires reconstructing a track in both MINERνA and MINOS and matching the two tracks together. It is observed that muon reconstruction is less efficient in data than the simulation predicts.

Some of this discrepancy is attributed to pile-up, the presence of additional neutrino interactions adjacent in time, which can obscure the event being reconstructed. Pile-up is modeled in the MINERνA detector by overlaying single simulated events onto actual data gates. Pile-up is not modeled in the MINOS detector for this analysis, though the feature has been added to more recent software releases.

The muon reconstruction efficiency in MINERνA is determined by identifying clean tracks in MINOS that point into the fiducial volume of the MINERνA detector and asking how often a track is reconstructed and matched[43]. This occurs approximately 2.5% less often in data than simulation; Table 7.2 lists the MINERνA efficiency corrections for each run period. The correction is applied flat across all muon energies. The systematic uncertainty is taken as plus or minus half the correction.

The muon reconstruction efficiency in MINOS is likewise determined by identifying clean tracks in MINERνA that point into MINOS and asking how often a track is reconstructed and matched[43]. This is implemented as a momentum-dependent correction in two regions ($p_\mu < 3\,\mathrm{GeV/c}$ or $p_\mu > 3\,\mathrm{GeV/c}$). The momentum of the muon is estimated by observing the scattering of the muon within the MINERνA detector. Tracks exhibiting

high scattering are lower momentum and vice versa. Table 7.2 lists the MINOS efficiency corrections for each run period. The systematic uncertainty is taken as half the correction.

Period	Data POT	MINERνA eff.	MINOS eff.	
			$p_\mu < 3\,\mathrm{GeV/c}$	$p_\mu > 3\,\mathrm{GeV/c}$
1	9.6e+19	0.973	0.934	0.982
5	1.1e+20	0.976	0.956	0.989
7	2.9e+18	0.978	0.969	0.994
9	6.8e+18	0.977	0.951	0.994
13	2.1e+20	0.976	0.942	0.987

TABLE 7.2: MINERνA and MINOS muon reconstruction efficiency corrections for the five run periods in the analysis. Run period 5 is reverse horn current (RHC), antineutrino-focusing; all others are forward horn current (FHC), neutrino-focusing. The MINOS efficiency corrections are divided into two muon momentum bins, defined as the momentum at the face of MINOS.

7.7 Muon energy scale

The MINOS detector determines muon momentum from either range or curvature. For contained events, in which the track stays within the MINOS detector, muon momentum is determined by integrating the estimated energy loss calculated from the amount of material the track has traversed. The systematic uncertainty on a range-based measurement is thus driven by the uncertainty on the mass model of the detector and the energy loss model of the muon. MINOS reports a 2% uncertainty on range-based momentum measurements[6].

The systematic uncertainty of curvature-based measurements is driven by the uncertainty on the magnetic field model of the detector and multiple scattering model of the muon. For events contained in the detector, the momentum is primarily determined by range but a curvature-based momentum is also calculated. The systematic uncertainty on curvature-based measurements can be determined by comparing to the range-based measurement for these events. Performing this analysis finds uncertainties of 0.6% for

$p_\mu > 1\,\mathrm{GeV/c}$ and 2.5% for $p_\mu < 1\,\mathrm{GeV/c}$, which is added in quadrature to the 2% uncertainty for range-based measurements[4]. Table 7.3 lists the final systematic uncertainties.

	$\pm 1\sigma$ Uncertainty	
	Range-based	Curvature-based
$p_\mu < 1\,\mathrm{GeV/c}$	2.0%	3.1%
$p_\mu > 1\,\mathrm{GeV/c}$		2.1%

TABLE 7.3: MINOS muon momentum systematic uncertainties for range-based and curvature-based measurements in two bins of muon momentum (defined at the face of MINOS)[6][4].

7.8 Recoil energy scale

The systematic uncertainty on calorimetric reconstruction of the recoil energy (ν) is determined by convolving individual particle uncertainties into the GENIE model of the neutrino interaction final state.

The systematic uncertainty on proton and meson response is derived from test beam studies. Note that the low-ν analysis uses an older version of the simulation than presented in Chapter 4, which does not incorporate the improvements derived from the test beam (primarily the constant determining Birks' suppression of scintillation), and thus the uncertainties are inflated relative to that presented before. Proton uncertainties are taken as 10%[15][44]; pion (and other meson) response is taken as 5%[15][45].

The electromagnetic ($e^{\pm}, \pi^0, \gamma$) response uncertainty is taken as 3% from a combination of the response of Michel electrons[4], π^0 mass reconstruction[13], and test beam studies[15][46].

The neutron response uncertainty is taken as 15% from comparisons of the inelastic cross section of neutrons on carbon as implemented in GEANT4 versus external measurements[12].

The fraction of energy in the recoil system for particle species $i = \{p,\, n,\, \pi^{\pm},\, K^{\pm},\, K^{0},\, \pi^{0},\, e^{\pm},\, \gamma\}$, f_i, is defined as

$$f_i \equiv \frac{E_i}{\nu}, \tag{7.13}$$

where E_i is the summed energy of all final state particles of species i. For protons and neutrons, E_i is the kinetic energy of the particle (rest mass subtracted). For all other species, the full energy is assumed. FIG. 7.9 displays a stacked plot of the average of this fraction, $\langle f_i \rangle$, versus ν for neutrino interactions; the equivalent for antineutrinos is shown in FIG. 7.10.

The systematic uncertainty on the calometrically reconstructed recoil energy for event e, σ_e, is defined as

$$\sigma_e \equiv \sqrt{\sum_i \frac{f_i}{d} \times \sigma_i^2} \tag{7.14}$$

$$d \equiv \sum_i f_i \tag{7.15}$$

$$\sigma_{\text{proton}} = 10\% \tag{7.16}$$

$$\sigma_{\text{neutron}} = 15\% \tag{7.17}$$

$$\sigma_{\text{meson}} = 5\% \tag{7.18}$$

$$\sigma_{\text{EM}} = 3\%. \tag{7.19}$$

The normalization factor, d, accounts for the sum of the fractions, f_i, being less than 1.0, primarily from the loss of energy due to final state interactions. The meson term includes charged pions and kaons. The electromagnetic (EM) term includes neutral pions, neutral kaons, electrons and photons.

For each bin of recoil energy, ν, the average systematic uncertainty on the recoil

energy, $\langle\sigma\rangle$, is computed as

$$\langle\sigma\rangle = \sqrt{\frac{1}{N}\sum_{e}\sigma_e^2}, \tag{7.20}$$

where the summation is over all events in the bin.

The average systematic uncertainty, $\langle\sigma\rangle$, is shown in FIG. 7.11. At low ν, where quasi-elastic final states dominate, the uncertainty tends to the 10% (15%) for protons (neutrons). At high ν, where the majority of the energy is carried by charged and neutral pions, the uncertainty is reduced.

7.9 Muon "fuzz" and pile-up

Muons traversing a material typically exhibit a steady energy loss per unit distance, $\mathrm{d}E/\mathrm{d}x$, with fluctuations characterized by a Landau distribution. Large energy losses occur when the muon scatters an energetic atomic electron (a δ-ray) or emits a photon upon scattering from a nucleus (bremsstrahlung). These energy depositions are internally referred to as "fuzz" on the muon track since these particles travel some distance from the muon's trajectory. During event reconstruction, heavy energy depositions will initially be associated with the muon, but a secondary algorithm then "cleans" the track by removing large depositions and associating them with the recoil system. The purpose of the secondary algorithm is to properly reconstruct the muon when the track is obscured by the recoil shower. However, in the case of a δ-ray or bremsstrahlung, the reconstruction algorithm overestimates the recoil energy (ν). Turning the secondary algorithm off often results in large showers (typically from a π^0) being incorrectly associated with the muon track, so the conservative choice is to run the algorithm and compensate for the bias in calorimetry.

An observation of rock muons (muons originating from neutrino interactions in the

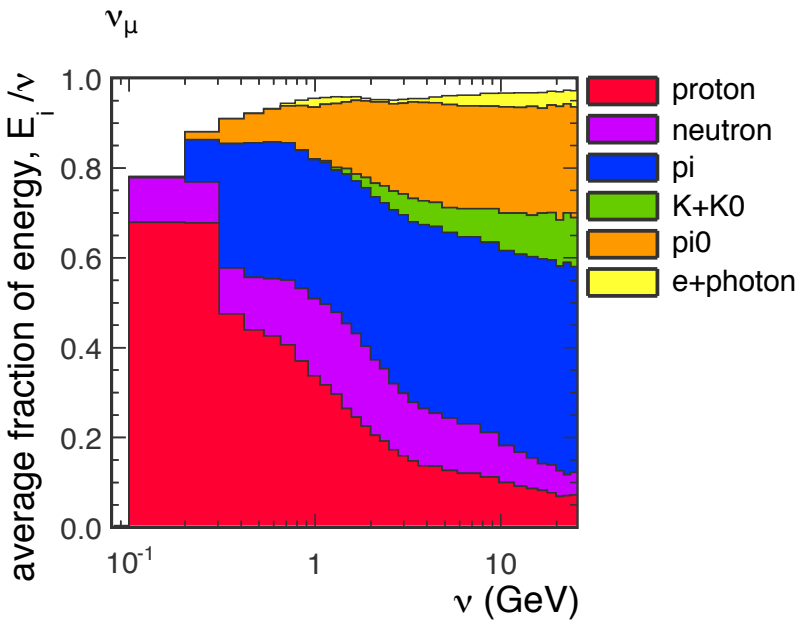

FIG. 7.9: Average fraction of energy, $\langle f_i \rangle \equiv \langle E_i \rangle / \nu$, carried by particle species in the final state of simulated neutrino interactions as a function of ν. At low ν, the recoil system is dominated by the proton; at high ν, by mesons. The deficit from 1.0 on the left is due to final state interactions; on the right is caused by more exotic particles not accounted for.

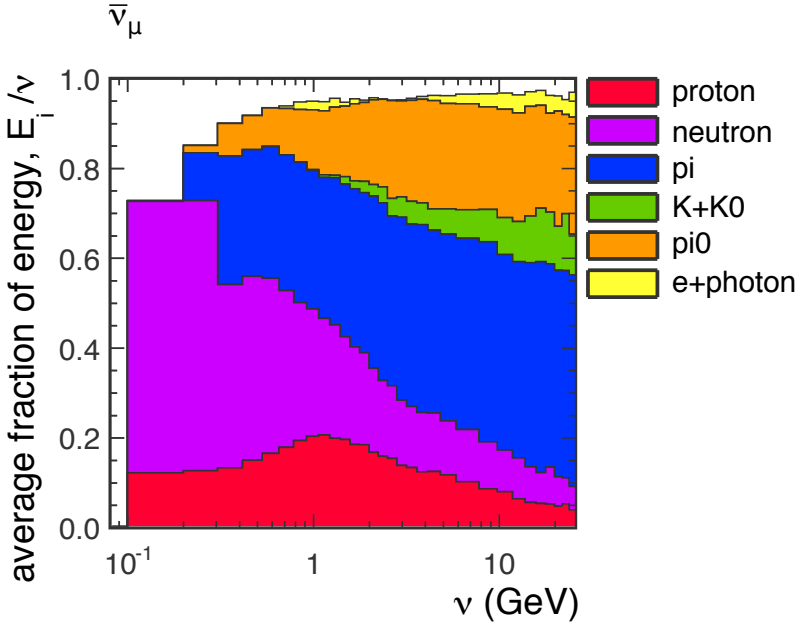

FIG. 7.10: Average fraction of energy, $\langle f_i \rangle \equiv \langle E_i \rangle / \nu$, carried by particle species in the final state of simulated antineutrino interactions as a function of ν. At low ν, the recoil system is dominated by the neutron; at high ν, by mesons. The deficit from 1.0 on the left is due to final state interactions; on the right is caused by more exotic particles not accounted for.

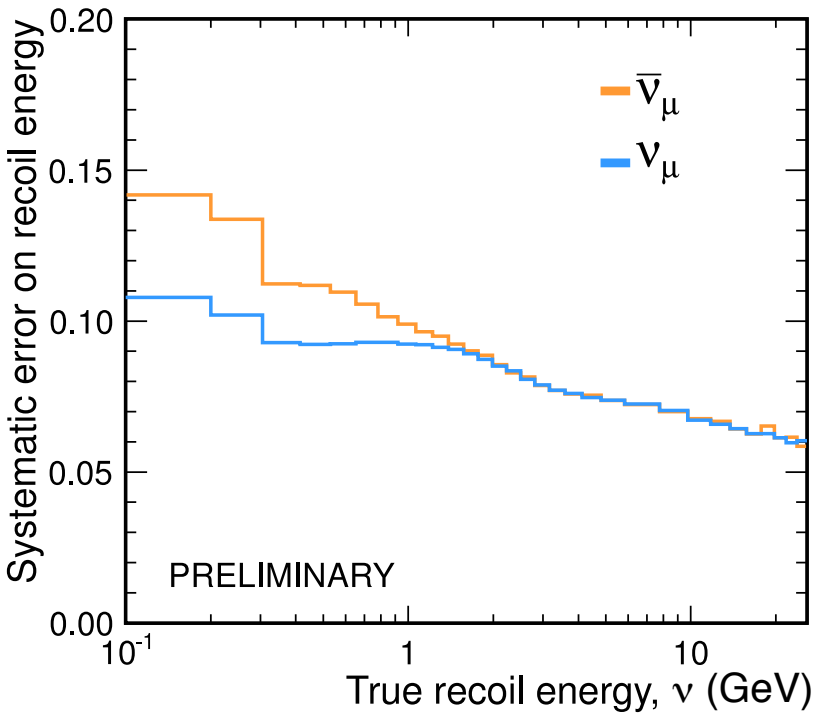

FIG. 7.11: Fractional systematic uncertainty on calorimetric reconstruction of the recoil energy as a function of true recoil energy, ν, for neutrinos and antineutrinos. The derivation of this uncertainty is described in Section 7.8

rock upstream of the MINERνA detector) reveals that more energy is cleaned from the muon track and added to the recoil energy in data than in simulation. This implies that δ-rays and bremsstrahlung occur more frequently in data and represents a bias in the calorimetry that will cause the migration across the ν cuts to be mis-modeled in the simulation. Inherently, this observation also includes a pile-up component from other interactions overlapping the narrow time window used for calorimetry (Section 5.6). Pile-up is incorporated into the simulation by overlaying a single simulated event onto an actual data gate.

A correction to the simulation is implemented by sampling from the recoil energy distribution in data for a random fraction of events. This correction is implemented in two muon energy bins, less than 10 GeV and greater than 10 GeV, defined at the face of the MINOS detector. A study in finer muon energy bins found a distinct change in the data-simulation discrepancy at 10 GeV muon energy. FIG. 7.12 – 7.13 show the distributions of calorimetric recoil energy for rock muon events in the two energy bins. As expected, the distributions are rapidly falling; for these events, the true recoil energy is always zero (only a muon). The first bin of the histogram (zero or very little recoil energy) is the most telling; in both the simulation is significantly greater than data.

For $E_\mu < 10\,\text{GeV}$, the simulation is corrected by randomly sampling a recoil energy value from the data distribution for 16% of events (randomly selected). The sampled energy value is simply added to the reconstructed recoil for the simulated event. A systematic uncertainty band is derived by varying the 16% parameter by $\pm 50\%$ of itself. For $E_\mu > 10\,\text{GeV}$, the simulation is corrected for 34% of events, with the same $\pm 50\%$ uncertainty band. The fraction of events to correct was determined by varying the parameter at 1% increments to achieve the best possible agreement in the first bin of calorimetric recoil energy (FIG. 7.12 – 7.13).

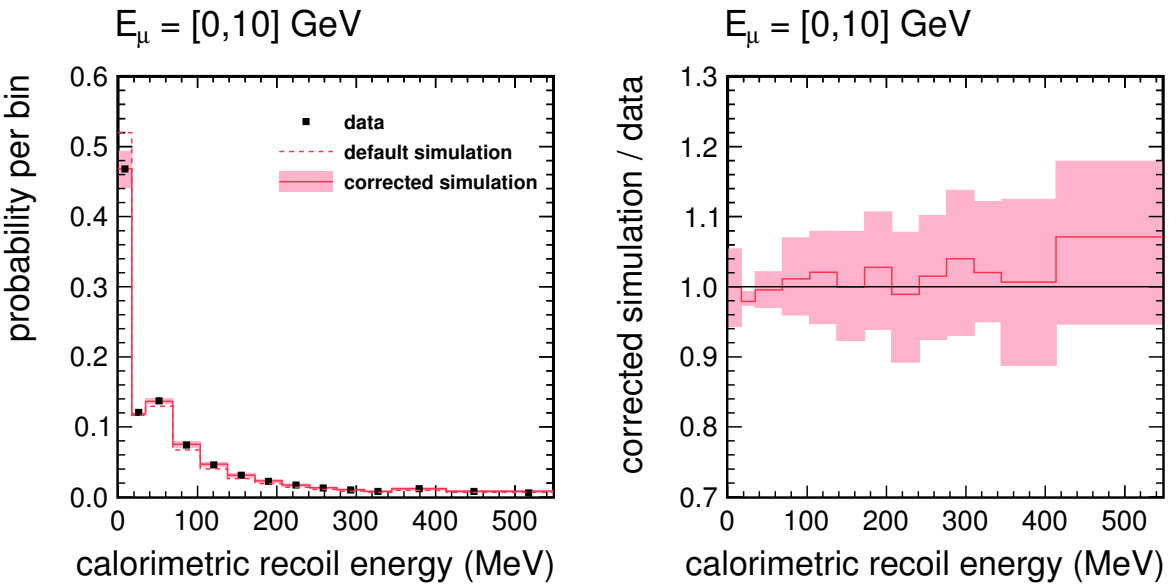

FIG. 7.12: Calorimetric off-track energy for rock muons of energy, $E_\mu < 10\,\text{GeV}$, area normalized to unity (left) and ratio of corrected simulation to data (right). Corrected simulation is plotted with systematic uncertainty; data and default simulation are plotted without uncertainty. Deviations of the central value of the corrected simulation outside the systematic uncertainty band arise from the stochastic nature of the correction.

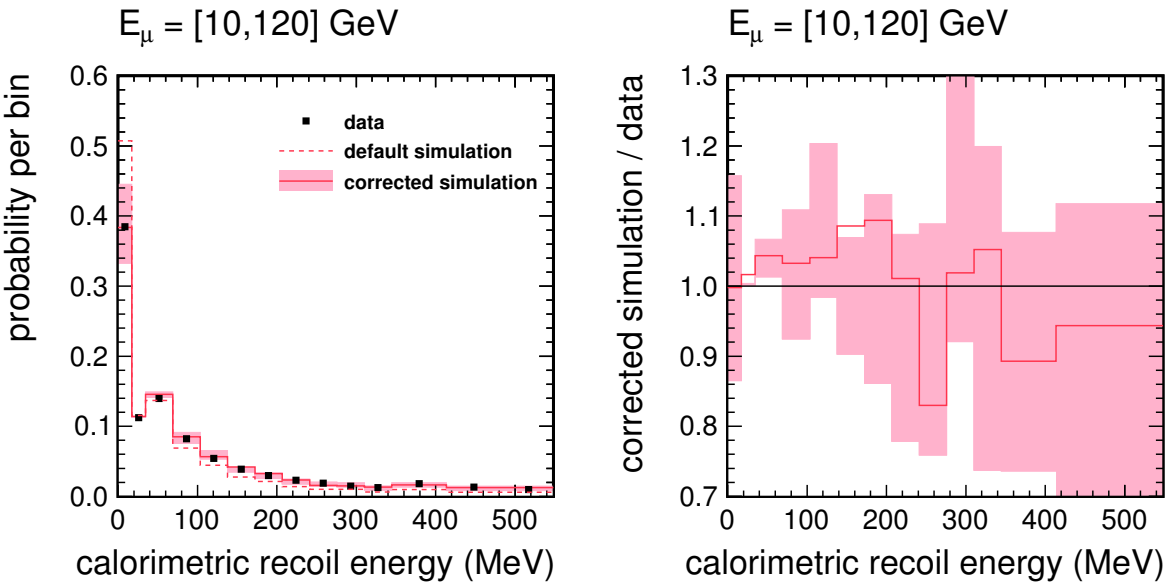

FIG. 7.13: Calorimetric off-track energy for rock muons of energy, $E_\mu > 10\,\text{GeV}$, area normalized to unity (left) and ratio of corrected simulation to data (right). Corrected simulation is plotted with systematic uncertainty; data and default simulation are plotted without uncertainty. Deviations of the central value of the corrected simulation outside the systematic uncertainty band arise from the stochastic nature of the correction.

7.10 Interaction rates and acceptance corrections

The systematic uncertainty summaries for the extracted cross sections and fluxes are reserved until Chapter 8; the uncertainties on the reconstructed interaction rates and acceptance corrections are presented here for the focused samples and in Appendix C for neutrinos in the reverse horn current (RHC), antineutrino-focusing beam and Appendix D for antineutrinos in the forward horn current (FHC), neutrino-focusing beam.

FIG. 7.14 – 7.17 show the systematic and statistical uncertainties of the reconstructed neutrino interaction rates in the forward horn current (FHC) beam for the inclusive sample and the three samples with ν cuts. FIG. 7.18 – 7.21 show the equivalent for antineutrinos in the reverse horn current (RHC) beam. Systematic uncertainties are dominated by the flux at high energies. At low energies, GENIE and reconstruction systematics become more prominent.

FIG. 7.22 – 7.25 show the systematic and statistical uncertainties of the acceptance correction for FHC neutrinos for the inclusive sample and the three samples with ν cuts. FIG. 7.26 – 7.29 show the equivalent for RHC antineutrinos. Flux uncertainties mostly cancel in the acceptance ratio, affecting the numerator and denominator equally. Acceptance correction uncertainties are driven by GENIE and recoil reconstruction, which affect migration over the ν cuts.

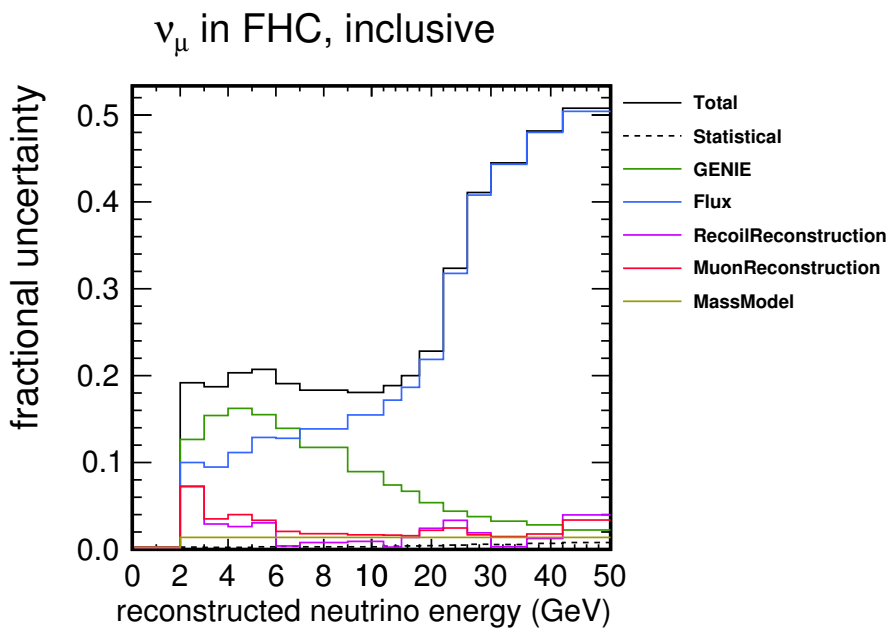

FIG. 7.14: Total systematic and statistical uncertainties of the reconstructed inclusive neutrino interaction rate in the forward horn current (FHC) beam (FIG. 6.3).

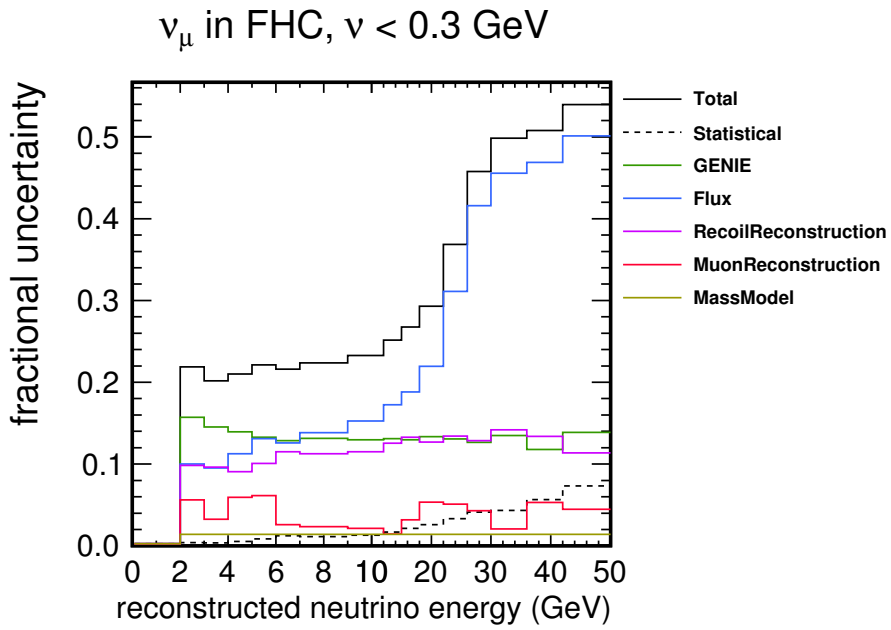

FIG. 7.15: Total systematic and statistical uncertainties of the reconstructed neutrino interaction rate for events with $\nu < 300\,\mathrm{MeV}$ in the forward horn current (FHC) beam (FIG. 6.4).

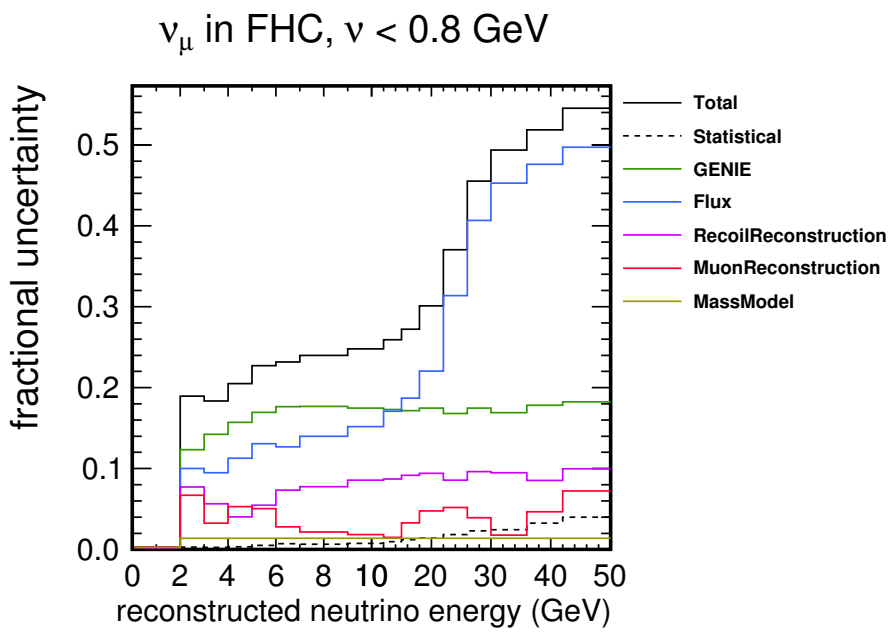

FIG. 7.16: Total systematic and statistical uncertainties of the reconstructed neutrino interaction rate for events with $\nu < 800\,\text{MeV}$ in the forward horn current (FHC) beam (FIG. 6.5).

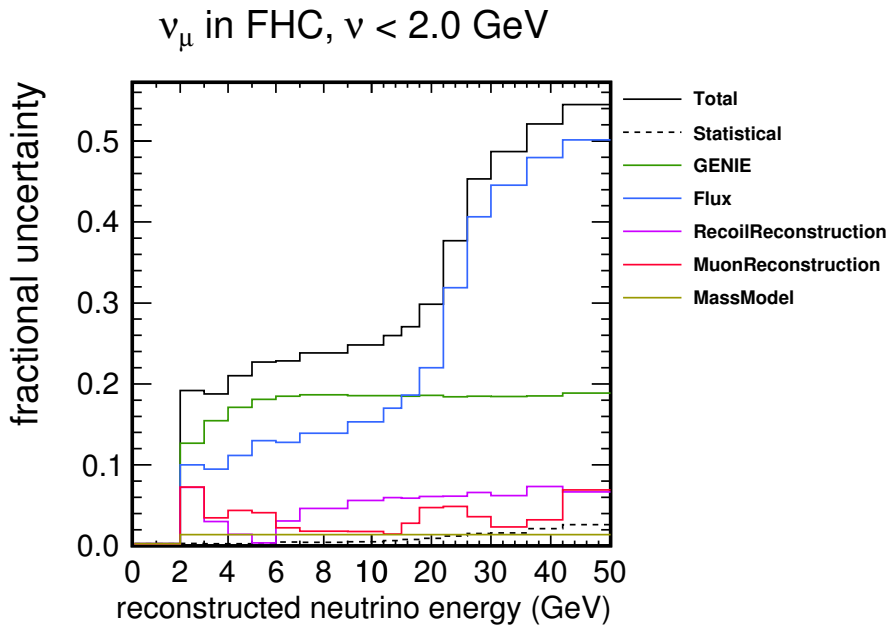

FIG. 7.17: Total systematic and statistical uncertainties of the reconstructed neutrino interaction rate for events with $\nu < 2\,\text{GeV}$ in the forward horn current (FHC) beam (FIG. 6.6).

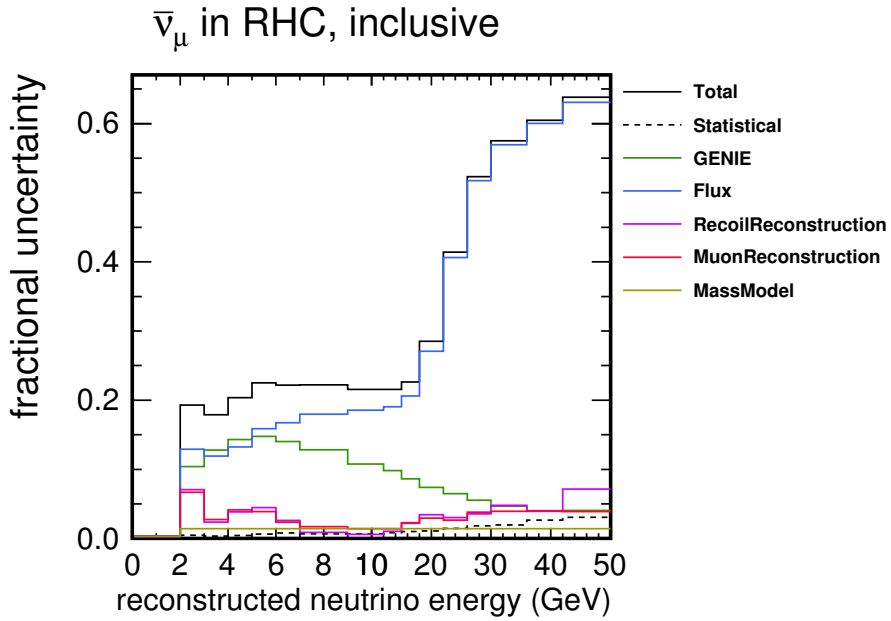

FIG. 7.18: Total systematic and statistical uncertainties of the reconstructed inclusive antineutrino interaction rate in the reverse horn current (RHC) beam (FIG. 6.7).

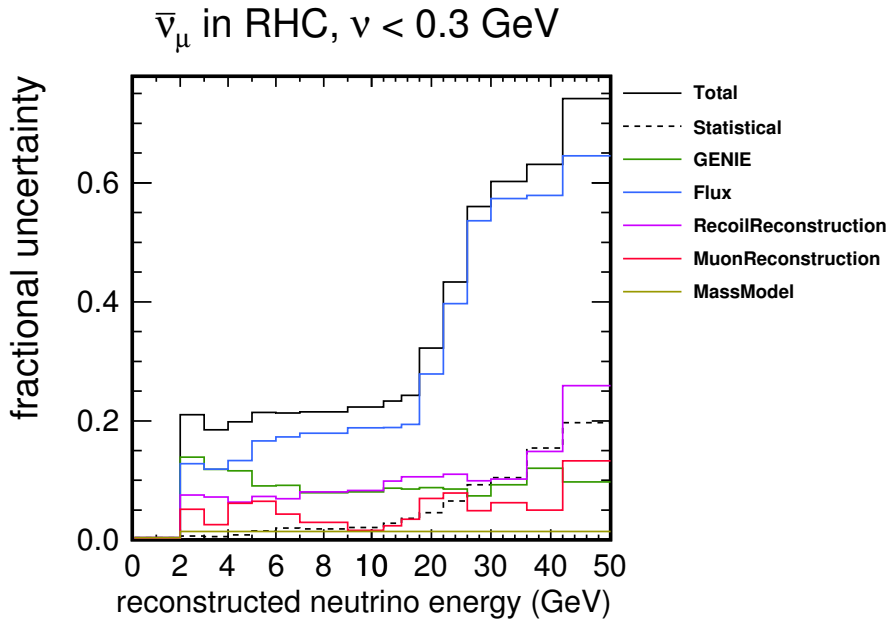

FIG. 7.19: Total systematic and statistical uncertainties of the reconstructed antineutrino interaction rate for events with $\nu < 300\,\text{MeV}$ in the reverse horn current (RHC) beam (FIG. 6.8).

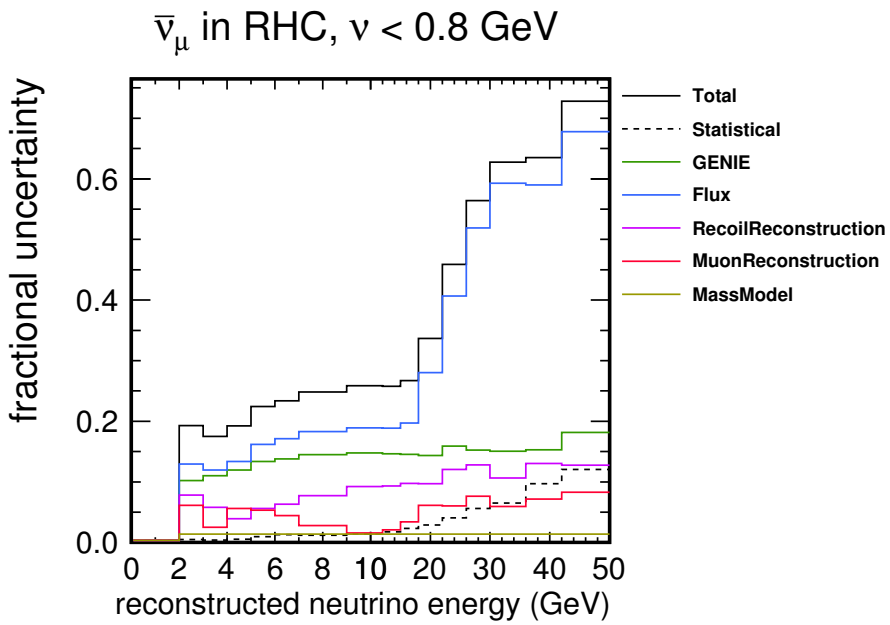

FIG. 7.20: Total systematic and statistical uncertainties of the reconstructed antineutrino interaction rate for events with $\nu < 800\,\text{MeV}$ in the reverse horn current (RHC) beam (FIG. 6.9).

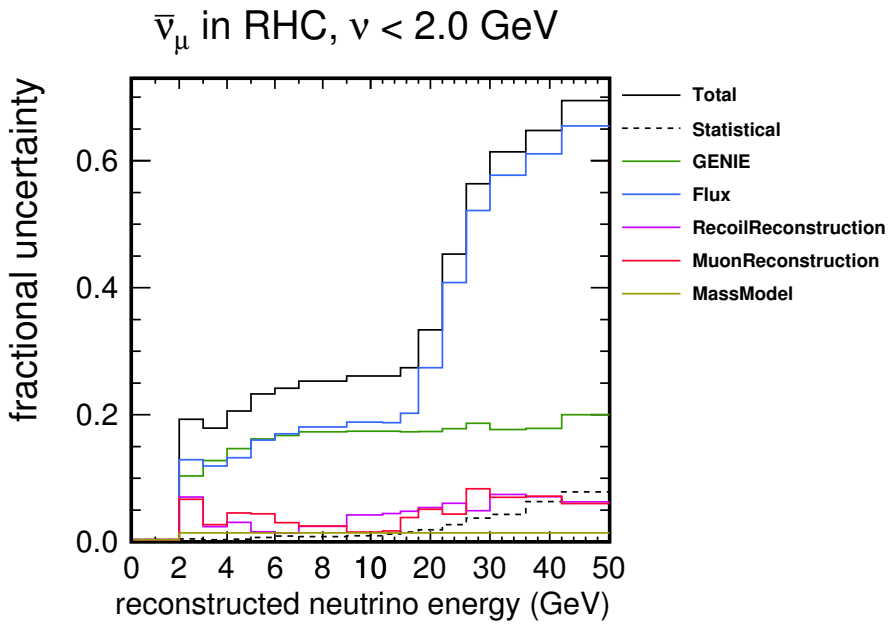

FIG. 7.21: Total systematic and statistical uncertainties of the reconstructed antineutrino interaction rate for events with $\nu < 2\,\text{GeV}$ in the reverse horn current (RHC) beam (FIG. 6.10).

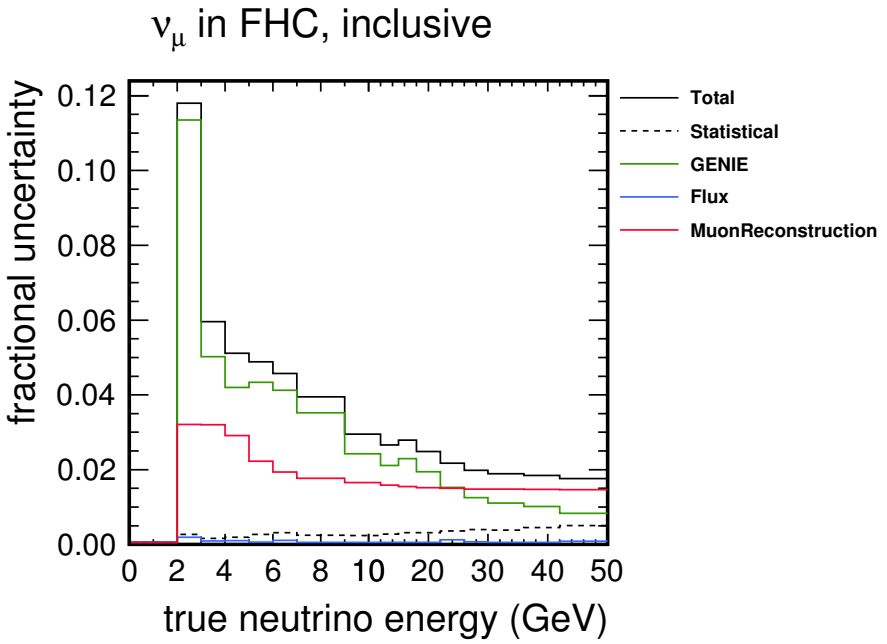

FIG. 7.22: Total systematic and statistical uncertainties of the inclusive acceptance for neutrino interactions in the forward horn current (FHC) beam (FIG. 6.15).

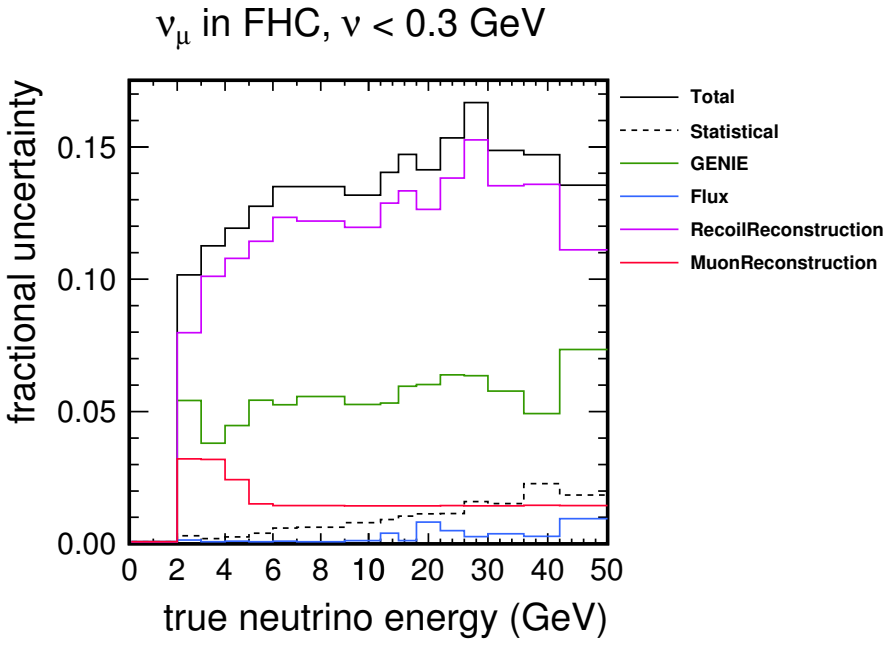

FIG. 7.23: Total systematic and statistical uncertainties of the acceptance for neutrino interactions with $\nu < 300\,\mathrm{MeV}$ in the forward horn current (FHC) beam (FIG. 6.15).

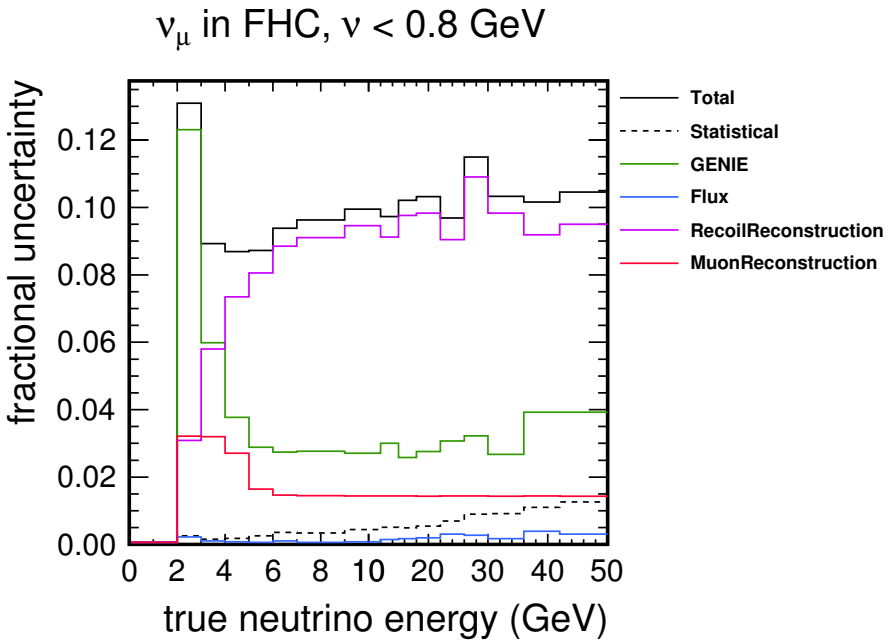

FIG. 7.24: Total systematic and statistical uncertainties of the acceptance for neutrino interactions with $\nu < 800\,\text{MeV}$ in the forward horn current (FHC) beam (FIG. 6.15).

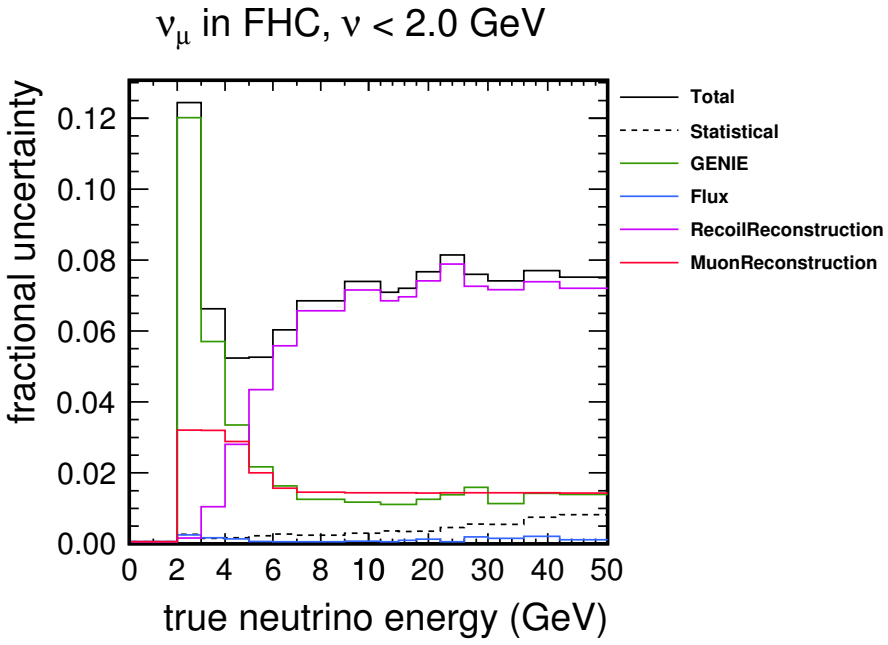

FIG. 7.25: Total systematic and statistical uncertainties of the acceptance for neutrino interactions with $\nu < 2\,\text{GeV}$ in the forward horn current (FHC) beam (FIG. 6.15).

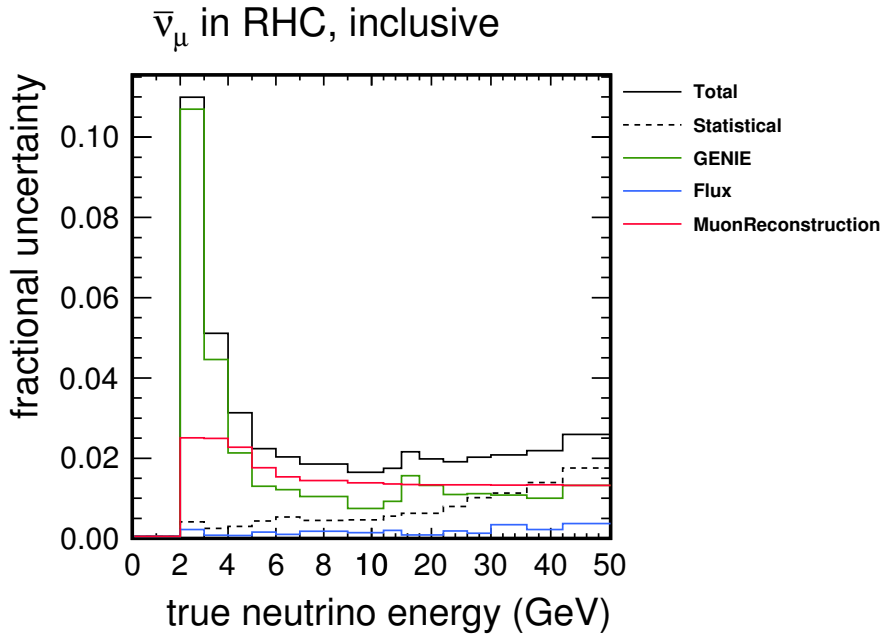

FIG. 7.26: Total systematic and statistical uncertainties of the inclusive acceptance for antineutrino interactions in the reverse horn current (RHC) beam (FIG. 6.16).

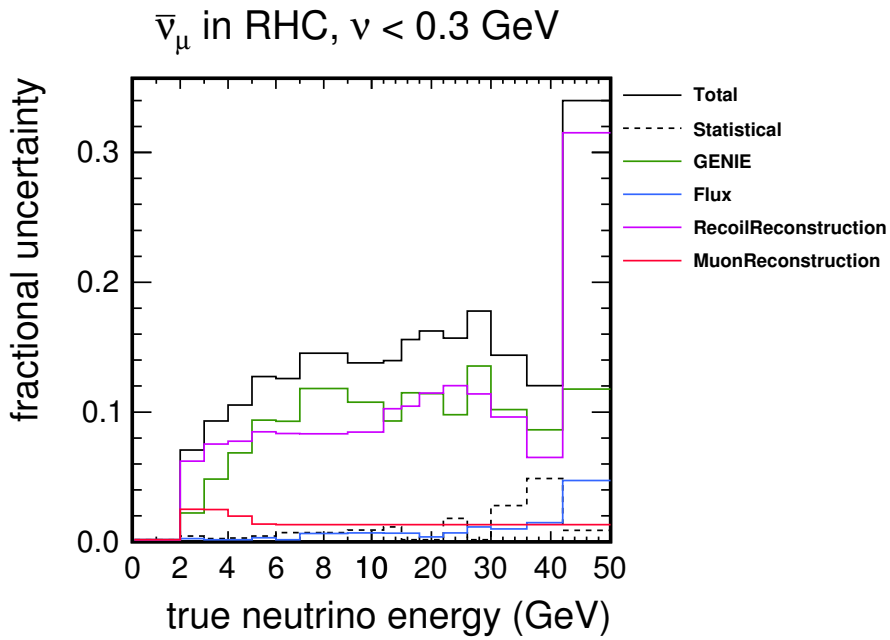

FIG. 7.27: Total systematic and statistical uncertainties of the acceptance for antineutrino interactions with $\nu < 300\,\text{MeV}$ in the reverse horn current (RHC) beam (FIG. 6.16).

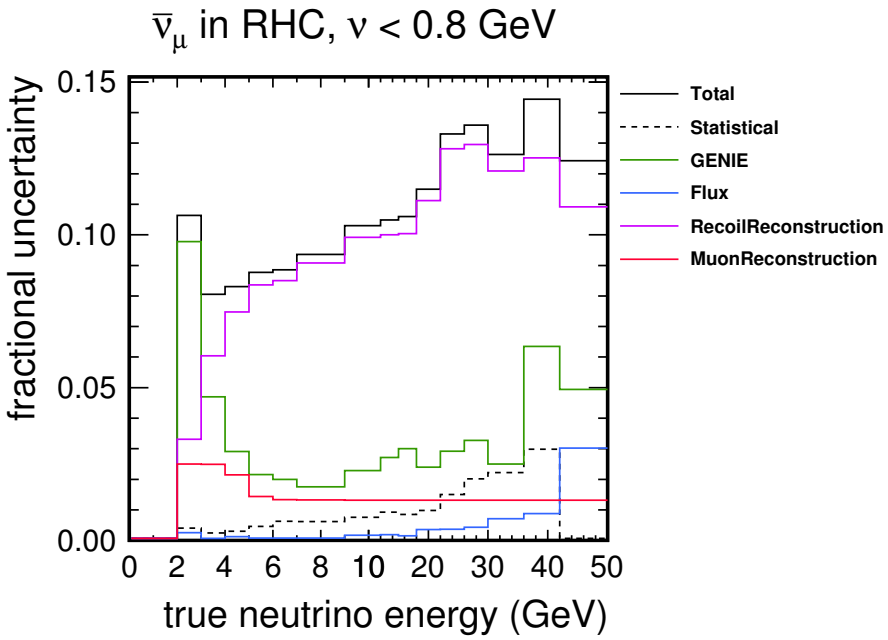

FIG. 7.28: Total systematic and statistical uncertainties of the acceptance for antineutrino interactions with $\nu < 800\,\text{MeV}$ in the reverse horn current (RHC) beam (FIG. 6.16).

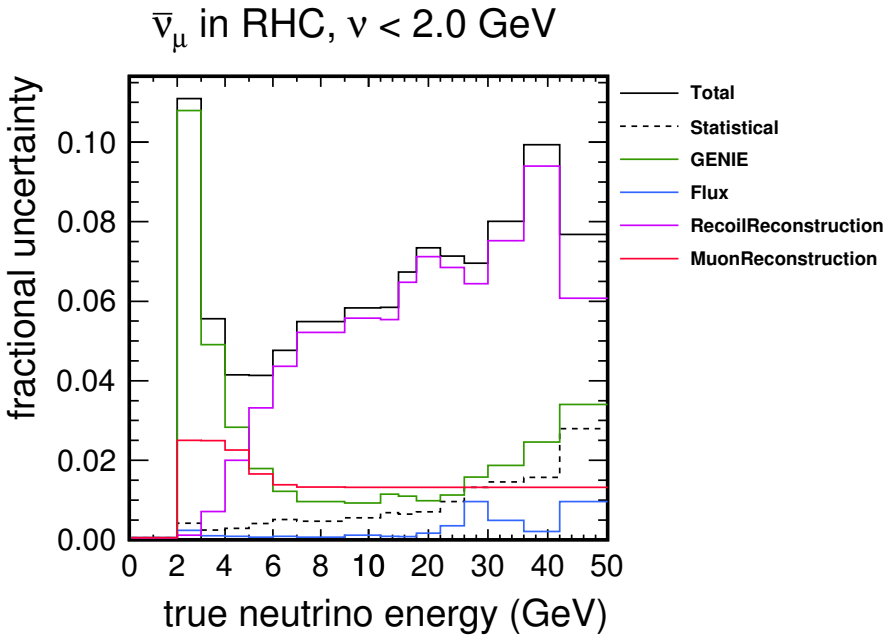

FIG. 7.29: Total systematic and statistical uncertainties of the acceptance for antineutrino interactions with $\nu < 2\,\text{GeV}$ in the reverse horn current (RHC) beam (FIG. 6.16).

CHAPTER 8

Results

8.1 Overview

The low-ν analysis results in a shape measurement of the neutrino flux and charged-current inclusive cross section, with the absolute normalization set by an external constraint. The choice of external constraint is effectively arbitrary. For the results presented in this chapter, the constraint is the neutrino or antineutrino cross section derived from the GENIE neutrino interaction simulation in the 9–12 GeV bin. Chapter 9 presents an alternative result, normalized to the neutrino cross section measured by the NOMAD experiment.

To be specific, the measured cross sections are for a ν_μ or $\bar{\nu}_\mu$ interacting via a charged-current in any channel (QE, resonance, DIS, etc. [Chapter 1]). The cross sections are normalized to a single nucleon. For this chapter, the target is the MINERνA tracking region, consisting of 87.6% carbon, 7.4% hydrogen, 3.2% oxygen and 1.8% miscellaneous by mass[4]. 81.9% of the tracking region is active scintillator. The target consists of 2.232×10^{30} nucleons, with a 15% excess of protons over neutrons. The NOMAD-normalized result

presented in Chapter 9 includes an isoscalar correction for this. The cross sections derived from the simulation (GENIE) are on the MINERνA tracking region for this chapter and on C^{12} for Chapter 9.

The extracted neutrino fluxes provide a valuable constraint to complement other methods of flux determination. The existing flux is based on a simulation of the NuMI beamline, reweighted using hadron production data from proton collisions on thin carbon targets[40]. An additional constraint is provided by measurements of neutrino-electron elastic scattering[14], $\nu_X + e \rightarrow \nu_X + e$, where X is either e, μ or τ. All channels can proceed via a neutral current; only the electron channel can proceed via a charged current. Since this is a purely leptonic process, the cross section is known to the order of 1% and the total neutrino flux (all flavors) integrated over energy can be determined by a measurement of the interaction rate.

Table 8.1 displays the total protons on target (POT) recorded in data and simulated for the two beam configurations. The data was recorded between March 2010 and April 2012. The forward horn current (FHC) data includes run periods 1, 7, 9 and 13. The reverse horn current (RHC) data is run period 5.

Beam configuration	Data POT	Simulation POT
Forward horn current (FHC)	3.175e+20	2.061e+21
Reverse horn current (RHC)	1.091e+20	9.974e+20

TABLE 8.1: Total protons on target (POT) in data and simulation for the two beam configurations. Forward horn current (FHC) primarily focuses neutrinos. Reverse horn current (RHC) primarily focuses antineutrinos.

8.2 Neutrino cross section

FIG. 8.1 shows the extracted cross section for neutrinos in the forward horn current (FHC), neutrino-focusing beam. As a cross-check, the analysis can be performed on the neutrino sample in the reverse horn current (RHC), antineutrino-focusing beam (FIG. 8.2).

In the RHC beam, the polarity of the MINOS magnet is set to focus antimuons (μ^+) in to the coil, with muons (μ^-) defocused out of the detector. This results in a different acceptance correction (compare FIG. 6.15 to FIG. C.9). The defocused sample also includes some background (FIG. C.2 – C.5) from misidentified muon charge in MINOS. In the focused sample, backgrounds are negligible. Despite the differences, the two extracted cross sections are within statistical uncertainties; FIG. 8.3 shows the RHC/FHC ratio.

Table 8.2 lists the normalization factors, $\eta' \equiv 1/\eta$, for the three ν cuts and two beam configurations (Section 6.4.5). The observation of $\eta' < 1$ indicates that the data prefers a lower low-ν cross section, $\sigma_\nu \equiv \sigma(\nu < \nu_0, E)$, than modeled in GENIE (FIG. 6.17). The RHC normalization factors, η', are greater than the FHC factors, though the relative magnitude between ν cuts is comparable.

Table 8.3 lists the extracted cross section for FHC neutrinos (FIG. 8.1) in tabular form. The extracted cross section for neutrinos agrees with the GENIE model within uncertainties. For the FHC result, a χ^2 comparison between data and simulation results in $\chi^2/\text{ndf} = 4.03/15 = 0.27$; for the RHC result, $\chi^2/\text{ndf} = 2.40/15 = 0.16$. Both the FHC and RHC results have similar features at high neutrino energy, with a point at 26–30 GeV at the limit of the uncertainties. The cross section is well measured by other experiments at these energies, so this likely arises from a systematic uncertainty in the analysis. The feature is also present in the antineutrino cross sections presented in the following section.

The fractional statistical and systematic uncertainties for FHC neutrinos are shown in FIG. 8.4 – 8.6. The equivalent for RHC neutrinos are shown in FIG. 8.7 – 8.9. Other than the first bin (2–3 GeV), the uncertainty is dominated by the 6.5% normalization uncertainty of the external constraint (GENIE in the 9–12 GeV bin). In the first bin, GENIE model uncertainties and recoil reconstruction each contribute approximately 10%. By definition, the systematic uncertainties collapse in the 9–12 GeV bin as the cross section is normalized independently in all universes of the many-universes uncertainty band.

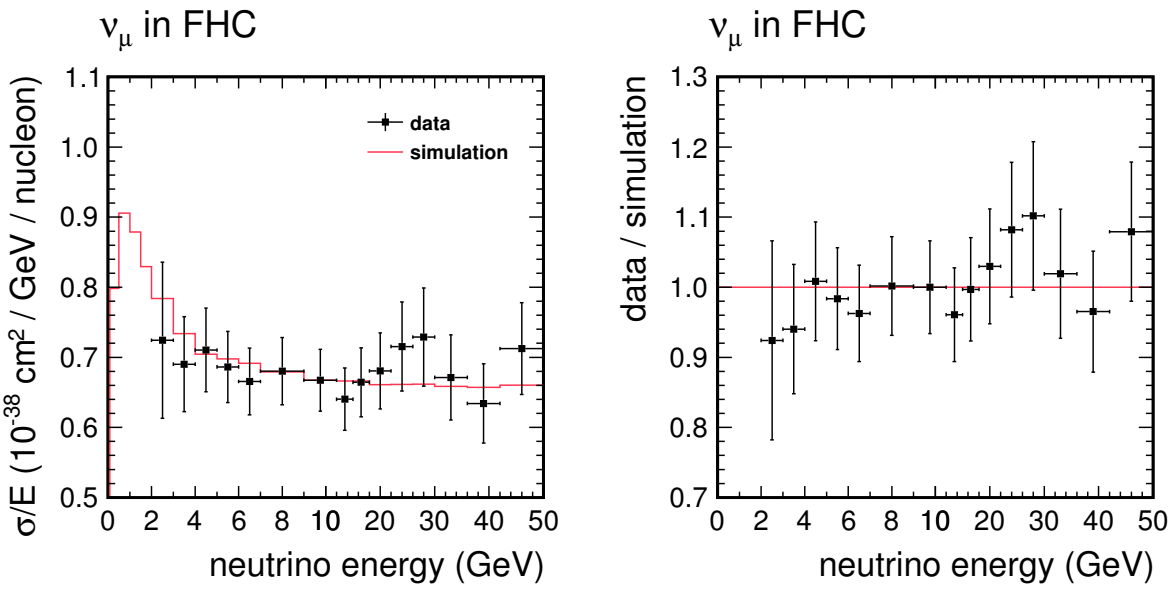

FIG. 8.1: Extracted cross section (left) and ratio of data to simulation (right) for neutrinos in the forward horn current (FHC), neutrino-focusing beam. The extracted cross section is normalized to the simulation in the 9–12 GeV bin. Data are plotted with statistical and systematic uncertainties.

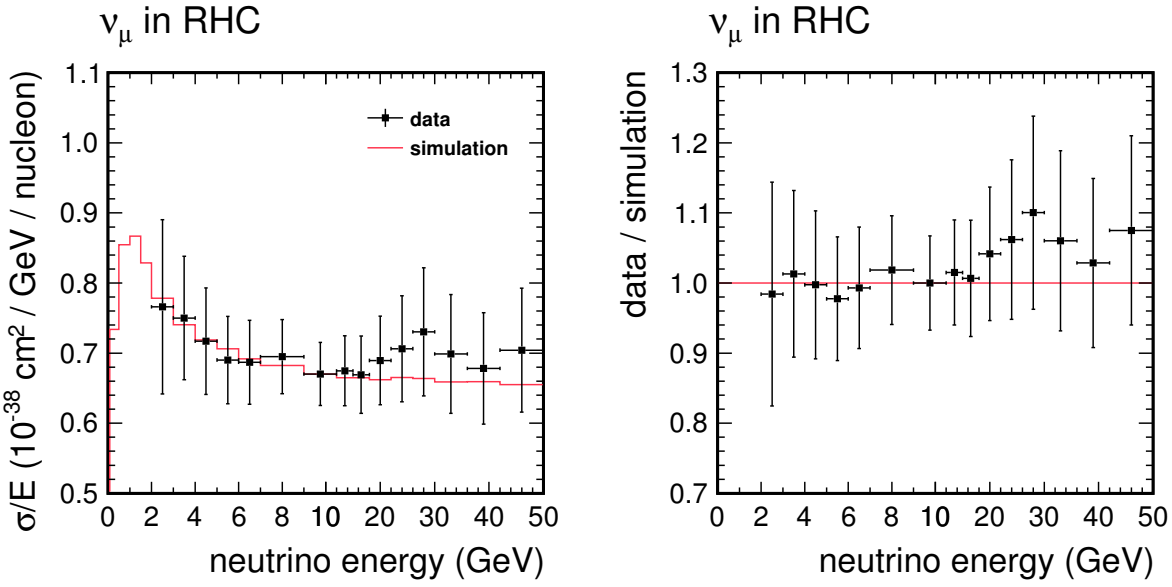

FIG. 8.2: Extracted cross section (left) and ratio of data to simulation (right) for neutrinos in the reverse horn current (RHC), antineutrino-focusing beam. The extracted cross section is normalized to the simulation in the 9–12 GeV bin. Data are plotted with statistical and systematic uncertainties.

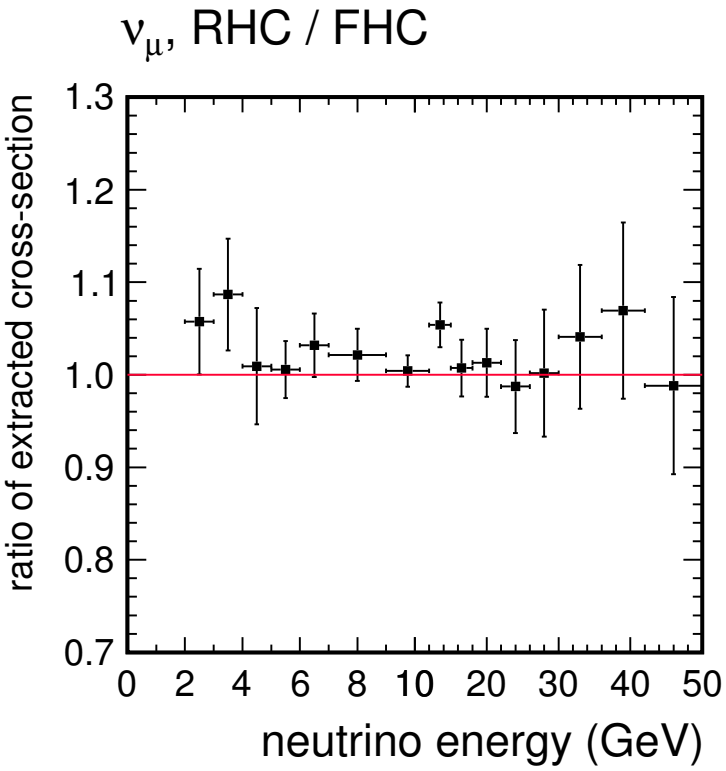

FIG. 8.3: Ratio of extracted cross section for neutrinos in the reverse horn current (RHC) beam (FIG. 8.2) to forward horn current (FHC) beam (FIG. 8.1). Plotted with statistical uncertainties only.

ν cut	FHC ν_μ	RHC ν_μ
$\nu < 2\,\text{GeV}$	0.925 ± 0.009	0.952 ± 0.014
$\nu < 800\,\text{MeV}$	0.958 ± 0.009	0.993 ± 0.014
$\nu < 300\,\text{MeV}$	0.946 ± 0.012	1.001 ± 0.022

TABLE 8.2: Normalization factor, $\eta' \equiv 1/\eta$, and statistical uncertainty for neutrinos in the forward horn current (FHC) and reverse horn current (RHC) beams. $\eta' < 1$ indicates that the result favors a lower low-ν cross section, $\sigma_\nu \equiv \sigma(\nu < \nu_0, E)$, than modeled in GENIE (FIG. 6.17).

E bin (GeV)	$\langle E \rangle$ (GeV)	$\sigma(E)/E$	Stat. error	Syst. error	Total error
			(10^{-38} cm^2 / GeV / nucleon)		
2–3	2.63	0.724	0.006	0.111	0.111
3–4	3.51	0.690	0.006	0.067	0.068
4–5	4.44	0.710	0.011	0.059	0.060
5–6	5.47	0.686	0.008	0.050	0.051
6–7	6.49	0.666	0.010	0.046	0.048
7–9	7.97	0.680	0.010	0.047	0.048
9–12	10.45	0.667	0.007	0.044	0.044
12–15	13.45	0.640	0.008	0.044	0.045
15–18	16.43	0.664	0.010	0.048	0.049
18–22	19.90	0.681	0.013	0.053	0.054
22–26	23.88	0.715	0.019	0.061	0.064
26–30	27.88	0.729	0.026	0.065	0.070
30–36	32.80	0.671	0.024	0.056	0.061
36–42	38.87	0.634	0.030	0.048	0.057
42–50	45.72	0.713	0.038	0.053	0.066

TABLE 8.3: Extracted cross section and statistical, systematic and total uncertainties for neutrinos in the forward horn current (FHC), neutrino-focusing beam (FIG. 8.1). $\langle E \rangle$ is the flux-averaged neutrino energy per bin. The covariance matrix is tabulated in Table 8.4.

	2–3	3–4	4–5	5–6	6–7	7–9	9–12	12–15	15–18	18–22	22–26	26–30	30–36	36–42	42–50
2–3	12.407	4.043	0.049	-0.572	-0.162	0.247	-0.000	-0.603	-1.085	-1.247	-1.676	-2.185	-1.416	-0.835	-0.226
3–4	4.043	4.581	0.892	0.205	0.169	0.212	-0.000	-0.301	-0.470	-0.588	-0.772	-1.002	-0.709	-0.511	-0.371
4–5	0.049	0.892	3.563	0.617	0.342	0.185	-0.000	-0.075	0.136	0.170	0.262	0.241	0.086	-0.048	-0.138
5–6	-0.572	0.205	0.617	2.573	0.255	0.143	0.000	-0.031	0.101	0.083	0.125	0.108	-0.020	-0.070	-0.137
6–7	-0.162	0.169	0.342	0.255	2.262	0.122	-0.000	-0.040	0.018	-0.022	-0.019	-0.063	-0.116	-0.107	-0.144
7–9	0.247	0.212	0.185	0.143	0.122	2.286	-0.000	-0.073	-0.038	-0.088	-0.128	-0.184	-0.191	-0.141	-0.108
9–12	-0.000	-0.000	-0.000	0.000	-0.000	-0.000	1.951	-0.000	0.000	-0.000	-0.000	-0.000	-0.000	0.000	-0.000
12–15	-0.603	-0.301	-0.075	-0.031	-0.040	-0.073	-0.000	1.986	0.111	0.139	0.194	0.280	0.221	0.157	0.089
15–18	-1.085	-0.470	0.136	0.101	0.018	-0.038	0.000	0.111	2.407	0.466	0.628	0.752	0.523	0.339	0.283
18–22	-1.247	-0.588	0.170	0.083	-0.022	-0.088	-0.000	0.139	0.466	2.937	0.968	1.131	0.815	0.538	0.492
22–26	-1.676	-0.772	0.262	0.125	-0.019	-0.128	-0.000	0.194	0.628	0.968	4.033	1.585	1.137	0.744	0.652
26–30	-2.185	-1.002	0.241	0.108	-0.063	-0.184	-0.000	0.280	0.752	1.131	1.585	4.920	1.393	0.917	0.775
30–36	-1.416	-0.709	0.086	-0.020	-0.116	-0.191	-0.000	0.221	0.523	0.815	1.137	1.393	3.682	0.700	0.600
36–42	-0.835	-0.511	-0.048	-0.070	-0.107	-0.141	0.000	0.157	0.339	0.538	0.744	0.917	0.700	3.205	0.455
42–50	-0.226	-0.371	-0.138	-0.137	-0.144	-0.108	-0.000	0.089	0.283	0.492	0.652	0.775	0.600	0.455	4.295

TABLE 8.4: Covariance matrix for the extracted cross section for neutrinos in the forward horn current (FHC) beam (Table 8.3). The bin boundaries are in units of GeV. The covariance elements are in units of 10^{-38} cm^2 / GeV / nucleon and scaled by a factor of 10^3.

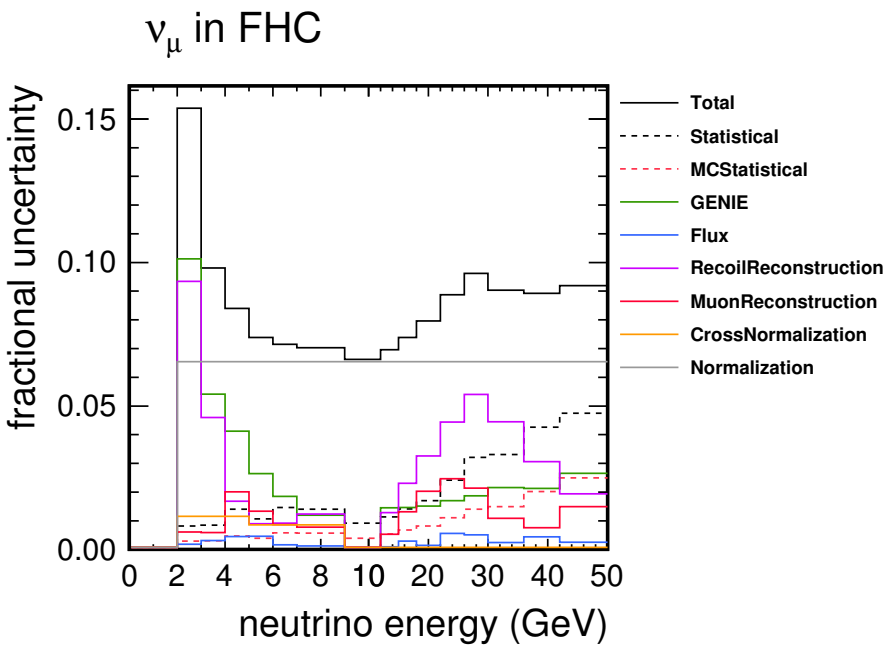

FIG. 8.4: Total systematic and statistical uncertainties of the extracted cross section for neutrinos in the forward horn current (FHC) beam (FIG. 8.1).

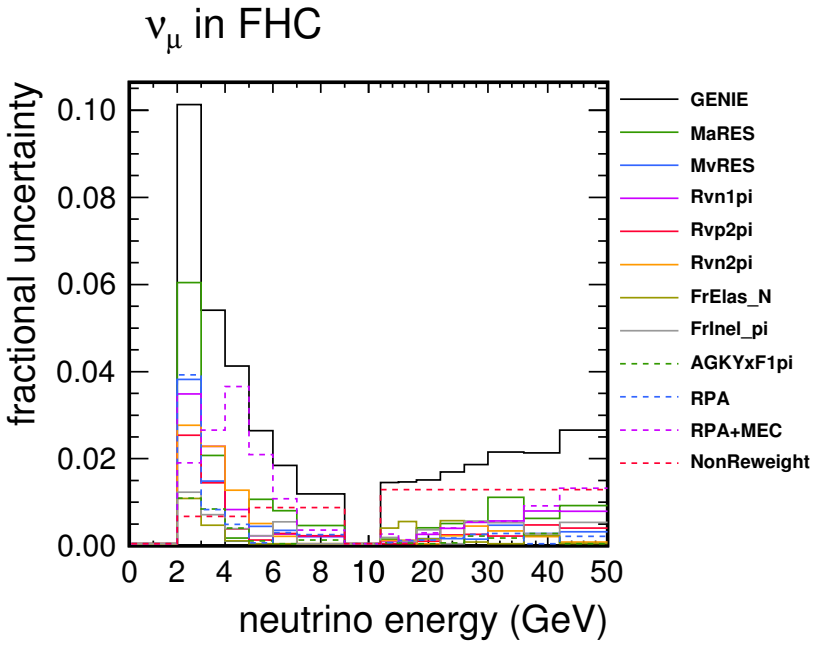

FIG. 8.5: GENIE cross section model uncertainties of the extracted cross section for neutrinos in the forward horn current (FHC) beam (FIG. 8.1).

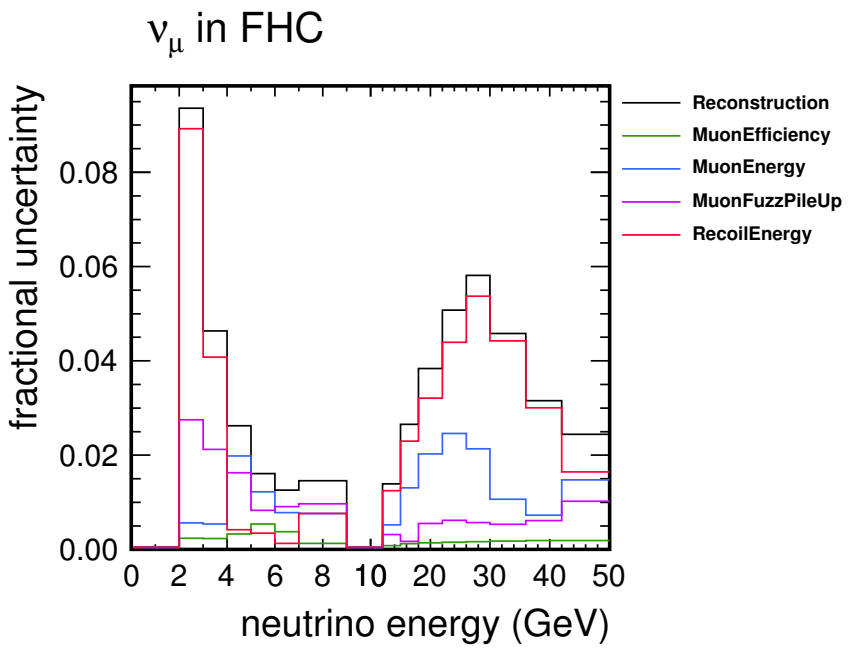

FIG. 8.6: Reconstruction uncertainties of the extracted cross section for neutrinos in the forward horn current (FHC) beam (FIG. 8.1).

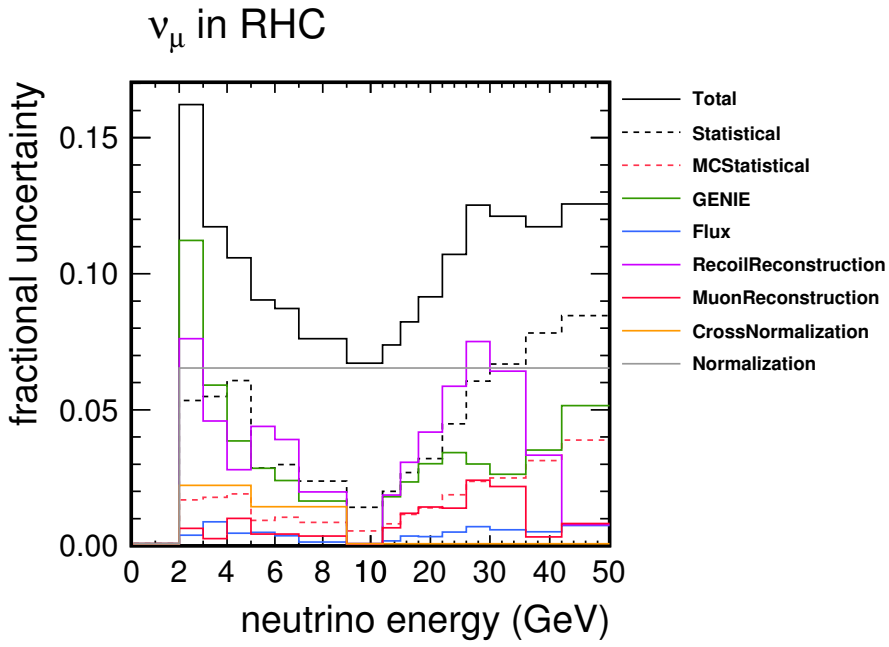

FIG. 8.7: Total systematic and statistical uncertainties of the extracted cross section for neutrinos in the reverse horn current (RHC) beam (FIG. 8.2).

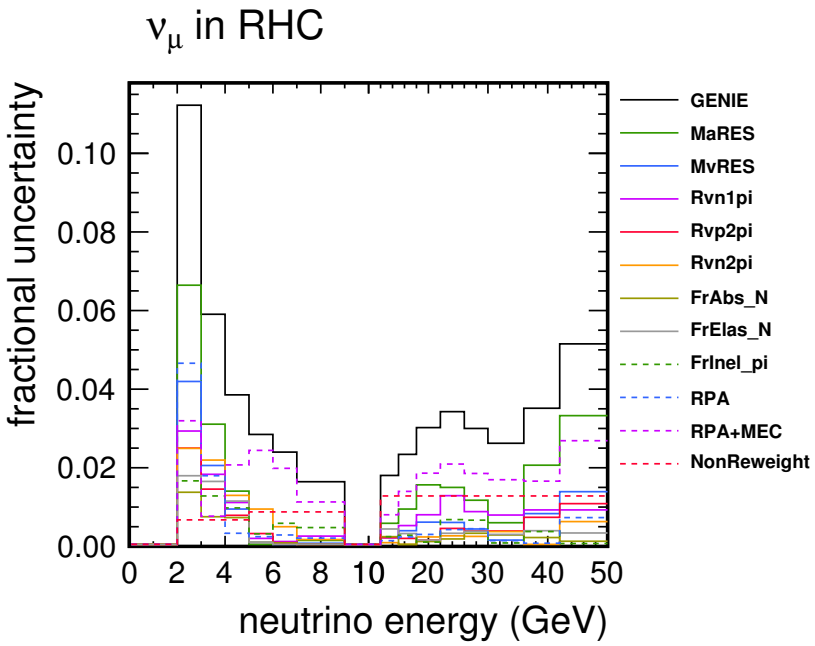

FIG. 8.8: GENIE cross section model uncertainties of the extracted cross section for neutrinos in the reverse horn current (RHC) beam (FIG. 8.2).

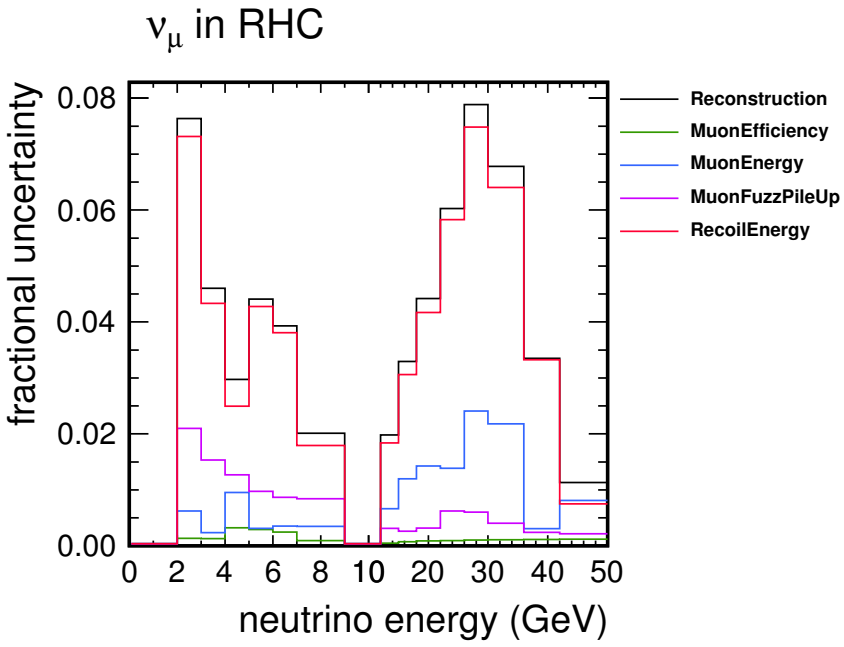

FIG. 8.9: Reconstruction uncertainties of the extracted cross section for neutrinos in the reverse horn current (RHC) beam (FIG. 8.2).

8.3 Antineutrino cross section

FIG. 8.10 shows the extracted cross section for antineutrinos in the reverse horn current (RHC), antineutrino-focusing beam. As a cross-check, the analysis is performed on the defocused sample; FIG. 8.11 shows the extracted cross section for antineutrinos in the forward horn current (FHC), neutrino-focusing beam. The FHC/RHC ratio is shown in FIG. 8.12. Despite the different acceptance corrections of the two samples (compare FIG. 6.16 to FIG. D.9), the two cross sections agree within statistical uncertainties validating the acceptance model in the simulation.

Table 8.5 lists the normalization factors, $\eta' \equiv 1/\eta$, for the three ν cuts and two beam configurations. $\eta' < 1$ indicates that the data prefers a lower low-ν cross section, $\sigma_\nu \equiv \sigma(\nu < \nu_0, E)$, than modeled in GENIE; $\eta' > 1$ indicates the opposite. Other than the lowest ν cut, the normalization factors derived from the two beam configurations agree within statistical uncertainties.

Table 8.6 lists the extracted cross section for RHC antineutrinos (FIG. 8.10) in tabular form. The extracted cross section for antineutrinos agrees with the GENIE model within uncertainties. For the RHC result, a χ^2 comparison between data and simulation results in $\chi^2/\text{ndf} = 3.59/15 = 0.24$; for the FHC result, $\chi^2/\text{ndf} = 1.80/15 = 0.12$. Similar to the neutrino cross sections, a shape is observed at high neutrino energy, peaking at 26–30 GeV, resulting from some systematic uncertainty. The existing uncertainty covers the discrepancy.

The fractional statistical and systematic uncertainties for RHC antineutrinos are shown in FIG. 8.13 – 8.15. The equivalent for FHC antineutrinos are shown in FIG. 8.16 – 8.18. The uncertainty is dominated by the 10.6% normalization uncertainty resulting from the cross section derived from GENIE in the 9–12 GeV bin. As with neutrinos, GENIE model uncertainties and recoil reconstruction are large at low neutrino energy.

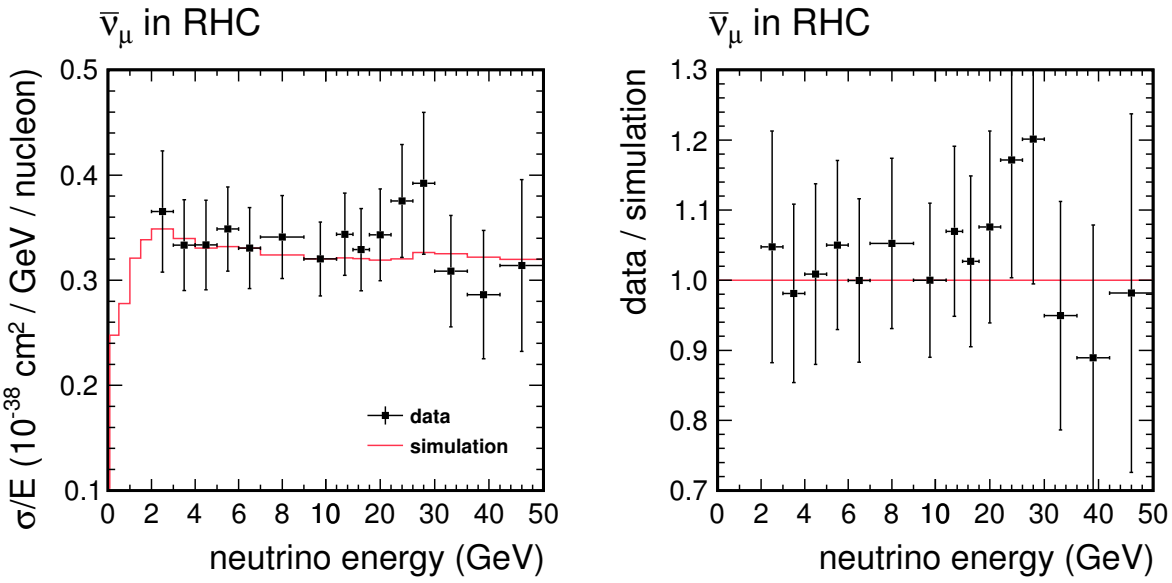

FIG. 8.10: Extracted cross section (left) and ratio of data to simulation (right) for antineutrinos in the reverse horn current (RHC), antineutrino-focusing beam. The extracted cross section is normalized to the simulation in the 9–12 GeV bin. Data are plotted with statistical and systematic uncertainties.

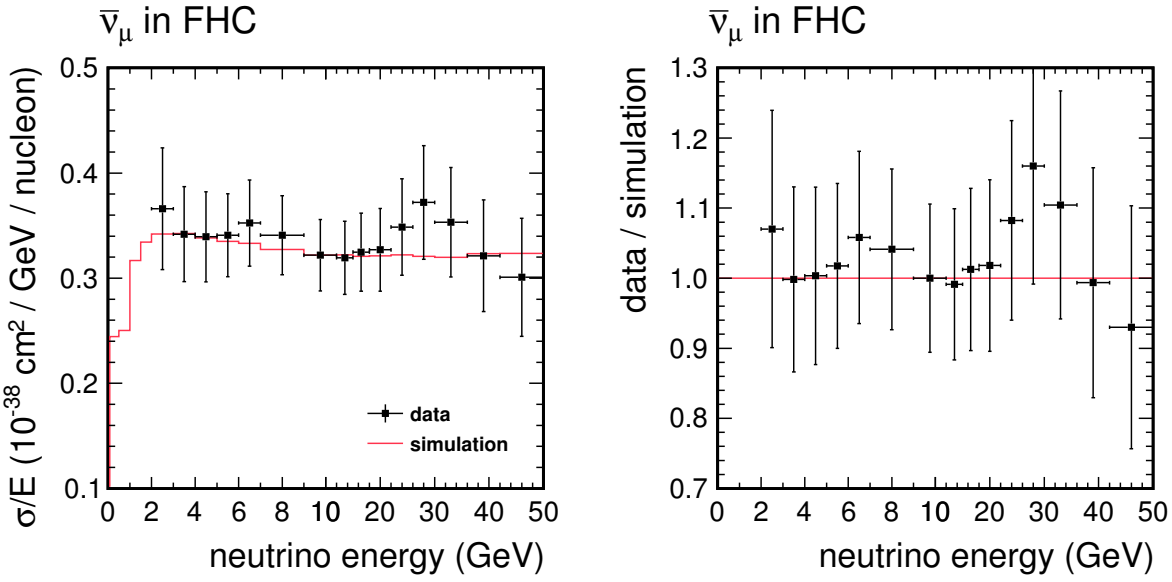

FIG. 8.11: Extracted cross section (left) and ratio of data to simulation (right) for antineutrinos in the forward horn current (FHC), neutrino-focusing beam. The extracted cross section is normalized to the simulation in the 9–12 GeV bin. Data are plotted with statistical and systematic uncertainties.

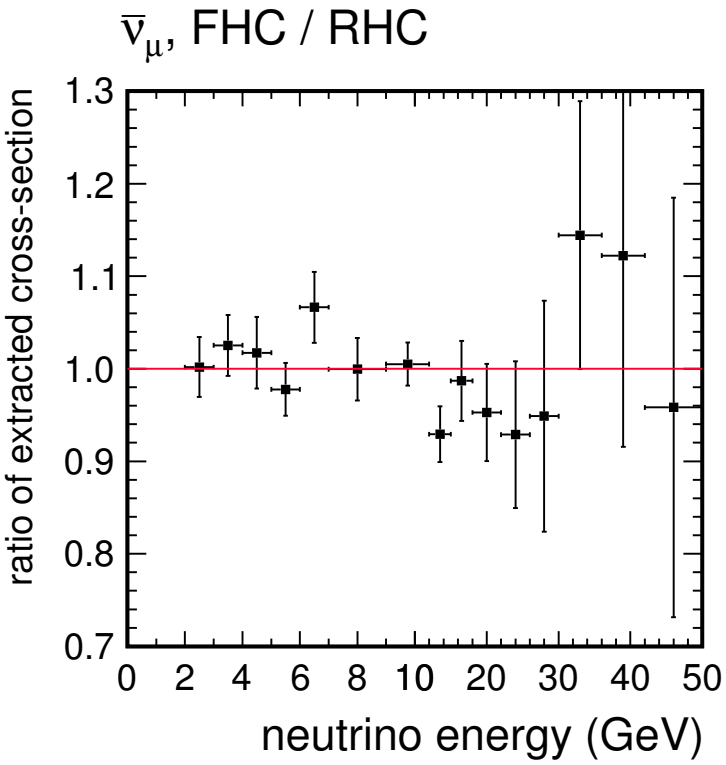

FIG. 8.12: Ratio of extracted cross section for antineutrinos in the forward horn current (FHC) beam (FIG. 8.11) to reverse horn current (RHC) beam (FIG. 8.10). Plotted with statistical uncertainties only.

ν cut	FHC $\bar{\nu}_\mu$	RHC $\bar{\nu}_\mu$
$\nu < 2\,\text{GeV}$	0.969 ± 0.012	0.943 ± 0.021
$\nu < 800\,\text{MeV}$	1.101 ± 0.012	1.085 ± 0.019
$\nu < 300\,\text{MeV}$	1.261 ± 0.014	1.200 ± 0.020

TABLE 8.5: Normalization factor, $\eta' \equiv 1/\eta$, and statistical uncertainty for antineutrinos in the forward horn current (FHC) and reverse horn current (RHC) beams. $\eta' < 1$ indicates that the result favors a lower low-ν cross section, $\sigma_\nu \equiv \sigma(\nu < \nu_0, E)$, than modeled in GENIE (FIG. 6.18); vice versa for $\eta' > 1$.

E bin (GeV)	$\langle E \rangle$ (GeV)	$\sigma(E)/E$	Stat. error	Syst. error	Total error
			(10^{-38} cm^2 / GeV / nucleon)		
2–3	2.61	0.365	0.004	0.058	0.058
3–4	3.48	0.333	0.004	0.043	0.043
4–5	4.43	0.334	0.008	0.042	0.043
5–6	5.46	0.349	0.008	0.039	0.040
6–7	6.47	0.331	0.010	0.037	0.039
7–9	7.95	0.341	0.010	0.038	0.039
9–12	10.41	0.320	0.007	0.034	0.035
12–15	13.40	0.344	0.010	0.038	0.039
15–18	16.41	0.329	0.013	0.037	0.039
18–22	19.82	0.343	0.017	0.040	0.044
22–26	23.85	0.375	0.029	0.045	0.054
26–30	27.81	0.392	0.047	0.049	0.067
30–36	32.71	0.309	0.034	0.040	0.053
36–42	38.68	0.286	0.048	0.038	0.061
42–50	45.44	0.314	0.068	0.045	0.082

TABLE 8.6: Extracted cross section and statistical, systematic and total uncertainties for antineutrinos in the reverse horn current (RHC), antineutrino-focusing beam (FIG. 8.10). $\langle E \rangle$ is the flux-averaged neutrino energy per bin. The covariance matrix is tabulated in Table 8.7.

	2–3	3–4	4–5	5–6	6–7	7–9	9–12	12–15	15–18	18–22	22–26	26–30	30–36	36–42	42–50
2–3	3.323	0.784	0.051	0.036	0.174	0.153	0.000	-0.139	-0.299	-0.458	-0.578	-0.680	-0.680	-0.580	-0.825
3–4	0.784	1.867	0.262	0.104	0.134	0.084	0.000	-0.037	-0.089	-0.164	-0.240	-0.293	-0.243	-0.195	-0.327
4–5	0.051	0.262	1.814	0.150	0.101	0.035	0.000	0.039	0.086	0.106	0.091	0.071	0.107	0.159	0.139
5–6	0.036	0.104	0.150	1.603	0.057	0.031	-0.000	0.018	0.028	0.030	0.018	-0.019	0.006	0.034	-0.016
6–7	0.174	0.134	0.101	0.057	1.484	0.044	-0.000	-0.003	-0.013	-0.022	-0.044	-0.094	-0.092	-0.030	-0.102
7–9	0.153	0.084	0.035	0.031	0.044	1.552	0.000	-0.007	-0.018	-0.032	-0.048	-0.082	-0.077	-0.042	-0.105
9–12	0.000	0.000	0.000	-0.000	-0.000	0.000	1.237	0.000	0.000	-0.000	-0.000	0.000	0.000	-0.000	-0.000
12–15	-0.139	-0.037	0.039	0.018	-0.003	-0.007	0.000	1.522	0.040	0.054	0.056	0.062	0.089	0.074	0.070
15–18	-0.299	-0.089	0.086	0.028	-0.013	-0.018	0.000	0.040	1.526	0.132	0.159	0.176	0.178	0.164	0.213
18–22	-0.458	-0.164	0.106	0.030	-0.022	-0.032	-0.000	0.054	0.132	1.908	0.294	0.301	0.251	0.292	0.374
22–26	-0.578	-0.240	0.091	0.018	-0.044	-0.048	-0.000	0.056	0.159	0.294	2.890	0.419	0.312	0.361	0.506
26–30	-0.680	-0.293	0.071	-0.019	-0.094	-0.082	0.000	0.062	0.176	0.301	0.419	4.548	0.448	0.415	0.632
30–36	-0.680	-0.243	0.107	0.006	-0.092	-0.077	0.000	0.089	0.178	0.251	0.312	0.448	2.807	0.380	0.515
36–42	-0.580	-0.195	0.159	0.034	-0.030	-0.042	-0.000	0.074	0.164	0.292	0.361	0.415	0.380	3.724	0.572
42–50	-0.825	-0.327	0.139	-0.016	-0.102	-0.105	-0.000	0.070	0.213	0.374	0.506	0.632	0.515	0.572	6.687

TABLE 8.7: Covariance matrix for the extracted cross section for antineutrinos in the reverse horn current (RHC) beam (Table 8.6). The bin boundaries are in units of GeV. The covariance elements are in units of 10^{-38} cm^2 / GeV / nucleon and scaled by a factor of 10^3.

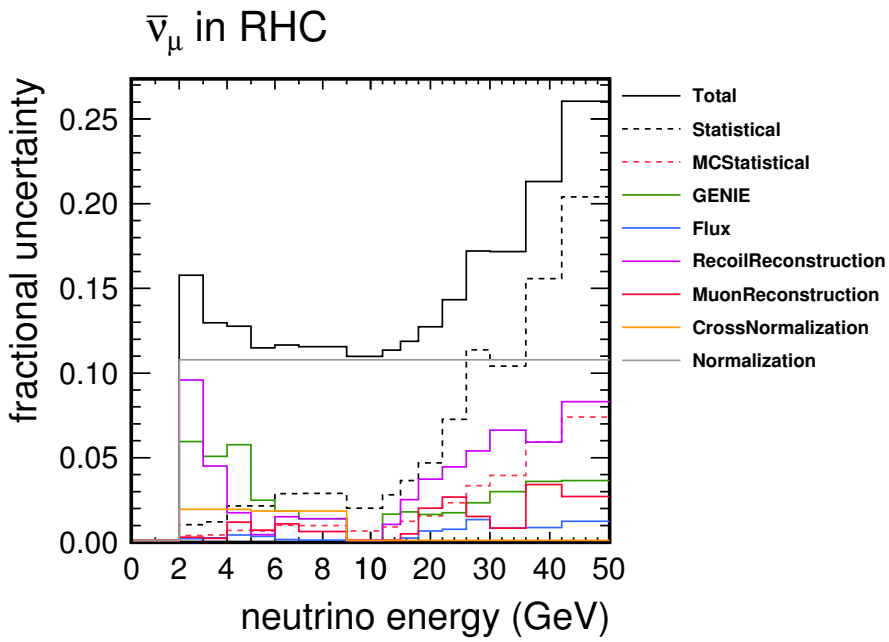

FIG. 8.13: Total systematic and statistical uncertainties of the extracted cross section for antineutrinos in the reverse horn current (RHC) beam (FIG. 8.10).

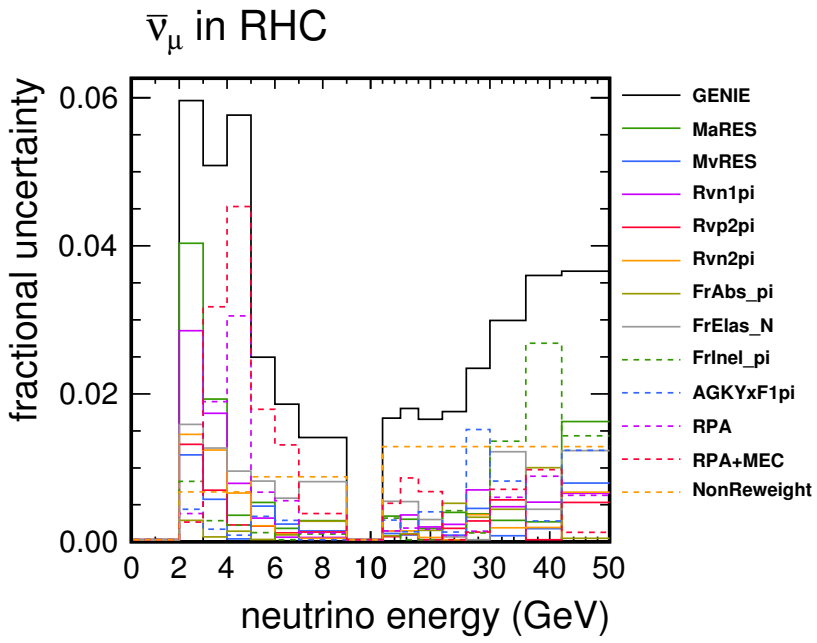

FIG. 8.14: GENIE cross section model uncertainties of the extracted cross section for antineutrinos in the reverse horn current (RHC) beam (FIG. 8.10).

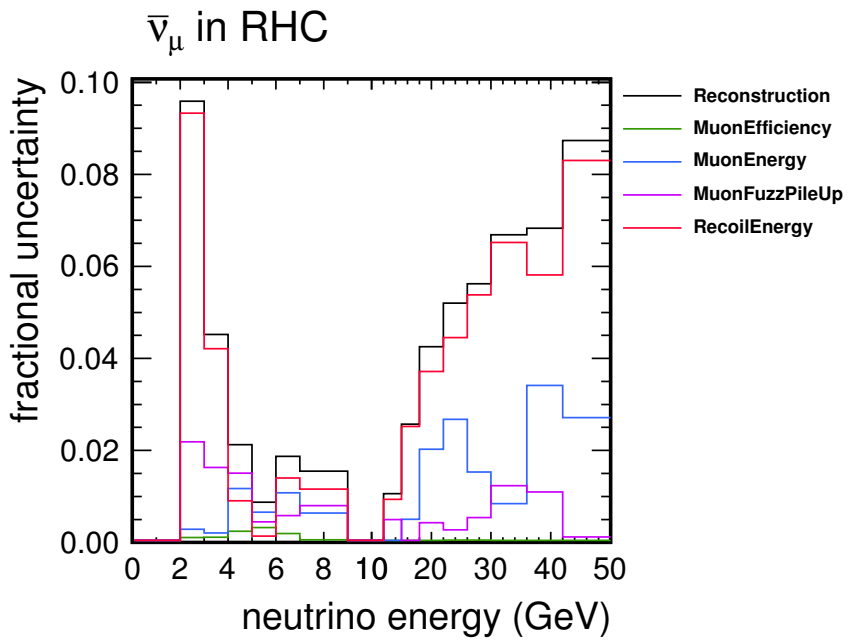

FIG. 8.15: Reconstruction uncertainties of the extracted cross section for antineutrinos in the reverse horn current (RHC) beam (FIG. 8.10).

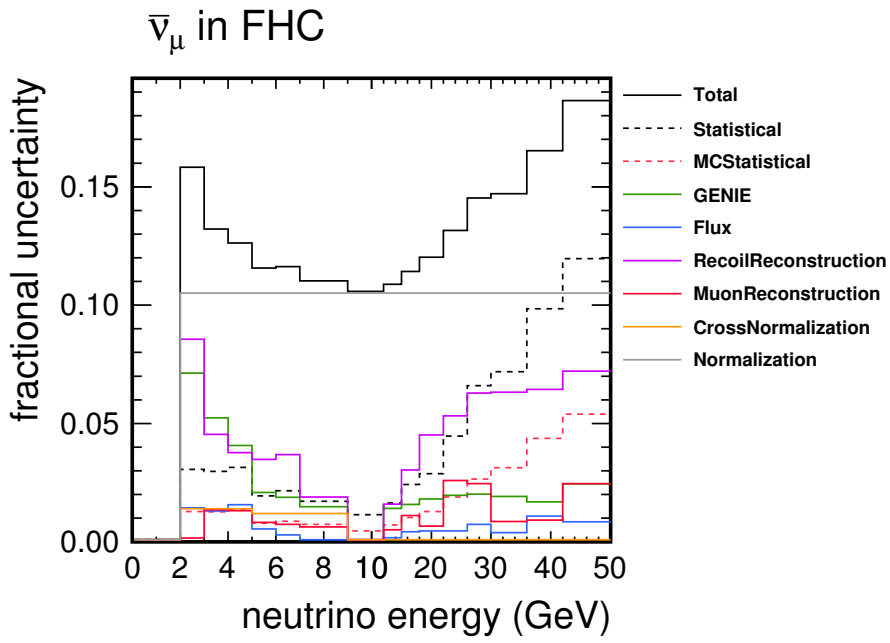

FIG. 8.16: Total systematic and statistical uncertainties of the extracted cross section for antineutrinos in the forward horn current (FHC) beam (FIG. 8.11).

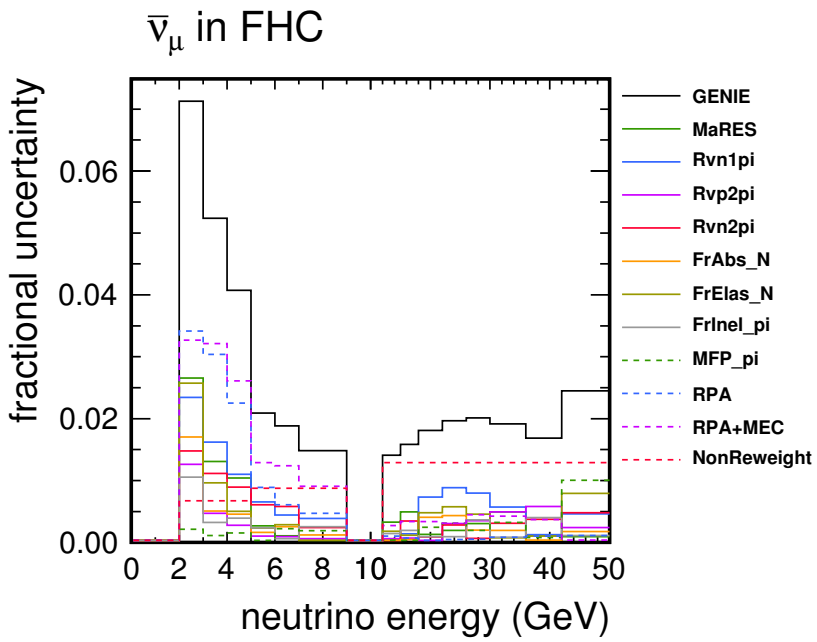

FIG. 8.17: GENIE cross section model uncertainties of the extracted cross section for antineutrinos in the forward horn current (FHC) beam (FIG. 8.11).

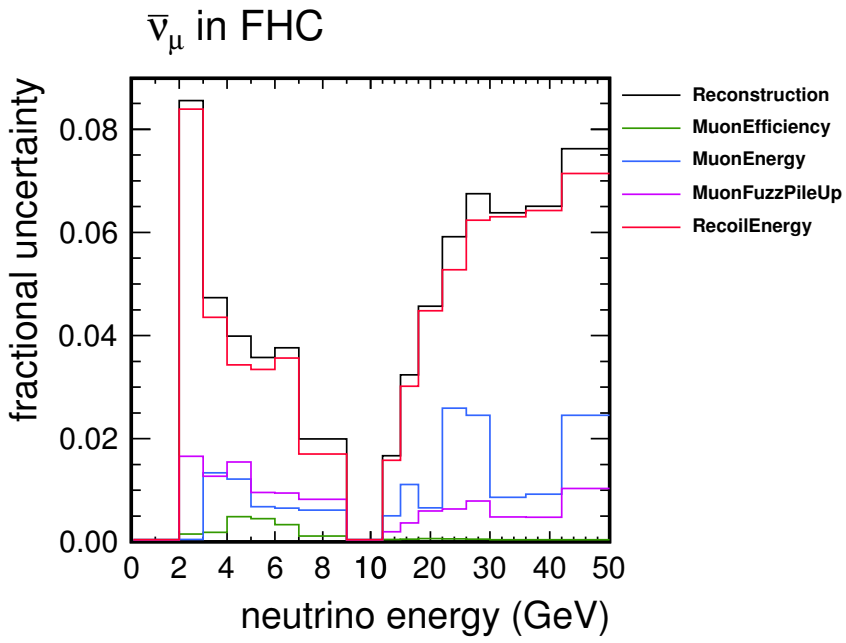

FIG. 8.18: Reconstruction uncertainties of the extracted cross section for antineutrinos in the forward horn current (FHC) beam (FIG. 8.11).

8.4 Neutrino and antineutrino flux

FIG. 8.19 shows the extracted flux of neutrinos in the forward horn current (FHC), neutrino-focusing beam. FIG. 8.20 shows the extracted flux of antineutrinos in the same beam. Table 8.8 lists the extracted neutrino flux (FIG. 8.19) in tabular form. Table 8.10 lists the extracted antineutrino flux (FIG. 8.20) in tabular form.

The existing, as simulated, flux is based on a simulation of the NuMI beamline starting with 120 GeV protons impacting the thick, complex, carbon NuMI target (Section 7.4). The exiting mesons are focused and decayed to produce a neutrino energy spectrum. The simulation is performed in GEANT4[16] with the FTFP model. The simulation has been corrected by reweighting with external hadron production data from proton collisions on thin carbon targets[40]. FIG. 7.7 – 7.8 show the effect of the reweighting.

FIG. 8.21 – 8.23 show the fractional statistical and systematic uncertainties for the extracted FHC neutrino flux. FIG. 8.24 – 8.26 show the equivalent for FHC antineutrinos. As with the cross section, the external normalization uncertainty dominates. Muon reconstruction becomes a more significant uncertainty than with the cross section as the flux is determined from low-ν events, with the majority of the initial neutrino energy going into the muon.

FIG. 8.27 shows the extracted flux of antineutrinos in the reverse horn current (RHC), antineutrino-focusing beam. FIG. 8.28 shows the extracted flux of neutrinos in the same beam. Table 8.12 lists the extracted antineutrino flux (FIG. 8.27) in tabular form. Table 8.14 lists the extracted neutrino flux (FIG. 8.28) in tabular form. FIG. 8.29 – 8.31 show the fractional statistical and systematic uncertainties for the extracted RHC antineutrino flux. FIG. 8.32 – 8.34 show the equivalent for RHC neutrinos.

Both of the focused results (FHC neutrinos and RHC antineutrinos) show similar discrepancies between data and simulation; a flux deficit is observed in the peak (2–5 GeV)

and an excess at higher energy. The defocused results (FHC antineutrinos and RHC neutrinos) also show a deficit in the peak, but the statistical uncertainties are larger.

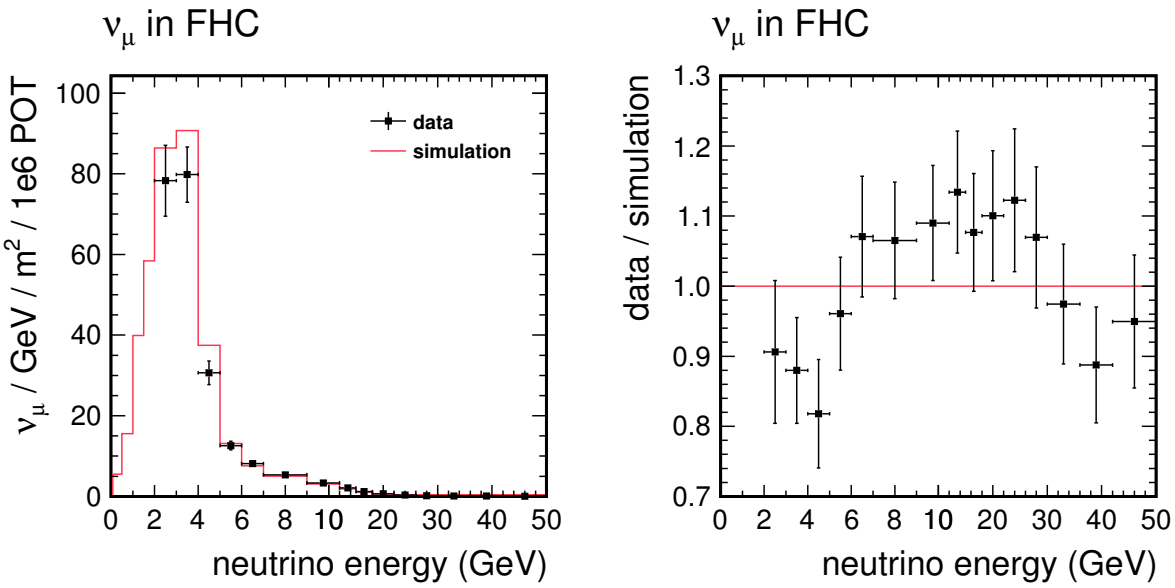

FIG. 8.19: Extracted neutrino flux (left) and ratio of data to simulation (right) in the forward horn current (FHC), neutrino-focusing beam. Data are plotted with statistical and systematic uncertainties.

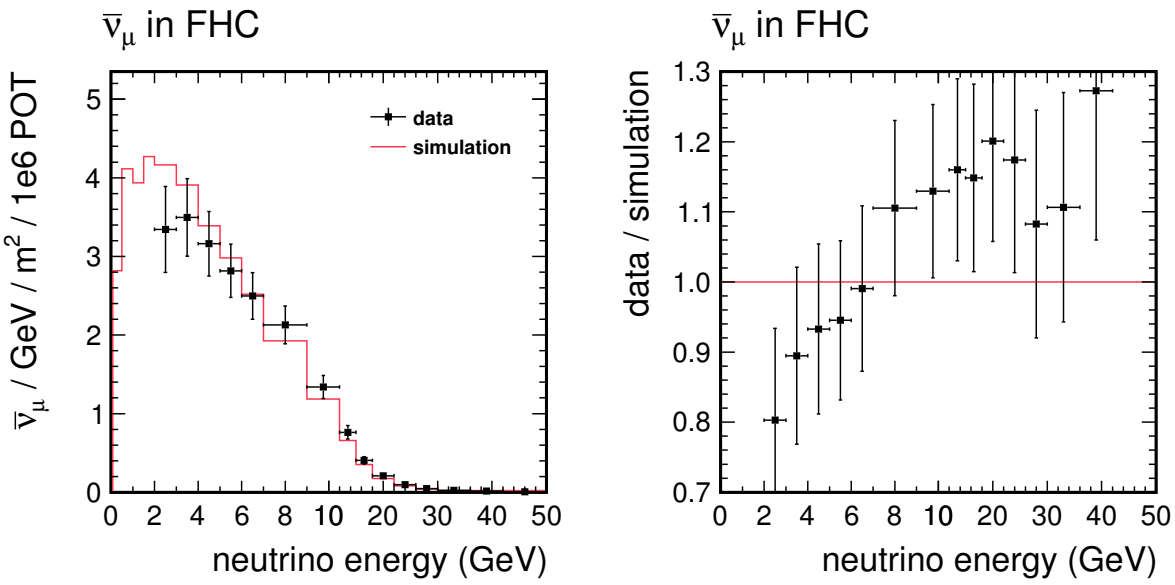

FIG. 8.20: Extracted antineutrino flux (left) and ratio of data to simulation (right) in the forward horn current (FHC), neutrino-focusing beam. Data are plotted with statistical and systematic uncertainties.

E bin (GeV)	$\Phi(E)$	Stat. error	Syst. error	Total error
	(ν_μ / m^2 / 1e6 POT)			
2–3	78.294	0.955	8.744	8.796
3–4	79.820	0.862	6.793	6.847
4–5	30.656	0.504	2.856	2.900
5–6	12.605	0.185	1.041	1.057
6–7	8.142	0.156	0.636	0.655
7–9	10.744	0.186	0.818	0.839
9–12	10.069	0.127	0.748	0.758
12–15	6.295	0.096	0.474	0.483
15–18	3.580	0.066	0.271	0.279
18–22	2.697	0.058	0.220	0.227
22–26	1.370	0.040	0.118	0.124
26–30	0.773	0.029	0.067	0.073
30–36	0.747	0.029	0.059	0.066
36–42	0.511	0.026	0.040	0.048
42–50	0.465	0.026	0.038	0.046

TABLE 8.8: Extracted neutrino flux and statistical, systematic and total uncertainties in the forward horn current (FHC), neutrino-focusing beam (FIG. 8.19). Note that the values and uncertainties are not bin width normalized. The covariance matrix is tabulated in Table 8.9.

	2–3	3–4	4–5	5–6	6–7	7–9	9–12	12–15	15–18	18–22	22–26	26–30	30–36	36–42	42–50
2–3	77.372	20.929	-1.621	-0.855	-0.006	0.366	0.670	0.537	-0.132	-0.327	-0.226	-0.116	-0.048	-0.034	-0.055
3–4	20.929	46.887	4.970	1.251	0.650	0.798	0.588	0.336	0.168	0.089	0.050	0.028	0.032	0.012	0.003
4–5	-1.621	4.970	8.410	1.079	0.367	0.362	0.132	0.015	0.140	0.157	0.100	0.053	0.035	0.016	0.017
5–6	-0.855	1.251	1.079	1.118	0.147	0.164	0.082	0.037	0.054	0.053	0.033	0.018	0.012	0.007	0.007
6–7	-0.006	0.650	0.367	0.147	0.429	0.119	0.085	0.050	0.035	0.029	0.016	0.009	0.007	0.005	0.005
7–9	0.366	0.798	0.362	0.164	0.119	0.703	0.124	0.075	0.046	0.036	0.018	0.010	0.010	0.007	0.006
9–12	0.670	0.588	0.132	0.082	0.085	0.124	0.575	0.077	0.040	0.030	0.014	0.008	0.009	0.006	0.006
12–15	0.537	0.336	0.015	0.037	0.050	0.075	0.077	0.233	0.024	0.016	0.007	0.004	0.005	0.004	0.003
15–18	-0.132	0.168	0.140	0.054	0.035	0.046	0.040	0.024	0.078	0.017	0.009	0.005	0.004	0.003	0.003
18–22	-0.327	0.089	0.157	0.053	0.029	0.036	0.030	0.016	0.017	0.052	0.009	0.005	0.004	0.003	0.003
22–26	-0.226	0.050	0.100	0.033	0.016	0.018	0.014	0.007	0.009	0.009	0.015	0.003	0.002	0.001	0.002
26–30	-0.116	0.028	0.053	0.018	0.009	0.010	0.008	0.004	0.005	0.005	0.003	0.005	0.001	0.001	0.001
30–36	-0.048	0.032	0.035	0.012	0.007	0.010	0.009	0.005	0.004	0.004	0.002	0.001	0.004	0.001	0.001
36–42	-0.034	0.012	0.016	0.007	0.005	0.007	0.006	0.004	0.003	0.003	0.001	0.001	0.001	0.002	0.001
42–50	-0.055	0.003	0.017	0.007	0.005	0.006	0.006	0.003	0.003	0.003	0.002	0.001	0.001	0.001	0.002

TABLE 8.9: Covariance matrix for the extracted neutrino flux in the forward horn current (FHC) beam (Table 8.8). The bin boundaries are in units of GeV. The covariance elements are in units of ν_μ / m^2 / 1e6 POT.

E bin (GeV)	$\Phi(E)$	Stat. error	Syst. error	Total error
		($\bar{\nu}_\mu$ / m^2 / 1e6 POT)		
2–3	3.344	0.157	0.523	0.546
3–4	3.496	0.143	0.472	0.493
4–5	3.161	0.130	0.390	0.411
5–6	2.817	0.086	0.327	0.338
6–7	2.497	0.079	0.287	0.297
7–9	4.256	0.102	0.471	0.482
9–12	4.017	0.075	0.433	0.440
12–15	2.287	0.056	0.250	0.256
15–18	1.217	0.040	0.136	0.142
18–22	0.838	0.032	0.095	0.100
22–26	0.380	0.021	0.047	0.052
26–30	0.179	0.014	0.023	0.027
30–36	0.145	0.013	0.017	0.021
36–42	0.081	0.010	0.010	0.014
42–50	0.054	0.008	0.007	0.010

TABLE 8.10: Extracted antineutrino flux and statistical, systematic and total uncertainties in the forward horn current (FHC), neutrino-focusing beam (FIG. 8.20). Note that the values and uncertainties are not bin width normalized. The covariance matrix is tabulated in Table 8.11.

	2–3	3–4	4–5	5–6	6–7	7–9	9–12	12–15	15–18	18–22	22–26	26–30	30–36	36–42	42–50
2–3	29.782	10.906	6.980	3.919	3.028	3.502	0.362	-0.347	-0.445	-0.333	-0.258	-0.140	-0.072	-0.042	-0.038
3–4	10.906	24.339	5.431	3.160	2.597	3.060	0.624	-0.089	-0.275	-0.213	-0.184	-0.105	-0.051	-0.030	-0.029
4–5	6.980	5.431	16.906	2.251	1.728	2.149	0.524	-0.085	-0.187	-0.139	-0.162	-0.087	-0.044	-0.026	-0.026
5–6	3.919	3.160	2.251	11.440	1.079	1.464	0.437	-0.037	-0.149	-0.119	-0.125	-0.069	-0.037	-0.021	-0.021
6–7	3.028	2.597	1.728	1.079	8.845	1.327	0.399	-0.053	-0.140	-0.108	-0.127	-0.068	-0.035	-0.018	-0.020
7–9	3.502	3.060	2.149	1.464	1.327	23.211	0.789	0.186	-0.020	-0.034	-0.082	-0.048	-0.021	-0.010	-0.016
9–12	0.362	0.624	0.524	0.437	0.399	0.789	19.332	0.530	0.293	0.201	0.080	0.042	0.034	0.019	0.011
12–15	-0.347	-0.089	-0.085	-0.037	-0.053	0.186	0.530	6.570	0.300	0.204	0.140	0.068	0.046	0.023	0.019
15–18	-0.445	-0.275	-0.187	-0.149	-0.140	-0.020	0.293	0.300	2.010	0.151	0.101	0.051	0.033	0.017	0.015
18–22	-0.333	-0.213	-0.139	-0.119	-0.108	-0.034	0.201	0.204	0.151	0.997	0.073	0.037	0.025	0.013	0.011
22–26	-0.258	-0.184	-0.162	-0.125	-0.127	-0.082	0.080	0.140	0.101	0.073	0.270	0.031	0.019	0.010	0.009
26–30	-0.140	-0.105	-0.087	-0.069	-0.068	-0.048	0.042	0.068	0.051	0.037	0.031	0.072	0.010	0.005	0.005
30–36	-0.072	-0.051	-0.044	-0.037	-0.035	-0.021	0.034	0.046	0.033	0.025	0.019	0.010	0.046	0.003	0.003
36–42	-0.042	-0.030	-0.026	-0.021	-0.018	-0.010	0.019	0.023	0.017	0.013	0.010	0.005	0.003	0.018	0.002
42–50	-0.038	-0.029	-0.026	-0.021	-0.020	-0.016	0.011	0.019	0.015	0.011	0.009	0.005	0.003	0.002	0.011

TABLE 8.11: Covariance matrix for the extracted antineutrino flux in the forward horn current (FHC) beam (Table 8.10). The bin boundaries are in units of GeV. The covariance elements are in units of $\bar{\nu}_\mu$ / m^2 / 1e6 POT and scaled by a factor of 10^2.

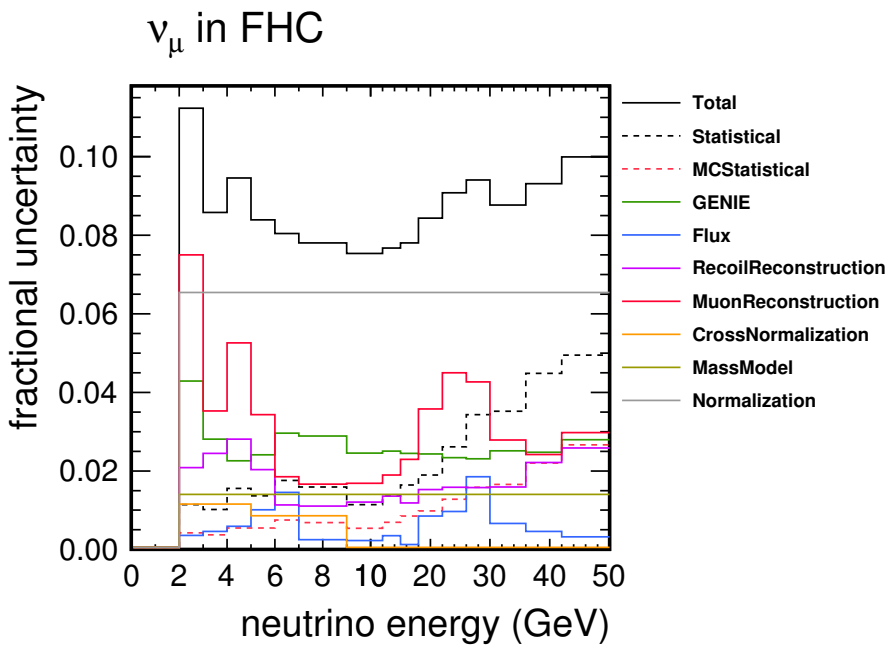

FIG. 8.21: Total systematic and statistical uncertainties of the extracted neutrino flux in the forward horn current (FHC) beam (FIG. 8.19).

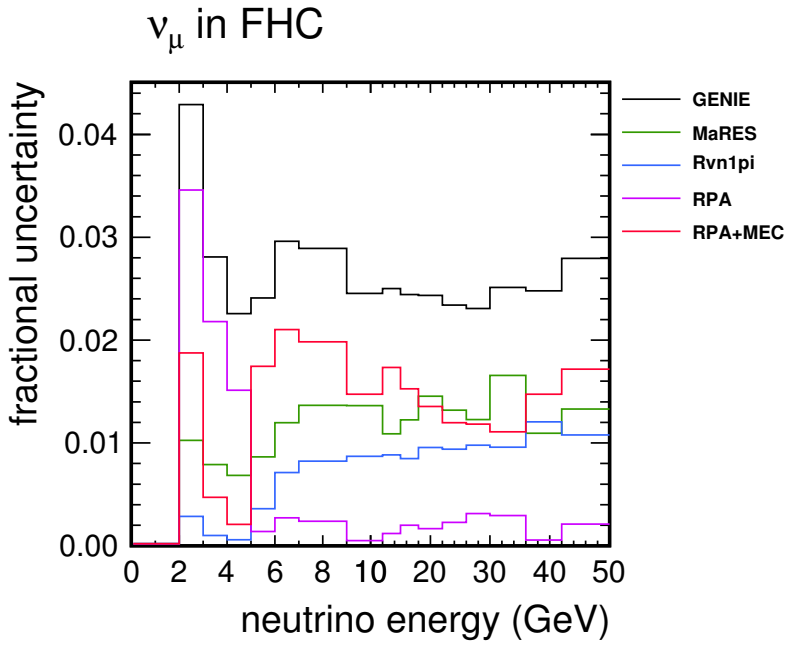

FIG. 8.22: GENIE cross section model uncertainties of the extracted neutrino flux in the forward horn current (FHC) beam (FIG. 8.19).

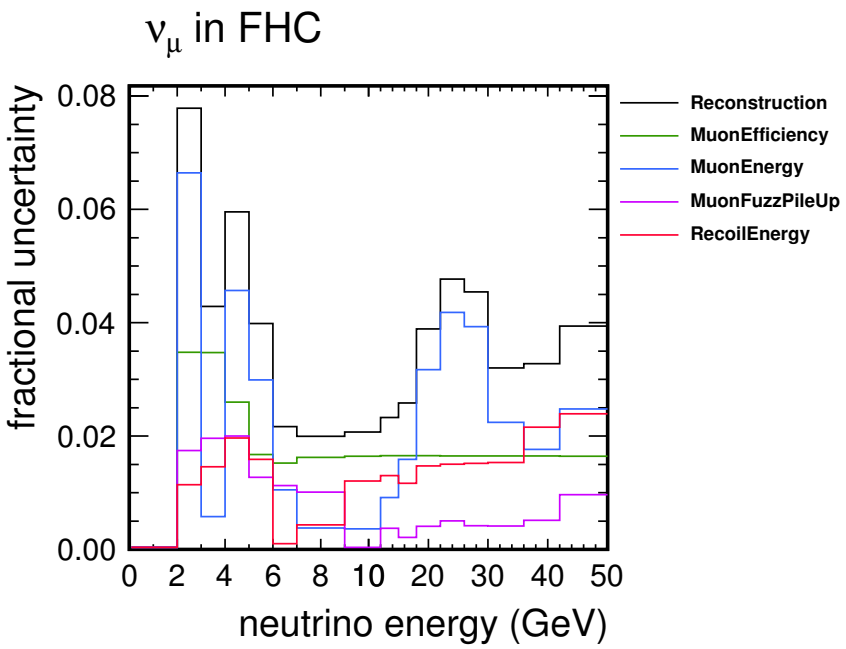

FIG. 8.23: Reconstruction uncertainties of the extracted neutrino flux in the forward horn current (FHC) beam (FIG. 8.19).

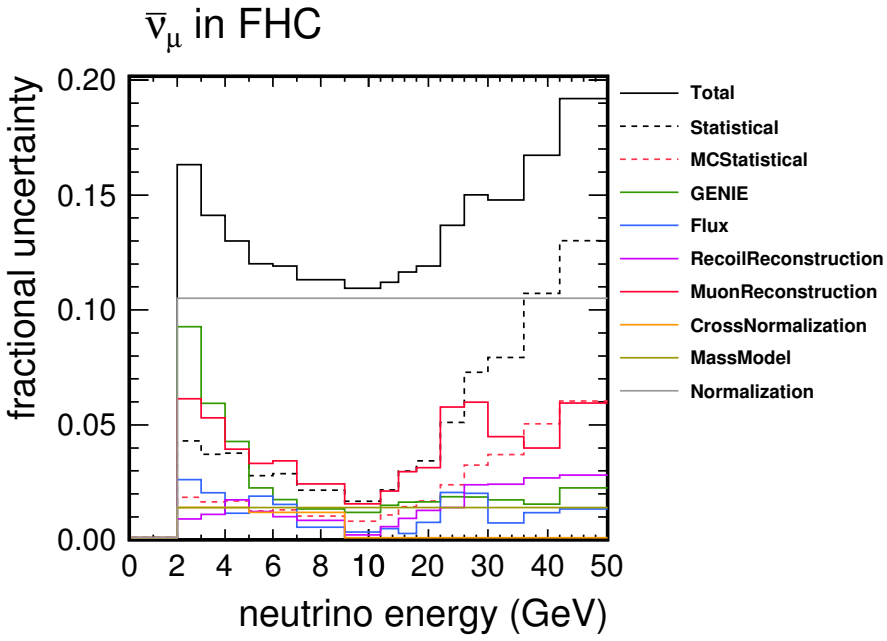

FIG. 8.24: Total systematic and statistical uncertainties of the extracted antineutrino flux in the forward horn current (FHC) beam (FIG. 8.20).

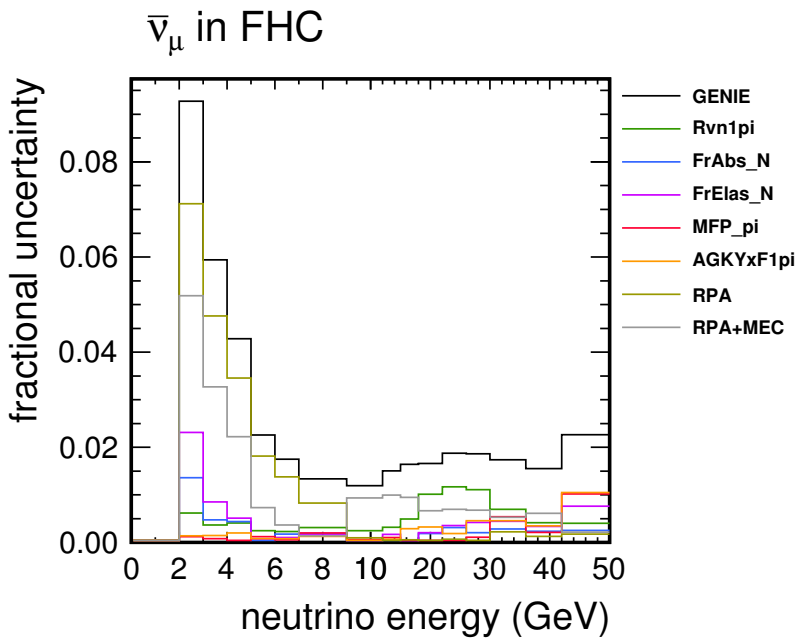

FIG. 8.25: GENIE cross section model uncertainties of the extracted antineutrino flux in the forward horn current (FHC) beam (FIG. 8.20).

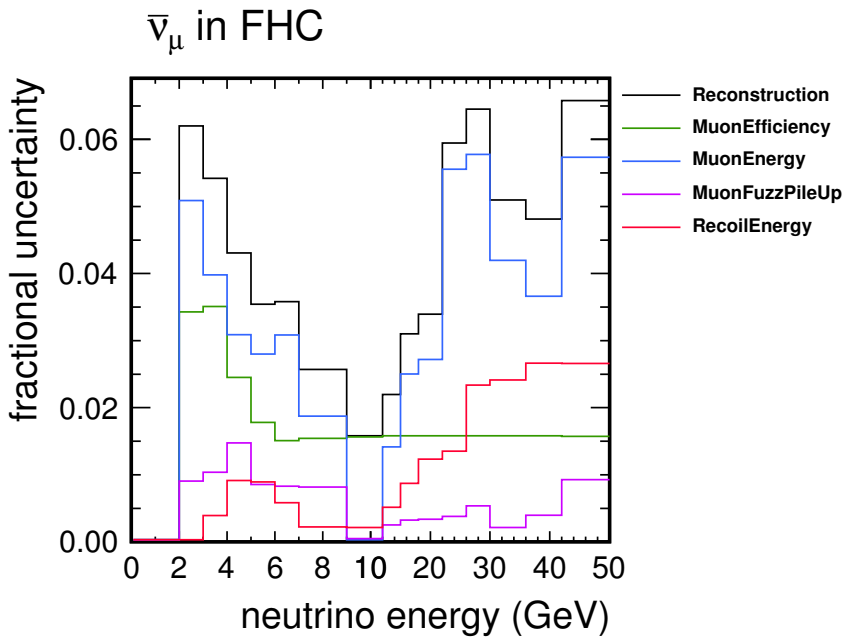

FIG. 8.26: Reconstruction uncertainties of the extracted antineutrino flux in the forward horn current (FHC) beam (FIG. 8.20).

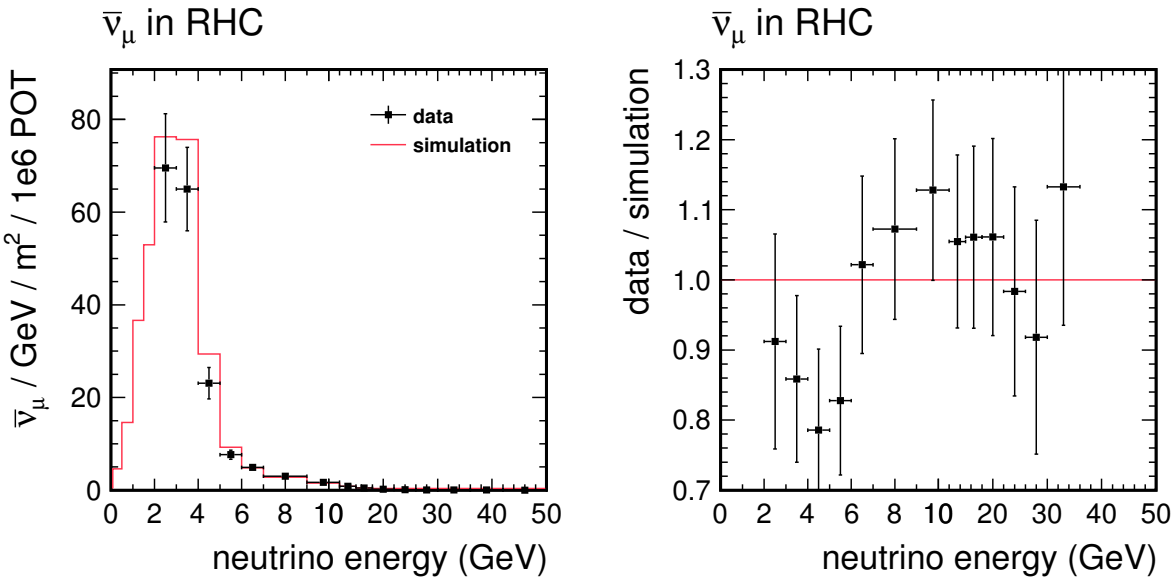

FIG. 8.27: Extracted antineutrino flux (left) and ratio of data to simulation (right) in the reverse horn current (RHC), antineutrino-focusing beam. Data are plotted with statistical and systematic uncertainties.

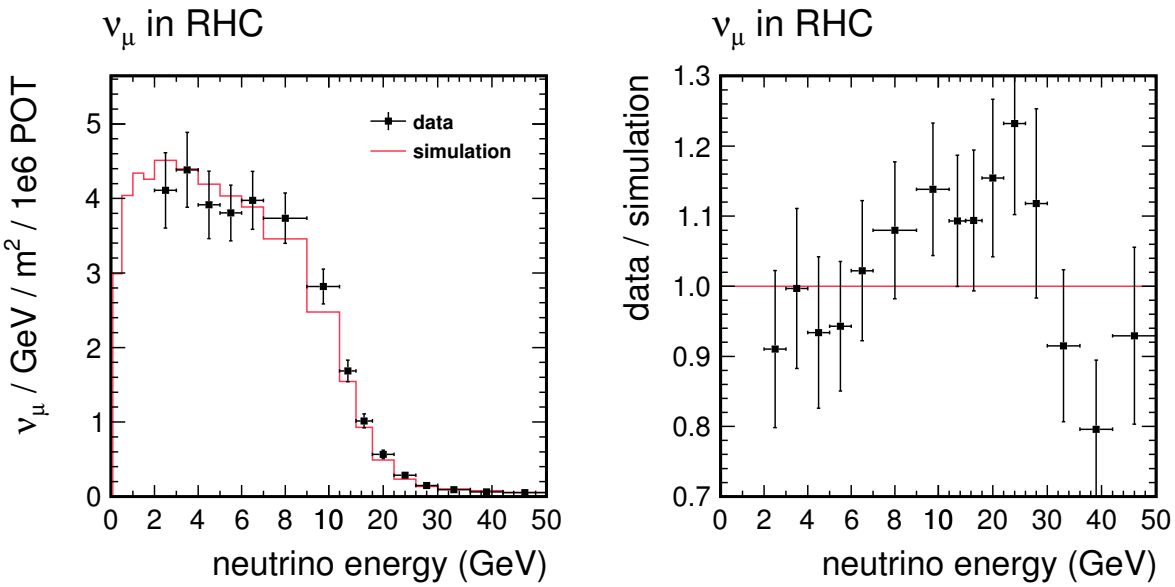

FIG. 8.28: Extracted neutrino flux (left) and ratio of data to simulation (right) in the reverse horn current (RHC), antineutrino-focusing beam. Data are plotted with statistical and systematic uncertainties.

E bin (GeV)	$\Phi(E)$	Stat. error	Syst. error	Total error
		($\bar{\nu}_\mu$ / m^2 / 1e6 POT)		
2–3	69.546	1.357	11.612	11.691
3–4	64.995	1.148	8.930	9.004
4–5	23.078	0.634	3.336	3.396
5–6	7.646	0.243	0.950	0.981
6–7	4.902	0.198	0.575	0.608
7–9	6.012	0.226	0.686	0.722
9–12	5.101	0.155	0.560	0.581
12–15	2.576	0.100	0.284	0.301
15–18	1.400	0.069	0.157	0.172
18–22	0.909	0.054	0.108	0.120
22–26	0.399	0.035	0.050	0.061
26–30	0.193	0.025	0.024	0.035
30–36	0.178	0.022	0.021	0.031
36–42	0.110	0.020	0.014	0.025
42–50	0.062	0.015	0.008	0.017

TABLE 8.12: Extracted antineutrino flux and statistical, systematic and total uncertainties in the reverse horn current (RHC), antineutrino-focusing beam (FIG. 8.27). Note that the values and uncertainties are not bin width normalized. The covariance matrix is tabulated in Table 8.13.

	2–3	3–4	4–5	5–6	6–7	7–9	9–12	12–15	15–18	18–22	22–26	26–30	30–36	36–42	42–50
2–3	136.690	41.023	7.723	0.381	0.308	0.078	0.216	0.081	-0.049	-0.137	-0.089	-0.049	-0.013	-0.022	-0.018
3–4	41.023	81.064	9.207	1.256	0.603	0.404	0.201	0.113	0.067	0.019	-0.001	-0.004	0.002	0.001	-0.002
4–5	7.723	9.207	11.534	0.802	0.330	0.245	0.061	0.048	0.060	0.054	0.025	0.012	0.005	0.007	0.005
5–6	0.381	1.256	0.802	0.962	0.079	0.071	0.021	0.013	0.013	0.011	0.006	0.003	0.000	0.001	0.001
6–7	0.308	0.603	0.330	0.079	0.370	0.033	0.011	0.007	0.006	0.004	0.002	0.001	0.000	0.000	0.000
7–9	0.078	0.404	0.245	0.071	0.033	0.521	0.014	0.008	0.006	0.004	0.002	0.001	0.000	0.000	0.000
9–12	0.216	0.201	0.061	0.021	0.011	0.014	0.338	0.005	0.003	0.002	0.001	0.000	0.000	0.000	0.000
12–15	0.081	0.113	0.048	0.013	0.007	0.008	0.005	0.091	0.002	0.001	0.001	0.000	0.000	0.000	0.000
15–18	-0.049	0.067	0.060	0.013	0.006	0.006	0.003	0.002	0.029	0.002	0.001	0.000	0.000	0.000	0.000
18–22	-0.137	0.019	0.054	0.011	0.004	0.004	0.002	0.001	0.002	0.014	0.001	0.000	0.000	0.000	0.000
22–26	-0.089	-0.001	0.025	0.006	0.002	0.002	0.001	0.001	0.001	0.001	0.004	0.000	0.000	0.000	0.000
26–30	-0.049	-0.004	0.012	0.003	0.001	0.001	0.000	0.000	0.000	0.000	0.000	0.001	0.000	0.000	0.000
30–36	-0.013	0.002	0.005	0.000	0.000	0.000	0.000	0.000	0.000	0.000	0.000	0.000	0.001	0.000	0.000
36–42	-0.022	0.001	0.007	0.001	0.000	0.000	0.000	0.000	0.000	0.000	0.000	0.000	0.000	0.001	0.000
42–50	-0.018	-0.002	0.005	0.001	0.000	0.000	0.000	0.000	0.000	0.000	0.000	0.000	0.000	0.000	0.000

TABLE 8.13: Covariance matrix for the extracted antineutrino flux in the reverse horn current (RHC) beam (Table 8.12). The bin boundaries are in units of GeV. The covariance elements are in units of $\bar{\nu}_\mu$ / m^2 / 1e6 POT.

E bin (GeV)	$\Phi(E)$	Stat. error	Syst. error	Total error
		(ν_μ / m^2 / 1e6 POT)		
2–3	4.108	0.314	0.397	0.506
3–4	4.383	0.298	0.404	0.502
4–5	3.914	0.279	0.357	0.453
5–6	3.805	0.157	0.338	0.373
6–7	3.973	0.159	0.355	0.389
7–9	7.470	0.225	0.638	0.676
9–12	8.453	0.172	0.681	0.703
12–15	5.059	0.133	0.412	0.433
15–18	3.044	0.104	0.259	0.280
18–22	2.266	0.089	0.202	0.221
22–26	1.141	0.061	0.104	0.120
26–30	0.595	0.042	0.058	0.072
30–36	0.557	0.042	0.051	0.066
36–42	0.381	0.034	0.033	0.047
42–50	0.405	0.040	0.038	0.055

TABLE 8.14: Extracted neutrino flux and statistical, systematic and total uncertainties in the reverse horn current (RHC), antineutrino-focusing beam (FIG. 8.28). Note that the values and uncertainties are not bin width normalized. The covariance matrix is tabulated in Table 8.15.

	2–3	3–4	4–5	5–6	6–7	7–9	9–12	12–15	15–18	18–22	22–26	26–30	30–36	36–42	42–50
2–3	25.635	6.856	5.532	5.118	5.019	7.871	5.803	1.770	0.347	-0.067	-0.068	-0.193	-0.187	0.163	0.187
3–4	6.856	25.219	5.769	5.002	5.388	8.801	7.363	3.075	1.281	0.777	0.344	0.063	0.043	0.269	0.316
4–5	5.532	5.769	20.512	4.494	4.617	8.025	6.941	3.082	1.407	0.950	0.439	0.114	0.108	0.270	0.318
5–6	5.118	5.002	4.494	13.886	4.206	7.380	6.273	2.479	1.015	0.653	0.252	0.011	0.028	0.217	0.254
6–7	5.019	5.388	4.617	4.206	15.103	8.491	7.322	2.995	1.328	1.000	0.410	0.043	0.078	0.275	0.327
7–9	7.871	8.801	8.025	7.380	8.491	45.734	14.318	6.868	3.725	2.767	1.342	0.501	0.462	0.609	0.741
9–12	5.803	7.363	6.941	6.273	7.322	14.318	49.374	8.873	5.286	4.155	2.097	0.973	0.835	0.753	0.946
12–15	1.770	3.075	3.082	2.479	2.995	6.868	8.873	18.746	3.921	3.160	1.637	0.859	0.704	0.492	0.642
15–18	0.347	1.281	1.407	1.015	1.328	3.725	5.286	3.921	7.821	2.222	1.172	0.643	0.528	0.319	0.421
18–22	-0.067	0.777	0.950	0.653	1.000	2.767	4.155	3.160	2.222	4.877	0.951	0.503	0.424	0.259	0.347
22–26	-0.068	0.344	0.439	0.252	0.410	1.342	2.097	1.637	1.172	0.951	1.450	0.287	0.234	0.136	0.174
26–30	-0.193	0.063	0.114	0.011	0.043	0.501	0.973	0.859	0.643	0.503	0.287	0.515	0.146	0.070	0.089
30–36	-0.187	0.043	0.108	0.028	0.078	0.462	0.835	0.704	0.528	0.424	0.234	0.146	0.436	0.058	0.072
36–42	0.163	0.269	0.270	0.217	0.275	0.609	0.753	0.492	0.319	0.259	0.136	0.070	0.058	0.223	0.055
42–50	0.187	0.316	0.318	0.254	0.327	0.741	0.946	0.642	0.421	0.347	0.174	0.089	0.072	0.055	0.302

TABLE 8.15: Covariance matrix for the extracted neutrino flux in the reverse horn current (RHC) beam (Table 8.14). The bin boundaries are in units of GeV. The covariance elements are in units of ν_μ / m^2 / 1e6 POT and scaled by a factor of 10^2.

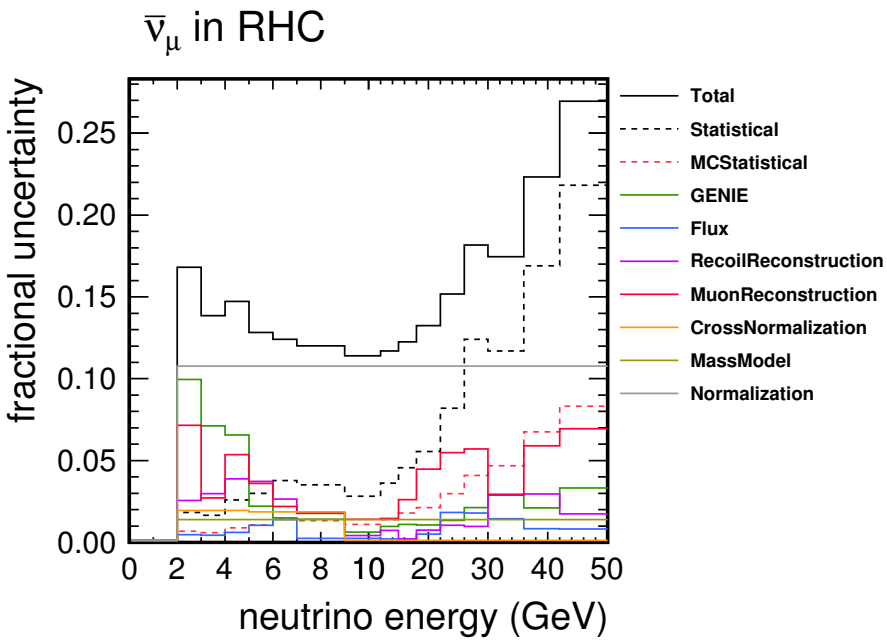

FIG. 8.29: Total systematic and statistical uncertainties of the extracted antineutrino flux in the reverse horn current (RHC) beam (FIG. 8.27).

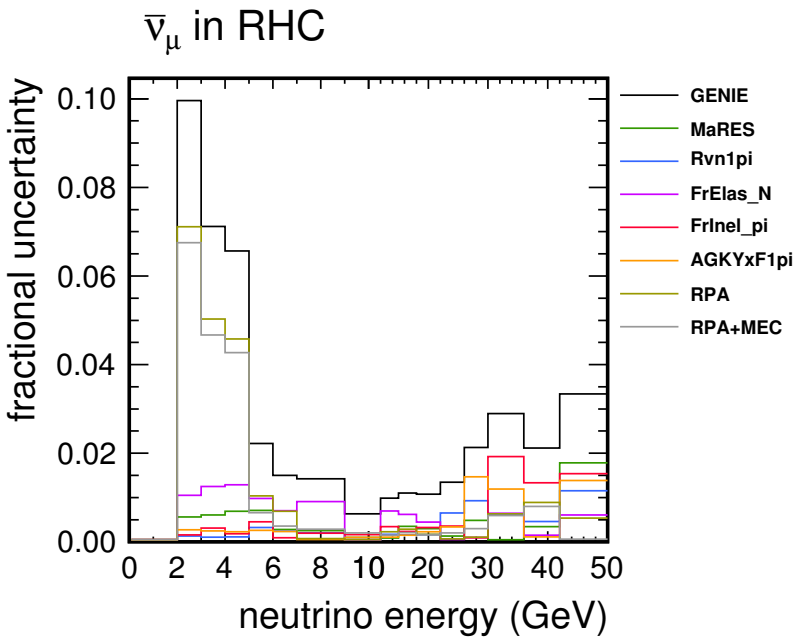

FIG. 8.30: GENIE cross section model uncertainties of the extracted antineutrino flux in the reverse horn current (RHC) beam (FIG. 8.27).

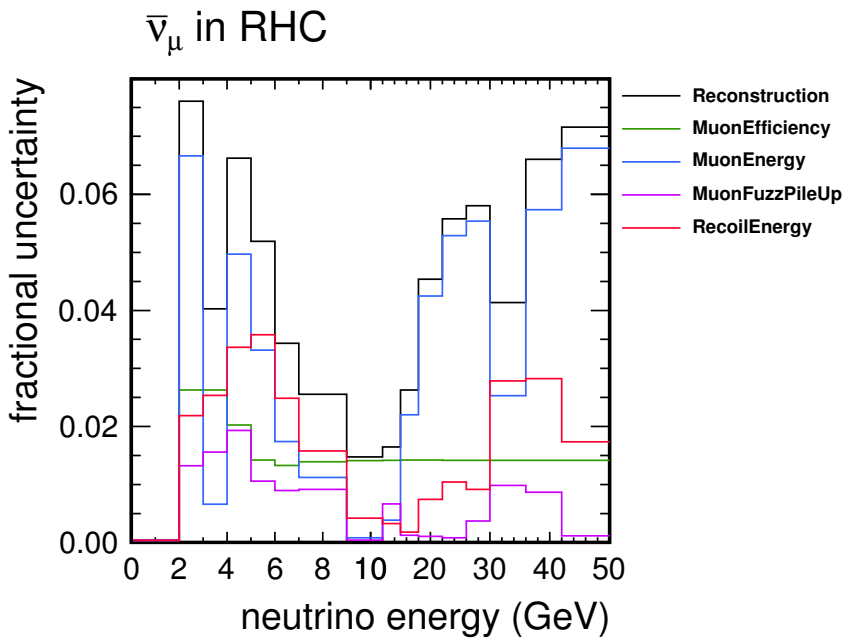

FIG. 8.31: Reconstruction uncertainties of the extracted antineutrino flux in the reverse horn current (RHC) beam (FIG. 8.27).

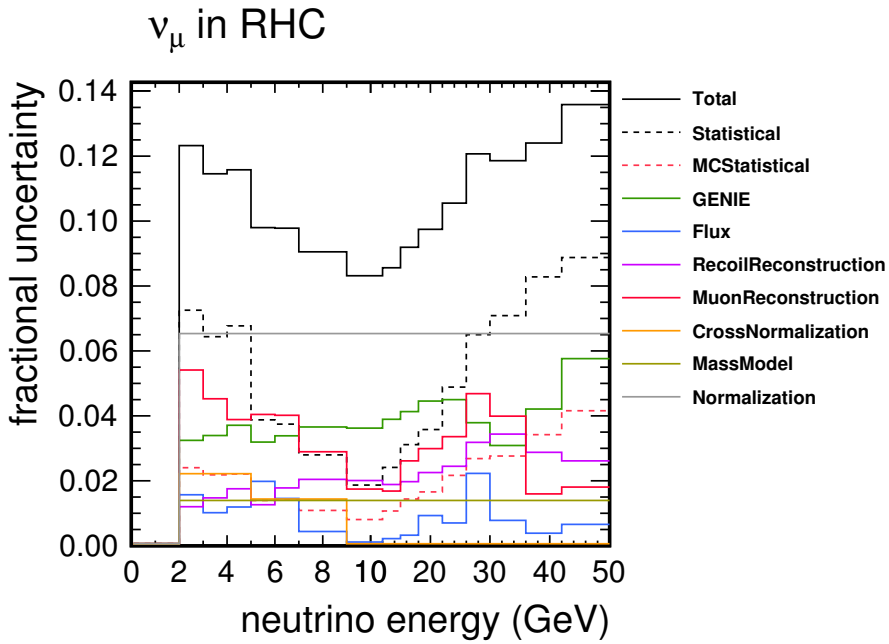

FIG. 8.32: Total systematic and statistical uncertainties of the extracted neutrino flux in the reverse horn current (RHC) beam (FIG. 8.28).

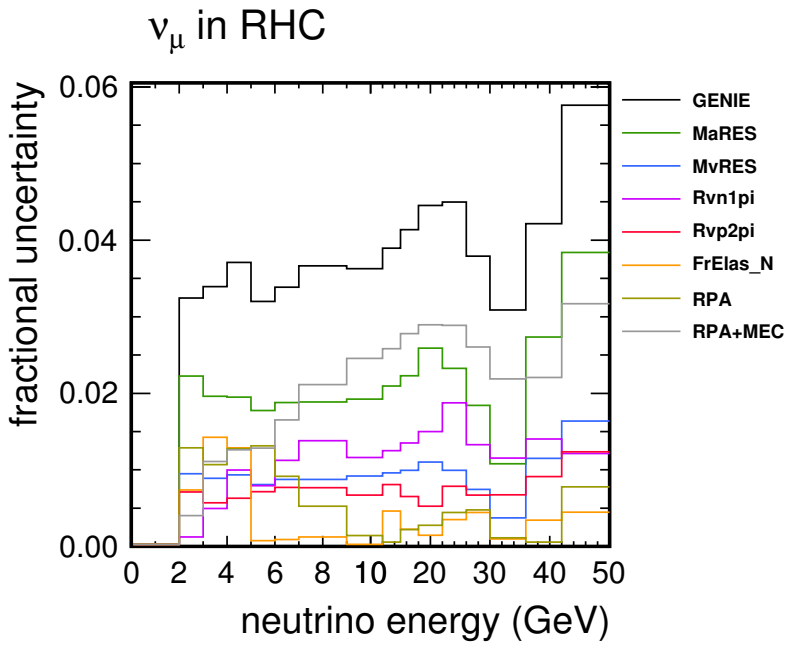

FIG. 8.33: GENIE cross section model uncertainties of the extracted neutrino flux in the reverse horn current (RHC) beam (FIG. 8.28).

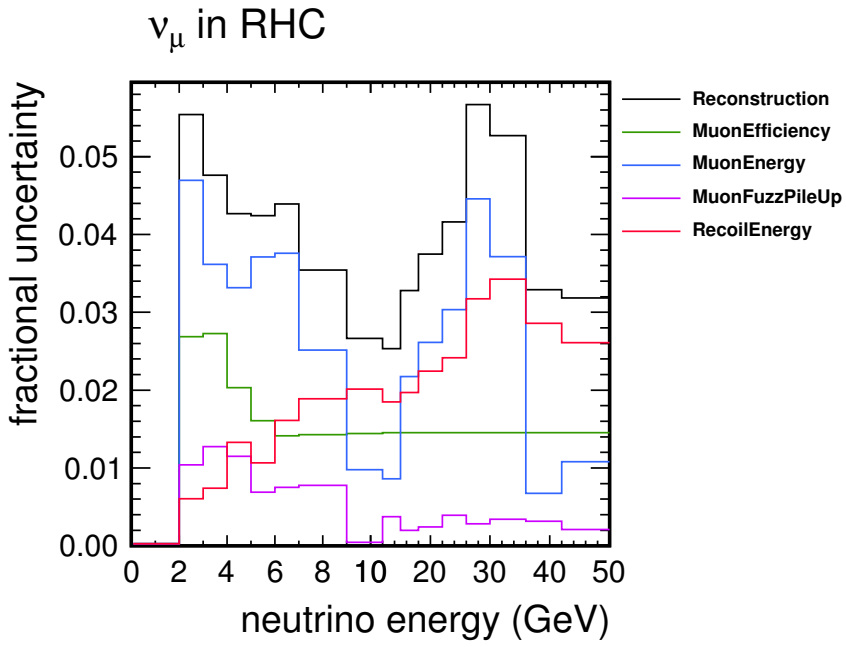

FIG. 8.34: Reconstruction uncertainties of the extracted neutrino flux in the reverse horn current (RHC) beam (FIG. 8.28).

CHAPTER 9

Conclusions

9.1 Overview

The first part of this chapter presents an iterative closure test in which the flux in the simulation is reweighted to the measured flux in data using the data/simulation ratio (right of FIG. 8.19 and FIG. 8.27). If, as desired, the analysis is insensitive to the simulated flux, the extracted cross section and flux will be unaffected.

The second part compares the extracted neutrino and antineutrino cross sections with available data from other experiments. The extracted cross sections are isoscalar corrected (Section 6.4.6) prior to this comparison. The neutrino cross section and flux are normalized to an external data constraint rather than the cross section model in GENIE – the results of the NOMAD experiment[24]. The antineutrino cross section and flux remain normalized to the simulation.

9.2 Flux reweighted results

Reweighting refers to a process of distorting a simulated model by attaching a weight to each event as a function of the properties of the event. As histograms are populated by events, the weight value is added to the histogram bin rather than 1.0. Thus, a weight less than 1.0 indicates that an event is less likely to occur and a weight greater than 1.0 indicates that an event is more likely to occur. Reweighting allows an existing Monte Carlo set to be utilized to study a modified model.

The simulated neutrino flux in the forward horn current (FHC), neutrino-focusing beam is reweighted to the measured flux using the data/simulation ratio from FIG. 8.19 applied as a function of neutrino energy. Note that the reweighting procedure changes only the simulated flux, not the simulated cross section model.

FIG. 9.1 shows the reconstructed inclusive neutrino interaction rate. As expected, the data/simulation discrepancy is comparable to the discrepancy observed in the extracted cross section (FIG. 8.1) with a deficit at low neutrino energy and a peak at 26–30 GeV likely caused by an undetermined systematic uncertainty.

FIG. 9.2 – 9.4 show the reconstructed interaction rate for the three ν cuts. The data/simulation discrepancy is consistent with the conclusions derived from the normalization factors, η', listed in Table 8.2; the data favors a lower low-ν cross section, $\sigma_\nu \equiv \sigma(\nu < \nu_0, E)$, than modeled in GENIE.

FIG. 9.5 shows the extracted FHC neutrino flux, which is now consistent with the reweighted flux in simulation. FIG. 9.6 shows the extracted cross section for neutrinos which is equivalent to the former utilizing the unweighted flux in simulation (FIG. 8.1). FIG. 9.7 shows the flux reweighted / nominal cross section ratio; consistent with one.

The antineutrino flux in the reverse horn current (RHC), antineutrino-focusing beam is reweighted using the data/simulation ratio in FIG. 8.27. FIG. 9.8 shows the recon-

structed inclusive antineutrino interaction rate, which is consistent with the observed data/simulation cross section discrepancy (FIG. 8.10). FIG. 9.9 – 9.11 show the low-ν interaction rates, which are consistent with the normalization factors, η', listed in Table 8.5.

The extracted RHC antineutrino flux is shown in FIG. 9.12, now consistent with the reweighted flux in simulation. FIG. 9.13 shows the cross section extracted with the reweighted flux. FIG. 9.14 shows the flux reweighted / nominal cross section ratio; consistent with one.

The flux reweighted results show no pathology in the process. The extracted cross sections and fluxes are unaffected by the underlying simulated flux.

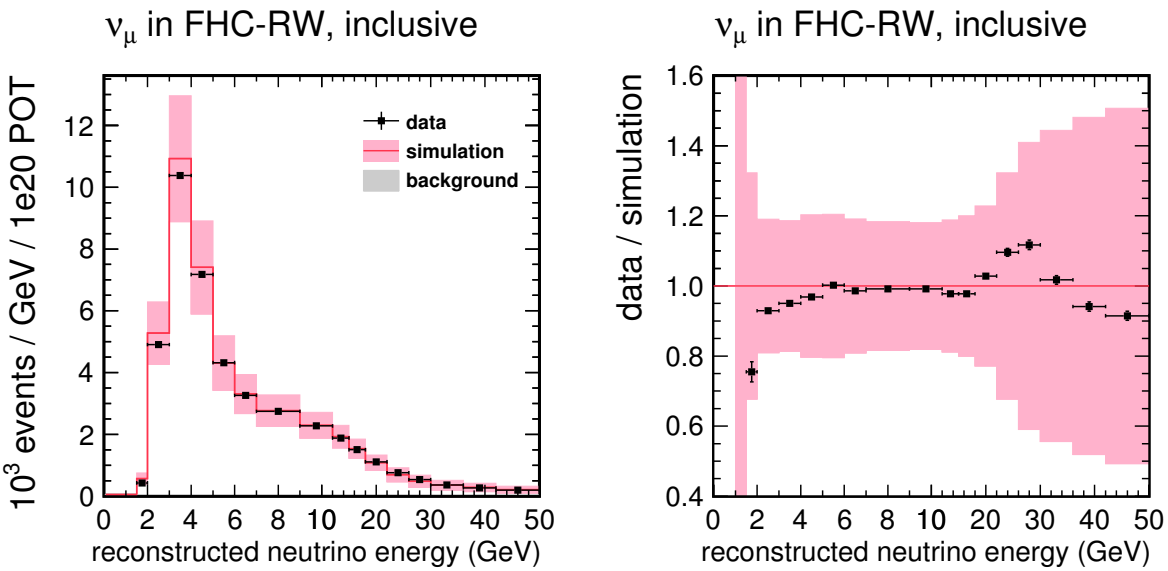

FIG. 9.1: Flux reweighted reconstructed inclusive neutrino interaction rate (left) and ratio of data to simulation (right) in the forward horn current (FHC), neutrino-focusing beam. The flux reweight is the ratio of data to simulation (right) in FIG. 8.19. Data are plotted with statistical uncertainties; simulated data are plotted with statistical and systematic uncertainties.

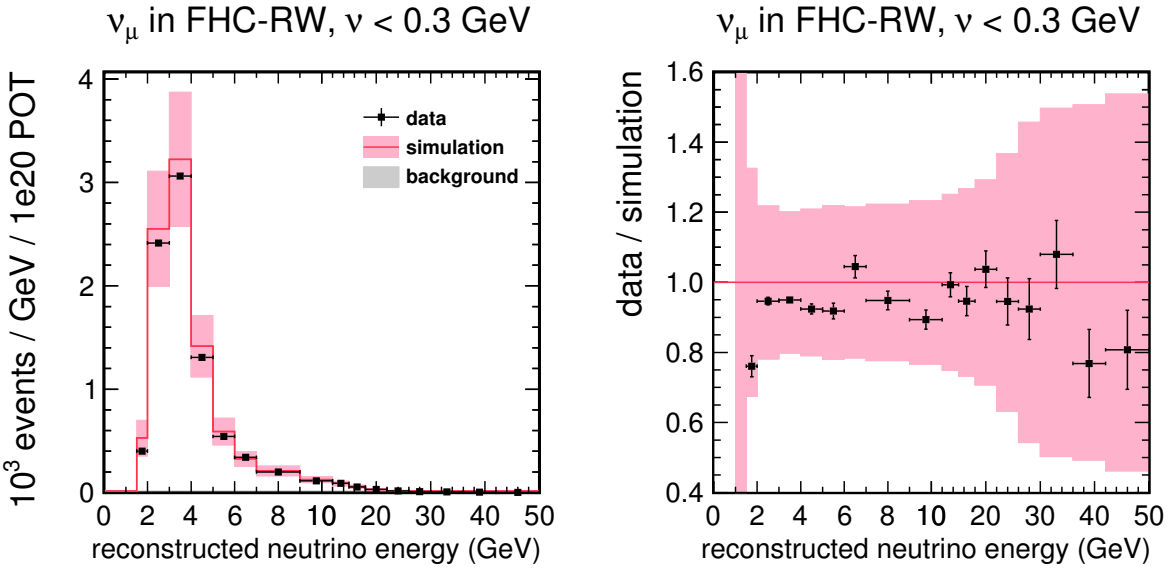

FIG. 9.2: Flux reweighted reconstructed $\nu < 300\,\text{MeV}$ neutrino interaction rate (left) and ratio of data to simulation (right) in the forward horn current (FHC), neutrino-focusing beam. The flux reweight is the ratio of data to simulation (right) in FIG. 8.19. Data are plotted with statistical uncertainties; simulated data are plotted with statistical and systematic uncertainties.

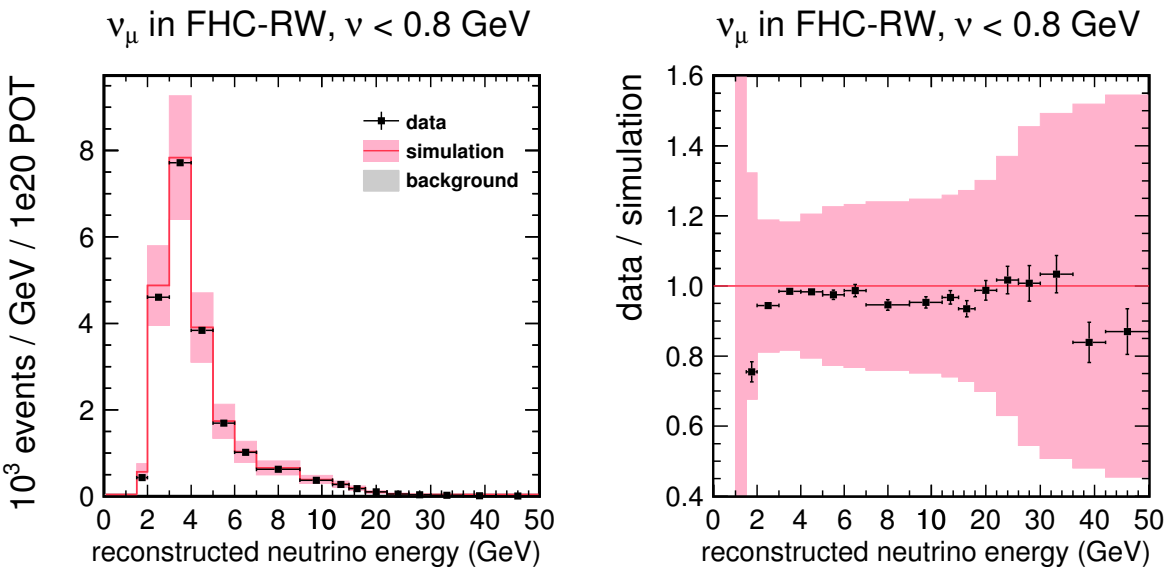

FIG. 9.3: Flux reweighted reconstructed $\nu < 800\,\text{MeV}$ neutrino interaction rate (left) and ratio of data to simulation (right) in the forward horn current (FHC), neutrino-focusing beam. The flux reweight is the ratio of data to simulation (right) in FIG. 8.19. Data are plotted with statistical uncertainties; simulated data are plotted with statistical and systematic uncertainties.

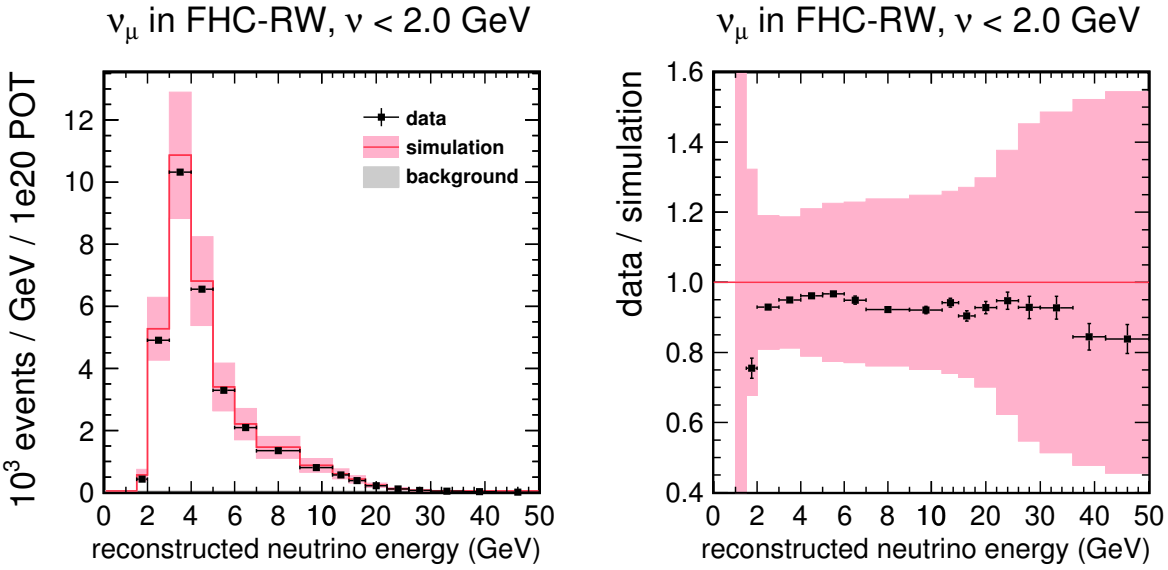

FIG. 9.4: Flux reweighted reconstructed $\nu < 2\,\text{GeV}$ neutrino interaction rate (left) and ratio of data to simulation (right) in the forward horn current (FHC), neutrino-focusing beam. The flux reweight is the ratio of data to simulation (right) in FIG. 8.19. Data are plotted with statistical uncertainties; simulated data are plotted with statistical and systematic uncertainties.

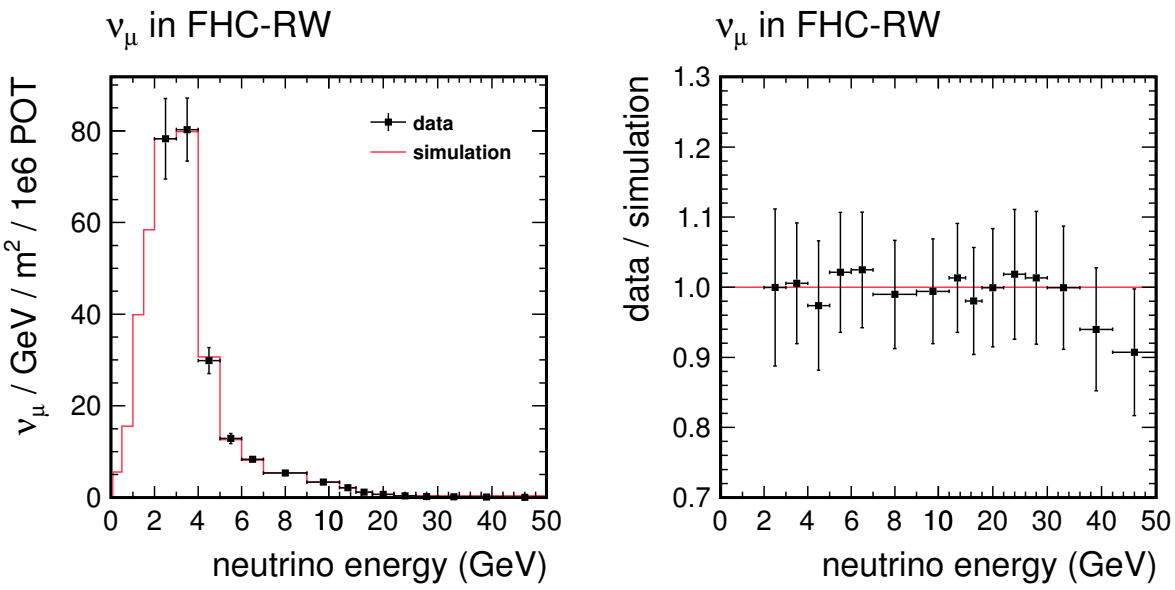

FIG. 9.5: Flux reweighted extracted neutrino flux (left) and ratio of data to simulation (right) in the forward horn current (FHC), neutrino-focusing beam. The flux reweight is the ratio of data to simulation (right) in FIG. 8.19. Data are plotted with statistical and systematic uncertainties.

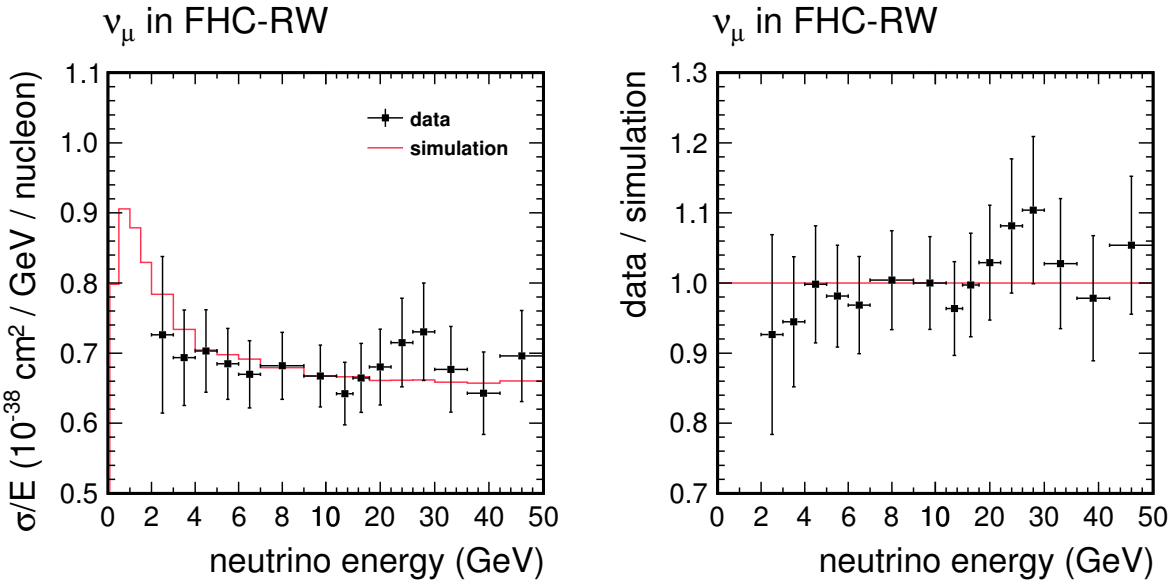

FIG. 9.6: Flux reweighted extracted cross section (left) and ratio of data to simulation (right) for neutrinos in the forward horn current (FHC), neutrino-focusing beam. The flux reweight is the ratio of data to simulation (right) in FIG. 8.19. The extracted cross section is normalized to the simulation in the 9–12 GeV bin. Data are plotted with statistical and systematic uncertainties.

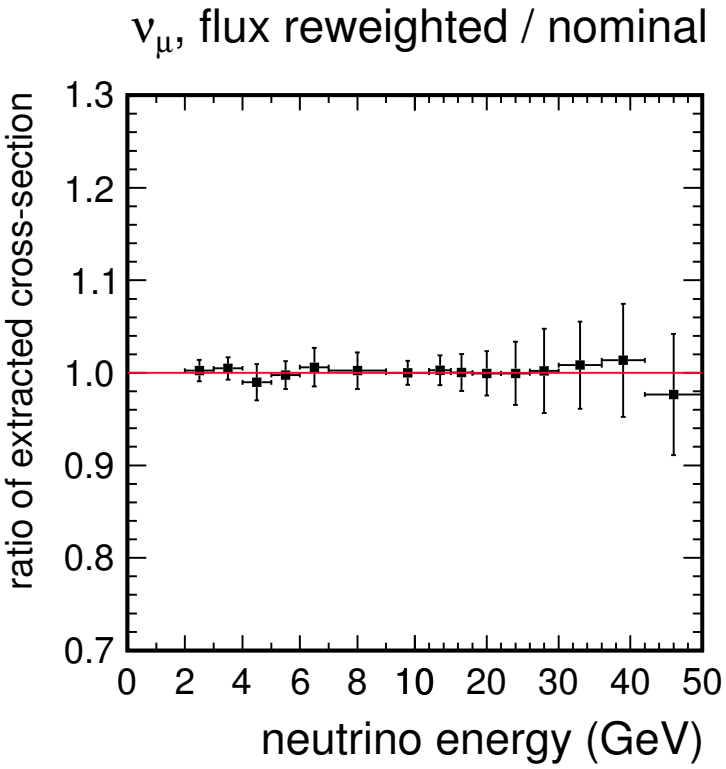

FIG. 9.7: Flux reweighted (FIG. 9.6) to nominal (FIG. 8.1) ratio of extracted cross section for neutrinos in the forward horn current (FHC) beam. The flux reweight is the ratio of data to simulation (right) in FIG. 8.19. Plotted with statistical uncertainties only.

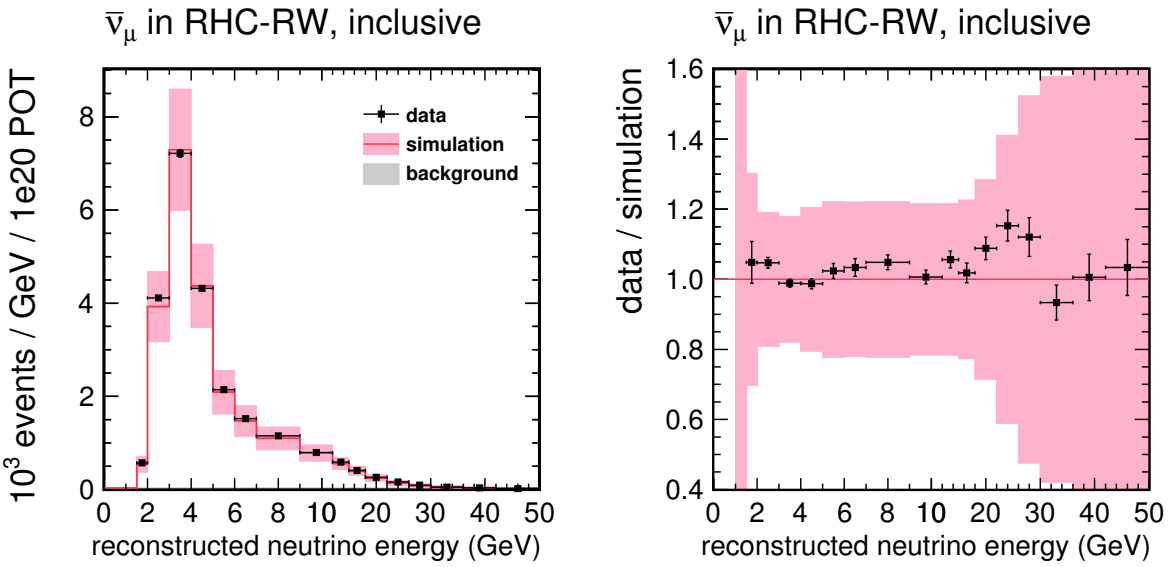

FIG. 9.8: Flux reweighted reconstructed inclusive antineutrino interaction rate (left) and ratio of data to simulation (right) in the reverse horn current (RHC), antineutrino-focusing beam. The flux reweight is the ratio of data to simulation (right) in FIG. 8.27. Data are plotted with statistical uncertainties; simulated data are plotted with statistical and systematic uncertainties.

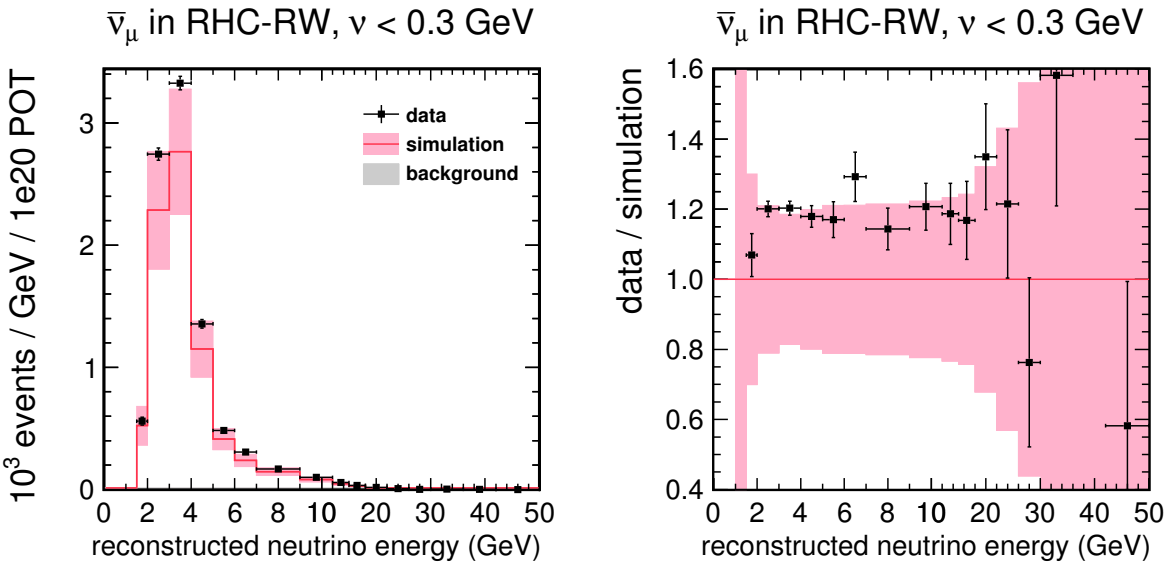

FIG. 9.9: Flux reweighted reconstructed $\nu < 300\,\text{MeV}$ antineutrino interaction rate (left) and ratio of data to simulation (right) in the reverse horn current (RHC), antineutrino-focusing beam. The flux reweight is the ratio of data to simulation (right) in FIG. 8.27. Data are plotted with statistical uncertainties; simulated data are plotted with statistical and systematic uncertainties.

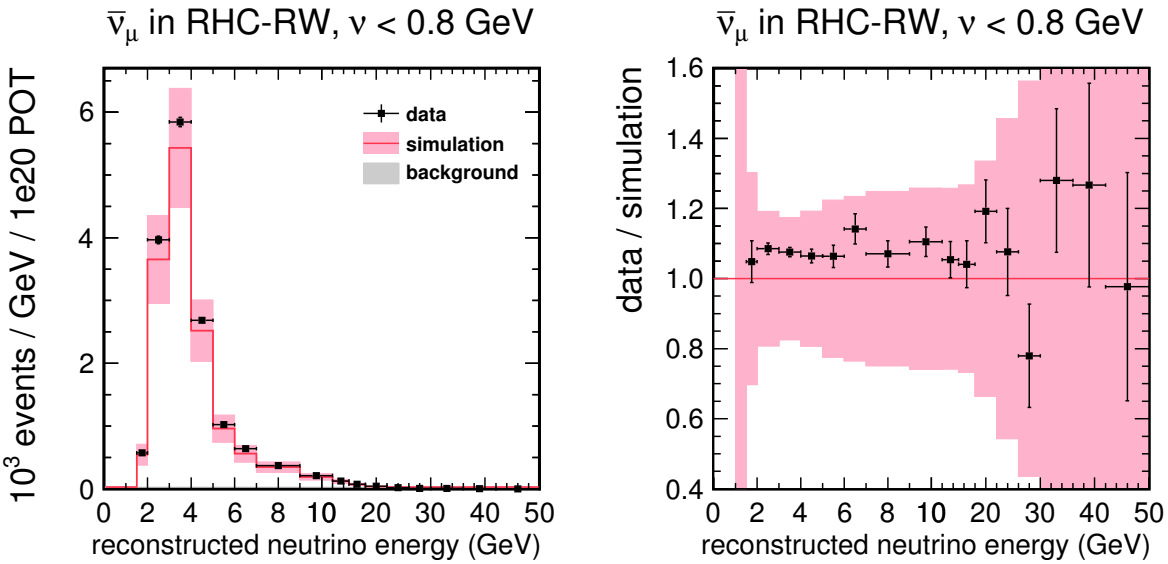

FIG. 9.10: Flux reweighted reconstructed $\nu < 800\,\text{MeV}$ antineutrino interaction rate (left) and ratio of data to simulation (right) in the reverse horn current (RHC), antineutrino-focusing beam. The flux reweight is the ratio of data to simulation (right) in FIG. 8.27. Data are plotted with statistical uncertainties; simulated data are plotted with statistical and systematic uncertainties.

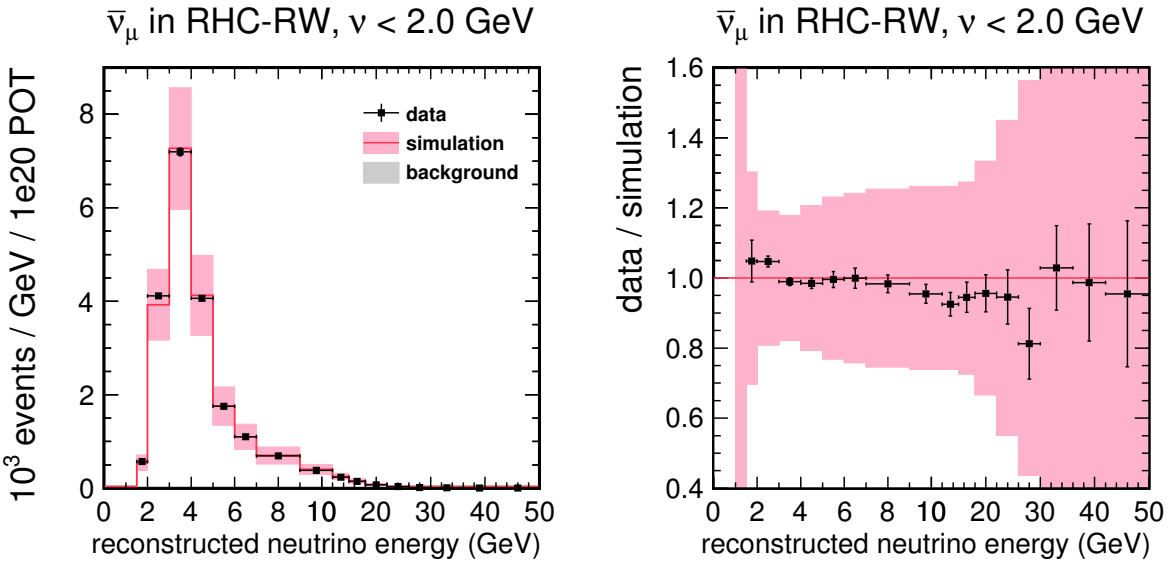

FIG. 9.11: Flux reweighted reconstructed $\nu < 2\,\text{GeV}$ antineutrino interaction rate (left) and ratio of data to simulation (right) in the reverse horn current (RHC), antineutrino-focusing beam. The flux reweight is the ratio of data to simulation (right) in FIG. 8.27. Data are plotted with statistical uncertainties; simulated data are plotted with statistical and systematic uncertainties.

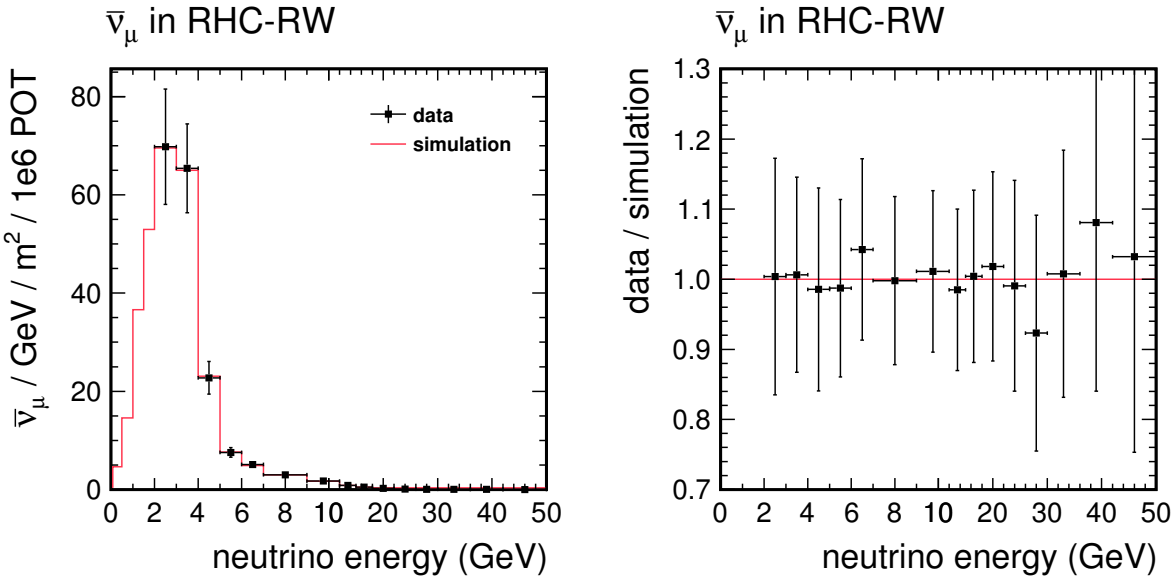

FIG. 9.12: Flux reweighted extracted antineutrino flux (left) and ratio of data to simulation (right) in the reverse horn current (RHC), antineutrino-focusing beam. The flux reweight is the ratio of data to simulation (right) in FIG. 8.28. Data are plotted with statistical and systematic uncertainties.

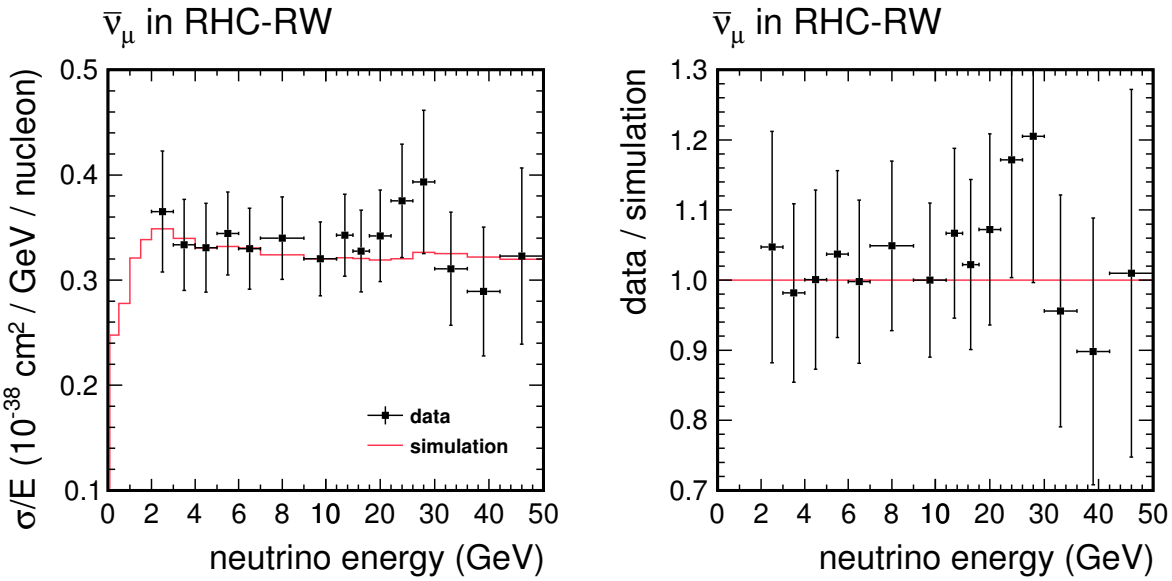

FIG. 9.13: Flux reweighted extracted cross section (left) and ratio of data to simulation (right) for antineutrinos in the reverse horn current (RHC), antineutrino-focusing beam. The flux reweight is the ratio of data to simulation (right) in FIG. 8.28. The extracted cross section is normalized to the simulation in the 9–12 GeV bin. Data are plotted with statistical and systematic uncertainties.

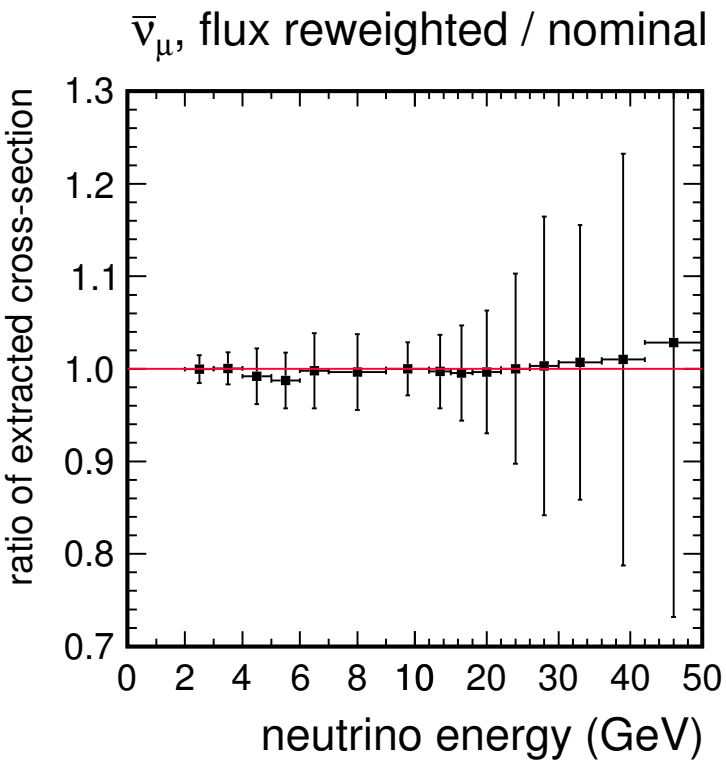

FIG. 9.14: Flux reweighted (FIG. 9.13) to nominal (FIG. 8.10) ratio of extracted cross section for antineutrinos in the reverse horn current (RHC) beam. The flux reweight is the ratio of data to simulation (right) in FIG. 8.27. Plotted with statistical uncertainties only.

9.3 NOMAD normalized neutrino cross section

The NOMAD experiment[24] measured the ν_μ charged-current inclusive cross section on a composite drift chamber target down to a neutrino energy of 2.5 GeV. As with this analysis, NOMAD employed the low-ν method, with the absolute normalization constrained to the world average cross section above 40 GeV. The result is isoscalar corrected.

FIG. 9.15 shows the extracted neutrino cross section in the forward horn current (FHC), neutrino-focusing beam normalized to the results of the NOMAD experiment. The normalization point is a value of 0.706×10^{-38} cm^2 / GeV / nucleon in the 9–12 GeV bin with an uncertainty of 3.7%. The cross section is isoscalar corrected by the ratio in FIG. 6.23. After applying the isoscalar correction, the extracted cross section is normalized up by 3.0%, reflecting the discrepancy between the cross section model in the simulation (GENIE on ^{12}C) and the NOMAD result in the 9–12 GeV bin.

FIG. 9.15 additionally shows the results of the MINOS[25] and T2K[47][48] experiments. MINOS measured the ν_μ and $\bar{\nu}_\mu$ charged-current inclusive cross sections on iron using the low-ν method for flux determination. T2K measured the ν_μ cross sections on the scintillator of the near detector[47] and on the iron of the INGRID detector[48]. T2K did not employ the low-ν method, the flux is determined from a simulation of the beamline constrained by particle production data on the actual target of the neutrino beam. All results are isoscalar corrected.

Relative to the GENIE normalized results in Chapter 8, the NOMAD normalized result has a lower uncertainty arising from the external normalization constraint (3.7% vs. 6.5%). Table 9.1 lists the NOMAD normalized extracted cross section and uncertainties in tabular form. Table 9.3 lists the NOMAD normalized extracted neutrino flux in the forward horn current (FHC) beam and uncertainties in tabular form. FIG. 9.16 shows the fractional statistical and systematic uncertainties of the extracted cross section.

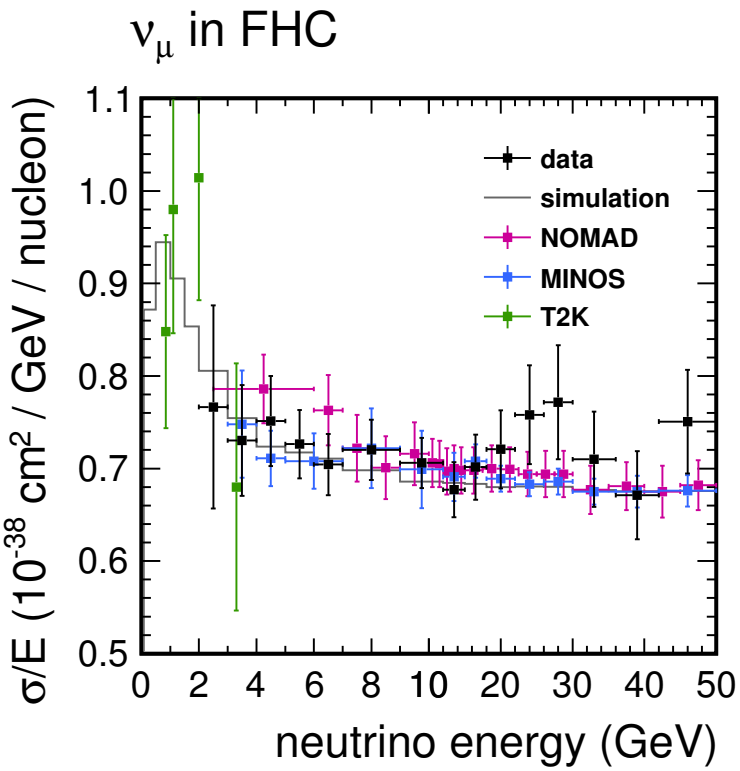

FIG. 9.15: Extracted cross section for neutrinos in the forward horn current (FHC), neutrino-focusing beam. The extracted cross section is normalized to NOMAD[24] in the 9–12 GeV bin. Data, NOMAD[24], MINOS[25] and T2K[47][48] are plotted with statistical and systematic uncertainties. The T2K results are isoscalar corrected with a value of 1.043 for the scintillator[47] point (0.85 GeV), derived from the lowest bin of FIG. 6.23, and a value of 0.98 for the iron[48] points (1.1, 2.0 and 3.3 GeV), derived from the MINOS correction[49].

E bin (GeV)	$\sigma(E)/E$	Stat. error (10^{-38} cm^2 / GeV / nucleon)	Syst. error	Total error
2–3	0.767	0.007	0.109	0.110
3–4	0.730	0.007	0.060	0.060
4–5	0.751	0.011	0.047	0.049
5–6	0.726	0.008	0.036	0.037
6–7	0.704	0.011	0.031	0.033
7–9	0.720	0.011	0.031	0.032
9–12	0.706	0.007	0.026	0.027
12–15	0.677	0.008	0.028	0.030
15–18	0.701	0.011	0.034	0.035
18–22	0.721	0.014	0.040	0.042
22–26	0.758	0.020	0.049	0.053
26–30	0.772	0.027	0.055	0.062
30–36	0.710	0.026	0.045	0.051
36–42	0.671	0.032	0.036	0.048
42–50	0.751	0.040	0.039	0.056

TABLE 9.1: Extracted cross section and statistical, systematic and total uncertainties for neutrinos in the forward horn current (FHC), neutrino-focusing beam normalized to NOMAD[24] (FIG. 9.15). The covariance matrix is tabulated in Table 9.2.

	2–3	3–4	4–5	5–6	6–7	7–9	9–12	12–15	15–18	18–22	22–26	26–30	30–36	36–42	42–50
2–3	12.016	4.494	0.063	-0.621	-0.155	0.284	-0.001	-0.668	-1.215	-1.407	-1.891	-2.439	-1.595	-0.932	-0.255
3–4	4.494	3.598	1.038	0.263	0.218	0.257	0.010	-0.325	-0.518	-0.658	-0.864	-1.113	-0.794	-0.567	-0.413
4–5	0.063	1.038	2.376	0.723	0.407	0.227	0.012	-0.072	0.162	0.193	0.299	0.279	0.097	-0.050	-0.152
5–6	-0.621	0.263	0.723	1.363	0.302	0.174	0.009	-0.026	0.121	0.097	0.145	0.128	-0.020	-0.074	-0.150
6–7	-0.155	0.218	0.407	0.302	1.094	0.147	0.006	-0.039	0.027	-0.022	-0.017	-0.065	-0.127	-0.114	-0.155
7–9	0.284	0.257	0.227	0.174	0.147	1.053	0.005	-0.076	-0.038	-0.095	-0.139	-0.199	-0.210	-0.153	-0.115
9–12	-0.001	0.010	0.012	0.009	0.006	0.005	0.728	0.004	0.003	0.002	0.003	0.006	0.002	0.005	0.005
12–15	-0.668	-0.325	-0.072	-0.026	-0.039	-0.076	0.004	0.883	0.127	0.160	0.221	0.319	0.251	0.180	0.103
15–18	-1.215	-0.518	0.162	0.121	0.027	-0.038	0.003	0.127	1.245	0.523	0.705	0.842	0.585	0.381	0.317
18–22	-1.407	-0.658	0.193	0.097	-0.022	-0.095	0.002	0.160	0.523	1.778	1.088	1.275	0.917	0.608	0.555
22–26	-1.891	-0.864	0.299	0.145	-0.017	-0.139	0.003	0.221	0.705	1.088	2.848	1.784	1.277	0.839	0.733
26–30	-2.439	-1.113	0.279	0.128	-0.065	-0.199	0.006	0.319	0.842	1.275	1.784	3.783	1.568	1.035	0.875
30–36	-1.595	-0.794	0.097	-0.020	-0.127	-0.210	0.002	0.251	0.585	0.917	1.277	1.568	2.650	0.790	0.679
36–42	-0.932	-0.567	-0.050	-0.074	-0.114	-0.153	0.005	0.180	0.381	0.608	0.839	1.035	0.790	2.281	0.516
42–50	-0.255	-0.413	-0.152	-0.150	-0.155	-0.115	0.005	0.103	0.317	0.555	0.733	0.875	0.679	0.516	3.133

TABLE 9.2: Covariance matrix for the extracted cross section for neutrinos in the forward horn current (FHC) beam normalized to NOMAD (Table 9.1). The bin boundaries are in units of GeV. The covariance elements are in units of 10^{-38} cm^2 / GeV / nucleon and scaled by a factor of 10^3.

E bin (GeV)	$\Phi(E)$	Stat. error	Syst. error	Total error
		(ν_μ / m^2 / 1e6 POT)		
2–3	76.046	0.927	7.431	7.488
3–4	77.528	0.838	5.094	5.162
4–5	29.776	0.490	2.258	2.311
5–6	12.243	0.180	0.764	0.785
6–7	7.908	0.151	0.446	0.471
7–9	10.435	0.181	0.559	0.587
9–12	9.780	0.123	0.498	0.513
12–15	6.115	0.093	0.320	0.333
15–18	3.477	0.064	0.185	0.196
18–22	2.620	0.056	0.160	0.170
22–26	1.331	0.039	0.089	0.097
26–30	0.751	0.028	0.050	0.058
30–36	0.726	0.028	0.041	0.050
36–42	0.497	0.025	0.028	0.038
42–50	0.452	0.025	0.028	0.038

TABLE 9.3: Extracted neutrino flux and statistical, systematic and total uncertainties in the forward horn current (FHC), neutrino-focusing beam normalized to NOMAD[24]. Note that the values and uncertainties are not bin width normalized. The covariance matrix is tabulated in Table 9.4.

	2–3	3–4	4–5	5–6	6–7	7–9	9–12	12–15	15–18	18–22	22–26	26–30	30–36	36–42	42–50
2–3	56.077	19.744	-1.529	-0.807	-0.005	0.345	0.632	0.507	-0.124	-0.309	-0.213	-0.109	-0.045	-0.032	-0.052
3–4	19.744	26.651	4.688	1.180	0.613	0.753	0.555	0.317	0.158	0.084	0.047	0.027	0.030	0.011	0.003
4–5	-1.529	4.688	5.340	1.018	0.346	0.341	0.125	0.014	0.132	0.149	0.095	0.050	0.033	0.015	0.016
5–6	-0.807	1.180	1.018	0.617	0.139	0.154	0.078	0.035	0.051	0.050	0.031	0.017	0.011	0.006	0.007
6–7	-0.005	0.613	0.346	0.139	0.222	0.112	0.080	0.047	0.033	0.028	0.015	0.008	0.007	0.005	0.004
7–9	0.345	0.753	0.341	0.154	0.112	0.345	0.117	0.071	0.043	0.034	0.017	0.010	0.009	0.006	0.006
9–12	0.632	0.555	0.125	0.078	0.080	0.117	0.263	0.073	0.038	0.029	0.013	0.007	0.008	0.006	0.006
12–15	0.507	0.317	0.014	0.035	0.047	0.071	0.073	0.111	0.023	0.015	0.007	0.004	0.005	0.004	0.003
15–18	-0.124	0.158	0.132	0.051	0.033	0.043	0.038	0.023	0.038	0.016	0.008	0.005	0.004	0.003	0.003
18–22	-0.309	0.084	0.149	0.050	0.028	0.034	0.029	0.015	0.016	0.029	0.009	0.005	0.004	0.003	0.003
22–26	-0.213	0.047	0.095	0.031	0.015	0.017	0.013	0.007	0.008	0.009	0.009	0.003	0.002	0.001	0.001
26–30	-0.109	0.027	0.050	0.017	0.008	0.010	0.007	0.004	0.005	0.005	0.003	0.003	0.001	0.001	0.001
30–36	-0.045	0.030	0.033	0.011	0.007	0.009	0.008	0.005	0.004	0.004	0.002	0.001	0.003	0.001	0.001
36–42	-0.032	0.011	0.015	0.006	0.005	0.006	0.006	0.004	0.003	0.003	0.001	0.001	0.001	0.001	0.000
42–50	-0.052	0.003	0.016	0.007	0.004	0.006	0.006	0.003	0.003	0.003	0.001	0.001	0.001	0.000	0.001

TABLE 9.4: Covariance matrix for the extracted neutrino flux in the forward horn current (FHC) beam normalized to NOMAD[24] (Table 9.3). The bin boundaries are in units of GeV. The covariance elements are in units of ν_μ / m^2 / 1e6 POT.

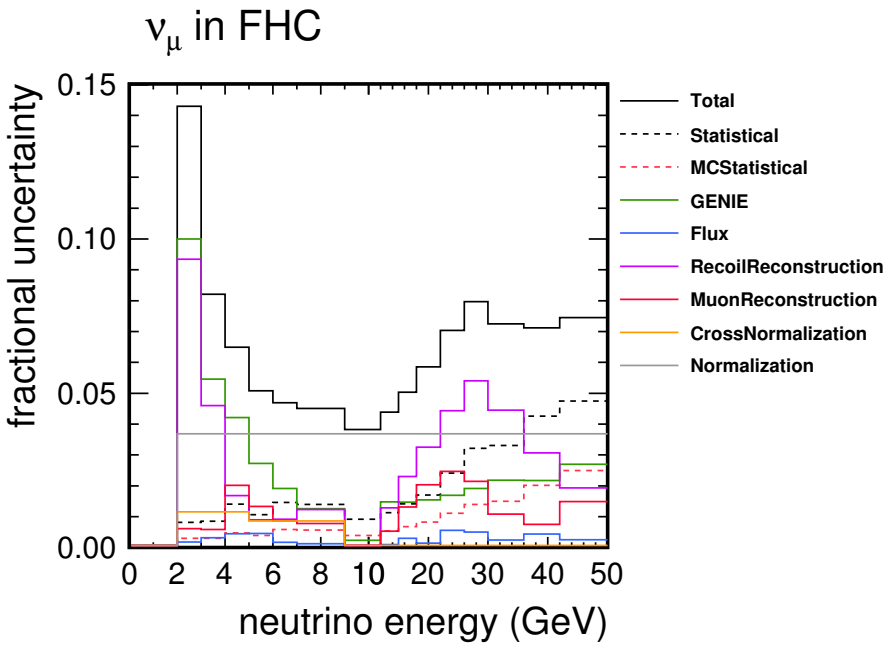

FIG. 9.16: Total systematic and statistical uncertainty summary of the extracted cross section for neutrinos normalized to NOMAD (FIG. 9.15). External normalization uncertainty is reduced relative to FIG. 8.4.

9.4 Isoscalar corrected antineutrino cross section

FIG. 9.17 shows the extracted antineutrino cross section in the reverse horn current (RHC), antineutrino-focusing beam compared to the results of the MINOS[25], IHEP-ITEP[50] and IHEP-JINR[51] experiments. The extracted cross section is isoscalar corrected by the ratio in FIG. 6.24 and normalized to the simulation (GENIE on ^{12}C) in the 9–12 GeV bin. Table 9.5 lists the isoscalar corrected extracted antineutrino cross section in tabular form.

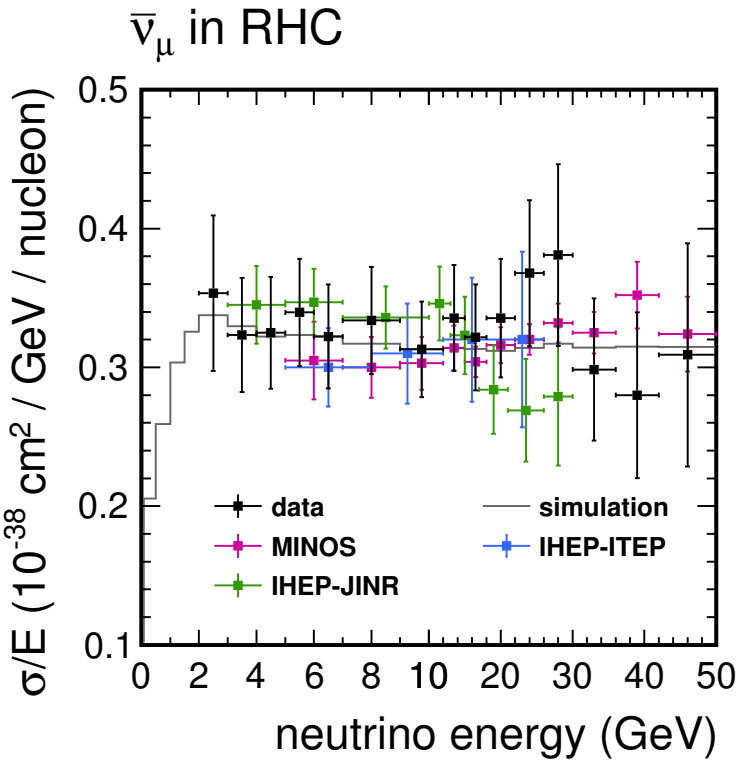

FIG. 9.17: Isoscalar corrected extracted cross section for antineutrinos in the reverse horn current (RHC), antineutrino-focusing beam. The extracted cross section is normalized to the simulation in the 9–12 GeV bin. Data, MINOS[25], IHEP-ITEP[50] and IHEP-JINR[51] are plotted with statistical and systematic uncertainties.

E bin (GeV)	$\sigma(E)/E$	Stat. error (10^{-38} cm^2 / GeV / nucleon)	Syst. error	Total error
2–3	0.354	0.004	0.056	0.056
3–4	0.323	0.004	0.041	0.041
4–5	0.325	0.007	0.040	0.040
5–6	0.340	0.008	0.038	0.039
6–7	0.322	0.010	0.036	0.037
7–9	0.334	0.010	0.037	0.039
9–12	0.313	0.007	0.034	0.034
12–15	0.336	0.010	0.037	0.038
15–18	0.322	0.012	0.036	0.038
18–22	0.336	0.017	0.039	0.043
22–26	0.368	0.028	0.045	0.053
26–30	0.381	0.045	0.047	0.066
30–36	0.298	0.033	0.039	0.051
36–42	0.280	0.047	0.037	0.060
42–50	0.309	0.067	0.044	0.080

TABLE 9.5: Isoscalar corrected extracted cross section and statistical, systematic and total uncertainties for antineutrinos in the reverse horn current (RHC), antineutrino-focusing beam. The covariance matrix is tabulated in Table 9.6.

	2–3	3–4	4–5	5–6	6–7	7–9	9–12	12–15	15–18	18–22	22–26	26–30	30–36	36–42	42–50
2–3	3.144	0.699	-0.031	0.009	0.148	0.150	0.005	-0.134	-0.294	-0.434	-0.549	-0.627	-0.652	-0.580	-0.802
3–4	0.699	1.686	0.157	0.051	0.093	0.064	-0.010	-0.050	-0.100	-0.166	-0.233	-0.275	-0.240	-0.211	-0.324
4–5	-0.031	0.157	1.626	0.085	0.053	0.006	-0.019	0.016	0.065	0.086	0.080	0.062	0.092	0.133	0.124
5–6	0.009	0.051	0.085	1.492	0.034	0.021	-0.006	0.009	0.018	0.021	0.016	-0.020	-0.001	0.023	-0.021
6–7	0.148	0.093	0.053	0.034	1.397	0.037	-0.003	-0.008	-0.018	-0.026	-0.043	-0.088	-0.090	-0.034	-0.100
7–9	0.150	0.064	0.006	0.021	0.037	1.488	0.002	-0.007	-0.020	-0.033	-0.044	-0.074	-0.075	-0.042	-0.105
9–12	0.005	-0.010	-0.019	-0.006	-0.003	0.002	1.185	-0.000	-0.002	-0.001	0.001	0.003	-0.002	-0.003	-0.001
12–15	-0.134	-0.050	0.016	0.009	-0.008	-0.007	-0.000	1.451	0.037	0.051	0.054	0.060	0.085	0.072	0.067
15–18	-0.294	-0.100	0.065	0.018	-0.018	-0.020	-0.002	0.037	1.456	0.124	0.153	0.168	0.169	0.160	0.206
18–22	-0.434	-0.166	0.086	0.021	-0.026	-0.033	-0.001	0.051	0.124	1.823	0.281	0.288	0.237	0.277	0.362
22–26	-0.549	-0.233	0.080	0.016	-0.043	-0.044	0.001	0.054	0.153	0.281	2.776	0.398	0.297	0.345	0.483
26–30	-0.627	-0.275	0.062	-0.020	-0.088	-0.074	0.003	0.060	0.168	0.288	0.398	4.293	0.423	0.397	0.598
30–36	-0.652	-0.240	0.092	-0.001	-0.090	-0.075	-0.002	0.085	0.169	0.237	0.297	0.423	2.627	0.363	0.485
36–42	-0.580	-0.211	0.133	0.023	-0.034	-0.042	-0.003	0.072	0.160	0.277	0.345	0.397	0.363	3.571	0.548
42–50	-0.802	-0.324	0.124	-0.021	-0.100	-0.105	-0.001	0.067	0.206	0.362	0.483	0.598	0.485	0.548	6.478

TABLE 9.6: Covariance matrix for the isoscalar corrected extracted cross section for antineutrinos in the reverse horn current (RHC) beam (Table 9.5). The bin boundaries are in units of GeV. The covariance elements are in units of 10^{-38} cm^2 / GeV / nucleon and scaled by a factor of 10^3.

9.5 Summary

The low-ν analysis results in a shape measurement of the neutrino flux and charged-current inclusive cross section. The absolute normalization is set by an external constraint. For the result normalized to the cross section model in GENIE, the neutrino (FIG. 8.1) and antineutrino (FIG. 8.10) cross sections agree with the simulation within uncertainties.

FIG. 9.15 compares the measured neutrino cross section to the results of the NOMAD[24], MINOS[25] and T2K[47][48] experiments. For this comparison, the cross section is isoscalar corrected and normalized to NOMAD in the 9–12 GeV bin. The results of this analysis agree with NOMAD and MINOS within uncertainties. The T2K results are more erratic, particularly the high point at 2 GeV, but the uncertainties are large. MINERνA could potentially measure a cross section at 1–2 GeV if events in which the muon failed to enter MINOS are included. This would lower the energy threshold for reconstruction at the expense of losing information on the charge of the muon.

FIG. 9.17 compares the measured antineutrino cross section to the results of the MINOS[25], IHEP-ITEP[50] and IHEP-JINR[51] experiments. For this comparison, the cross section is isoscalar corrected, but the normalization remains as the simulation in the 9–12 GeV bin. Not shown on the plot is the result of the Gargamelle[52] bubble chamber experiment, which measured a cross section of $0.26 \pm 0.02 \times 10^{-38}\text{cm}^2/\text{GeV/nucleon}$ for neutrino energy less than 8 GeV. Gargamelle lacked the statistics to measure the energy depedence of the cross section within this range. The results of this analysis and IHEP-JINR are the only measurements of the energy dependence of the antineutrino cross section below 5 GeV.

The measured neutrino (FIG. 8.19) and antineutrino (FIG. 8.27) fluxes provide a valuable constraint on the existing flux model derived from a simulation of the NuMI beamline weighted by hadron production data[40]. The measured fluxes show a deficit in

the peak of the energy spectrum (2–5 GeV) relative to the simulated flux which has also been observed by other MINERνA analyses.

APPENDIX A

Calorimetry for Charged-Current Neutrino Interactions

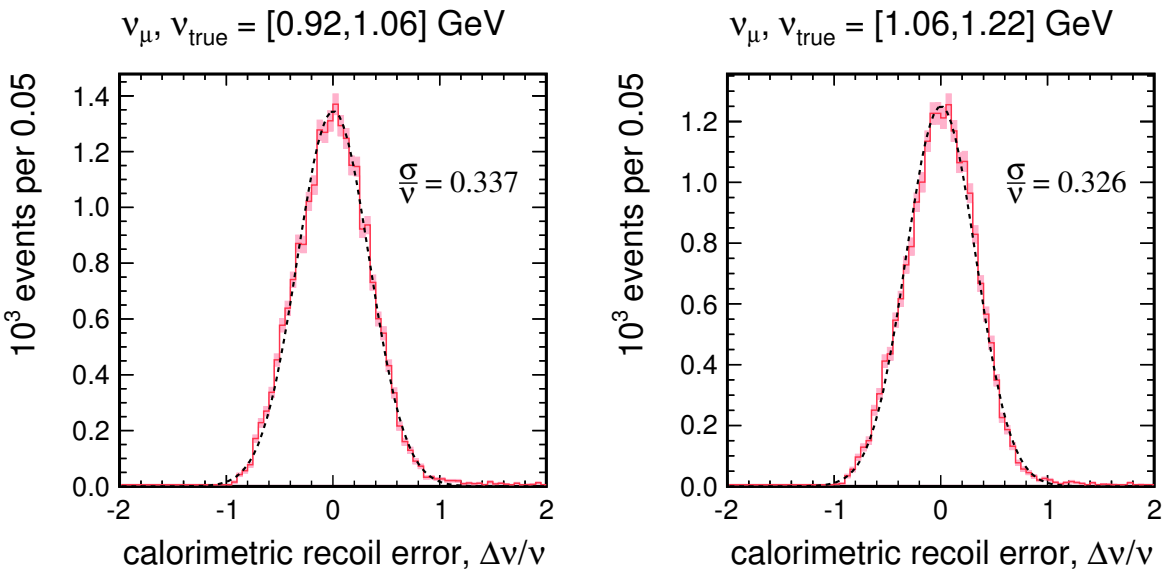

(a) $\nu_{true} = [0.92, 1.06]$ GeV

(b) $\nu_{true} = [1.06, 1.22]$ GeV

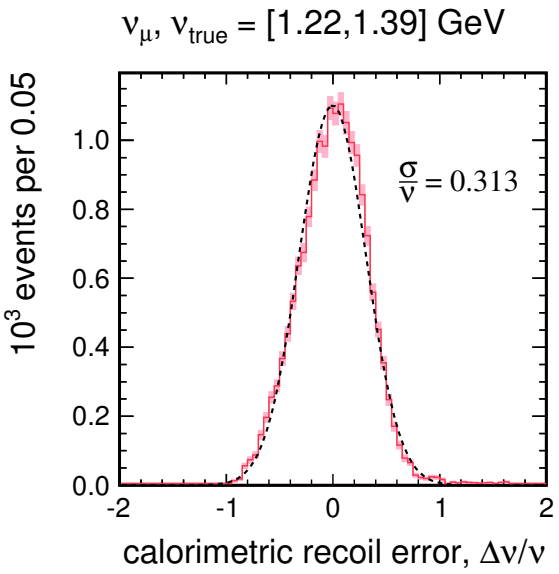

(c) $\nu_{true} = [1.22, 1.39]$ GeV

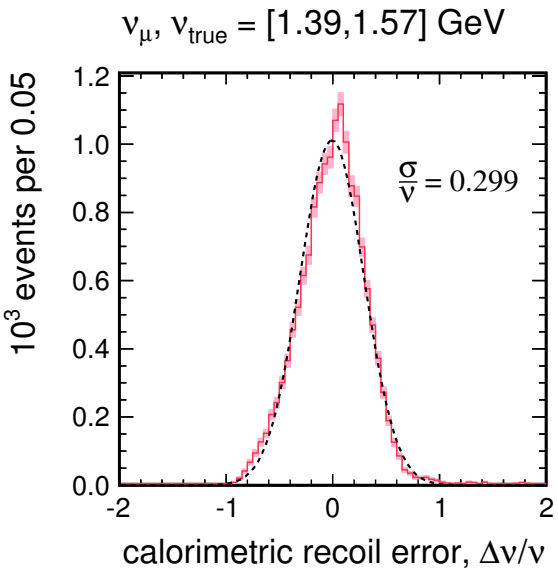

(d) $\nu_{true} = [1.39, 1.57]$ GeV

FIG. A.1: Calorimetric recoil error, $\Delta\nu/\nu = (\nu_{reco} - \nu_{true})/\nu_{true}$ for charged-current neutrino interactions; $\nu_{true} = [0.92, 1.57]$ GeV.

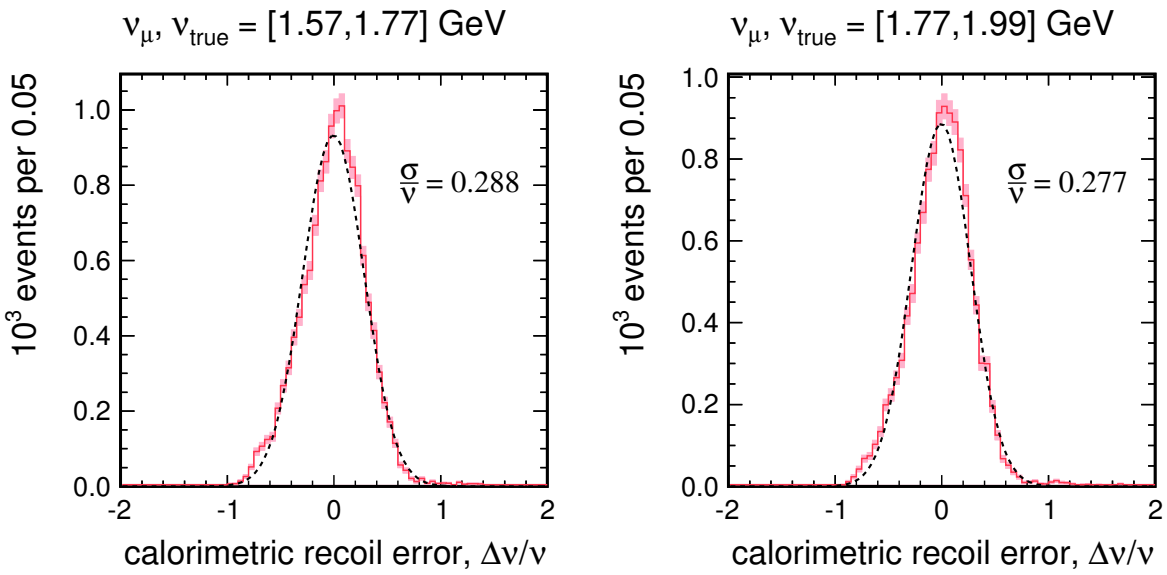

(a) $\nu_{true} = [1.57, 1.77]$ GeV

(b) $\nu_{true} = [1.77, 1.99]$ GeV

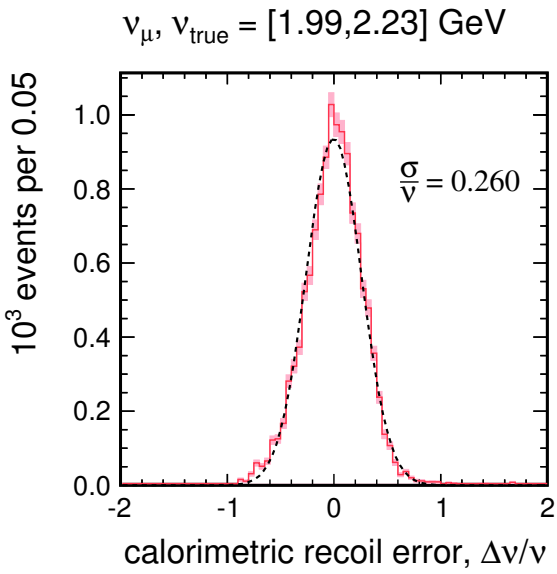

(c) $\nu_{true} = [1.99, 2.23]$ GeV

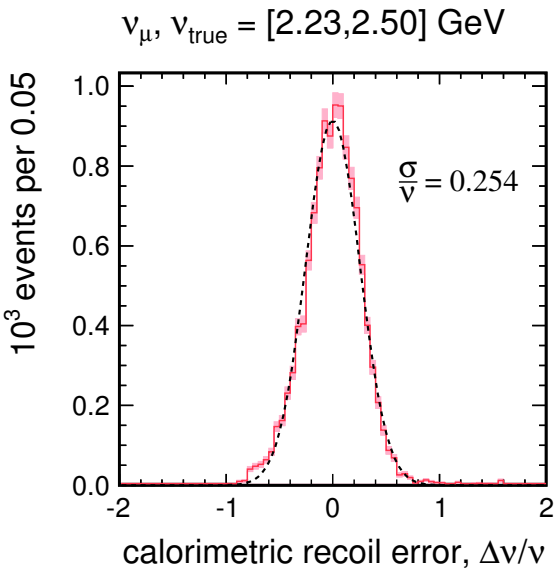

(d) $\nu_{true} = [2.23, 2.50]$ GeV

FIG. A.2: Calorimetric recoil error, $\Delta\nu/\nu = (\nu_{reco} - \nu_{true})/\nu_{true}$ for charged-current neutrino interactions; $\nu_{true} = [1.57, 2.50]$ GeV.

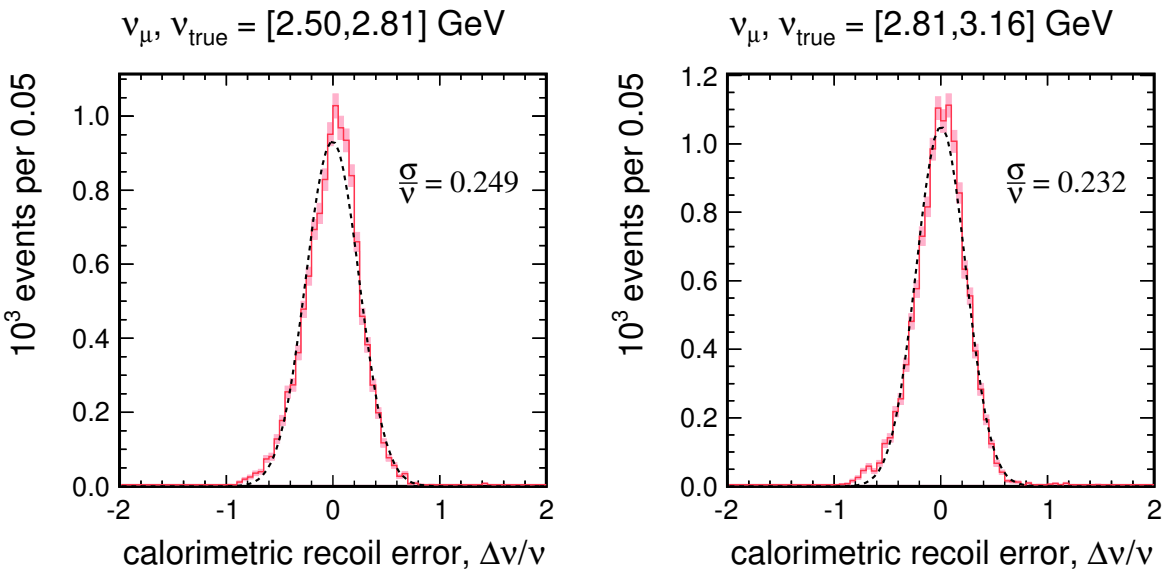

(a) $\nu_{true} = [2.50, 2.81]$ GeV

(b) $\nu_{true} = [2.81, 3.16]$ GeV

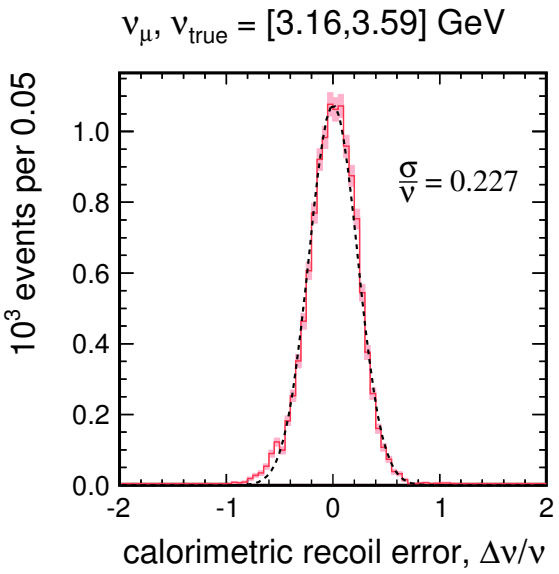

(c) $\nu_{true} = [3.16, 3.59]$ GeV

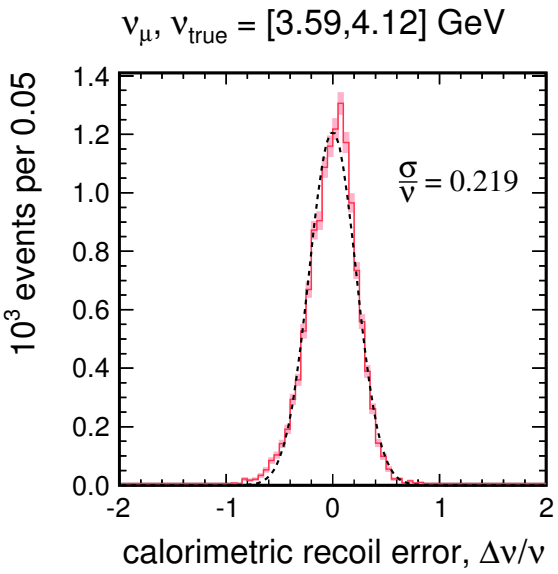

(d) $\nu_{true} = [3.59, 4.12]$ GeV

FIG. A.3: Calorimetric recoil error, $\Delta\nu/\nu = (\nu_{reco} - \nu_{true})/\nu_{true}$ for charged-current neutrino interactions; $\nu_{true} = [2.50, 4.12]$ GeV.

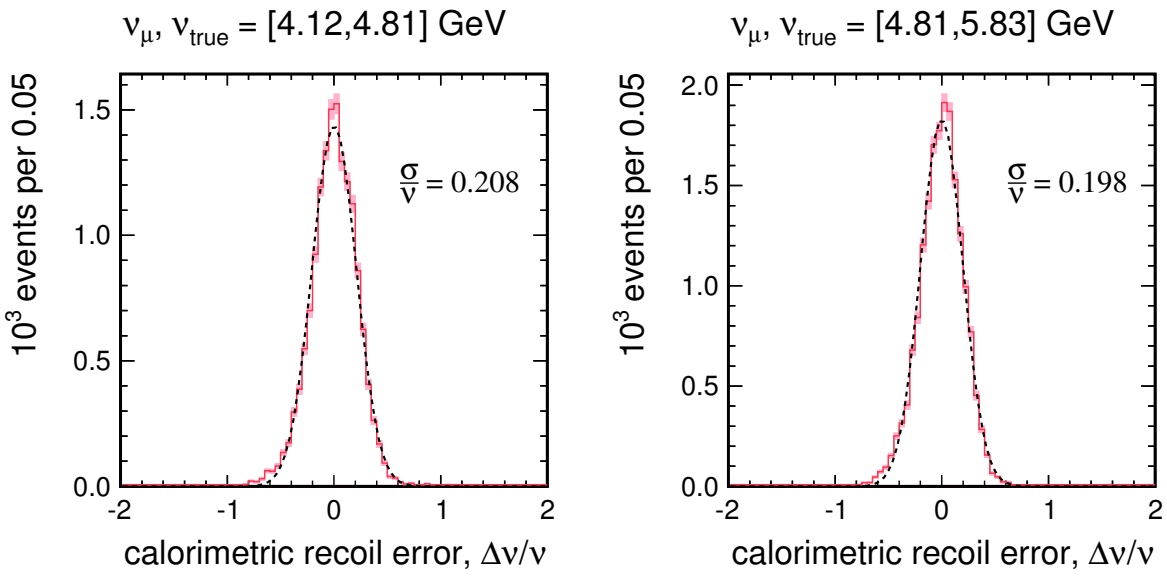

(a) $\nu_{true} = [4.12, 4.81]$ GeV

(b) $\nu_{true} = [4.81, 5.83]$ GeV

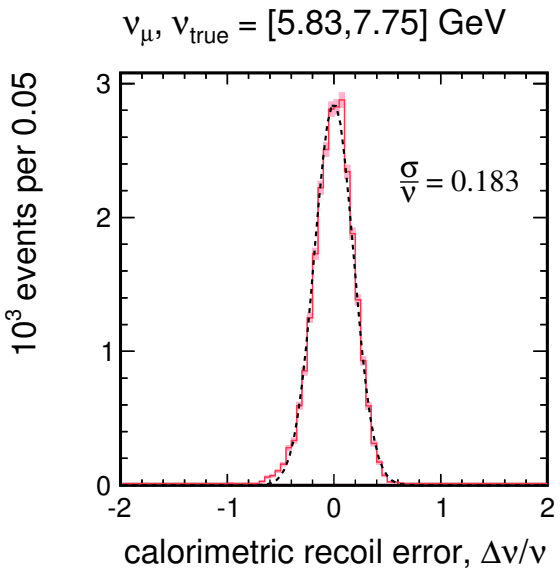

(c) $\nu_{true} = [5.83, 7.75]$ GeV

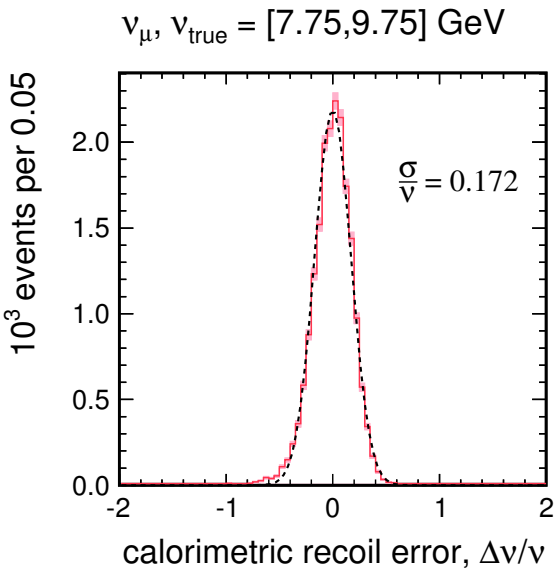

(d) $\nu_{true} = [7.75, 9.75]$ GeV

FIG. A.4: Calorimetric recoil error, $\Delta\nu/\nu = (\nu_{reco} - \nu_{true})/\nu_{true}$ for charged-current neutrino interactions; $\nu_{true} = [4.12, 9.75]$ GeV.

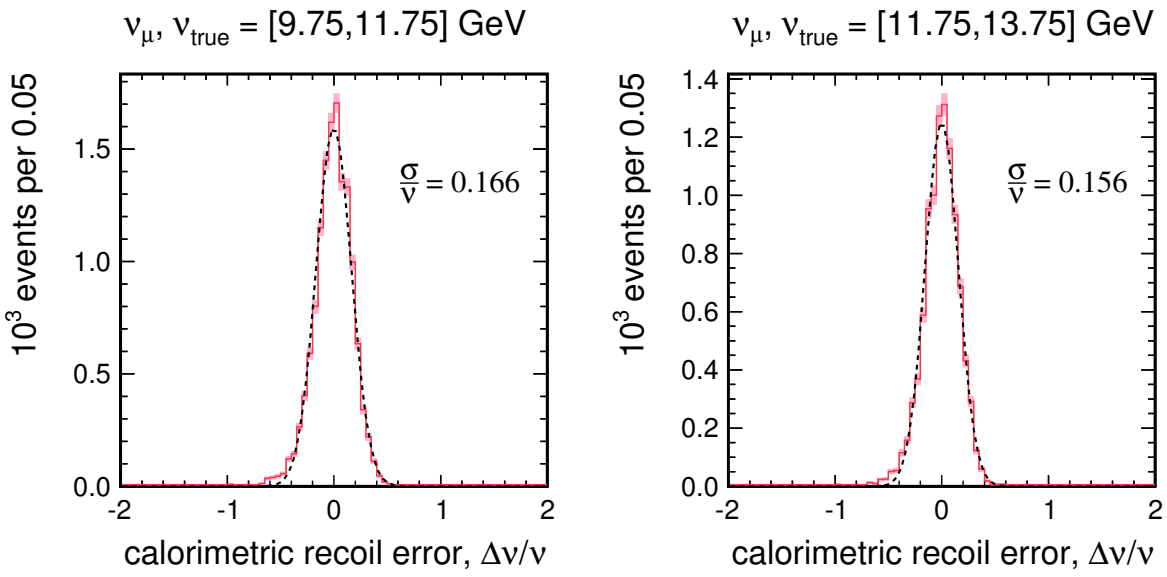

(a) $\nu_{true} = [9.75, 11.75]$ GeV

(b) $\nu_{true} = [11.75, 13.75]$ GeV

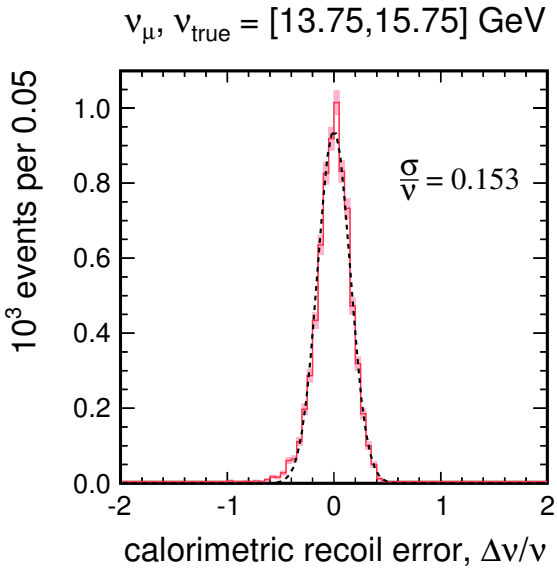

(c) $\nu_{true} = [13.75, 15.75]$ GeV

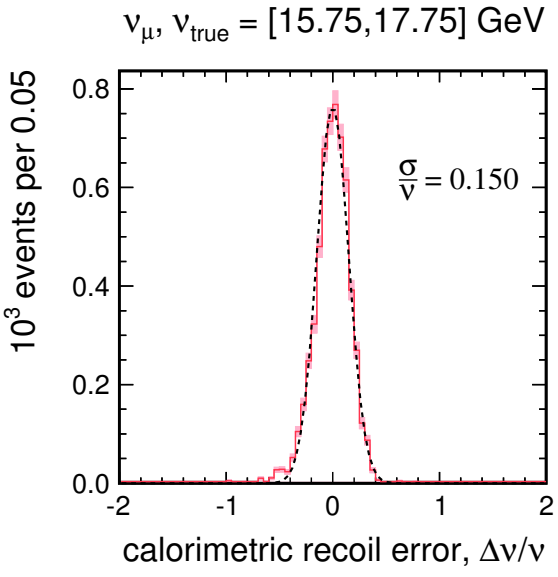

(d) $\nu_{true} = [15.75, 17.75]$ GeV

FIG. A.5: Calorimetric recoil error, $\Delta\nu/\nu = (\nu_{reco} - \nu_{true})/\nu_{true}$ for charged-current neutrino interactions; $\nu_{true} = [9.75, 17.75]$ GeV.

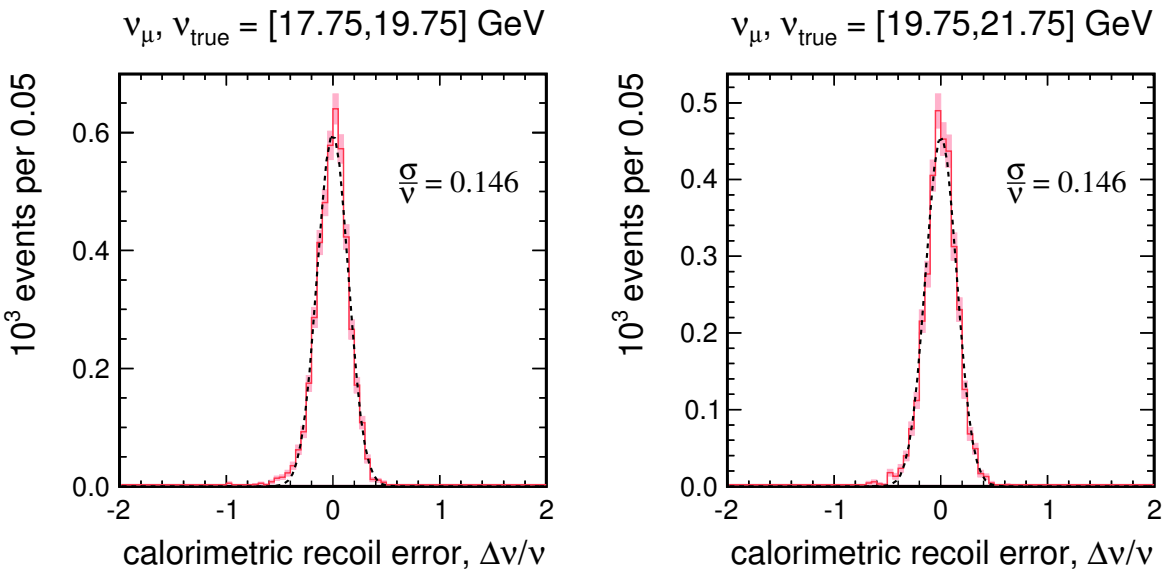

(a) $\nu_{true} = [17.75, 19.75]$ GeV

(b) $\nu_{true} = [19.75, 21.75]$ GeV

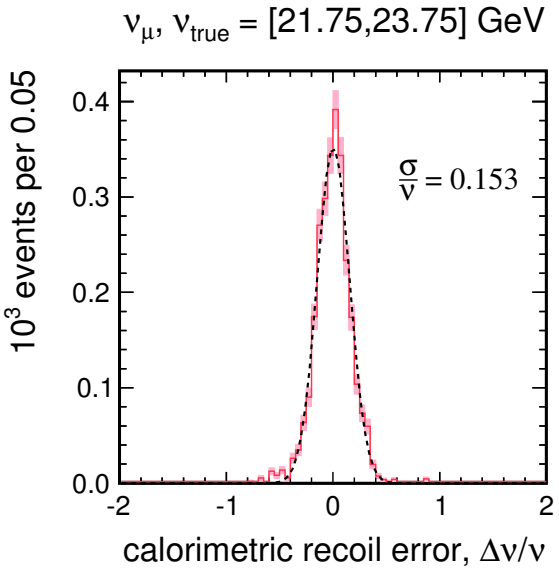

(c) $\nu_{true} = [21.75, 23.75]$ GeV

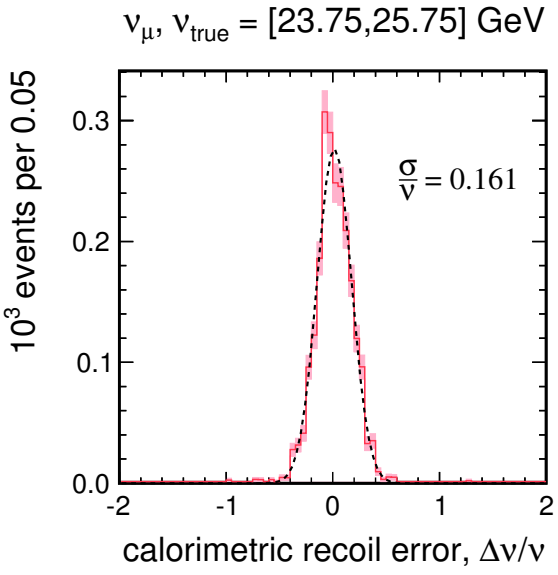

(d) $\nu_{true} = [23.75, 25.75]$ GeV

FIG. A.6: Calorimetric recoil error, $\Delta\nu/\nu = (\nu_{reco} - \nu_{true})/\nu_{true}$ for charged-current neutrino interactions; $\nu_{true} = [17.75, 25.75]$ GeV.

APPENDIX B

Calorimetry for Charged-Current Antineutrino Interactions

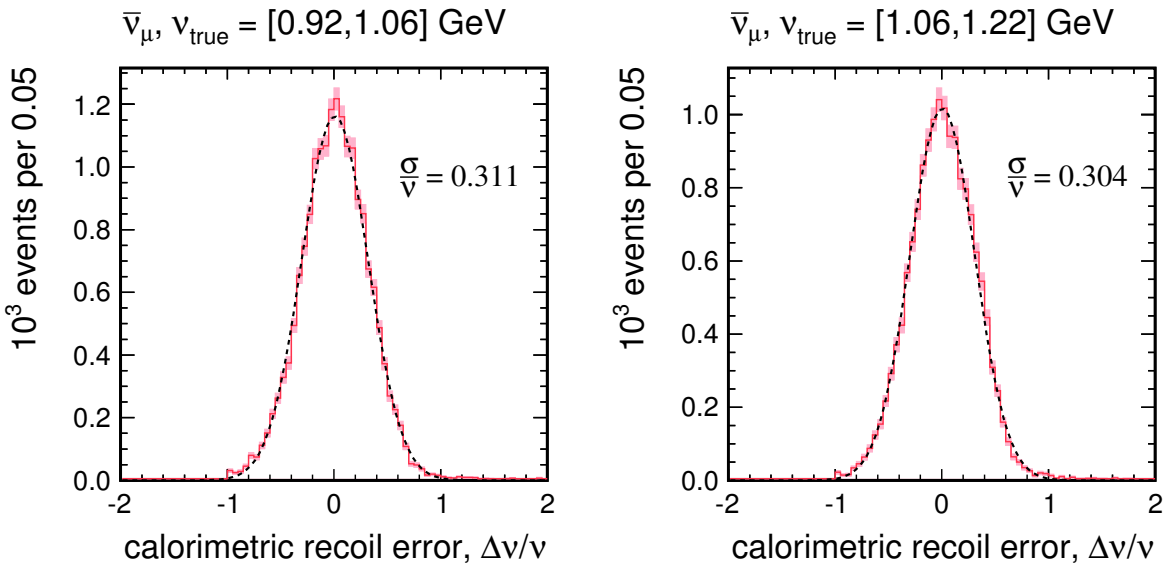

(a) $\nu_{true} = [0.92, 1.06]$ GeV

(b) $\nu_{true} = [1.06, 1.22]$ GeV

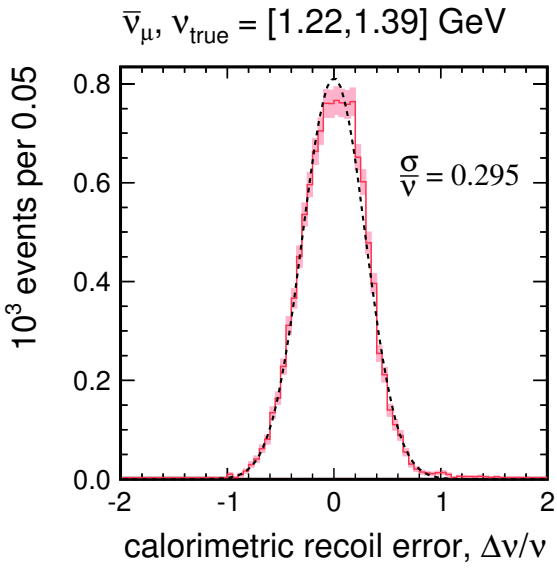

(c) $\nu_{true} = [1.22, 1.39]$ GeV

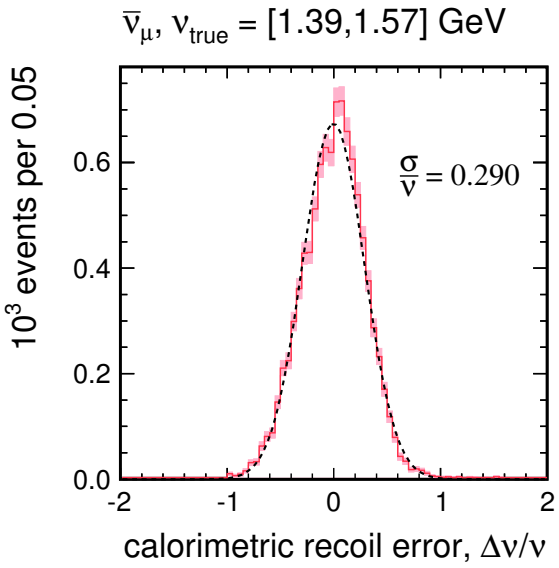

(d) $\nu_{true} = [1.39, 1.57]$ GeV

FIG. B.1: Calorimetric recoil error, $\Delta\nu/\nu = (\nu_{reco} - \nu_{true})/\nu_{true}$ for charged-current antineutrino interactions; $\nu_{true} = [0.92, 1.57]$ GeV.

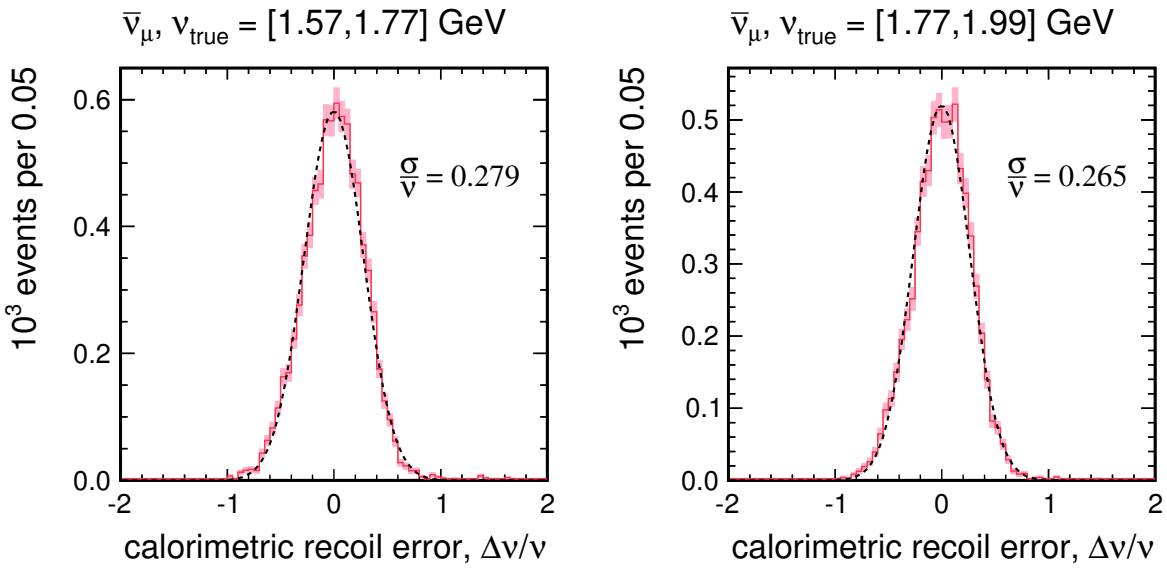

(a) $\nu_{true} = [1.57, 1.77]$ GeV

(b) $\nu_{true} = [1.77, 1.99]$ GeV

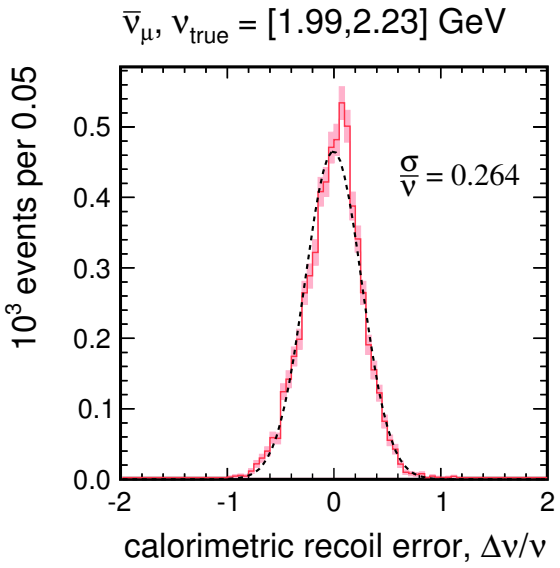

(c) $\nu_{true} = [1.99, 2.23]$ GeV

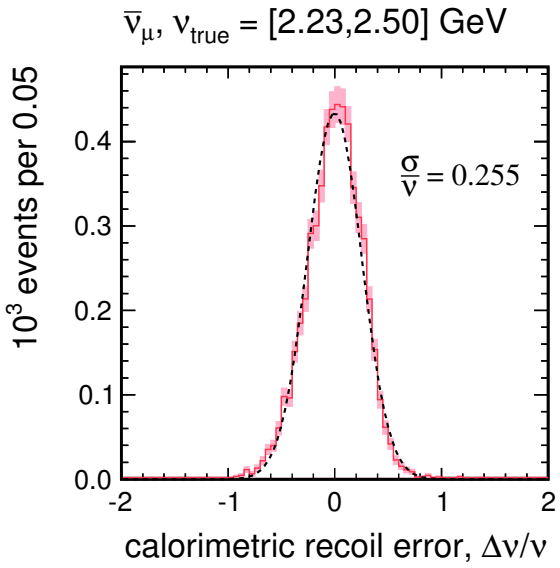

(d) $\nu_{true} = [2.23, 2.50]$ GeV

FIG. B.2: Calorimetric recoil error, $\Delta\nu/\nu = (\nu_{reco} - \nu_{true})/\nu_{true}$ for charged-current antineutrino interactions; $\nu_{true} = [1.57, 2.50]$ GeV.

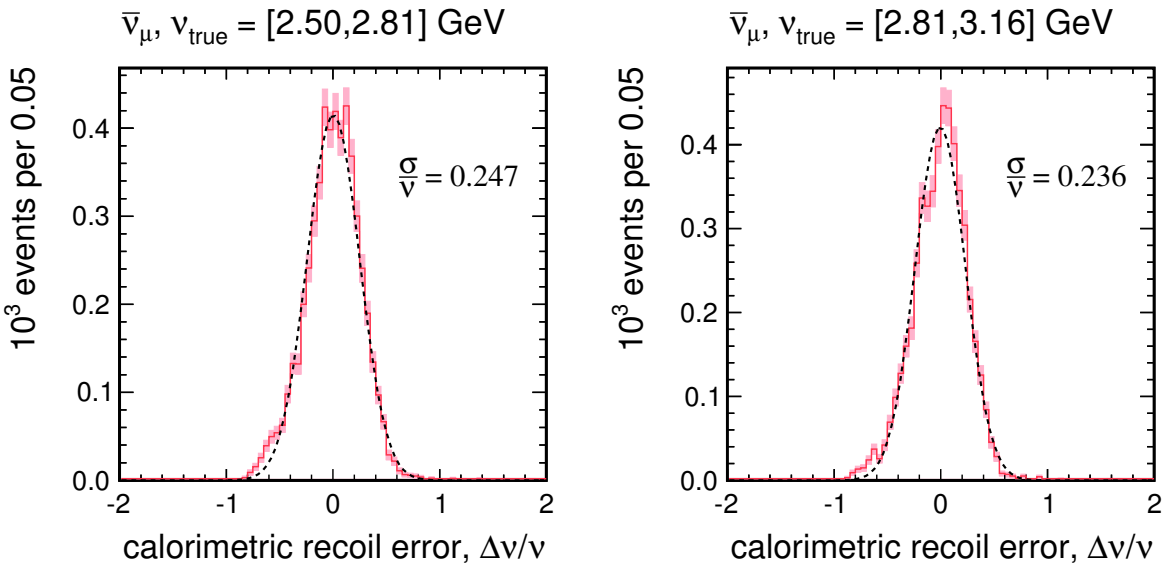

(a) $\nu_{true} = [2.50, 2.81]$ GeV

(b) $\nu_{true} = [2.81, 3.16]$ GeV

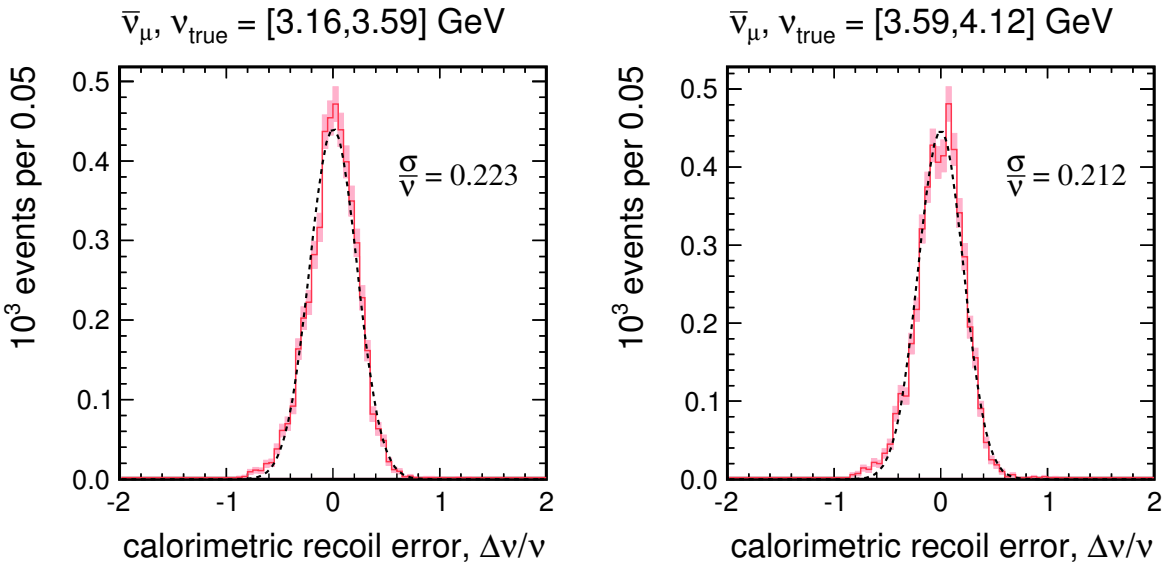

(c) $\nu_{true} = [3.16, 3.59]$ GeV

(d) $\nu_{true} = [3.59, 4.12]$ GeV

FIG. B.3: Calorimetric recoil error, $\Delta\nu/\nu = (\nu_{reco} - \nu_{true})/\nu_{true}$ for charged-current antineutrino interactions; $\nu_{true} = [2.50, 4.12]$ GeV.

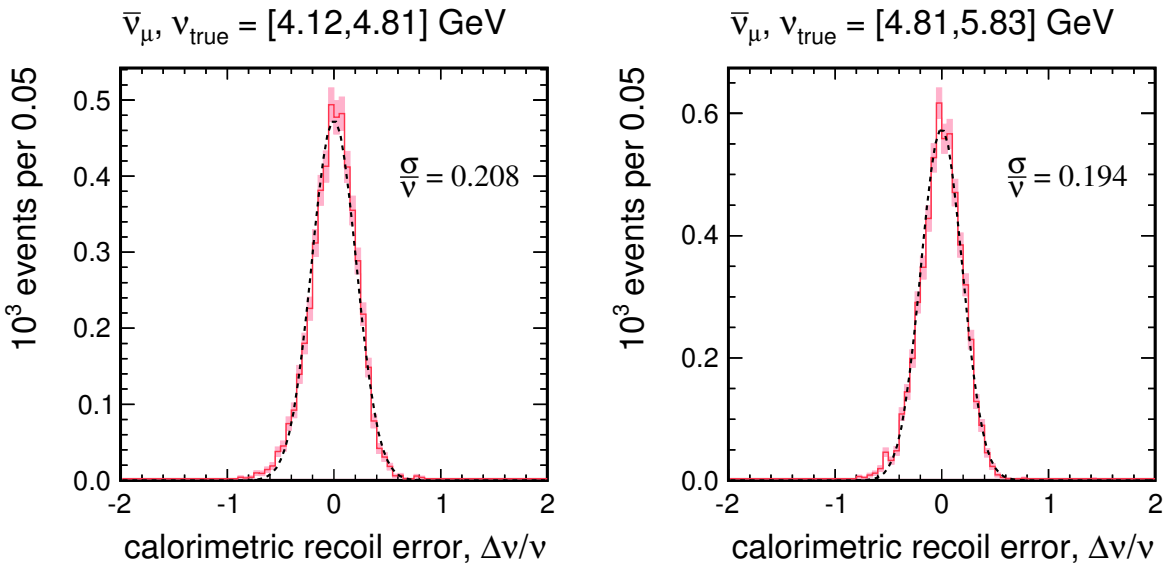

(a) $\nu_{true} = [4.12, 4.81]$ GeV

(b) $\nu_{true} = [4.81, 5.83]$ GeV

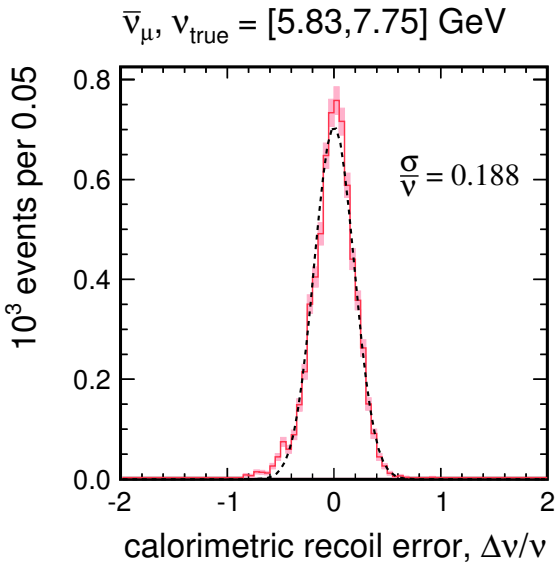

(c) $\nu_{true} = [5.83, 7.75]$ GeV

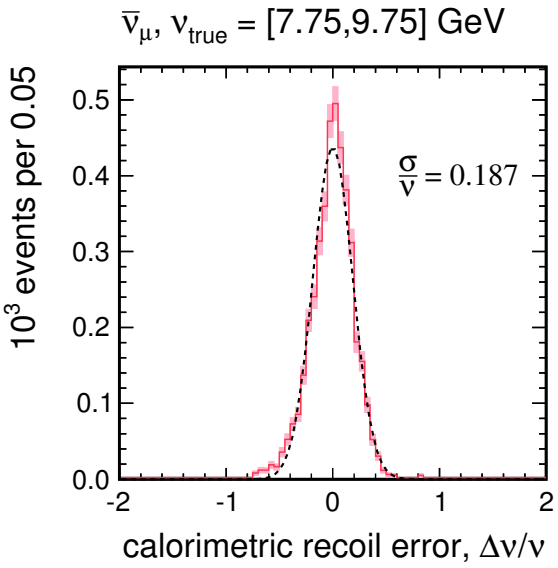

(d) $\nu_{true} = [7.75, 9.75]$ GeV

FIG. B.4: Calorimetric recoil error, $\Delta\nu/\nu = (\nu_{reco} - \nu_{true})/\nu_{true}$ for charged-current antineutrino interactions; $\nu_{true} = [4.12, 9.75]$ GeV.

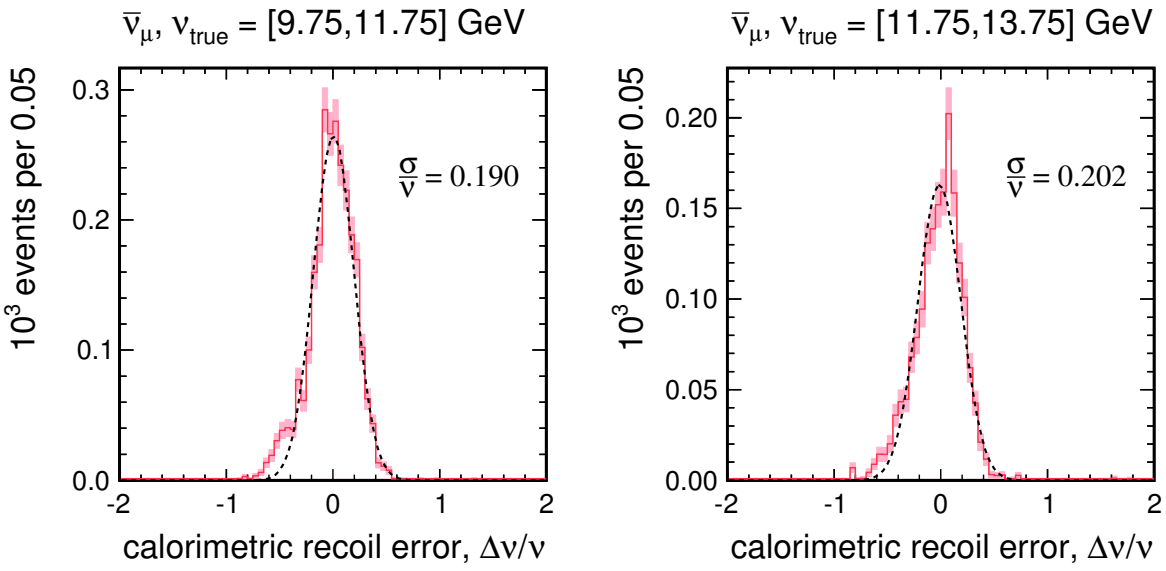

(a) $\nu_{true} = [9.75, 11.75]$ GeV

(b) $\nu_{true} = [11.75, 13.75]$ GeV

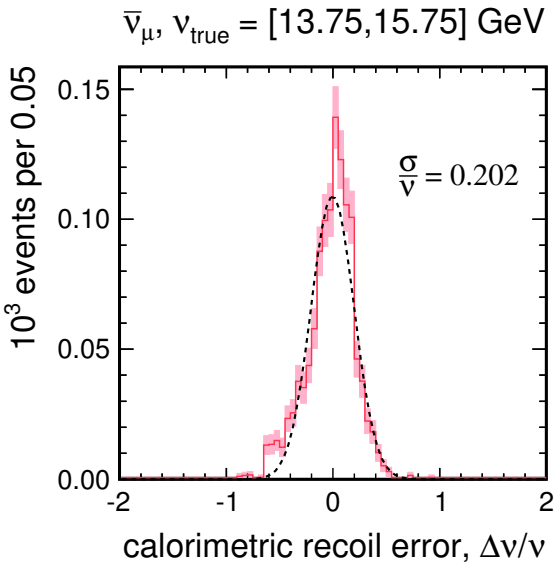

(c) $\nu_{true} = [13.75, 15.75]$ GeV

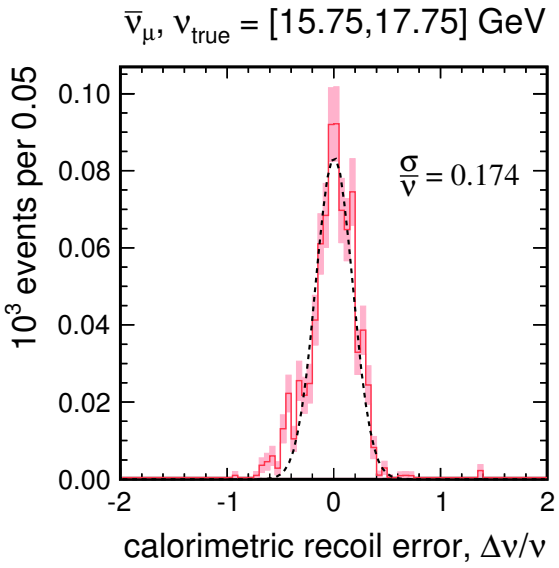

(d) $\nu_{true} = [15.75, 17.75]$ GeV

FIG. B.5: Calorimetric recoil error, $\Delta\nu/\nu = (\nu_{reco} - \nu_{true})/\nu_{true}$ for charged-current antineutrino interactions; $\nu_{true} = [9.75, 17.75]$ GeV.

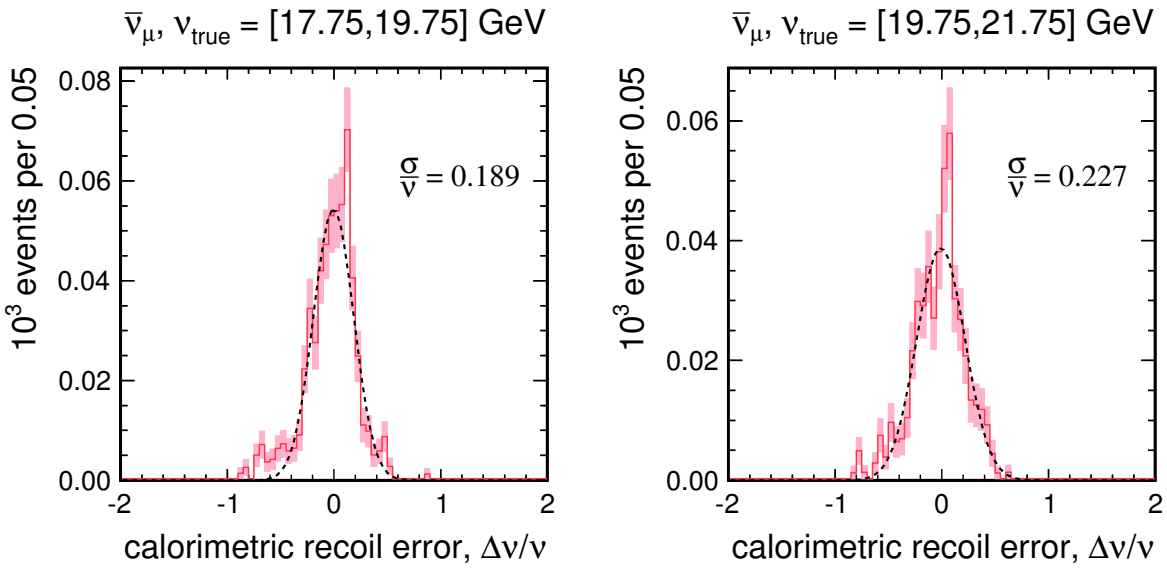

(a) $\nu_{true} = [17.75, 19.75]$ GeV

(b) $\nu_{true} = [19.75, 21.75]$ GeV

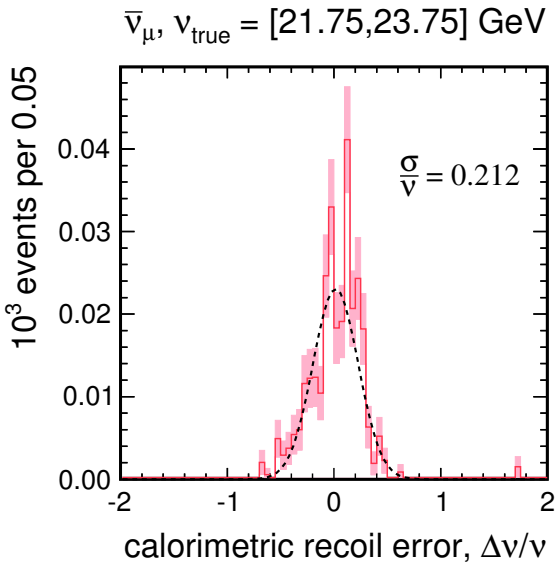

(c) $\nu_{true} = [21.75, 23.75]$ GeV

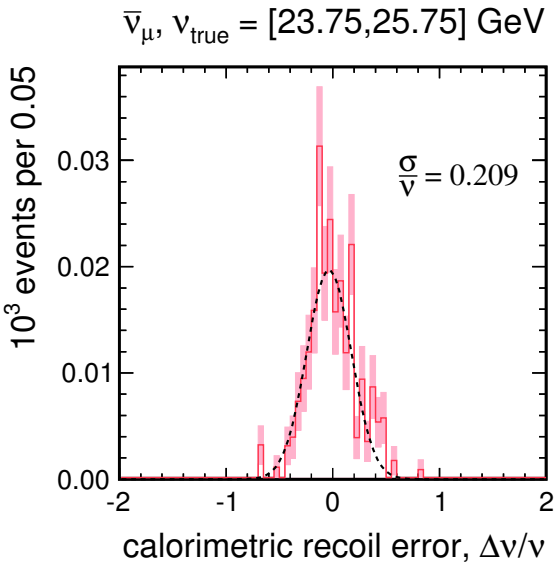

(d) $\nu_{true} = [23.75, 25.75]$ GeV

FIG. B.6: Calorimetric recoil error, $\Delta\nu/\nu = (\nu_{reco} - \nu_{true})/\nu_{true}$ for charged-current antineutrino interactions; $\nu_{true} = [17.75, 25.75]$ GeV.

APPENDIX C

Neutrinos in the Reverse Horn Current (RHC) Beam

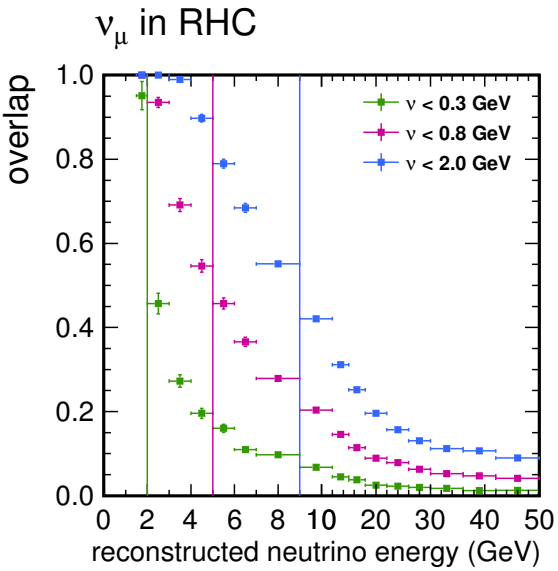

FIG. C.1: The fraction of the inclusive data sample with reconstructed ν less than the given ν cut for neutrinos in the reverse horn current (RHC), antineutrino-focusing beam; equivalent to the ratio of the low-ν interaction rates (FIG. C.3 – C.5) to the inclusive interaction rate (FIG. C.2). Error bars show statistical uncertainties only. Vertical lines mark the minimum neutrino energy for each ν cut.

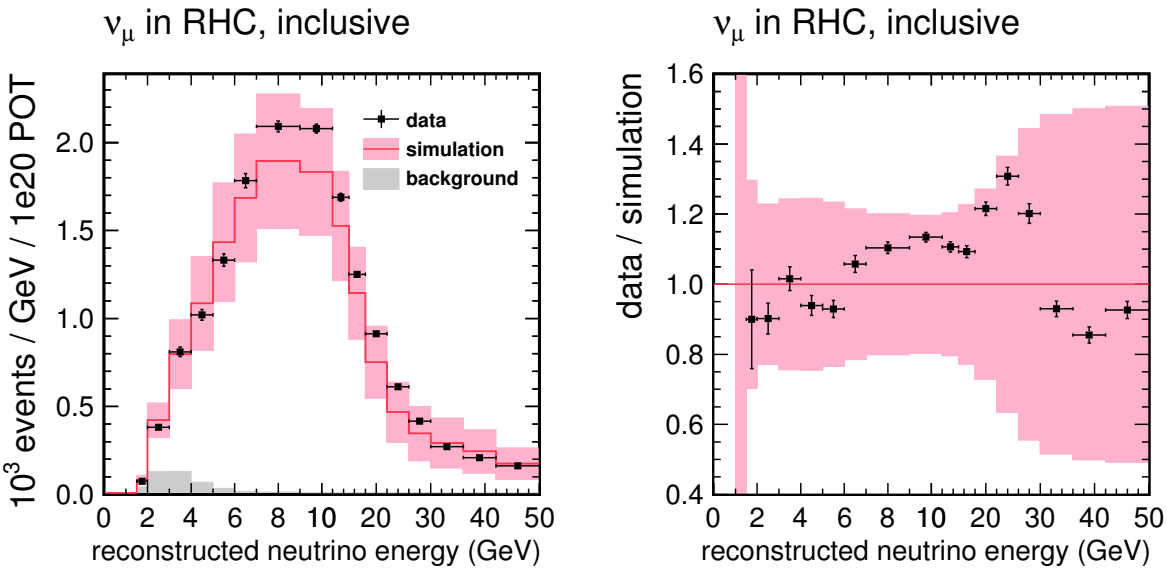

FIG. C.2: Reconstructed inclusive neutrino interaction rate (left) and ratio of data to simulation (right) in the reverse horn current (RHC), antineutrino-focusing beam. Data are plotted with statistical uncertainties; simulated data are plotted with statistical and systematic uncertainties.

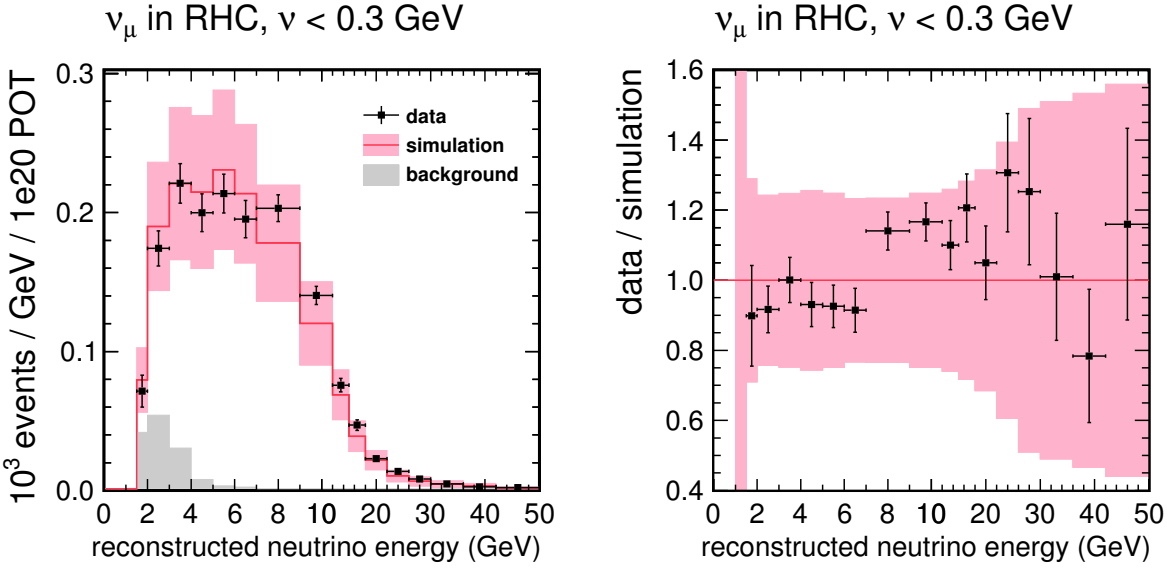

FIG. C.3: Reconstructed $\nu < 300$ MeV neutrino interaction rate (left) and ratio of data to simulation (right) in the reverse horn current (RHC), antineutrino-focusing beam. Data are plotted with statistical uncertainties; simulated data are plotted with statistical and systematic uncertainties.

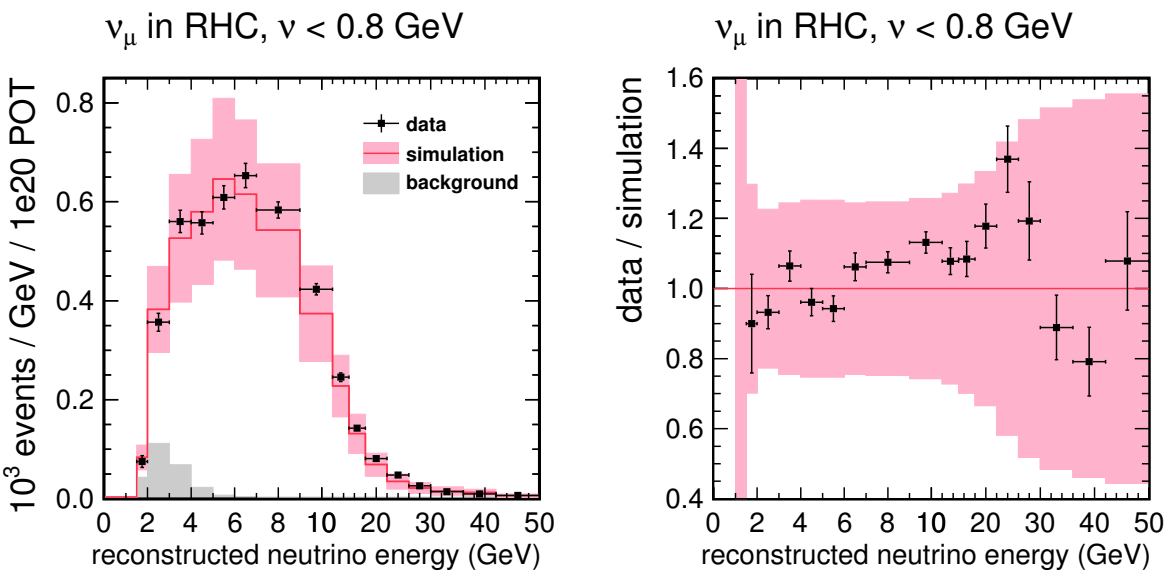

FIG. C.4: Reconstructed $\nu < 800$ MeV neutrino interaction rate (left) and ratio of data to simulation (right) in the reverse horn current (RHC), antineutrino-focusing beam. Data are plotted with statistical uncertainties; simulated data are plotted with statistical and systematic uncertainties.

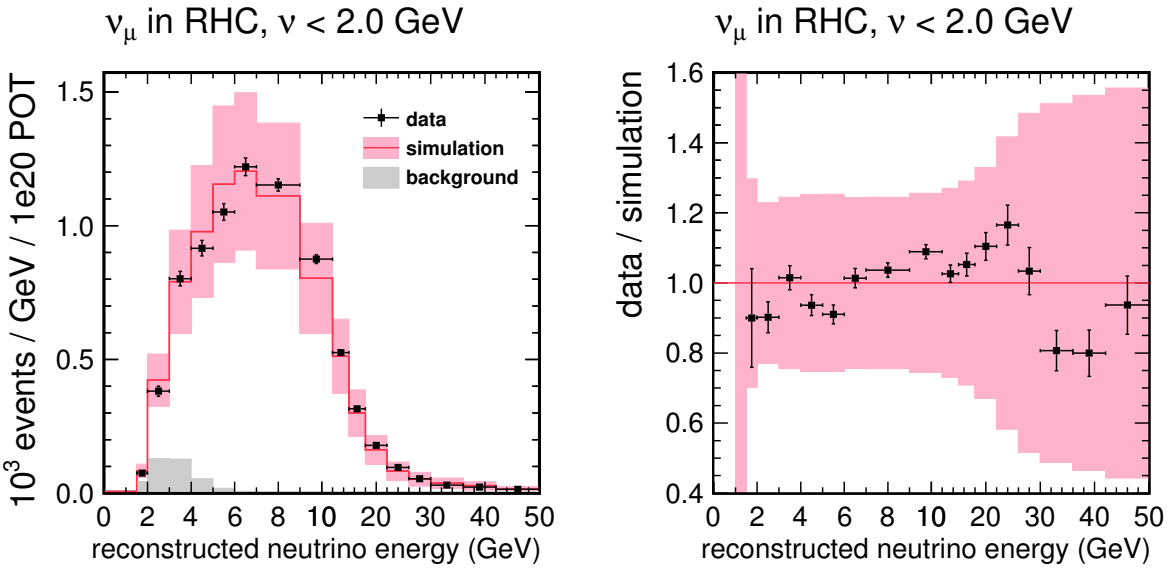

FIG. C.5: Reconstructed $\nu < 2$ GeV neutrino interaction rate (left) and ratio of data to simulation (right) in the reverse horn current (RHC), antineutrino-focusing beam. Data are plotted with statistical uncertainties; simulated data are plotted with statistical and systematic uncertainties.

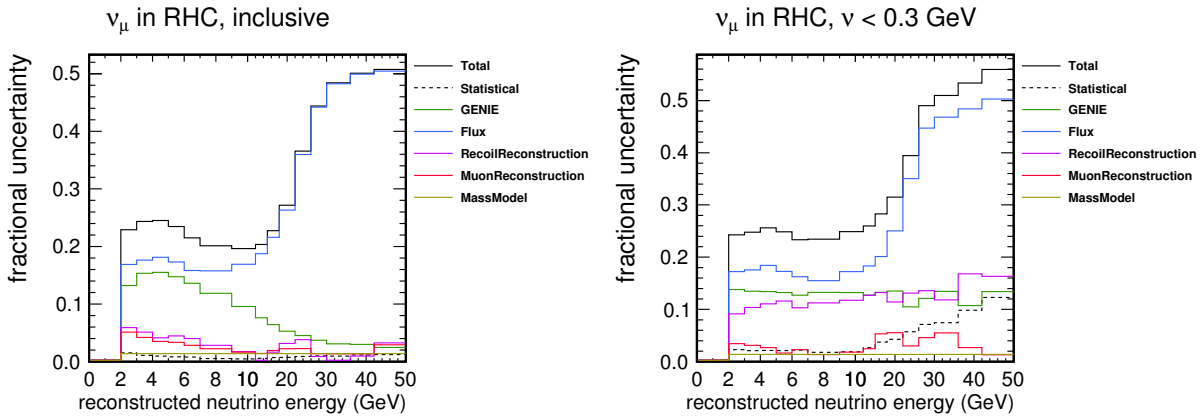

(a) Inclusive interaction rate.

(b) $\nu < 300$ MeV interaction rate.

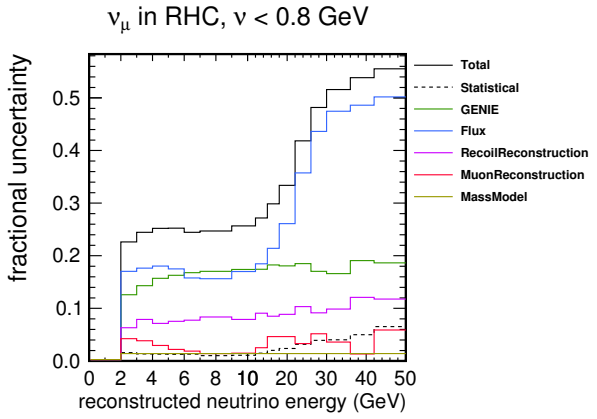

(c) $\nu < 800$ MeV interaction rate.

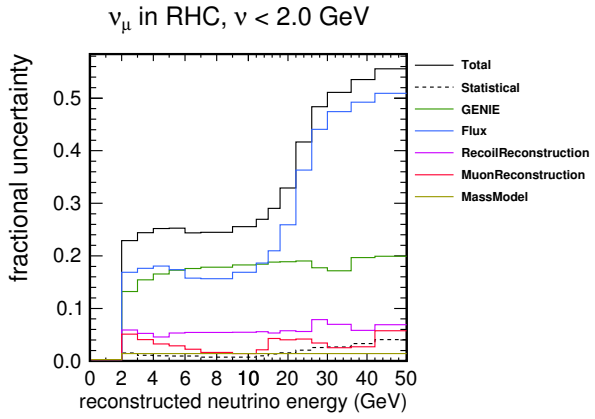

(d) $\nu < 2$ GeV interaction rate.

FIG. C.6: Total systematic and statistical uncertainties of the reconstructed neutrino interaction rate in the reverse horn current (RHC) beam (FIG. C.2 – C.5).

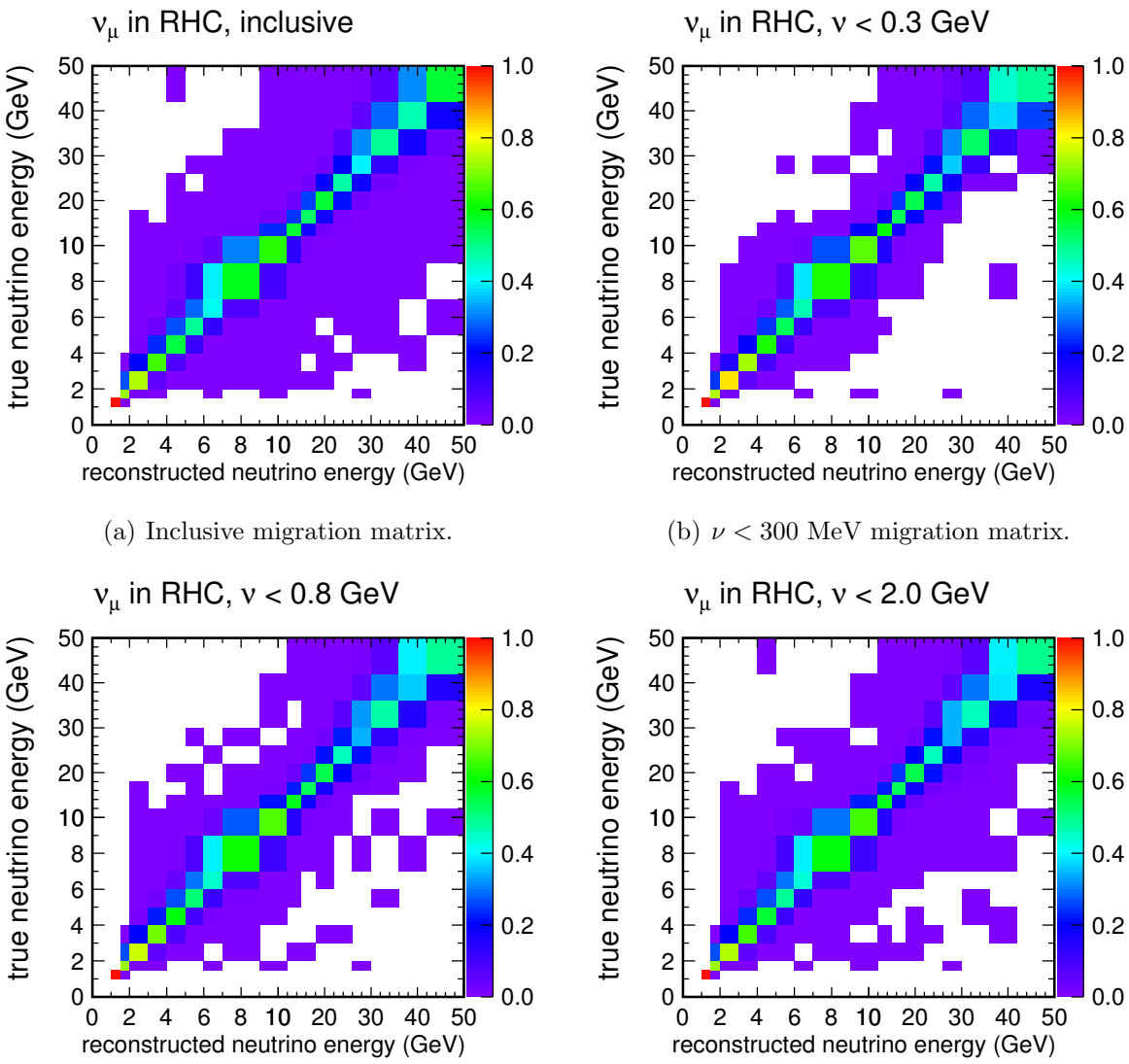

(a) Inclusive migration matrix.

(b) $\nu < 300$ MeV migration matrix.

(c) $\nu < 800$ MeV migration matrix.

(d) $\nu < 2$ GeV migration matrix.

FIG. C.7: Migration matrices for the inclusive and low-ν samples for neutrinos in the reverse horn current (RHC) beam.

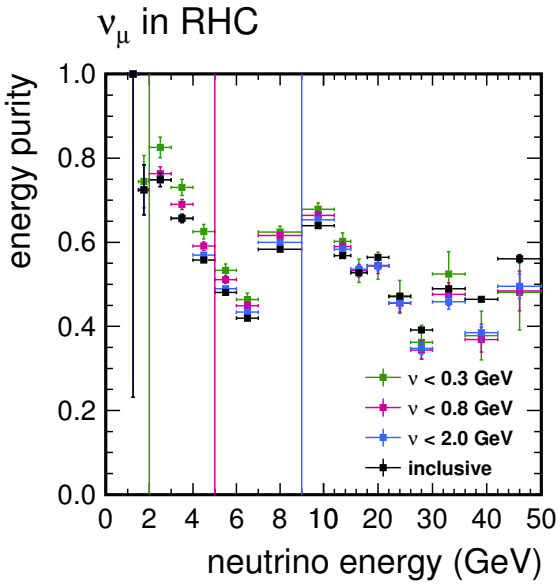

FIG. C.8: The fraction of events reconstructed to a given neutrino energy bin with true energy also within the bin for neutrinos in the reverse horn current (RHC) beam; equivalent to the diagonal elements of the migration matrices in FIG. C.7. Error bars show statistical uncertainties only. Vertical lines mark the minimum neutrino energy for each ν cut.

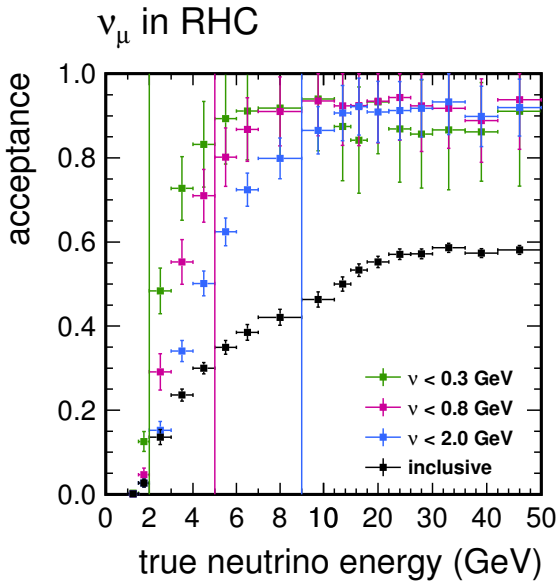

FIG. C.9: The ratio of reconstructed signal events (reconstructed $\nu < \nu_i$ or inclusive, true CC ν_μ) to all simulated signal events (true $\nu < \nu_i$ or inclusive, true CC ν_μ) for neutrinos in the reverse horn current (RHC) beam. See the text for a complete definition (Section 6.4.3). Error bars show statistical and systematic uncertainties (Chapter 7). Vertical lines mark the minimum neutrino energy for each ν cut.

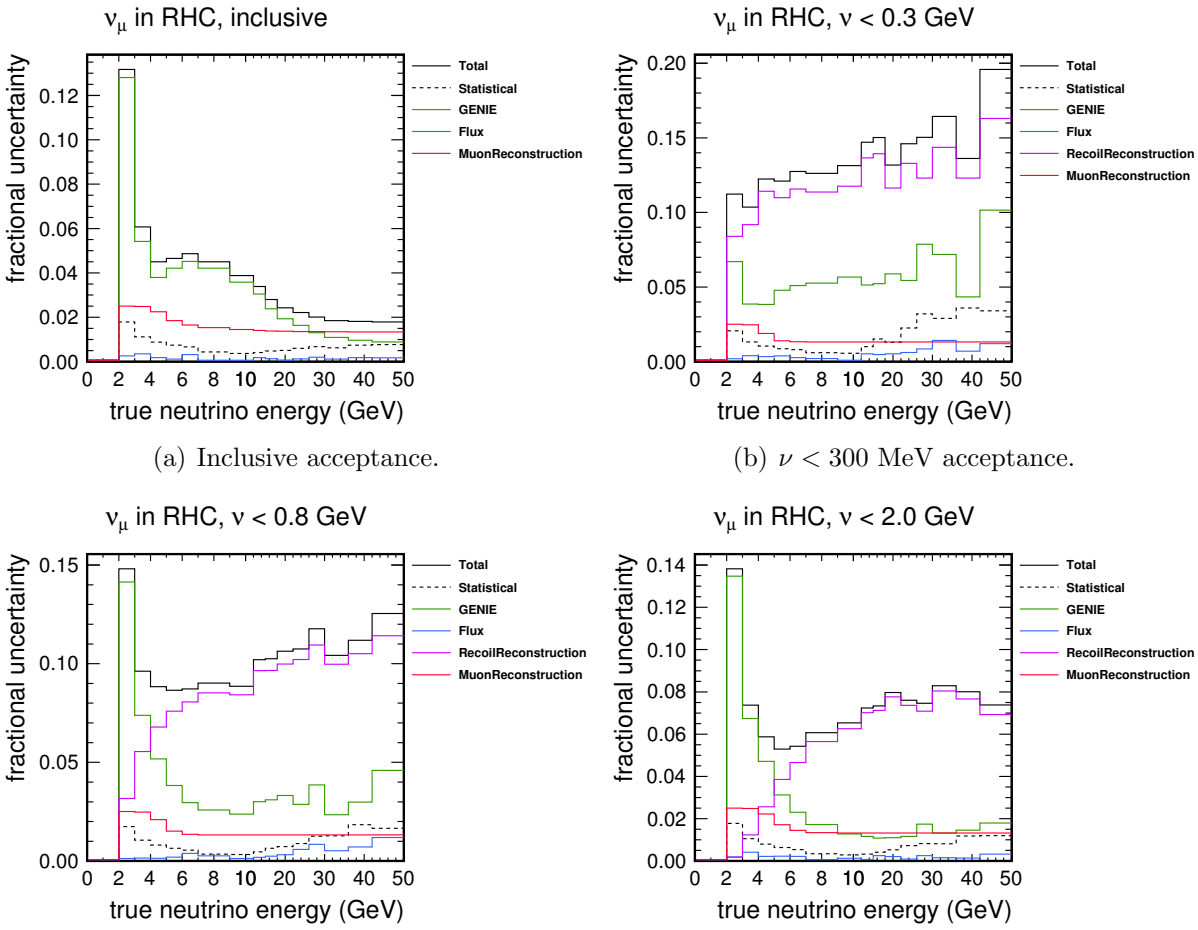

(a) Inclusive acceptance.

(b) $\nu < 300$ MeV acceptance.

(c) $\nu < 800$ MeV acceptance.

(d) $\nu < 2$ GeV acceptance.

FIG. C.10: Total systematic and statistical uncertainties of the acceptance for neutrinos in the reverse horn current (RHC) beam (FIG. C.9).

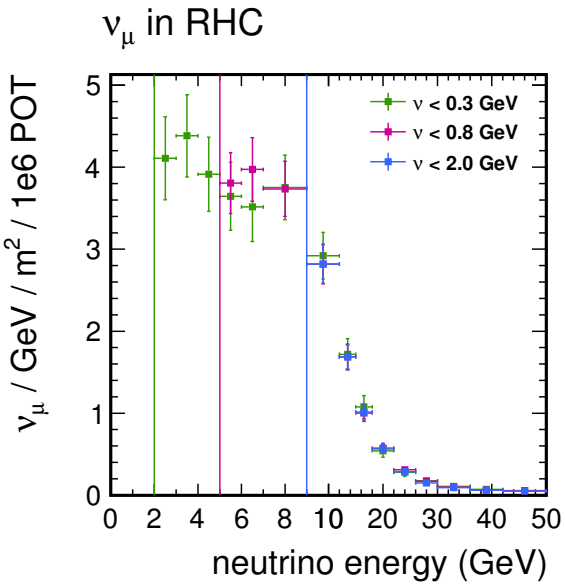

FIG. C.11: Extracted neutrino flux from the three low-ν samples in the reverse horn current (RHC) beam. Error bars show statistical and systematic uncertainties (Chapter 7). Vertical lines mark the minimum neutrino energy for each ν cut.

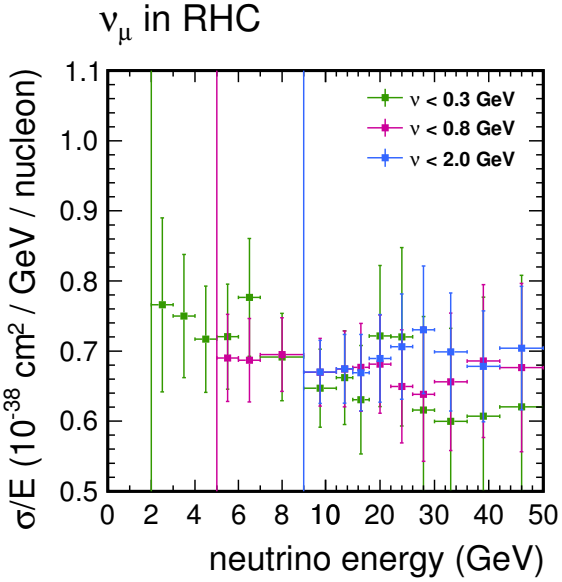

FIG. C.12: Extracted cross section divided by energy for neutrinos as derived from the three low-ν fluxes (FIG. C.11) in the reverse horn current (RHC) beam. Error bars show statistical and systematic uncertainties (Chapter 7). Vertical lines mark the minimum neutrino energy for each ν cut.

APPENDIX D

Antineutrinos in the Forward Horn Current (FHC) Beam

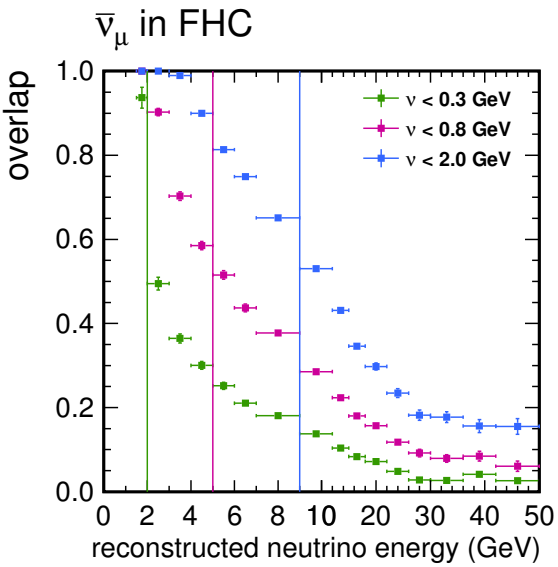

FIG. D.1: The fraction of the inclusive data sample with reconstructed ν less than the given ν cut for antineutrinos in the forward horn current (FHC), neutrino-focusing beam; equivalent to the ratio of the low-ν interaction rates (FIG. D.3 – D.5) to the inclusive interaction rate (FIG. D.2). Error bars show statistical uncertainties only. Vertical lines mark the minimum neutrino energy for each ν cut.

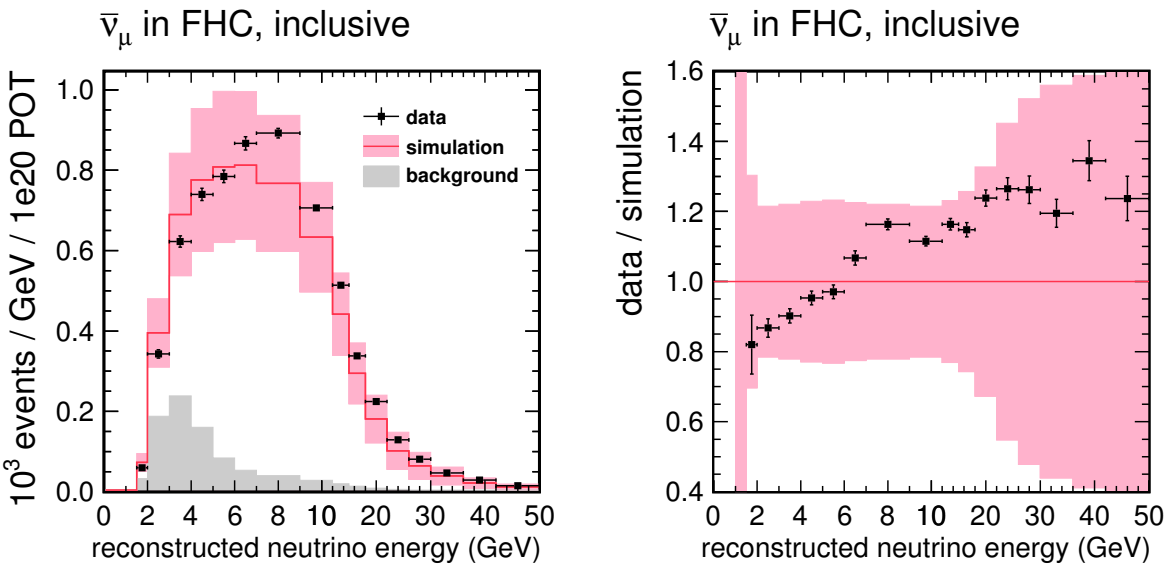

FIG. D.2: Reconstructed inclusive antineutrino interaction rate (left) and ratio of data to simulation (right) in the forward horn current (FHC), neutrino-focusing beam. Data are plotted with statistical uncertainties; simulated data are plotted with statistical and systematic uncertainties.

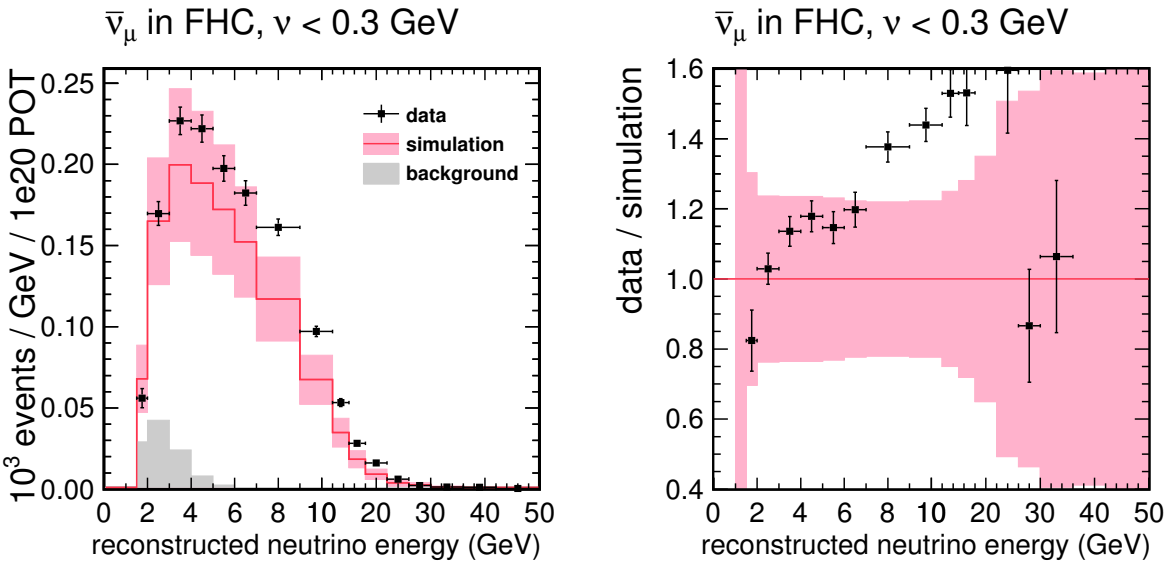

FIG. D.3: Reconstructed $\nu < 300$ MeV antineutrino interaction rate (left) and ratio of data to simulation (right) in the forward horn current (FHC), neutrino-focusing beam. Data are plotted with statistical uncertainties; simulated data are plotted with statistical and systematic uncertainties.

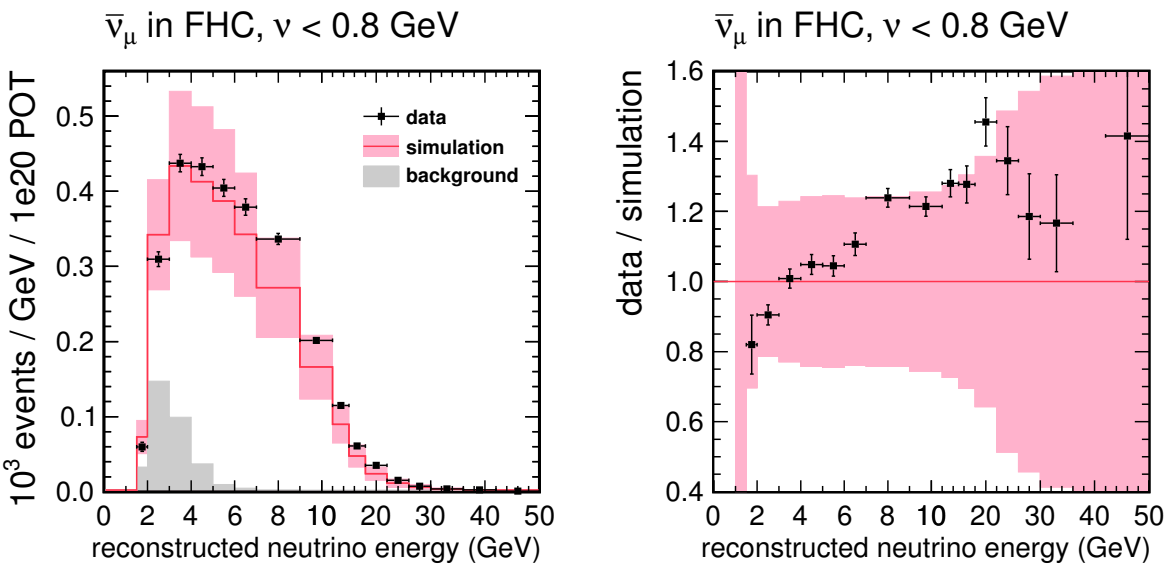

FIG. D.4: Reconstructed $\nu < 800$ MeV antineutrino interaction rate (left) and ratio of data to simulation (right) in the forward horn current (FHC), neutrino-focusing beam. Data are plotted with statistical uncertainties; simulated data are plotted with statistical and systematic uncertainties.

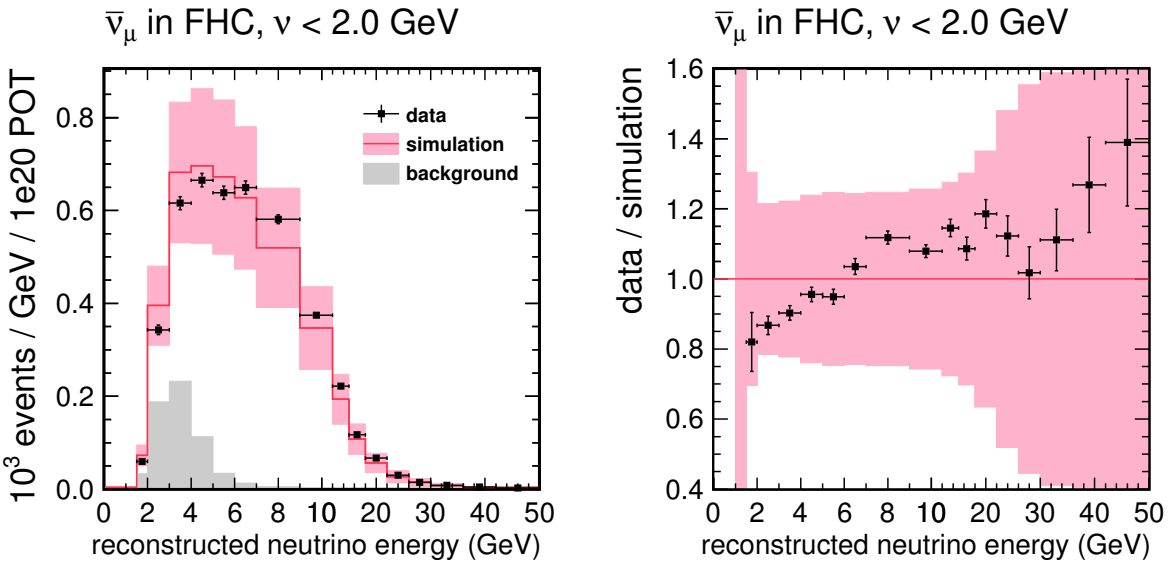

FIG. D.5: Reconstructed $\nu < 2$ GeV antineutrino interaction rate (left) and ratio of data to simulation (right) in the forward horn current (FHC), neutrino-focusing beam. Data are plotted with statistical uncertainties; simulated data are plotted with statistical and systematic uncertainties.

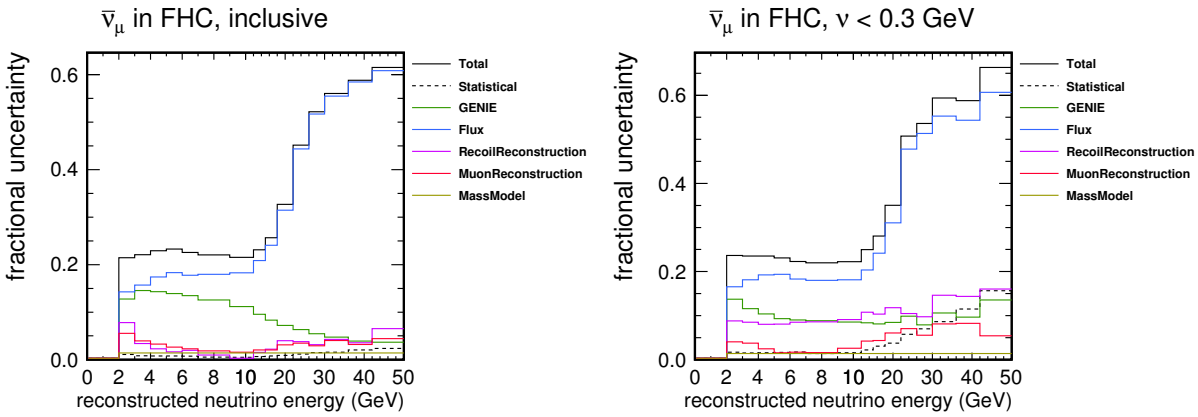

(a) Inclusive interaction rate.

(b) $\nu < 300$ MeV interaction rate.

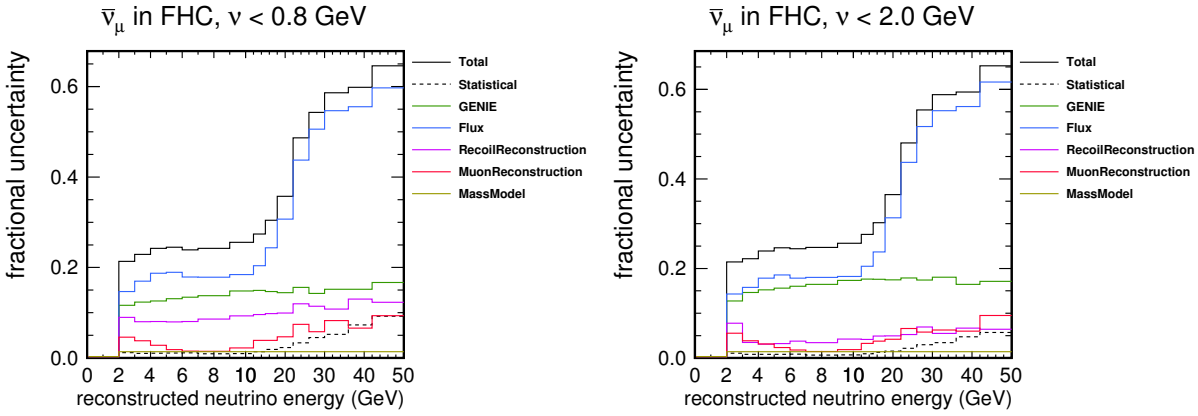

(c) $\nu < 800$ MeV interaction rate.

(d) $\nu < 2$ GeV interaction rate.

FIG. D.6: Total systematic and statistical uncertainties of the reconstructed antineutrino interaction rate in the forward horn current (FHC) beam (FIG. D.2 – D.5).

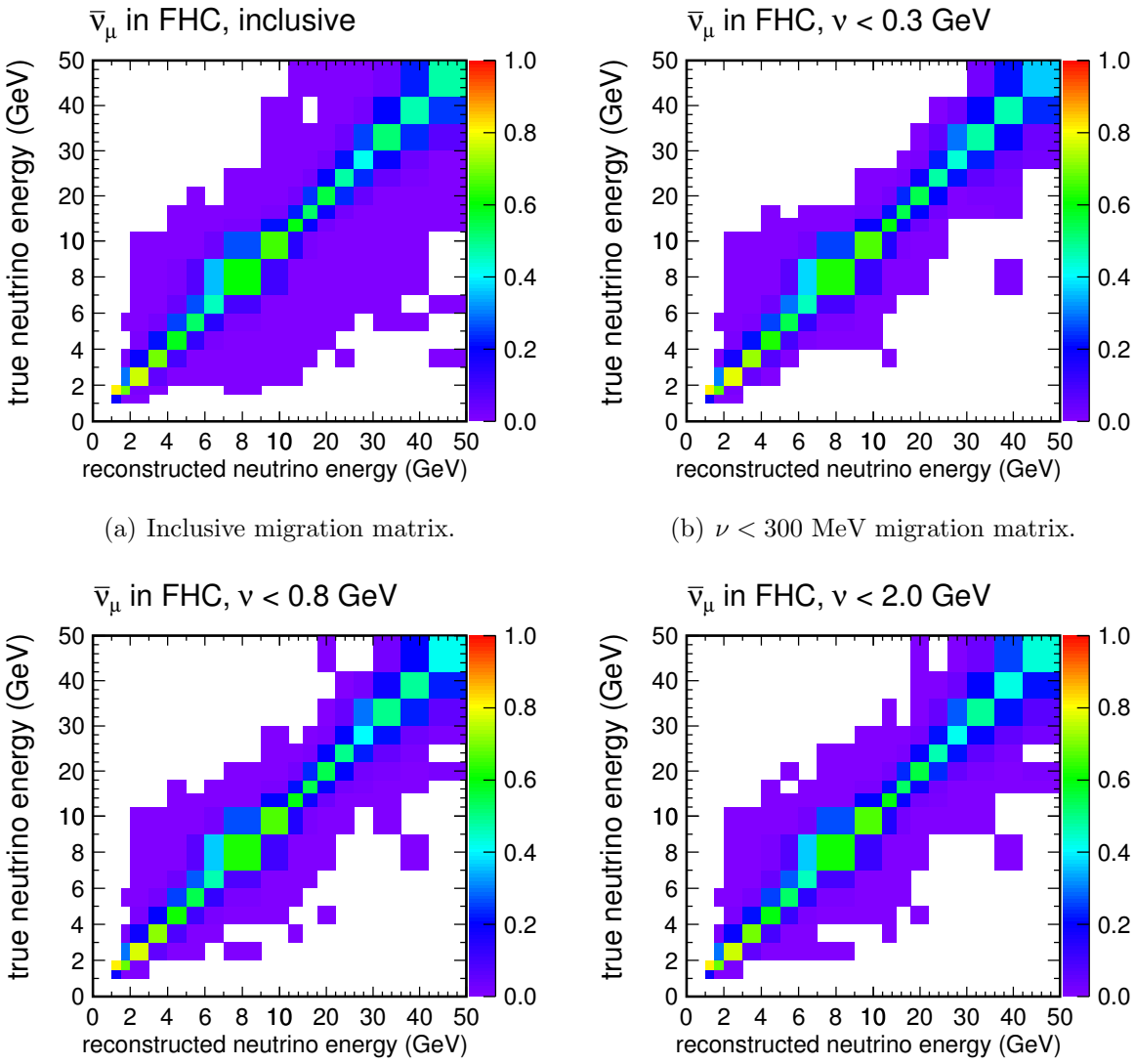

(a) Inclusive migration matrix.

(b) $\nu < 300$ MeV migration matrix.

(c) $\nu < 800$ MeV migration matrix.

(d) $\nu < 2$ GeV migration matrix.

FIG. D.7: Migration matrices for the inclusive and low-ν samples for antineutrinos in the forward horn current (FHC) beam.

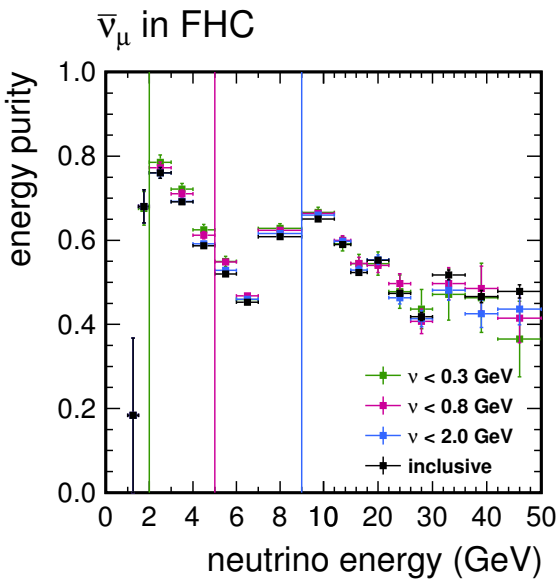

FIG. D.8: The fraction of events reconstructed to a given neutrino energy bin with true energy also within the bin for antineutrinos in the forward horn current (FHC) beam; equivalent to the diagonal elements of the migration matrices in FIG. D.7. Error bars show statistical uncertainties only. Vertical lines mark the minimum neutrino energy for each ν cut.

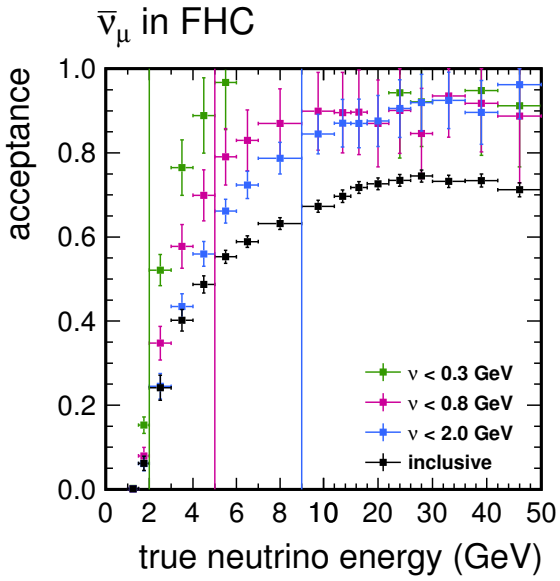

FIG. D.9: The ratio of reconstructed signal events (reconstructed $\nu < \nu_i$ or inclusive, true CC $\bar{\nu}_\mu$) to all simulated signal events (true $\nu < \nu_i$ or inclusive, true CC $\bar{\nu}_\mu$) for antineutrinos in the forward horn current (FHC) beam. See the text for a complete definition (Section 6.4.3). Error bars show statistical and systematic uncertainties (Chapter 7). Vertical lines mark the minimum neutrino energy for each ν cut.

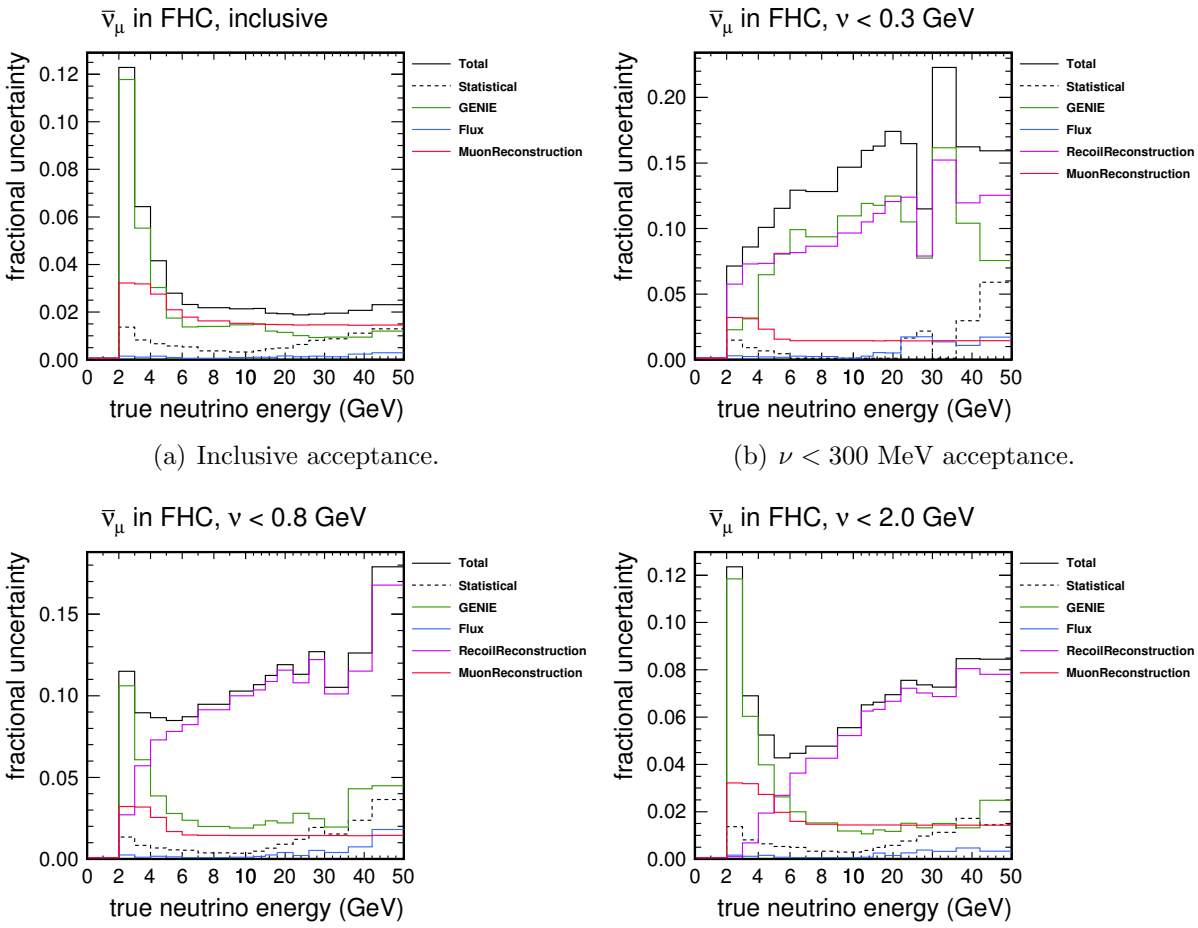

(a) Inclusive acceptance.

(b) $\nu < 300$ MeV acceptance.

(c) $\nu < 800$ MeV acceptance.

(d) $\nu < 2$ GeV acceptance.

FIG. D.10: Total systematic and statistical uncertainties of the acceptance for antineutrinos in the forward horn current (FHC) beam (FIG. D.9).

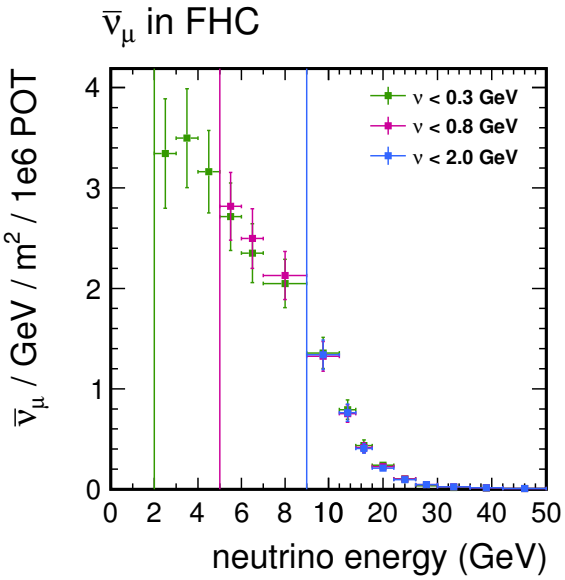

FIG. D.11: Extracted antineutrino flux from the three low-ν samples in the forward horn current (FHC) beam. Error bars show statistical and systematic uncertainties (Chapter 7). Vertical lines mark the minimum neutrino energy for each ν cut.

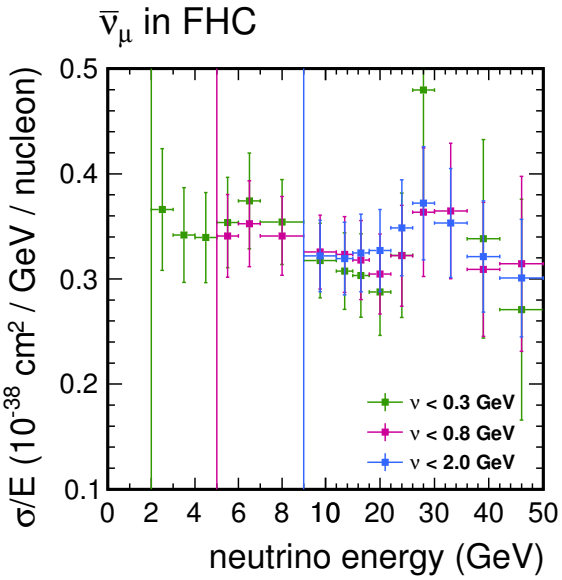

FIG. D.12: Extracted cross section divided by energy for antineutrinos as derived from the three low-ν fluxes (FIG. D.11) in the forward horn current (FHC) beam. Error bars show statistical and systematic uncertainties (Chapter 7). Vertical lines mark the minimum neutrino energy for each ν cut.

APPENDIX E

ν and $y = \nu/E$ Distributions for Neutrinos

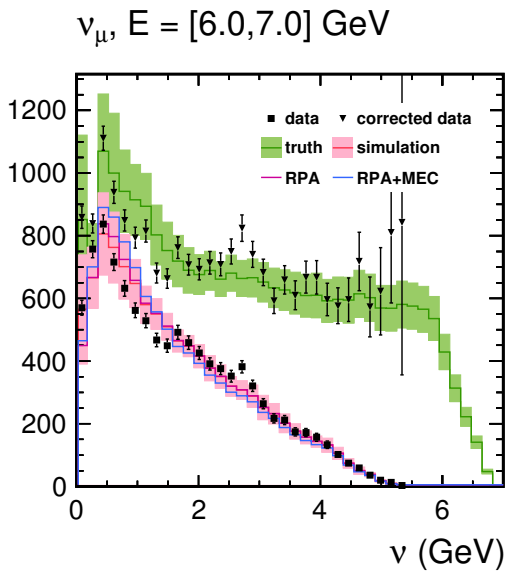

(a) $\nu, E = [6.0, 7.0]$ GeV

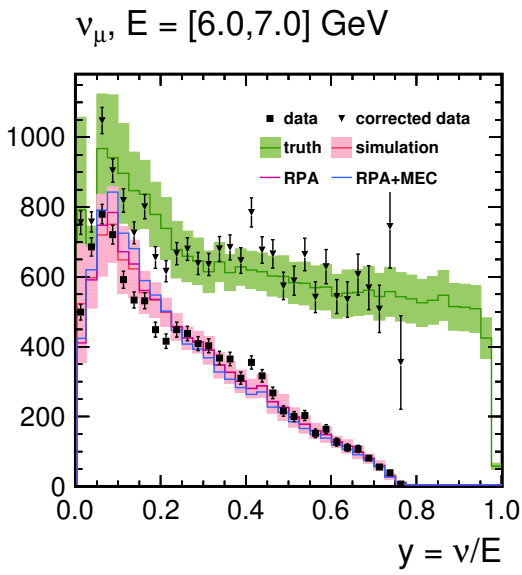

(b) $y = \nu/E, E = [6.0, 7.0]$ GeV

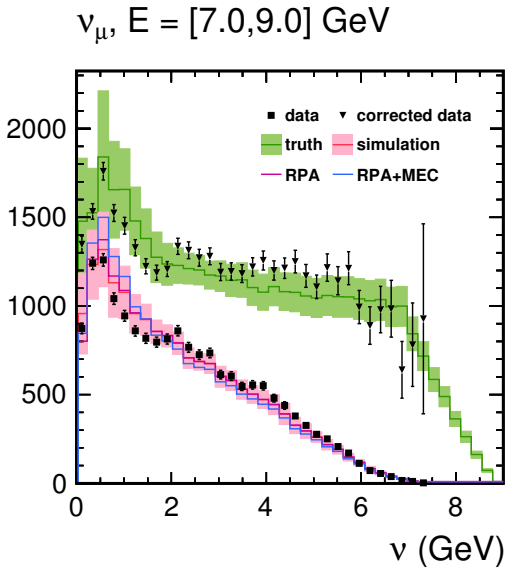

(c) $\nu, E = [7.0, 9.0]$ GeV

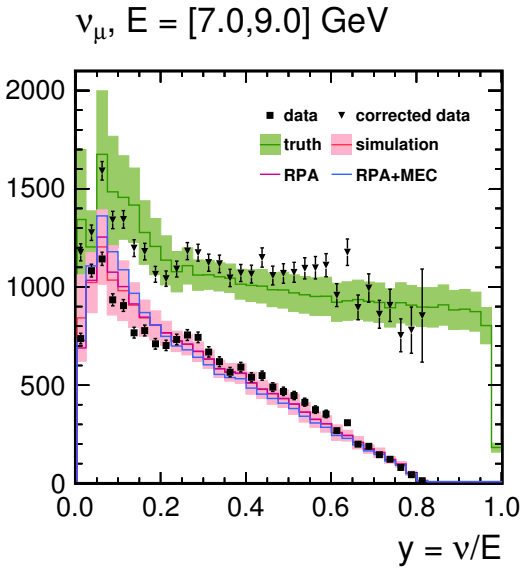

(d) $y = \nu/E, E = [7.0, 9.0]$ GeV

FIG. E.1: ν and $y = \nu/E$ for neutrino energy, $E = [6.0, 9.0]$ GeV for neutrinos in the forward horn current (FHC) beam. "Simulation" (red) is reconstructed, simulated events. "Truth" (green) is all simulated events, absent acceptance losses. Simulation is area normalized to data in all universes of the many universe uncertainty band, truth is scaled by the same value. "Corrected data" (black triangles) is acceptance corrected with the ratio of truth to simulation. Data and corrected data are plotted with statistical uncertainties; truth and simulation are plotted with statistical and systematic uncertainties. Two universes of the simulation uncertainty band, RPA and RPA+MEC, are plotted overlaid.

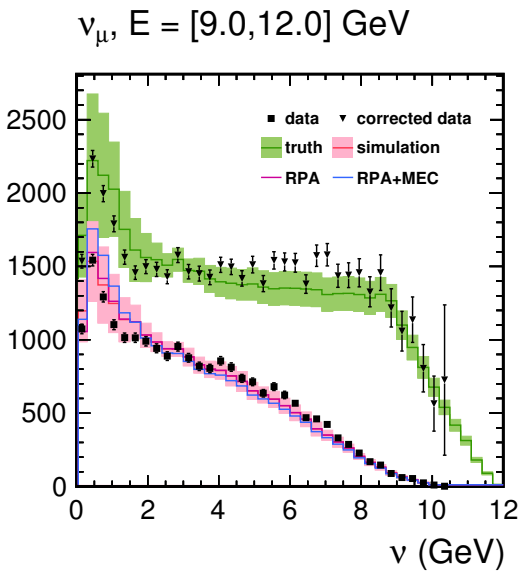

(a) $\nu, E = [9.0, 12.0]$ GeV

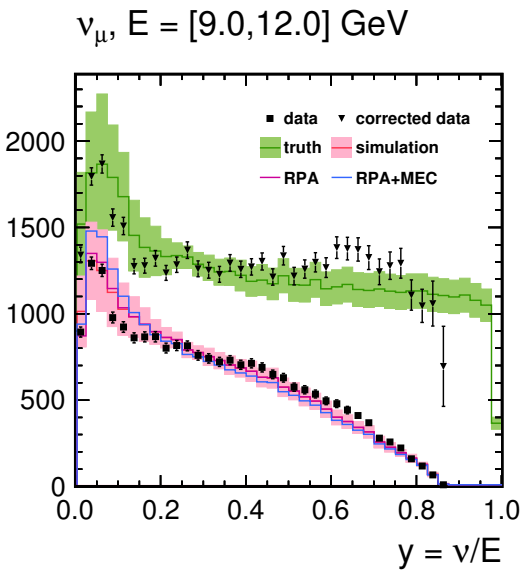

(b) $y = \nu/E, E = [9.0, 12.0]$ GeV

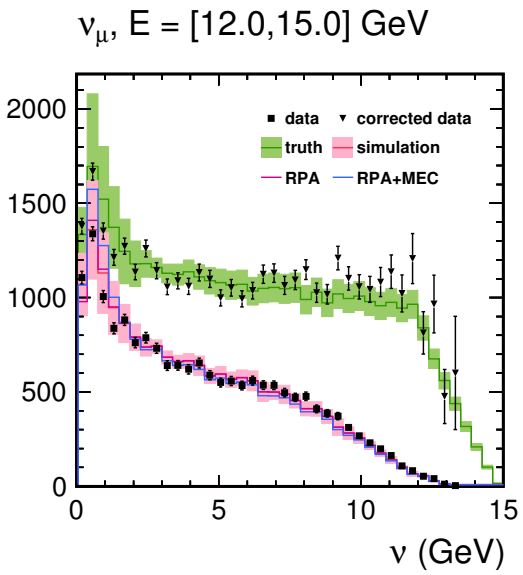

(c) $\nu, E = [12.0, 15.0]$ GeV

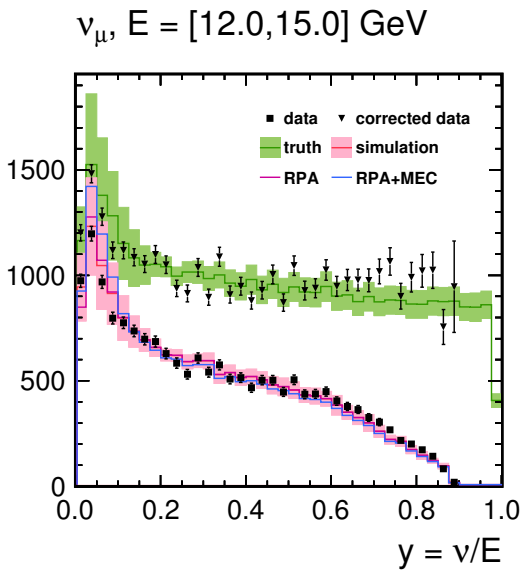

(d) $y = \nu/E, E = [12.0, 15.0]$ GeV

FIG. E.2: ν and $y = \nu/E$ for neutrino energy, $E = [9.0, 15.0]$ GeV for neutrinos in the forward horn current (FHC) beam. "Simulation" (red) is reconstructed, simulated events. "Truth" (green) is all simulated events, absent acceptance losses. Simulation is area normalized to data in all universes of the many universe uncertainty band, truth is scaled by the same value. "Corrected data" (black triangles) is acceptance corrected with the ratio of truth to simulation. Data and corrected data are plotted with statistical uncertainties; truth and simulation are plotted with statistical and systematic uncertainties. Two universes of the simulation uncertainty band, RPA and RPA+MEC, are plotted overlaid.

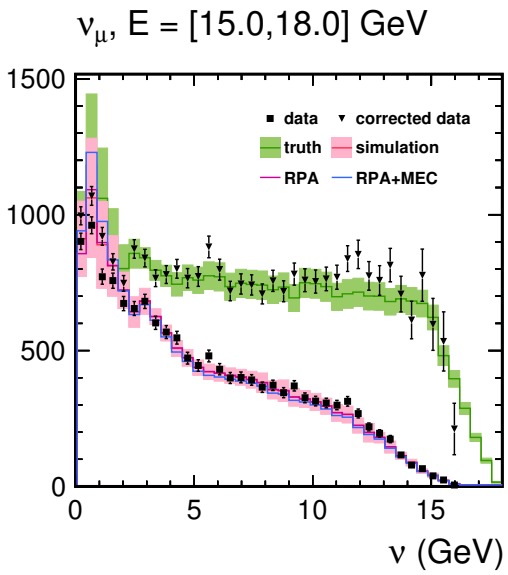

(a) $\nu, E = [15.0, 18.0]$ GeV

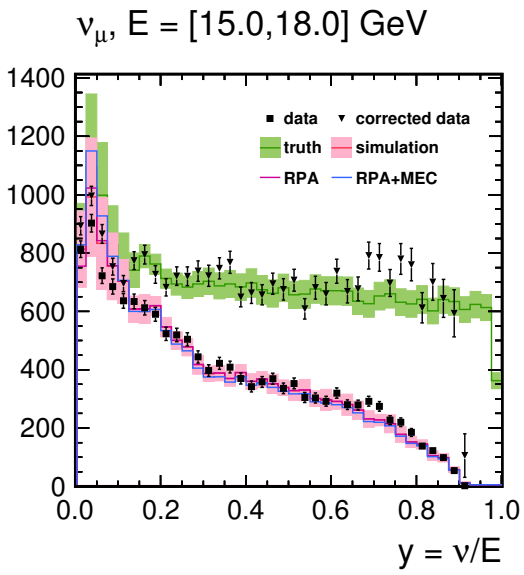

(b) $y = \nu/E, E = [15.0, 18.0]$ GeV

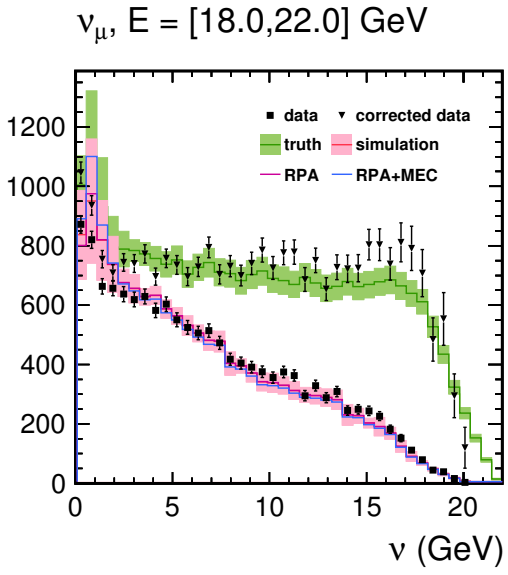

(c) $\nu, E = [18.0, 22.0]$ GeV

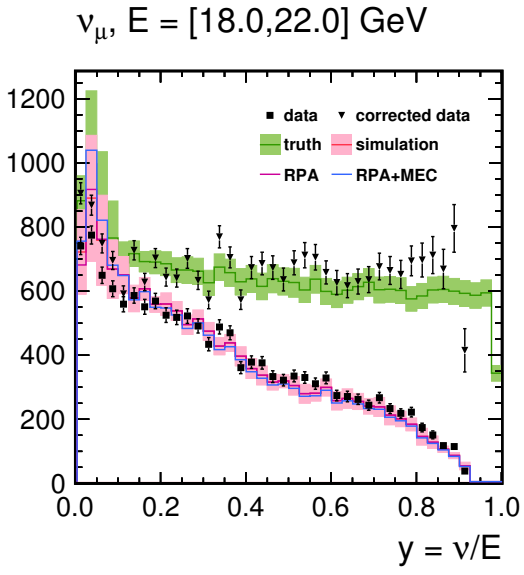

(d) $y = \nu/E, E = [18.0, 22.0]$ GeV

FIG. E.3: ν and $y = \nu/E$ for neutrino energy, $E = [15.0, 22.0]$ GeV for neutrinos in the forward horn current (FHC) beam. "Simulation" (red) is reconstructed, simulated events. "Truth" (green) is all simulated events, absent acceptance losses. Simulation is area normalized to data in all universes of the many universe uncertainty band, truth is scaled by the same value. "Corrected data" (black triangles) is acceptance corrected with the ratio of truth to simulation. Data and corrected data are plotted with statistical uncertainties; truth and simulation are plotted with statistical and systematic uncertainties. Two universes of the simulation uncertainty band, RPA and RPA+MEC, are plotted overlaid.

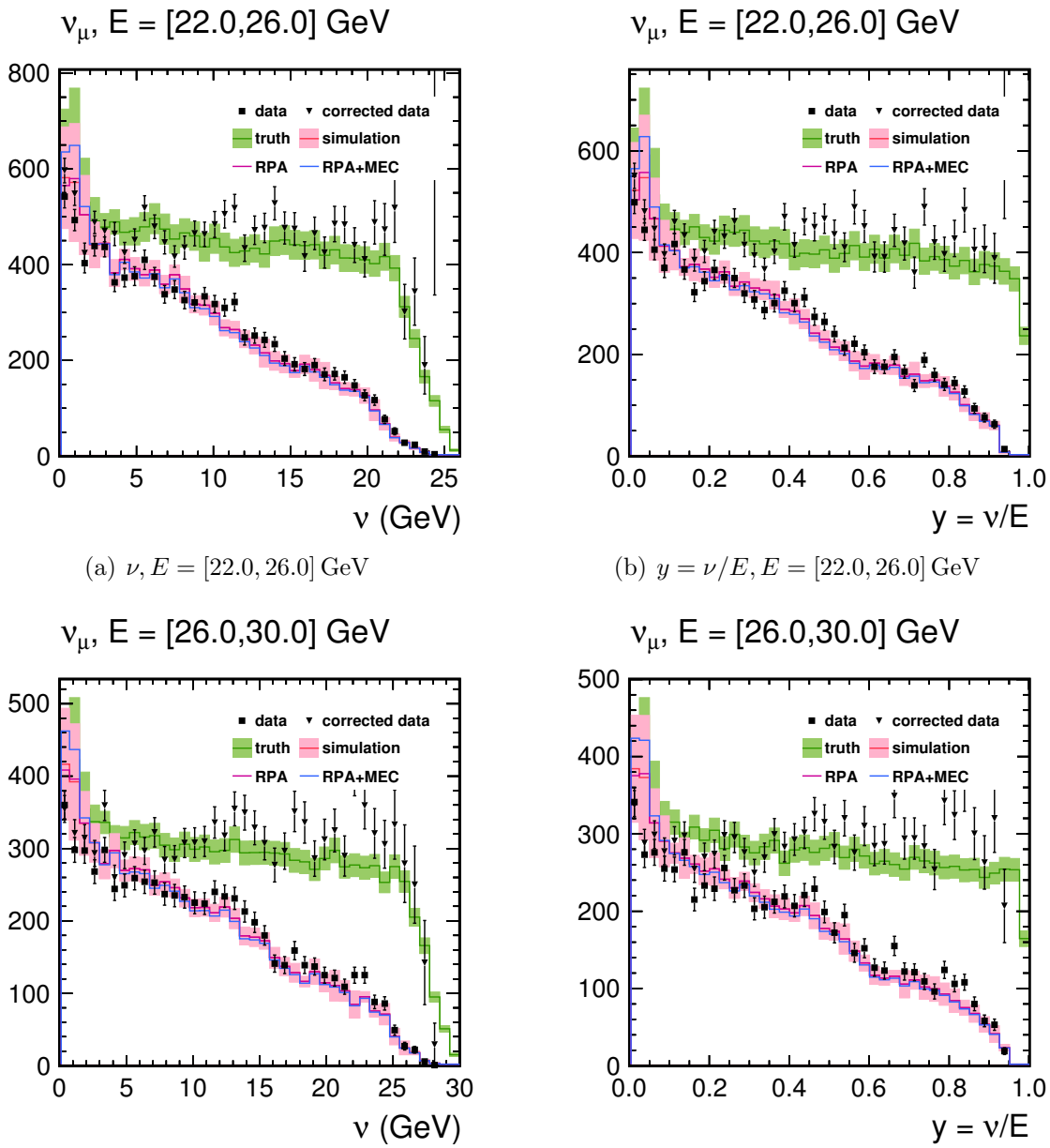

(a) $\nu, E = [22.0, 26.0]$ GeV

(b) $y = \nu/E, E = [22.0, 26.0]$ GeV

(c) $\nu, E = [26.0, 30.0]$ GeV

(d) $y = \nu/E, E = [26.0, 30.0]$ GeV

FIG. E.4: ν and $y = \nu/E$ for neutrino energy, $E = [22.0, 30.0]$ GeV for neutrinos in the forward horn current (FHC) beam. "Simulation" (red) is reconstructed, simulated events. "Truth" (green) is all simulated events, absent acceptance losses. Simulation is area normalized to data in all universes of the many universe uncertainty band, truth is scaled by the same value. "Corrected data" (black triangles) is acceptance corrected with the ratio of truth to simulation. Data and corrected data are plotted with statistical uncertainties; truth and simulation are plotted with statistical and systematic uncertainties. Two universes of the simulation uncertainty band, RPA and RPA+MEC, are plotted overlaid.

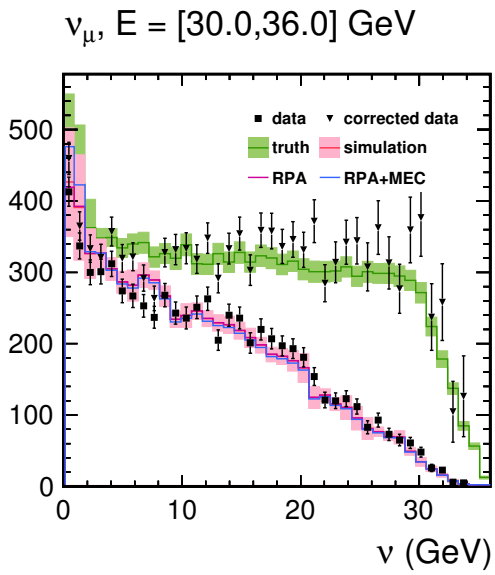

(a) $\nu, E = [30.0, 36.0]$ GeV

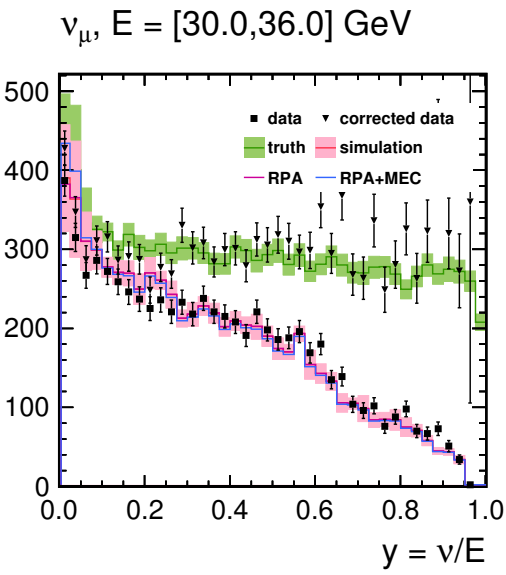

(b) $y = \nu/E, E = [30.0, 36.0]$ GeV

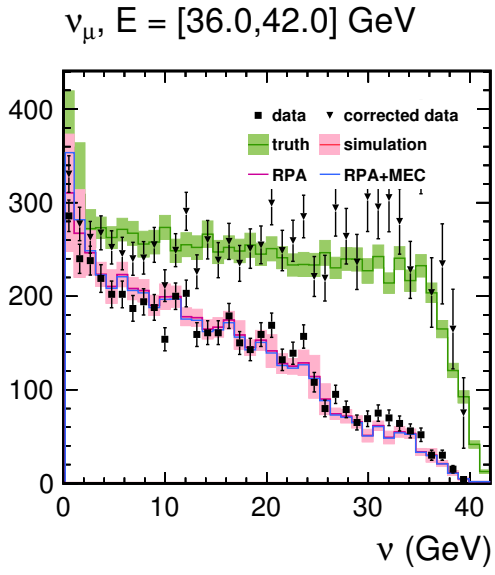

(c) $\nu, E = [36.0, 42.0]$ GeV

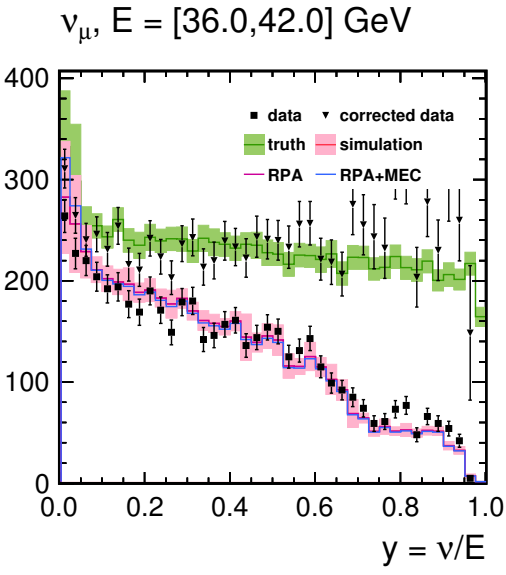

(d) $y = \nu/E, E = [36.0, 42.0]$ GeV

FIG. E.5: ν and $y = \nu/E$ for neutrino energy, $E = [30.0, 42.0]$ GeV for neutrinos in the forward horn current (FHC) beam. "Simulation" (red) is reconstructed, simulated events. "Truth" (green) is all simulated events, absent acceptance losses. Simulation is area normalized to data in all universes of the many universe uncertainty band, truth is scaled by the same value. "Corrected data" (black triangles) is acceptance corrected with the ratio of truth to simulation. Data and corrected data are plotted with statistical uncertainties; truth and simulation are plotted with statistical and systematic uncertainties. Two universes of the simulation uncertainty band, RPA and RPA+MEC, are plotted overlaid.

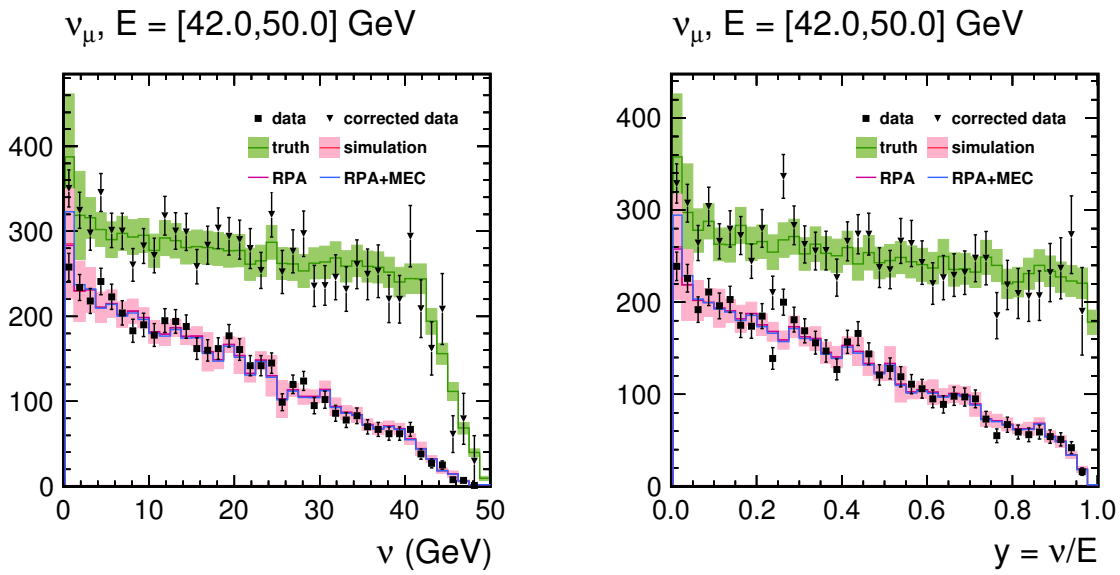

(a) $\nu, E = [42.0, 50.0]$ GeV

(b) $y = \nu/E, E = [42.0, 50.0]$ GeV

FIG. E.6: ν and $y = \nu/E$ for neutrino energy, $E = [42.0, 50.0]$ GeV for neutrinos in the forward horn current (FHC) beam. "Simulation" (red) is reconstructed, simulated events. "Truth" (green) is all simulated events, absent acceptance losses. Simulation is area normalized to data in all universes of the many universe uncertainty band, truth is scaled by the same value. "Corrected data" (black triangles) is acceptance corrected with the ratio of truth to simulation. Data and corrected data are plotted with statistical uncertainties; truth and simulation are plotted with statistical and systematic uncertainties. Two universes of the simulation uncertainty band, RPA and RPA+MEC, are plotted overlaid.

APPENDIX F

ν and $y = \nu/E$ Distributions for Antineutrinos

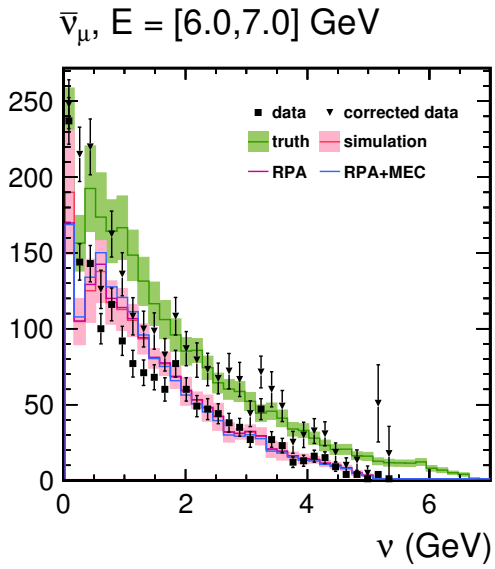

(a) $\nu, E = [6.0, 7.0]$ GeV

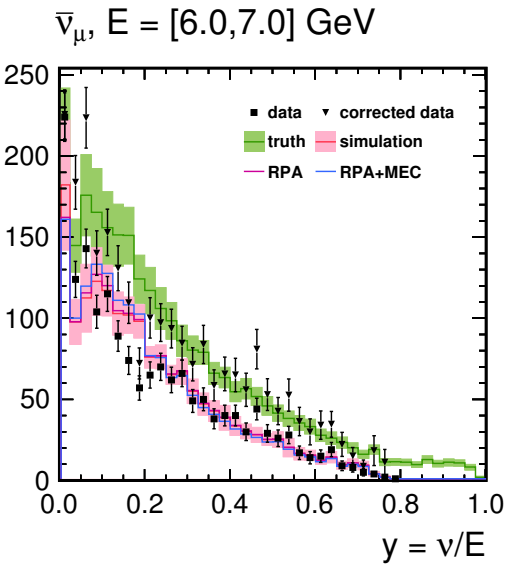

(b) $y = \nu/E, E = [6.0, 7.0]$ GeV

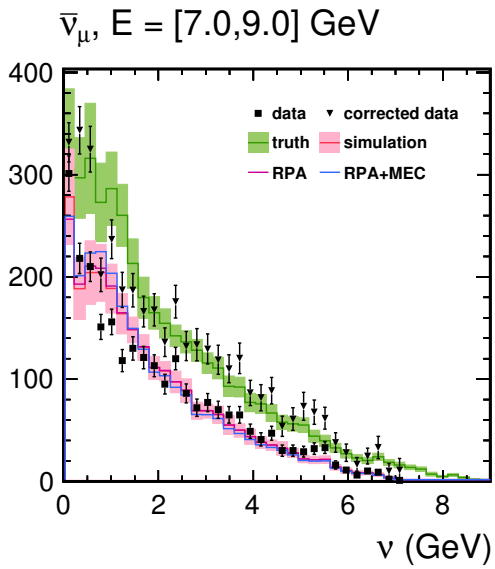

(c) $\nu, E = [7.0, 9.0]$ GeV

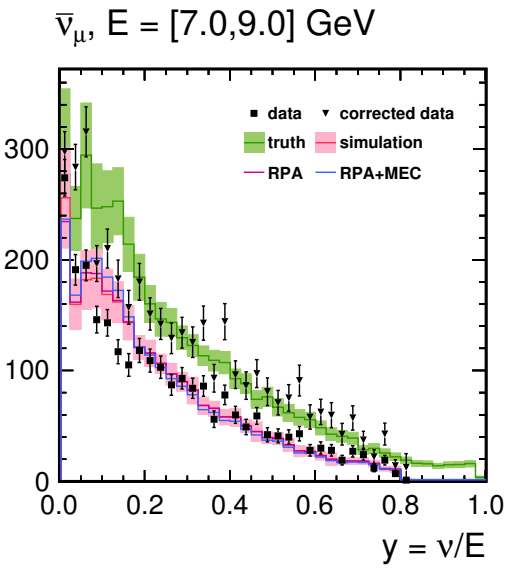

(d) $y = \nu/E, E = [7.0, 9.0]$ GeV

FIG. F.1: ν and $y = \nu/E$ for neutrino energy, $E = [6.0, 9.0]$ GeV for antineutrinos in the reverse horn current (RHC) beam. "Simulation" (red) is reconstructed, simulated events. "Truth" (green) is all simulated events, absent acceptance losses. Simulation is area normalized to data in all universes of the many universe uncertainty band, truth is scaled by the same value. "Corrected data" (black triangles) is acceptance corrected with the ratio of truth to simulation. Data and corrected data are plotted with statistical uncertainties; truth and simulation are plotted with statistical and systematic uncertainties. Two universes of the simulation uncertainty band, RPA and RPA+MEC, are plotted overlaid.

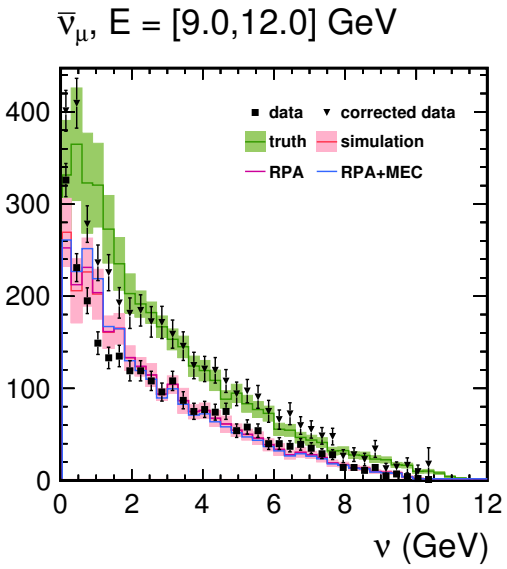

(a) $\nu, E = [9.0, 12.0]$ GeV

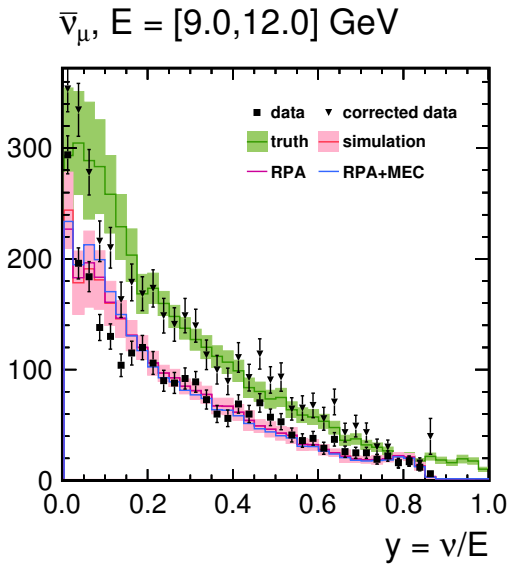

(b) $y = \nu/E, E = [9.0, 12.0]$ GeV

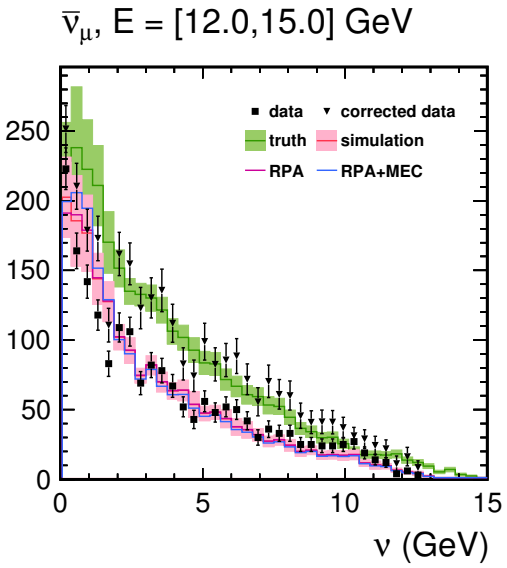

(c) $\nu, E = [12.0, 15.0]$ GeV

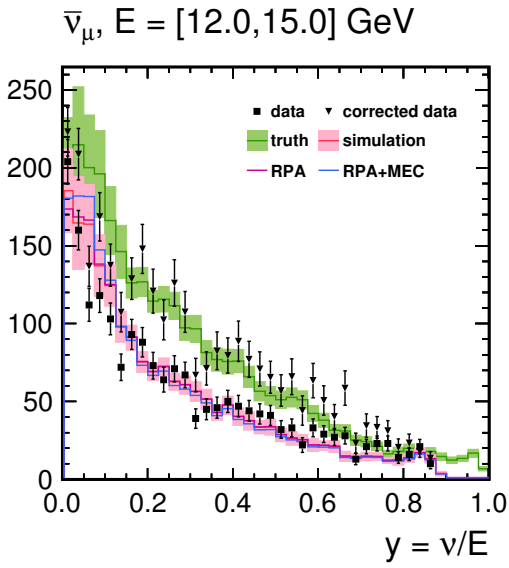

(d) $y = \nu/E, E = [12.0, 15.0]$ GeV

FIG. F.2: ν and $y = \nu/E$ for neutrino energy, $E = [9.0, 15.0]$ GeV for antineutrinos in the reverse horn current (RHC) beam. "Simulation" (red) is reconstructed, simulated events. "Truth" (green) is all simulated events, absent acceptance losses. Simulation is area normalized to data in all universes of the many universe uncertainty band, truth is scaled by the same value. "Corrected data" (black triangles) is acceptance corrected with the ratio of truth to simulation. Data and corrected data are plotted with statistical uncertainties; truth and simulation are plotted with statistical and systematic uncertainties. Two universes of the simulation uncertainty band, RPA and RPA+MEC, are plotted overlaid.

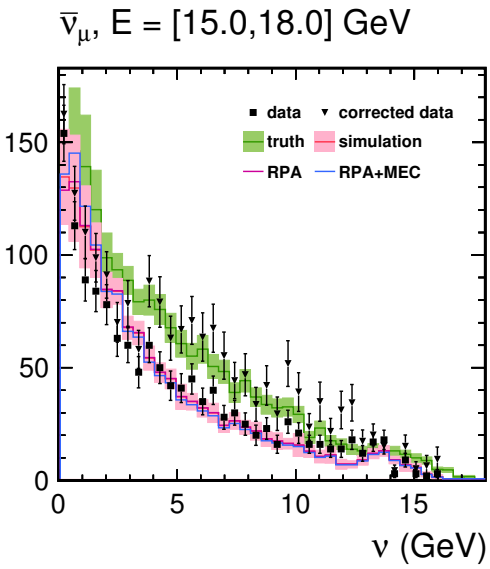

(a) $\nu, E = [15.0, 18.0]$ GeV

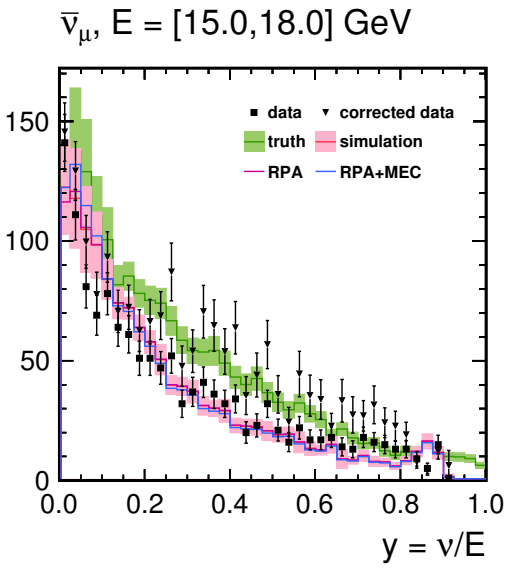

(b) $y = \nu/E, E = [15.0, 18.0]$ GeV

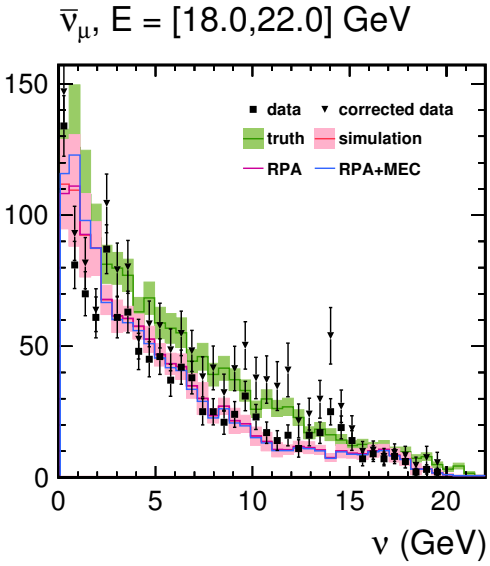

(c) $\nu, E = [18.0, 22.0]$ GeV

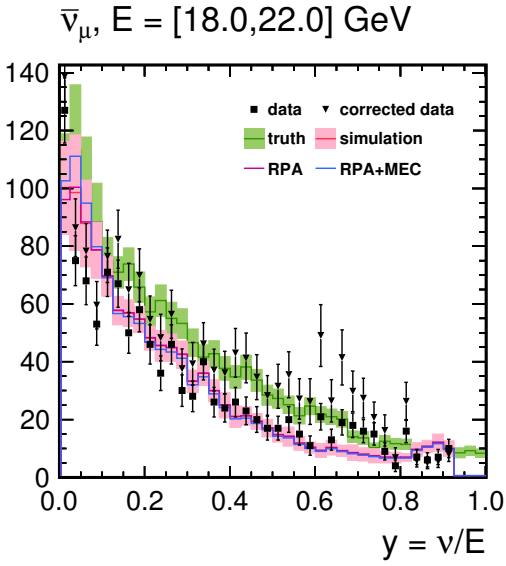

(d) $y = \nu/E, E = [18.0, 22.0]$ GeV

FIG. F.3: ν and $y = \nu/E$ for neutrino energy, $E = [15.0, 22.0]$ GeV for antineutrinos in the reverse horn current (RHC) beam. "Simulation" (red) is reconstructed, simulated events. "Truth" (green) is all simulated events, absent acceptance losses. Simulation is area normalized to data in all universes of the many universe uncertainty band, truth is scaled by the same value. "Corrected data" (black triangles) is acceptance corrected with the ratio of truth to simulation. Data and corrected data are plotted with statistical uncertainties; truth and simulation are plotted with statistical and systematic uncertainties. Two universes of the simulation uncertainty band, RPA and RPA+MEC, are plotted overlaid.

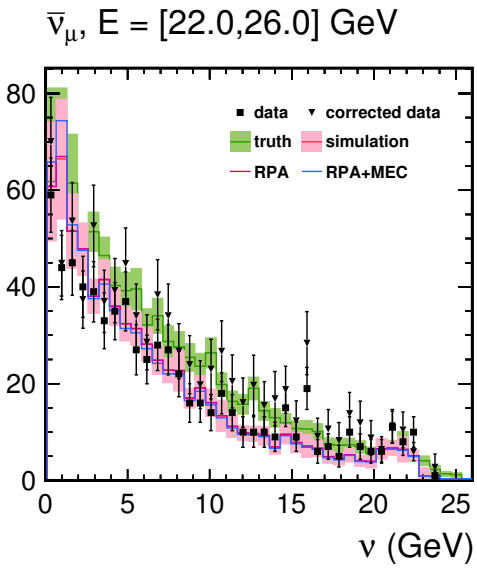

(a) $\nu, E = [22.0, 26.0]$ GeV

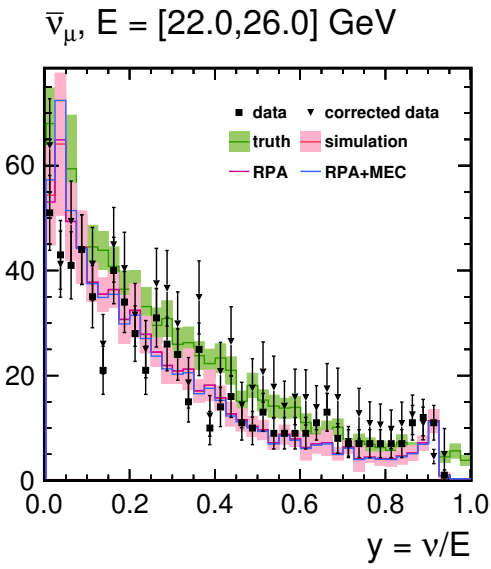

(b) $y = \nu/E, E = [22.0, 26.0]$ GeV

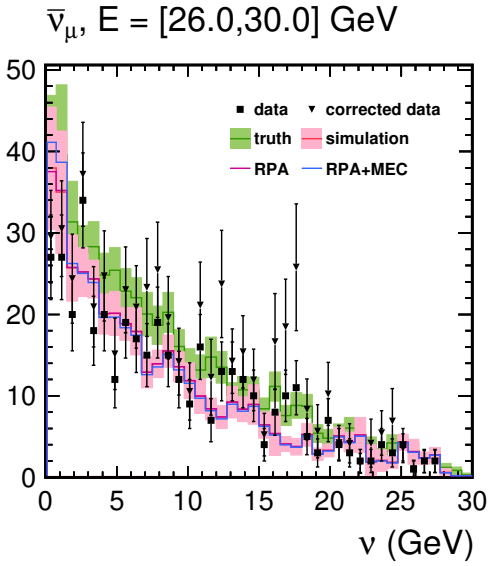

(c) $\nu, E = [26.0, 30.0]$ GeV

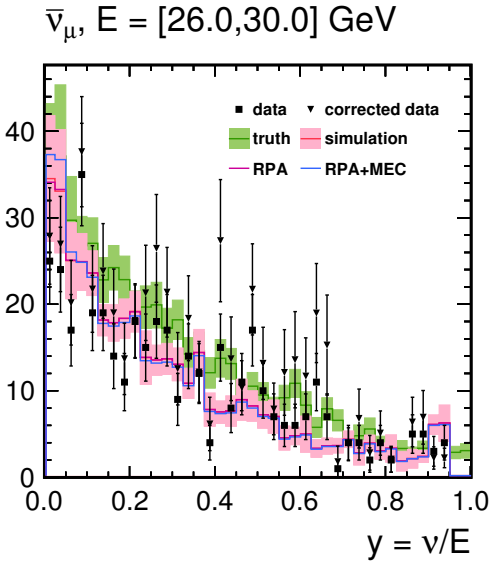

(d) $y = \nu/E, E = [26.0, 30.0]$ GeV

FIG. F.4: ν and $y = \nu/E$ for neutrino energy, $E = [22.0, 30.0]$ GeV for antineutrinos in the reverse horn current (RHC) beam. "Simulation" (red) is reconstructed, simulated events. "Truth" (green) is all simulated events, absent acceptance losses. Simulation is area normalized to data in all universes of the many universe uncertainty band, truth is scaled by the same value. "Corrected data" (black triangles) is acceptance corrected with the ratio of truth to simulation. Data and corrected data are plotted with statistical uncertainties; truth and simulation are plotted with statistical and systematic uncertainties. Two universes of the simulation uncertainty band, RPA and RPA+MEC, are plotted overlaid.

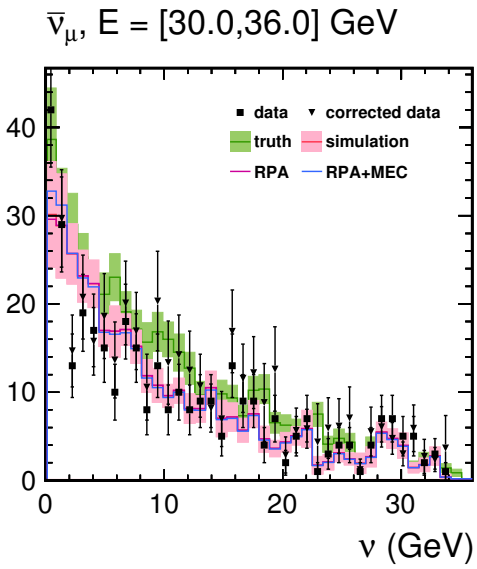

(a) $\nu, E = [30.0, 36.0]$ GeV

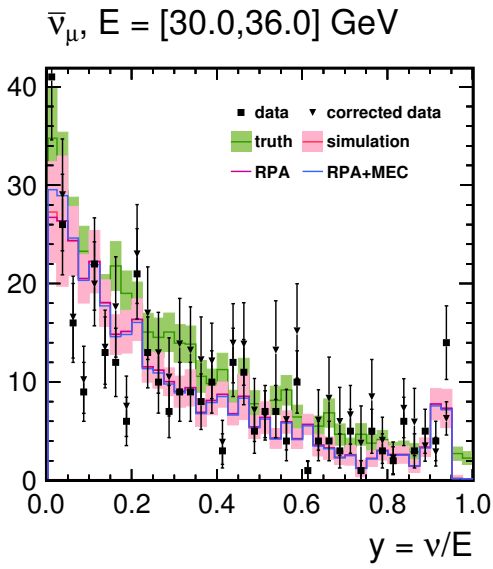

(b) $y = \nu/E, E = [30.0, 36.0]$ GeV

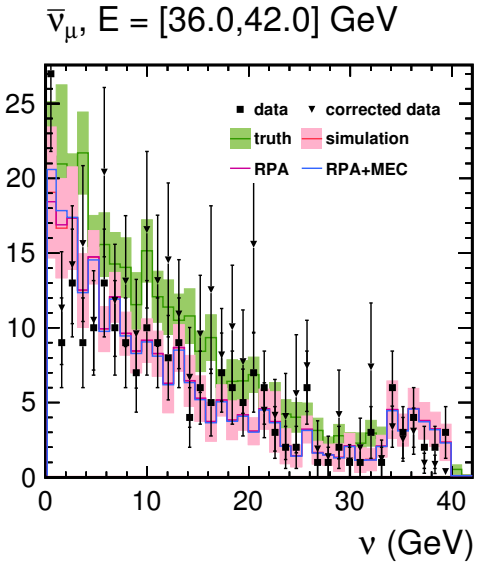

(c) $\nu, E = [36.0, 42.0]$ GeV

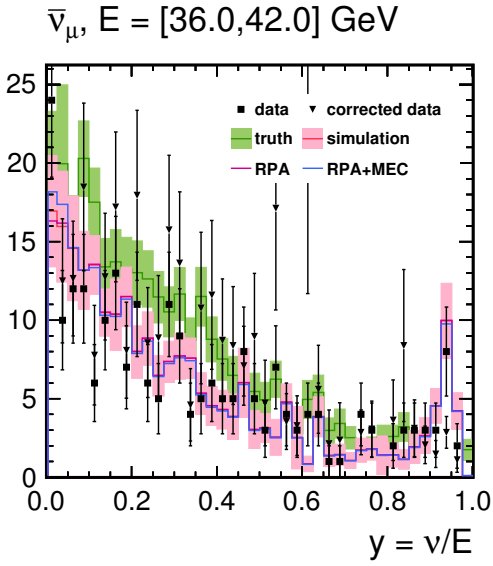

(d) $y = \nu/E, E = [36.0, 42.0]$ GeV

FIG. F.5: ν and $y = \nu/E$ for neutrino energy, $E = [30.0, 42.0]$ GeV for antineutrinos in the reverse horn current (RHC) beam. "Simulation" (red) is reconstructed, simulated events. "Truth" (green) is all simulated events, absent acceptance losses. Simulation is area normalized to data in all universes of the many universe uncertainty band, truth is scaled by the same value. "Corrected data" (black triangles) is acceptance corrected with the ratio of truth to simulation. Data and corrected data are plotted with statistical uncertainties; truth and simulation are plotted with statistical and systematic uncertainties. Two universes of the simulation uncertainty band, RPA and RPA+MEC, are plotted overlaid.

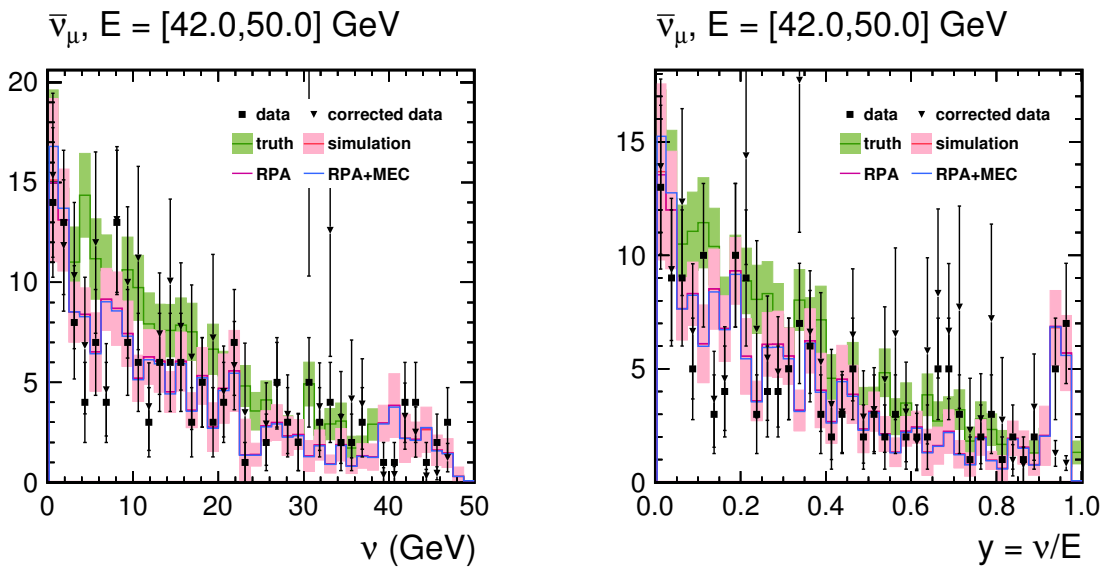

(a) $\nu, E = [42.0, 50.0]$ GeV

(b) $y = \nu/E, E = [42.0, 50.0]$ GeV

FIG. F.6: ν and $y = \nu/E$ for neutrino energy, $E = [42.0, 50.0]$ GeV for antineutrinos in the reverse horn current (RHC) beam. "Simulation" (red) is reconstructed, simulated events. "Truth" (green) is all simulated events, absent acceptance losses. Simulation is area normalized to data in all universes of the many universe uncertainty band, truth is scaled by the same value. "Corrected data" (black triangles) is acceptance corrected with the ratio of truth to simulation. Data and corrected data are plotted with statistical uncertainties; truth and simulation are plotted with statistical and systematic uncertainties. Two universes of the simulation uncertainty band, RPA and RPA+MEC, are plotted overlaid.

BIBLIOGRAPHY

[1] P. D. Group, Chin.Phys.C **38**, 090001 (2014).

[2] V. Aseev et al., Phys.Rev.D **84**, 112003 (2011).

[3] P. Adamson et al., Phys.Rev.D **77**, 072002 (2008).

[4] L. Aliaga et al., NIM A **743**, 130 (2014).

[5] G. Perdue et al., NIM A **694**, 179 (2012).

[6] D. Michael et al., NIM A **596**, 190 (2008).

[7] K. Anderson et al., Tech. Rep. FERMILAB-DESIGN-1998-01, Fermilab (1998).

[8] P. Adamson et al., arXiv:1507.06690 (2015).

[9] R. Burnstein et al., NIM A **541**, 516 (2005).

[10] R. Fruhwirth, NIM A **262**, 444 (1987).

[11] J.Devan and R. Gran, MINERvA TN017 doc:8547 (internal).

[12] S. Dytman et al., MINERvA doc:7532 (internal).

[13] T. Le et al., Phys.Lett.B **749**, 130 (2015).

[14] J. Park, Ph.D. thesis, University of Rochester (2013).

[15] L. Aliaga et al., NIM A **789**, 28 (2015).

[16] http://geant4.cern.ch.

[17] H. Budd, MINERvA doc:9311 (internal).

[18] C. Marshall, MINERvA doc:7589 (internal).

[19] J. Birks, Proc.Phys.Soc.A **64**, 874 (1951).

[20] H. Budd, MINERvA doc:9951 (internal).

[21] S. Mishra, Proceedings of the Workshop on Hadron Structure Functions and Parton Distributions pp. 84–123 (1990).

[22] W. Seligman, Ph.D. thesis, Columbia University (1997).

[23] M. Tzanov et al., Phys.Rev.D **74**, 012008 (2006).

[24] Q. Wu et al., Phys.Lett.B **660**, 19 (2008).

[25] P. Adamson et al., Phys.Rev.D **81**, 072002 (2010).

[26] J. Conrad and M. Shaevitz, Rev.Mod.Phys. **70**, 1341 (1998).

[27] G. D'Agostini, NIM A **362**, 487 (1995).

[28] https://seal.web.cern.ch/seal/MathLibs/Minuit2/html/.

[29] M. Kordosky, MINERvA doc:7433 (internal).

[30] C. Andreopoulos et al., NIM A **614**, 87 (2010).

[31] A. Bodek and J. Ritchie, Phys.Rev.D **24**, 1400 (1981).

[32] S. M. T. Sjostrand and P. Skands, JHEP **0605**, 026 (2006).

[33] S. Dytman, Acta Phys.Polon.B **40**, 2445 (2009).

[34] C. L. Smith, Phys.Rep. **3**, 261 (1972).

[35] D. Rein and L. Sehgal, Ann.Phys. **133**, 79 (1981).

[36] A. Bodek and U. Yang, J.Phys.G **29**, 1899 (2003).

[37] V. Lyubushkin et al., Eur.Phys.J.C **63**, 355 (2009).

[38] A. Aguilar-Arevalo et al., Phys.Rev.D **81**, 092005 (2010).

[39] F. S. R. Gran, J. Nieves and M. V. Vacas, Phys.Rev.D **88**, 113007 (2013).

[40] M. Kordosky et al., MINERvA TN004 doc:7634 (internal).

[41] L. Aliaga and M. Kordosky, MINERvA doc:9472 (internal).

[42] R. Ransome, MINERvA doc:6016 (internal).

[43] D. Schmitz, MINERvA TN016 doc:8646 (internal).

[44] J. Devan, MINERvA TN051 doc:9986 (internal).

[45] R. Gran, MINERvA TN045 doc:9474 (internal).

[46] W. Bergan, MINERvA doc:9929 (internal).

[47] K. Abe et al., Phys.Rev.D **87**, 092003 (2013).

[48] K. Abe et al., arXiv:1509.06940 (2015).

[49] D. Bhattacharya, Ph.D. thesis, Columbia University (1997).

[50] A. Mukhin et al., Sov.J.Nucl.Phys. **30**, 528 (1979).

[51] V. Anikeev et al., Z.Phys.C **70**, 39 (1996).

[52] O. Erriquez et al., Phys.Lett.B **80**, 309 (1979).

VITA

Joshua D. Devan

[redacted]. He attended North Carolina State University, earning a Bachelor of Science in Computer Engineering in 2004. In 2008, he earned a Master of Engineering in Electrical Engineering from Old Dominion University. That same year, he entered the physics program at William and Mary. In 2009, he earned a Master of Science in Physics. [redacted].